



The
University
Of
Sheffield.

INSIGNEO Institute for
in silico Medicine

Mechanical characterisation of bone cells and their glycocalyx

A DISSERTATION PRESENTED
BY
STEFANIA MARCOTTI
TO
THE DEPARTMENT OF MECHANICAL ENGINEERING
UNIVERSITY OF SHEFFIELD
SHEFFIELD, UNITED KINGDOM

IN PARTIAL FULFILMENT OF THE REQUIREMENTS
FOR THE DEGREE OF
DOCTOR OF PHILOSOPHY

SUPERVISOR: PROF. DAMIEN LACROIX
CO-SUPERVISOR: DR. GWENDOLEN C REILLY

NOVEMBER 2017

ABSTRACT

Mechanotransduction refers to the process by which a cell is able to translate mechanical stimulation into biochemical signals. In bone, mechanotransduction regulates how cells detect environmental stimuli and use these to direct towards bone deposition or resorption. The mechanical properties of bone cells have an impact on the way mechanical stimulation is sensed, however, little evidence is available about how these properties influence mechanotransduction.

The aim of the present Thesis was to quantify the mechanical properties of bone cells with a combined experimental and computational approach. Atomic force microscopy was employed to quantify the stiffness of bone cells and their glycocalyx. Changes in cell stiffness during osteocytogenesis were explored. Single molecule force spectroscopy of glycocalyx components was performed to evaluate their anchoring to the cytoskeleton. A single cell finite element model was designed to discern the contributions of sub-cellular components in response to simulated cell nano-indentation.

Wide ranges of variation were found for bone cell stiffness and a method was proposed to determine suitable sample sizes to capture population heterogeneity. By targeting single components of the bone glycocalyx, it was possible to hypothesise different mechanotransduction mechanisms depending on the hyaluronic acid attachment to the cytoskeleton. The developed computational framework showed similar results to the nano-indentation experiments and highlighted the role of the actin cytoskeleton in withstanding compression and distributing strain within the cell.

PUBLICATIONS AND CONFERENCE PRESENTATIONS

BOOK CHAPTERS

Marcotti S and Reilly GC (2017). Chapter: *Sugar-Coating the Cell: The Role of the Glycocalyx in Mechanobiology*. *Mechanobiology: Exploitation for Medical Benefit* (ed. Rawlinson SCF). Wiley Blackwell.

ORAL PRESENTATIONS AT CONFERENCES

Marcotti S. *Do cells in our body know what is happening around us?* Doctoral Academy Conference, Sheffield (UK). June 21, 2016.

Marcotti S, Reilly GC, Lacroix D. *Atomic Force Microscopy evaluation of bone cells and their cell coat*. Annual congress of the European Society of Biomechanics, Lyon (France). July 10-13, 2016.

Marcotti S, Maki K, Adachi T, Reilly GC, Lacroix D. *Characterisation of bone cells and their glycocalyx by Atomic Force Microscopy*. Mechanobiology Club, Sheffield (UK). July 20, 2016.

Marcotti S, Maki K, Adachi T, Reilly GC, Lacroix D. *Nanofishing of Hyaluronic Acid on murine osteoblast precursor cells*. MEIBioeng, Oxford (UK). September 5-6, 2016.

Marcotti S, Reilly GC, Lacroix D. *Indentation properties of bone cell lines showed greater intra-variability than inter-variability*. Annual congress of the European Society of Biomechanics, Seville (Spain). July 2-5, 2017.

POSTER PRESENTATIONS AT CONFERENCES

Marcotti S, Reilly GC, Lacroix D. *Novel engineering approaches to study mechanosensing by the cell coat*. MEIBioeng, Leeds (UK). September 7-8, 2015.

Marcotti S, Reilly GC, Lacroix D. *Bone cell coat mechanical properties evaluation*. Annual meeting of the Biomaterials and Tissue Engineering Group, York (UK). December 15, 2015.

Marcotti S, Maki K, Adachi T, Reilly GC, Lacroix D. *Nanofishing of Hyaluronic Acid on Murine Osteoblast Precursor Cells*. Annual meeting of the Orthopaedic Research Society, San Diego (CA). March 19-22, 2017.

Marcotti S, Reilly GC, Lacroix D. *Experimental and computational investigation of bone cell nanoindentation*. Insigneo showcase, Sheffield (UK). May 11, 2017.

Marcotti S, Reilly GC, Lacroix D. *Experimental and computational investigation of bone cell nanoindentation*. Mechanical Engineering PhD Poster Day, Sheffield (UK). May 15, 2017.

Marcotti S, Reilly GC, Lacroix D. *Cell stiffness dynamically changes during bone cell differentiation*. European Cell Mechanics Meeting, Lake Windermere (UK). June 21-23, 2017.

Marcotti S, Reilly GC, Lacroix D. *Cell stiffness dynamically changes during bone cell differentiation*. Joint Mechanobiology Club / CMIAD workshop, Sheffield (UK). July 18, 2017.

Marcotti S, Reilly GC, Lacroix D. *A multi-structural single cell finite element model to study bone cell mechanical properties*. Simulia Regional User Meeting, Warrington (UK). October 18-19, 2017.

Acknowledgements

To my supervisors, Prof. Damien Lacroix and Dr. Gwen Reilly, for giving me the freedom to explore and learn, and for their guidance and advice.

To Prof. Taiji Adachi, for hosting me in his lab in Kyoto and for his supervision on the single molecule force spectroscopy experiments. To Dr. Koichiro Maki, for his friendly support throughout my experience in Japan.

To the people of Insigneo, for their help and smiles every day of the last three years.

To Silvia, for being my family away from home. To Alessandro, for the much needed tech advice and the photography side business. To Claudia, for the music and puns. To Claudi, for the fruitful discussions in front of a cup of tea. To Katia, for the cooking and lavish food experiments. You all have made the difference.

TO MY PARENTS,
WHO TAUGHT ME HOW TO DANCE IN THE RAIN

Contents

ABSTRACT	iii
LIST OF FIGURES	xiii
LIST OF TABLES	xvii
LIST OF ABBREVIATIONS	xix
1 INTRODUCTION	3
1.1 Background	3
1.2 Objectives	4
1.3 Chapters synopsis	5
2 LITERATURE REVIEW	7
2.1 Bone at the cellular scale	7
2.2 Mechanotransduction	13
2.3 Measuring mechanical properties by AFM	17
2.4 Single cell computational modelling	28
3 VARIABILITY OF THE MECHANICAL PROPERTIES OF A SINGLE BONE CELL POPULATION	35
3.1 Introduction	35
3.2 Materials & Methods	37
3.3 Results	48
3.4 Discussion	57

3.5	Conclusions	65
4	EVALUATION OF THE BONE GLYCOCALYX MECHANICAL PROPERTIES BY AFM NANO-INDENTATION	67
4.1	Introduction	67
4.2	Materials & Methods	70
4.3	Results	81
4.4	Discussion	96
4.5	Conclusions	98
5	CHANGES IN CELL MECHANICAL PROPERTIES DURING BONE DIFFER- ENTIATION	101
5.1	Introduction	101
5.2	Materials & Methods	103
5.3	Results	110
5.4	Discussion	131
5.5	Conclusions	133
6	SINGLE MOLECULE FORCE SPECTROSCOPY OF HYALURONIC ACID	135
6.1	Introduction	135
6.2	Materials & Methods	140
6.3	Results	154
6.4	Discussion	161
6.5	Conclusions	164
7	SINGLE CELL FINITE ELEMENT MODELLING	167
7.1	Introduction	167
7.2	Materials & Methods	169
7.3	Results	178
7.4	Discussion	183
7.5	Conclusions	185
8	DISCUSSION	187
8.1	General discussion	187

8.2	Limitations and future directions	190
8.3	Summary and conclusions	194
	REFERENCES	196
	ALPHABETICAL INDEX	219

List of Figures

2.1.1	Components of an animal eukaryotic cell	8
2.1.2	Bone cell types	11
2.1.3	Basic multicellular unit	12
2.2.1	Proposed mechanism for osteocyte mechanotransduction	16
2.3.1	AFM basic configuration	18
2.3.2	AFM force spectroscopy diagram	20
2.3.3	AFM single molecule force spectroscopy	27
3.2.1	Cell nucleus indentation grid	39
3.2.2	Methodology summary	41
3.2.3	Data pre-processing - step 1	42
3.2.4	Data pre-processing - step 2	43
3.2.5	Data pre-processing - step 3	43
3.2.6	Data pre-processing - step 4	44
3.2.7	Hertz model fitting	46
3.3.1	Young's modulus vs. indentation locations and series	49
3.3.2	Young's modulus vs. indentation depth	52
3.3.3	Cell morphology	53
3.3.4	Young's modulus vs. sample size	55
3.3.5	Percent deviation vs. sample size	56
3.4.1	Quantitative Imaging of cell	59
4.1.1	Electron microscopy of the endothelial glycocalyx	69
4.2.1	Brush model: geometrical considerations	74

4.2.2	Brush model: cantilever deflection vs. height	78
4.2.3	Brush model: undeformed sample position	78
4.2.4	Brush model: brush grafting density and length fitting	79
4.2.5	Point-wise approach: indentation calculation	81
4.3.1	Confocal image of HA	82
4.3.2	Confocal image of HA: Z-stack reconstruction	82
4.3.3	Slope detection: force vs. height, linear	83
4.3.4	Slope detection: force vs. height, logarithmic	84
4.3.5	Hertz model: Young's modulus for probes of different sizes	86
4.3.6	Hertz model and point-wise approach: Young's modulus	92
4.3.7	Point-wise approach: glycocalyx thickness	93
4.3.8	All models: cell body Young's modulus	95
5.2.1	Differentiated IDG-SW ₃ cells	106
5.2.2	Cell nucleus and periphery indentation grids	109
5.3.1	Confocal images of the basal actin cytoskeleton	111
5.3.2	Confocal Z-stack reconstruction	111
5.3.3	Confocal images of the apical actin cytoskeleton	111
5.3.4	Young's modulus vs. indentation depth - preOB, nucleus	113
5.3.5	Young's modulus vs. indentation depth - OB, nucleus	114
5.3.6	Young's modulus vs. indentation depth - preOC, nucleus	115
5.3.7	Young's modulus vs. indentation depth - OC, nucleus	116
5.3.8	Young's modulus vs. indentation depth - preOB, periphery	117
5.3.9	Young's modulus vs. indentation depth - preOC, periphery	118
5.3.10	Young's modulus vs. indentation depth - OC, periphery	119
5.3.11	Young's modulus vs. indentation depth - preOB	120
5.3.12	Young's modulus vs. indentation depth - preOC	121
5.3.13	Young's modulus vs. indentation depth - OC	122
5.3.14	Young's modulus vs. indentation depth - nucleus	123
5.3.15	Young's modulus vs. indentation depth - periphery	124
5.3.16	Young's modulus vs. indentation depth	125
5.3.17	Cell morphology	129
6.1.1	Classification of rupture events	139

6.2.1	Localisation of rupture events - step 1	144
6.2.2	Localisation of rupture events - step 2	145
6.2.3	Localisation of rupture events - step 3	145
6.2.4	Localisation of rupture events - step 4	146
6.2.5	Localisation of rupture events - step 5	147
6.2.6	Localisation of rupture events - step 6	148
6.2.7	Localisation of rupture events - step 7	149
6.2.8	Classification of rupture events	151
6.2.9	Histogram of extend baseline slope	152
6.3.1	Rupture distance from contact point	155
6.3.2	Rupture distance from contact point vs. slope	156
6.3.3	Membrane tethers force	157
6.3.4	Rupture events count	158
6.3.5	Multiple rupture events slope	159
6.3.6	Force-dependent system lifetime	160
7.2.1	Confocal images segmentation	170
7.2.2	Three-dimensional image reconstruction	171
7.2.3	Basal and apical actin bundles	173
7.2.4	FE model - single cell	174
7.2.5	FE model - indenting locations	177
7.3.1	Reaction forces at the cell base	179
7.3.2	FE vs. AFM comparison	180
7.3.3	Strain of the apical actin bundles	182

List of Tables

2.3.1	Young's modulus of bone cells	23
2.3.2	Stiffness of the endothelial glycocalyx	25
3.3.1	Population Young's modulus	50
3.3.2	Morphological parameters	54
3.4.1	Literature on Young's modulus of bone cell nucleus	63
4.3.1	Hertz model: population Young's modulus	87
4.3.2	Brush model: fitted parameters	89
4.3.3	Point-wise approach: population Young's modulus	91
4.3.4	Point-wise approach: glycocalyx and cell body Young's modulus	92
5.3.1	Young's modulus - nucleus	126
5.3.2	Young's modulus - periphery	127
5.3.3	Morphological parameters	130
5.3.4	Sample size	130
6.3.1	Successful target rate	154
7.2.1	Material and finite element properties	175

List of abbreviations

ALP	Alkaline Phosphatase
AFM	Atomic Force Microscopy
APTES	(3 – <i>Aminopropyl</i>) <i>triethoxysilane</i>
ATP	Adenosine Triphosphate
BMU	Basic Multicellular Unit
β -GP	β -Glycerophosphate
BSA	Bovine Serum Albumin
CoD	Coefficient of Dispersion
CS	Chondroitin Sulphate
DAPI	4',6 – <i>diamidino</i> – 2 – <i>phenylindole</i>
Dmp ₁	Dentin matrix acidic phosphoprotein 1
DMT	Derjaguin-Muller-Toporov model
E	Young's modulus
ECM	Extracellular Matrix
ERM	Ezrin-Radixin-Moesin protein family
FBS	Foetal Bovine Serum
FE	Finite Element
FRET	Fluorescence-resonance energy transfer
GAG	Glycosaminoglycan
GFP	Green Fluorescent Protein

HA	Hyaluronic Acid
HAase	Hyaluronidase
HABP	Hyaluronic Acid Binding Protein
HAS	Hyaluronic Acid Synthase
HS	Heparan Sulphate
INF- γ	Interferon- γ
IQR	Inter-Quartile Range
JKR	Johnson-Kendall-Roberts model
MEM	Minimum Essential Alpha Eagle medium
NO	Nitric Oxide
ν	Poisson's ratio
OB	Osteoblast
OC	Osteocyte
PBS	Phosphate Buffer Solution
PGE ₂	Prostaglandin E ₂
PS	Penicillin-Streptomycin
PSG	Penicillin-Streptomycin-Glutamine
QI	Quantitative Imaging
R^2	Coefficient of Determination
ρ	Spearman's Coefficient of Correlation
RoV	Ratio of Variances
SEM	Standard Error of the Mean
SMAD	Small Mother Against Decapentaplegic homolog
SMFS	Single Molecule Force Spectroscopy
TRITC	Tetramethylrhodamine
Wnt	Wingless-related Integration Site

1

Introduction

This chapter includes an overview of the Thesis project background, a list of its objectives and a detailed index of what can be found in each chapter.

1.1 BACKGROUND

Mechanotransduction is the process for which a cell is able to translate mechanical stimulation into biochemical signals. This process is involved in the maintenance of cell homoeostasis and often plays a role in pathological situations [1]. In bone, mechanotransduction regulates bone adaptation and therefore how cells sense environmental stimuli and direct towards bone deposition or resorption [2].

The elements of the cell responsible for this process in a generic cell are considered to be the ones with functions of generating and bearing the cellular internal forces, such as the cytoskeleton and the adhesion complexes [3]. The glycocalyx, a proteoglycan matrix on the outer cell membrane, has also been proposed as a transmitter of mechanical signals into the internal cell compartments [4].

The mechanisms by which bone mechanotransduction occurs are not fully understood [5]. While various studies focused on the biological pathways by which the bone mechanotransduction signalling works [5–8], less evidence is available on how cell mechanical properties affect this process. The mechanical properties of single cell components and of the cell as a whole have in fact a strong impact in the way the mechanical stimulation is sensed [9, 10].

The aim of the present Thesis is to quantify the mechanical properties of bone cells and of their glycocalyx as a starting point for further investigations on bone mechanotransduction. Both experimental and computational approaches have been used to obtain a range of quantitative data. The experimental approach consisted in using the Atomic Force Microscopy (AFM) technique to test cell mechanical properties by nano-indentation and to get quantitative stiffness values in terms of the Young's modulus. The same technique has been also employed to pull single glycocalyx molecules and to study their mechanical behaviour. The computational approach was based on designing a single cell Finite Element (FE) model comprising different subcellular components. This model was tested to evaluate the contributions of these elements when nano-indentation was simulated.

1.2 OBJECTIVES

The objectives of the present work are:

1. To design a protocol to reliably test and analyse large samples of bone cells by AFM.
2. To use the aforementioned protocol to gain quantitative stiffness measures of bone cells.
3. To verify if during indentation the glycocalyx is detected and its mechanical properties can be quantified.
4. To compare the mechanical properties of bone cells at different stages of differentiation.
5. To characterise the bone glycocalyx main component (hyaluronic acid) by single molecule mechanical testing.

6. To build an FE single cell model to quantify the contributions of single cell components during indentation.

1.3 CHAPTERS SYNOPSIS

- *Chapter 1 - Introduction*: this chapter includes an overview of the Thesis project background, a list of its objectives and a detailed index of what can be found in each chapter.
- *Chapter 2 - Literature Review*: this chapter presents an introduction to the topics discussed in the Thesis. It includes an overview of the bone cell features, the concept of mechanotransduction and its investigation by AFM and by FE computational modelling.
- *Chapter 3 - Variability of the mechanical properties in a single bone cell population*: this chapter presents the results obtained by AFM nano-indentation on bone cells focusing on the variability of the mechanical properties of a single bone cell population. The protocol design and an evaluation of the necessary sample size to reflect standard population heterogeneity are reported.
- *Chapter 4 - Evaluation of the bone glycocalyx mechanical properties by AFM nano-indentation*: the protocol developed in Chapter 3 is applied to verify the possibility of sensing the glycocalyx during nano-indentation experiments. Additional methods and results are presented in this chapter.
- *Chapter 5 - Changes in cell mechanical properties at different stages of bone cell differentiation*: in this chapter, an application is designed to test different bone cell lines by means of AFM nano-indentation. The focus is on the changes in mechanical properties during bone differentiation.
- *Chapter 6 - Single molecule force spectroscopy of Hyaluronic Acid*: this chapter includes the results of single glycocalyx molecule testing. The experiments presented in this chapter were performed under the additional supervision of Prof. Taiji Adachi at the Institute for Frontier Life and Medical Sciences (Department of Biosystems Science, Kyoto University, Japan).

- *Chapter 7 - Single cell Finite Element modelling:* in this chapter, the computational results are presented. The Finite Element single cell model design and the simulation parameters are explained together with the obtained outcomes.
- *Chapter 8 - Discussion:* the overall results of the Thesis are discussed in this chapter, with focus on the limitations and possible future directions of the present work. The concluding remarks and the scientific impact of the Thesis are summarised.

2

Literature Review

This chapter presents an introduction to the topics discussed in the Thesis. It includes an overview of the bone cell features, the concept of mechanotransduction and its investigation by AFM and by FE computational modelling.

2.1 BONE AT THE CELLULAR SCALE

The following section introduces the components of a generic animal cell and the types and functions of cells in bone.

2.1.1 THE ANIMAL EUKARYOTIC CELL

Eukaryotic cells are the building blocks of eukaryotic organisms, such as animals, plants and fungi. Their defining feature which sets them apart from prokaryotic cells is the presence of membrane-bound organelles, such as the nucleus. A schematic of the animal eukaryotic cell components is depicted in Fig. 2.1.1.

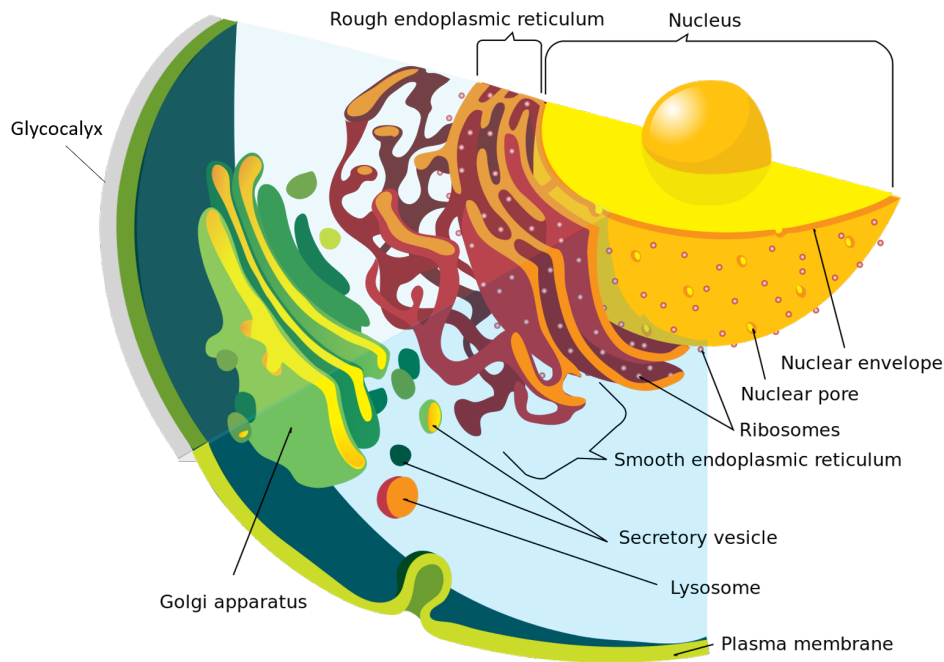


Figure 2.1.1: Schematic of the components of an animal eukaryotic cell

The main cell components are [11]:

- *plasma membrane*: the plasma membrane encloses the cell and defines the boundary between the internal and the external compartments. It is composed of a lipid bilayer of about 5 nm which provides the structure and serves as an impermeable barrier. The bilayer is decorated with various proteins, which mediate most of the membrane functions, such as molecule transport, catalysis, adhesion to the extra-cellular membrane and neighbouring cells, signal reception and transduction.
- *nucleus*: the nucleus contains the main genome and synthesises the DNA and RNA. It is enclosed by a double membrane called the nuclear envelope which controls the passage of molecules from and to the cytoplasm. The DNA is organised into chromosomes.
- *cytoplasm*: the cytoplasm consists of everything enclosed by the plasma membrane except the nucleus. This includes the cytosol and the cytoplasmic organelles.

- *endoplasmatic reticulum*: the endoplasmatic reticulum produces lipids and stores Ca^{2+} ions. The ribosomes are tethered to its surface and play a central role in the production of proteins.
- *Golgi apparatus*: the Golgi apparatus is located close to the nucleus. It receives proteins and lipids from the endoplasmatic reticulum. After the relevant modifications, it delivers them to other cell compartments.
- *mitochondria*: mitochondria are organelles of about $0.5 - 1 \mu\text{m}$ diameter and can be considered the energy producers in the cell. They generate ATP (adenosine triphosphate) molecules which are used by the cell as chemical energy for metabolic reactions.
- *lysosomes*: lysosomes are organelles responsible for the digestion of complexes no longer of use in the cell.
- *cytoskeleton*: the cytoskeleton is a system of filaments which represents the structural scaffold of the cell. Its functions relate to cell shape maintenance, cell movement, cell mechanical interaction with the environment, cell internal structural rearrangement and intracellular trafficking. It is composed of three families of protein molecules arranged into filaments: the actin filaments which are involved in cell locomotion and determine the cell surface shape, the microtubules which control intracellular transport and organelles positioning, the intermediate filaments which provide resistance to shear stress.
- *glycocalyx*: the glycocalyx is a proteoglycan-rich coating on the external surface of the cell membrane. Its components can be connected to the cell membrane via proteoglycan-binding receptors or can span through the membrane double layer. The glycocalyx has overall a negative charge and attracts water, causing it to be a very soft and water-saturated material. Its gel-like characteristics modulate cell adhesion, cell communication and cell sensing [12].
- *adhesion complexes*: the adhesion complexes are protein complexes which regulate cell-cell and cell-substrate adhesion.

2.1.2 THE BONE CELL

Osteogenesis defines the process of bone formation. This process involves the progression of mesenchymal stem cells into bone tissue following one of two distinct modes [13]. The first mode is denominated *intramembranous ossification* and mainly occurs in the skull bones. During intramembranous ossification, mesenchymal cells proliferate and differentiate into capillaries and bone precursor cells. The second mode is *endochondral ossification* and consists of mesenchymal cells forming cartilage tissue which is subsequently replaced by bone.

Four different cell types are present in bone [14]: osteoblasts, bone lining cells, osteocytes and osteoclasts (Fig. 2.1.2).

- *Osteoblasts*: osteoblasts are the bone precursor cells and are derived from mesenchymal stem cells. They are located on the bone surface and their main function is to form bone by secreting bone matrix. Firstly, the organic matrix (osteoid) is deposited by secretion of collagen proteins, proteoglycans and other proteins, such as osteonectin and osteopontin. Secondly, mineralisation occurs by means of hydroxyapatite-like crystals. These crystals consist of mostly calcium and phosphate and are formed in vesicles released by the osteoblast membrane (matrix vesicles). When these vesicles rupture the hydroxyapatite crystals are seeded into the organic matrix promoting its mineralisation. Mature osteoblasts can undergo apoptosis or can differentiate into osteocytes or bone lining cells.
- *Bone lining cells*: bone lining cells are quiescent osteoblasts which line the bone surfaces when bone remodelling is not occurring. The function of these cells is not completely understood but they do play a role in osteoclast differentiation and communication between osteoclasts and bone matrix during resorption. They are also involved in the formation of the bone remodelling sites, referred to as basic multicellular units (BMU).
- *Osteocytes*: osteocytes are derived from the mesenchymal stem cell lineage via osteoblast differentiation. This process is called osteocytogenesis and involves dramatic morphological and structural changes with the formation of long dendritical processes (or dendrites) spanning long distances in the

mineralised bone matrix. Osteocytes are located in a system of channels called the lacunocanalicular network. Their processes can connect to neighbouring osteocytes and to bone lining cells on the bone surface. They have been recognised as bone mechanosensors due to their network being able to sense mechanical stimuli and therefore to orchestrate bone remodelling through signalling.

- *Osteoclasts*: osteoclasts are terminally differentiated multinucleated cells originating from the haematopoietic cell lineage. Their main function is to reabsorb bone, contrasting the action of osteoblasts. The osteoclasts reabsorb the bone matrix by acidifying the surrounding area and therefore dissolving the hydroxyapatite crystals.

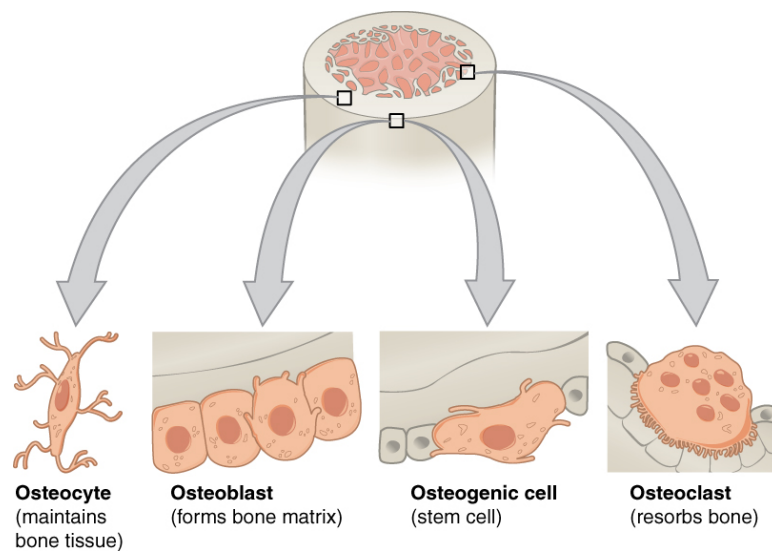


Figure 2.1.2: Schematic of bone cell types. Osteoblasts are the bone forming cells, derived from osteogenic stem cells and differentiating into osteocytes when completely surrounded by bone matrix. Osteoclasts are the bone reabsorbing cells. By OpenStax College - Anatomy and Physiology [CC-BY-3.0].

All the bone cells dynamically participate in the processes of bone modelling and remodelling [15] (Fig. 2.1.3). Bone modelling refers to skeletal growth and the fracture healing mechanism. Bone remodelling happens continuously in adult bone and represents the balance between bone deposition and bone loss. Any abnormal increase in osteoclast or osteoblast activity results in bone pathologies, such as osteoporosis (resorption exceeds formation) or osteopetrosis (formation exceeds resorption) [14].

A strong interdependence occurs between bone remodelling and mechanical stimulation. Effectively, the balance between bone formation and bone resorption is finely tuned in response to any changes in mechanical loading of the skeleton [2, 16, 17]. Understanding the mechanisms that lead to this mechanical signalling would allow for the development of new treatments for highly common diseases and pathological conditions, such as osteoporosis or bone fracture [18].

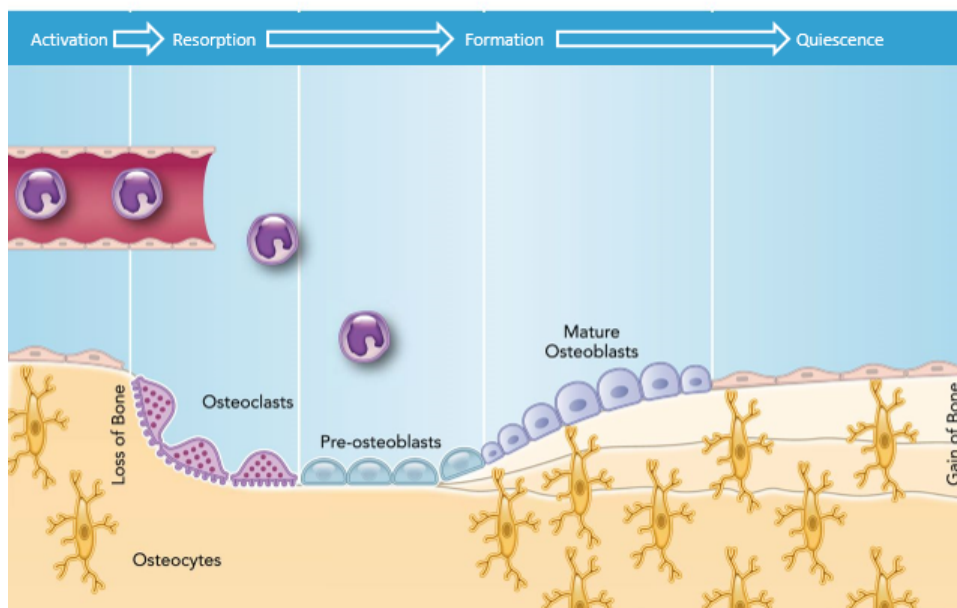


Figure 2.1.3: Schematic of a basic multicellular unit (BMU) for bone remodelling. Figure adapted from Siddiqui et al. 2016 [19], no permission required.

2.2 MECHANOTRANSDUCTION

The following section introduces the concept of mechanotransduction, together with the cell components involved in this process with particular focus on bone cells.

Mechanotransduction is defined as the process used by cells to convert mechanical signals into electrical/biochemical response [2]. In bone, evidence has been provided that there is a relationship between mechanical forces and gene expression, protein synthesis, cell function and skeletal integrity. However, the mechanisms leading to this response are not fully understood [5]. Diverse signalling cascades have been proposed suggesting that not a single pathway controls the mechanoreponse. The regulation of bone remodelling seems to be mediated by different pathways used by growth factors and mediators, such as nitric oxide (NO), prostaglandin E₂ (PGE₂), calcium (Ca²⁺) and ion channels, small mother against decapentaplegic homolog (SMAD) signalling, and Wingless-related integration site (Wnt) signalling [5–8].

Various mechanisms triggering bone cellular mechanoreponse have been proposed such as matrix strain, hydraulic pressure, and interstitial fluid flow driven by bone matrix deformations [16, 18]. For each of these mechanical load-derived stimuli experimental evidence has been reported suggesting possible interactions among different mechanical triggers. The most studied physical trigger of bone mechanoreponse is fluid flow-induced shear stress, first proposed in 1994 by Weinbaum and co-workers [20]. It was demonstrated shortly after, that bone cells *in vitro* respond to mechanical stimulation within values ranging consistently with those expected to occur *in vivo* [21]. Those values correspond to 1 – 3 Pa of shear stress on the cell membrane at frequencies ranging between 1 and 3 Hz and were predicted to occur on osteocytes in the lacunocanalicular network during normal activity [5, 22].

A generic cell has various elements sensitive to mechanical loading that are able to dynamically change their structural conformation due to external forces. These sensitive structures are the same as those involved in the generation and bearing of the cellular internal forces, such as cytoskeletal proteins and both cell-cell and cell-substrate adhesion complexes [3]. The cytoskeleton is considered to be the

major structure influencing biomechanical response, i.e. the transmission of load-induced forces through the extracellular matrix (ECM), the cell surface and the cytoskeletal network [1].

In endothelial cells the glycocalyx, the proteoglycan-rich coating on the outer cell membrane, plays a role in this transmission by sensing the blood fluid flow induced shear stress and transferring the mechanical information onto the cytoskeleton (see [4] for a review). The ‘wind in the trees’ model was suggested to explain the mechanotransductive function of the endothelial glycocalyx: the fluid flow (wind) is sensed by the proteoglycan glycosaminoglycans (GAGs) (branches) and transmitted to the cell membrane or the cytoskeleton (ground) through the proteoglycan core protein (tree trunk) [4]. The glycocalyx core proteins are sufficiently stiff to act as transmitters without significant deflection [23, 24] and it has been experimentally showed that mechanoresponsive signals can be transferred by the endothelial glycocalyx [25, 26].

Similar mechanisms of mechanical force transmission by the glycocalyx have been proposed for other cell types, among which are bone cells [27]. An idealised mathematical model of the osteocyte dendrites has been proposed to explain the mechanical transmission of forces in bone from the ECM through the adhesion proteins onto the cytoskeleton. This model represents an individual canaliculus with its central cell process as two concentric cylinders connected through a series of filamentous tethering elements [20]. These elements represent a proteoglycan matrix called the bone glycocalyx with an analogy to the endothelial glycocalyx and act as strain-amplifiers in respect to the cell membrane and its intracellular actin cytoskeleton [28] (Fig. 2.2.1).

This hypothesis was supported by *in vitro* studies by this group and others which characterised the bone cell glycocalyx to include a substantial hyaluronic acid (HA) component [29–31], with other proteoglycans in minor percentage [32, 33]. Given the role of HA in endothelium mechanobiology [34, 35] and its function in cell attachment [36], it was hypothesised that an HA-rich glycocalyx in bone would be important for mechanotransduction [12].

Since the initial model for the osteocyte glycocalyx [20], further works from the same group highlighted the importance of integrins, as it was shown with ultrastructural studies that the dendritic processes would contain small hillocks dir-

ectly in contact with the bone wall by protein binding [37]. It was then postulated that the integrin attachments would be more important for mechanotransduction than the tethering elements. In parallel, studies showed heparan sulphate proteoglycans (i.e. perlecan) to be present around osteocytes in the lacunocanalicular network and to be critical to maintaining the size of the pericellular space [38]. Gathering together these findings, it could be hypothesised that heparan sulphate proteoglycans possibly supported by HA would represent the tethering elements stabilising the integrin attachments and that all three components could be key players in bone mechanotransduction [12] (Fig. 2.2.1).

It should be noted, however, that very limited experimental evidence is available on the osteocyte pericellular matrix, in particular regarding its viscosity and stiffness, which could help elucidating the mechanical stimuli sensed by the cell *in situ*, as discussed in the following paragraphs.

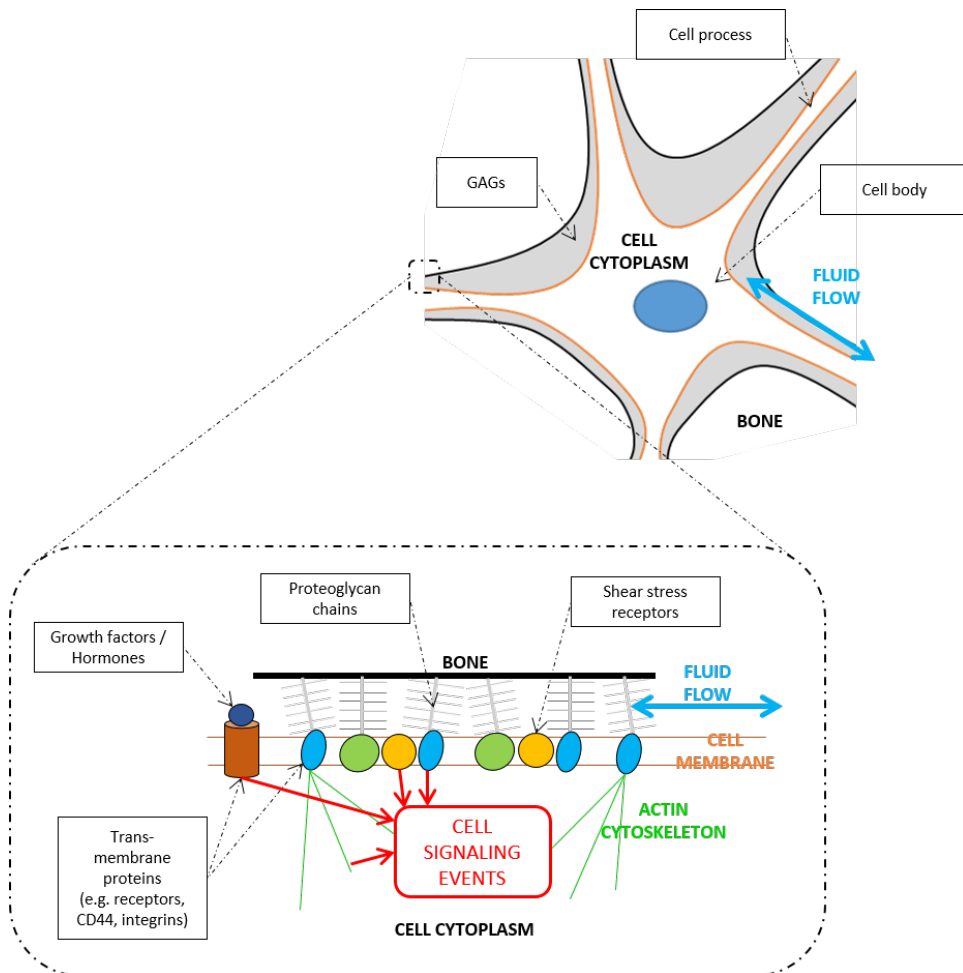


Figure 2.2.1: Proposed mechanism for osteocyte mechanotransduction in the lacunocanalicular network [20, 28]. The cell outer space is filled with tethering elements, i.e. the bone glycocalyx, which are able to transmit forces from the ECM onto the cytoskeleton. Figure adapted from [12] with permission.

2.3 MEASURING MECHANICAL PROPERTIES BY AFM

The following section reviews the Atomic Force Microscopy (AFM) method and its application to test mechanical properties of biological samples in the context of mechanotransduction.

A better understanding of the intrinsic properties of the cell is needed to elucidate mechanotransduction mechanisms. The cell's mechanical properties play a crucial role in the transmission of mechanical forces. They determine the magnitude of the mechanical stimuli sensed [9] and govern the relationship between local forces and deformation [10]. Single cell mechanical properties have been tested with various methods, such as micro-aspiration, optical tweezers and AFM [39]. Recently, the latter technique has been largely employed due to its ability to perform controlled nano-indentation of biological samples [40, 41].

2.3.1 ATOMIC FORCE MICROSCOPY

The working principle of the AFM relies on the measured and controlled interaction between a tip and a sample [10]. The tip can track surface morphology with nanometric resolution or can be force-controlled to probe mechanical properties of the specimen by pressing or pulling it. The basic configuration includes the following parts (Fig. 2.3.1):

- *piezoelectric scanner*: the piezoelectric scanner allows for positioning and movement of the sample by application of voltage on a reversibly deformable piezoelectric ceramic material.
- *cantilever*: a sharp tip at the end of a flexible cantilever allows for sample probing by force interaction. Cantilevers are normally made of silicon nitride and present tips of various shapes and dimensions depending on the specific application. The geometry of the cantilever determines its mechanical properties and they are normally classified depending on their spring constant and resonance frequency. When mounted on the AFM the cantilever is fixed to a rigid substrate and depending on whether the interaction is attractive or repulsive it moves towards or away from the sample.

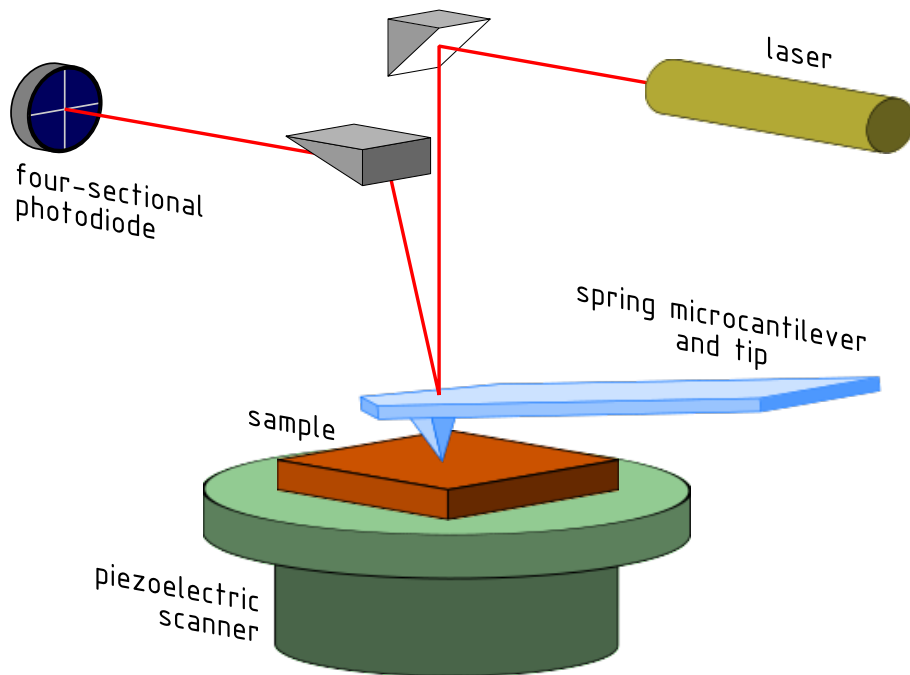


Figure 2.3.1: Schematic of the AFM basic configuration. The sample mounted on a moving scanner is probed by a cantilever which deflection is monitored by a detection system. By GregorioW [CC-BY-SA-3.0].

- *deflection detecting system:* the cantilever vertical deflection is detected by a specific system relying on the optical beam deflection method. A laser beam is reflected on the cantilever onto a photo-detector. The photo-detector consists of multiple sectors each carrying a photo-diode. When the cantilever is deflected, the laser moves between the sectors and its position is recorded. High sensitivity is achieved by exploiting the optical magnification caused by the fact that the distance between the cantilever and the detector is much greater than the length of the cantilever.

AFM testing can be performed in dry or liquid environment. The latter condition is important for biological applications as it enables the probing of samples in physiological conditions immersed in liquid solutions. The measurements that can be performed by AFM fall in two main categories, imaging or spectroscopy.

- When imaging, the tip is scanned over the surface to obtain a map of the

sample morphology. This can be obtained by measuring the interactions between the sample and the cantilever in static or resonant mode. In *static mode*, the static deflection of the cantilever is measured. The most common operation method in static mode is contact mode: the tip is maintained in contact with the sample and the deflection is clamped during scanning by a feedback loop. Contact mode is often not suitable for soft biological samples such as living cells as the sample surface experiences strong shear stress and can be irreversibly damaged. In *resonant mode*, the cantilever is forced to resonate and the changes in oscillation due to interactions with the sample are measured. A common operation method in resonant mode is non-contact mode: the oscillating tip is brought close to the sample and senses the van der Waals attractive forces which shift its resonance frequency. The amplitude of these shifts in the oscillation is monitored and used for feedback while scanning the sample. In non-contact mode the damage to the sample is minimised but this mode is not suitable for liquid environments.

- During spectroscopy measurements, the amount of force exerted on the probe when brought close to the sample surface is recorded. By doing so it is possible to obtain additional data to the morphology, as the long range interaction forces contain information on the mechanical and chemical properties of the sample. Force curves show the deflection of the cantilever during a vertical movement of the scanner: the tip extends towards the surface, indents it and is then retracted until no contact is recorded, as shown in Fig. 2.3.2. The movement of the cantilever towards the sample is referred to as “extend”, the movement of the cantilever away from it as “retract”. Force spectroscopy mode can be employed in liquid and has various applications in the biomedical field, such as measuring binding forces of ligand-molecule complexes, imaging substrates depending on their physical properties or obtain maps of the sample mechanical properties (e.g. stiffness).

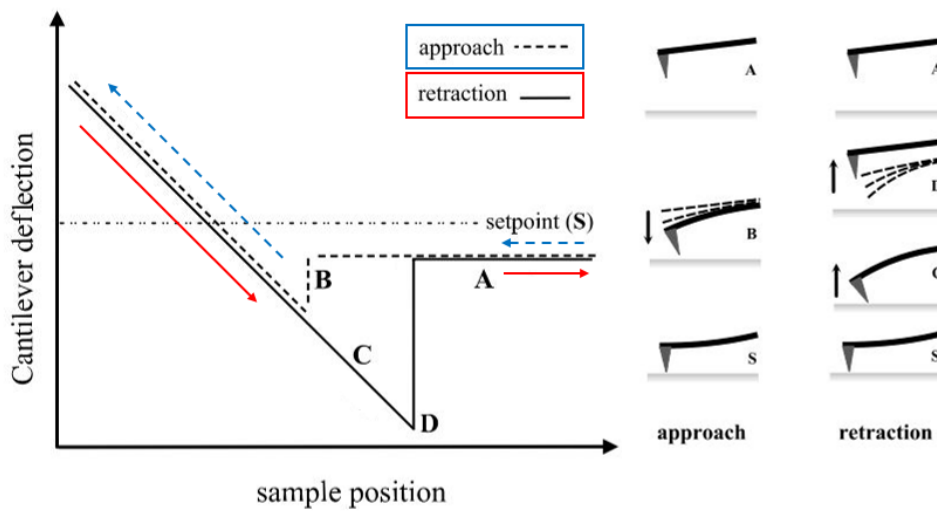


Figure 2.3.2: Schematic of the AFM force spectroscopy deflection vs. position curve. A-B: the tip is approaching the surface, B: the tip is in contact with the surface, B-C: the sample is indented, D: the contact between the tip and the surface ends, D-A: the tip is resting and no force is applied to it. The direction of the approach is depicted in blue (dashed line), the direction of the retraction in red (solid line). Figure adapted from [10] with permission.

2.3.2 MECHANICAL PROPERTIES OF BONE CELLS BY NANO-INDENTATION

AFM force spectroscopy has been widely used to probe living cells. By analysing the force-deformation experimental data, it is possible to investigate elastic and viscoelastic, local and global cell mechanical properties [10]. A commonly used stiffness descriptor for global elastic properties is the Young's modulus, which is obtained by Hertz model fitting on the extend force spectroscopy curve. The Hertz model [42] and its variations have been widely used for cell and biological sample indentation [40, 43], despite strong assumptions of infinitesimal deformation of a homogeneous, isotropic and linear elastic sample. Cells are in fact heterogeneous in composition and present time-dependent mechanical properties [43].

Available Young's modulus values for bone cells tested by AFM are reported in Table 2.3.1.

- *Pre-Osteoblasts*: Takai and co-workers [44] measured the elastic modulus of MC₃T₃ murine pre-osteoblasts when attached to different substrates to study the contribution of the actin and microtubule cytoskeleton when the cell was adherent to various ECM proteins. They found the elastic modulus to be significantly altered by the chosen substrate and binding proteins with an average modulus of about 1 – 2 kPa. The disruption of the actin cytoskeleton caused a significant decrease in the elastic modulus, while the microtubules disruption had no effect. The same cell line was used to study the effect of the cell cycle on the mechanical properties [45]. An increase of elastic modulus during S phase in respect to G₁ phase was found reflecting the mechanical rearrangement of the cytoskeleton. It has been also demonstrated that osteogenic differentiation of pre-osteoblasts affected their mechanical properties [46] with a steady increase of the elastic modulus during culture in osteogenic media on gelatin matrices.
- *Osteoblasts*: Titushkin and co-workers [47] observed distinct mechanical properties of human mesenchymal stem cells in the undifferentiated state compared with those differentiated into osteoblasts, with a decrease in the Young's modulus during differentiation. Similar results were found in another study [48] where a correlation between the day of the differentiation and the resulting mechanical properties was also shown. On the other hand,

much higher Young's moduli and increased values during osteogenic differentiation were found by Yourek and co-workers [49], while Docheva and co-authors [50] observed comparable stiffness values by using separate lines representing mesenchymal stem cells and osteoblasts. Osteoblast mechanical properties have been shown to decrease in the presence of estrogen, a hormone involved in the onset of osteoporosis [51].

- *Osteocytes*: Sugawara *et al.* [52] isolated bone cells from embryonic chicken calvariae and studied their mechanical properties during differentiation from osteoblasts to pre-osteocytes and osteocytes testing both the nuclear and peripheral areas. They observed a progressive decrease of the Young's modulus, with the cell edges stiffer than the centre. Some values for osteocyte elasticity were also made available for a murine osteocyte cell line (MLO-Y4) [53].

From Table 2.3.1 it is possible to note that no agreement has been found on absolute elasticity values for the different cell types. The possible causes of this variation might reside in physiological variability between samples or in different AFM technical methods. Moreover, no guidelines are available on the minimum sample size required to obtain reliable data and the strong assumptions made when using mathematical models to fit specific properties are not always taken into account. In the present work, these issues will be addressed as further discussed in the following chapters.

2.3.3 MECHANICAL PROPERTIES OF THE GLYCOCALYX BY NANO-INDENTATION

AFM force spectroscopy has been also applied to study the mechanical properties of the glycocalyx. The available data in literature relates to the endothelial glycocalyx due to its involvement in mechanotransduction and pathological conditions in blood vessels, while no information is available on the bone glycocalyx mechanical properties. The obtained results for the endothelial glycocalyx stiffness are reported in Table 2.3.2.

Oberleithner and co-workers [54] measured the stiffness of the endothelial glycocalyx of split open *ex-vivo* human umbilical cord arteries. As a proof of concept

Table 2.3.1: Available Young's modulus values for bone cells tested by AFM. Cell type indicates the bone cell family tested; cell origin indicates the species the cells belong to; probing location indicates the region of the cell tested and other additional information on the cell cycle phase if available, (- indicates not stated probing location); Young's modulus values are expressed as mean (standard error of the mean) but for entries marked with * which are expressed as mean (standard deviation).

Cell type	Cell origin	Probing location	Young's modulus [kPa]	Ref
Pre-Osteoblast	Mouse	Nucleus	0.9 (0.4)	[44]
		Periphery, G1 phase	3.5 (0.3)	[45]
		Periphery, S phase	5.9 (0.5)	[45]
		-	1.5 (0.4)*	[46]
Osteoblast	Chicken	Periphery	12.1 (0.9)	[52]
		Nucleus	8.3 (0.4)	[52]
	Human	Whole cell	1.7 (1.0)	[47]
		Nucleus	2.6 (1.8)	[50]
		Nucleus	0.6 (0.1)	[51]
		Nucleus	1.4 (0.2)	[48]
Pre-Osteocyte	Chicken	-	52.0 (6.0)	[49]
		Periphery	8.0 (0.4)	[52]
		Nucleus	3.2 (0.3)	[52]
Osteocyte	Mouse	Nucleus	3.2, 2.2, 2.0	[53]
	Chicken	Periphery	4.5 (0.2)	[52]
		Nucleus	2.7 (0.3)	[52]

of glycocalyx indentation, they treated bovine aortic endothelial cells with degrading enzymes and measured the stiffness and thickness of the glycocalyx before and after by means of a coupled AFM/fluorescence microscopy set-up. Their measurements showed a glycocalyx thickness of 400 nm and stiffness of 0.25 pN/nm. The same group [55] recently applied a similar protocol to *ex vivo* and *in vitro* samples to analyse the mechanical property changes when the endothelial glycocalyx was subjected to enzymatic degradation or sepsis. Both treatments resulted in softening (i.e. reduced stiffness) and reduction in thickness of the glycocalyx.

O'Callaghan *et al.* [56] tested bovine lung micro-vasculature endothelial cells (BLMVEC) by measuring the glycocalyx elastic properties after selective enzymatic degradation. They treated cells with a cytoskeleton disruptor to discern the cell from the glycocalyx contribution. The resultant glycocalyx elastic modulus was in the range of 250 Pa for an expected glycocalyx thickness of 200 nm. Enzymatic degradation affected the rate of stiffness increase in relation to indentation depth, while the disruption of the cytoskeleton changed the mechanical properties so that the relationship between the modulus and the indentation was lost.

Bai and Wang [57] investigated the spatial and temporal distribution and the mechanical properties of human umbilical vein endothelial cells (HUVEC). They analysed cells at different time points with an intact or degraded glycocalyx. Their findings highlighted a developed glycocalyx after day 14 with a thickness of 300 – 1000 nm and a Young's modulus of 390 Pa.

Marsch and Waugh [58] investigated the endothelial glycocalyx of HUVECs cultured under fluid flow. By using a two-layer model derived from polymer analysis they obtained a glycocalyx thickness of 380 ± 50 nm and a stiffness of 700 ± 500 Pa.

Sokolov and co-workers [59, 60] proposed a protocol to quantitatively measure the elastic modulus of cells by taking into account the contribution of the surface brush. To validate the protocol, human cervical epithelial cells were evaluated obtaining a thickness of the brush of about 1.4 μ m. However, the stiffness of the glycocalyx could not be extrapolated from the customised model.

Glycocalyx stiffness measurements are difficult because of its mesh-like structure. The AFM probe could penetrate it without compression or could not be sensitive enough to detect it. Recently, a different approach has been proposed

Table 2.3.2: Available stiffness values for the endothelial glycocalyx, expressed as average (dispersion) where available. The sample type, the location of testing and the resulting stiffness values are reported. Unavailable data are indicated with -.

Sample	Location	Stiffness		Ref
		[pN/nm]	[Pa]	
<i>Ex vivo</i> bovine arteries	-	0.25	-	[54]
Bovine endothelial cells	Nucleus	-	250 (30)	[56]
Human endothelial cells	Whole cell	-	390	[57]
Human endothelial cells	Nucleus	-	700 (500)	[58]

with application on bacteria cell wall indentation experiments [61]. The force-indentation curves were log-log plotted and it was possible to discern between the contributions of structures presenting different stiffness, i.e. to verify if different structures were sensed. Two straight lines of nonzero gradient were found, implying the indentation of substrates with different mechanical properties. This observation led to the application of a mathematical fitting to the different parts of the data separately.

No information is available in the literature for bone glycocalyx stiffness. This would be needed to help elucidate the bone mechanotransduction mechanisms which allow bone cells to detect mechanical signals from the ECM and to transmit them into the inner cell compartment. In the present work, a protocol will be proposed to investigate the bone glycocalyx by use of AFM nano-indentation. Different mathematical models previously employed to study the endothelial glycocalyx stiffness will be compared.

2.3.4 MECHANICAL PROPERTIES OF THE GLYCOCALYX BY SINGLE MOLECULE FORCE SPECTROSCOPY

A different application of AFM force spectroscopy allows for studying the interactions between single molecules. To this aim, one ligand is immobilised on the cantilever tip and its binding molecule is placed on a sample surface [10]. During the extend of the cantilever towards the sample the ligand is brought in contact

to the molecule and the interactions begin. The cantilever is then retracted and the ligand-molecule bond is loaded with increasing force until rupture. During the retraction, it is possible to observe subsequent tension releases when a force rearrangement occurs in the molecule, e.g. in case of a protein domain unfolding [62], as shown in Fig. 2.3.3. The force-displacement retract curve needs to be interpreted to discern between spurious peaks caused by interactions with the substrate or molecules entanglement and the actual molecule unfolding. The analysis of the unfolding patterns provides information on the mechanical properties of the stretched molecules.

Classical applications of this technique, called Single Molecule Force Spectroscopy (SMFS), involved testing of proteins, DNA strands and molecular motors [63]. Recently, a study focused on SMFS of perlecan, one of the proteoglycans which compose the osteocyte glycoalyx [64]. The rationale was to investigate if the perlecan core protein could sustain physiological fluid flow induced forces without being mechanically degraded, so to demonstrate its involvement in mechanotransduction within the lacunocanicular network. This hypothesis was shown plausible by measuring a Young's modulus of 71 MPa for the perlecan core protein. A different approach was used by Sun and co-authors [65], who were interested in studying the cell membrane properties. They plated cells on a substrate and kept the AFM tip in contact with the cell membrane for 2 – 30 s to then retract it and observe tip-cell interactions. Typical retraction curves showed a series of rupture-like events in force representing the formation and breaking of multiple membrane tethers. The degradation of the glycoalyx caused a decrease in the tether's extraction force, suggesting that the glycoalyx contributed to the biomechanical integrity and heterogeneity of the cell.

No SMFS experiments have been carried out to study the mechanical properties of HA, the main component of bone glycoalyx [29–31]. It was suggested that HA would play a role in bone mechanotransduction [12], given its role in endothelium mechanobiology [34, 35] and in cell attachment [36]. The ability of HA to selectively bind to the actin cytoskeleton has been proposed [66, 67], corroborating the hypothesis of its role in transmitting mechanical forces. However, no quantitative data are available on the mechanical properties of this bond and on the amount of HA molecules bound to the cytoskeleton at a given time. A protocol for SMFS of

HA was designed in the present work and this hypothesis was evaluated.

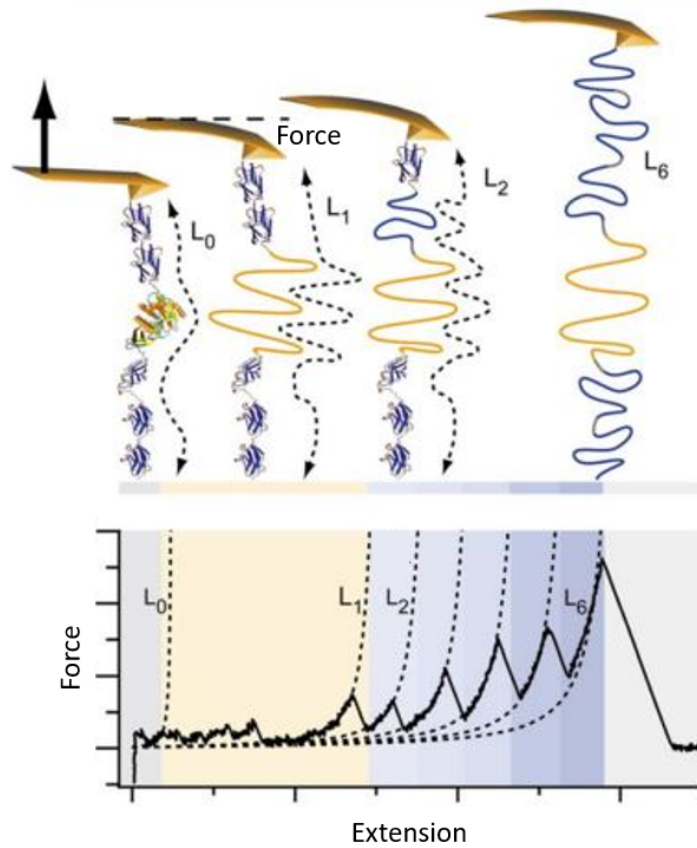


Figure 2.3.3: Schematic of the AFM single molecule force spectroscopy technique. The ligand-loaded tip is lowered in contact with the target molecule and then retracted to visualise domains unfolding corresponding to force drops in the force-distance curves. Figure adapted from [68] with permission.

2.4 SINGLE CELL COMPUTATIONAL MODELLING

This section reviews the available computational models of single cell with a focus on the Finite Element (FE) method .

The interpretation of experimental evidence is key to understand the relationship between cell mechanics and function [69]. To this aim, various computational frameworks have been developed to complement experiments and to provide new insights into cell mechanics. Computational modelling of cells has been demonstrated to be difficult by the interplay between different length-scales and time-scales and between structure, function and external cues.

2.4.1 FINITE ELEMENT METHOD

Continuum mechanics can be used to simulate cell mechanics if the smallest length scale of interest is shorter than the length scale at which the cell properties vary [69]. The FE method is the most common technique to solve continuum mechanics constitutive equations in cell mechanics as non-linearities can be easily included and commercial software is available to solve numerical associated frameworks.

The FE analysis is a numerical method widely used to solve engineering problems in the context of structural analysis, heat transfer, fluid flow, mass transport and electromagnetic potential [70]. It relies on the approximate solution of algebraic equations on discrete points of the continuum: the domain is discretised in smaller units (finite elements) connected at common points (nodes); the equations are formulated for each element and the solution for the whole body is obtained by combining them. For structural analysis problems the displacements and stresses are to be determined in the equilibrium state under a given load, typically using the nodal displacements as variables and the equilibrium equations and force-displacement governing laws to write the algebraic equations. The generalised FE method can be summarised in the following steps [70, 71]:

- *discretisation*: the domain is divided into an equivalent system of finite elements with connected nodes. The size and number of elements need to be balanced between results accuracy and computational expense. Elements

can be one-, two- or three-dimensional: one-dimensional elements consist of truss and beam elements, constituted by a line with one node at each end (linear element) or more (three nodes: quadratic element, four nodes: cubic elements, etc.); two-dimensional elements can be triangular or quadrilateral and present corner nodes (linear elements) or corner and mid-side nodes (quadratic elements); three-dimensional elements are tetrahedral or hexahedral and can be linear or quadratic similarly to two-dimensional ones.

- *element equations*: let us consider a generic triangular linear element with three nodes marked as 1 – 3 in a two-dimensional coordinate system. The forces acting on the nodes are defined by the nodal displacements, the load applied to the element and its initial strain. Forces and corresponding displacements are decomposed in suitable components in (x, y) . The matrices of forces \mathbf{r} and corresponding displacements \mathbf{u} are defined as:

$$\mathbf{r} = \begin{Bmatrix} r_1 \\ r_2 \\ r_3 \end{Bmatrix}, \quad (2.1)$$

$$\mathbf{u} = \begin{Bmatrix} u_1 \\ u_2 \\ u_3 \end{Bmatrix}. \quad (2.2)$$

Assuming linear elastic behaviour of the element, the characteristic relationship between force and displacement can be written as:

$$\mathbf{r} = \mathbf{K}\mathbf{u} - \mathbf{f}, \quad (2.3)$$

where \mathbf{f} represents the nodal forces required to balance any load applied on the element and \mathbf{K} defined as the stiffness matrix for the element.

- *assembly equations*: if considering a domain constituted by multiple elements two conditions need to be met: displacement compatibility and equilibrium. The nodal displacement matrix written for all the elements automatically satisfies the first condition. The equilibrium has been postulated for

the single elements, therefore conditions at the nodes need to be set to satisfy the total equilibrium of the structure. The resulting equations have the displacement as a variable and their solutions define the structural problem. For a generic node, the equilibrium equation is the sum of the force components acting on the elements meeting on that particular node. If all the nodal equilibrium equations are assembled the following condition is obtained:

$$\mathbf{Ku} - \mathbf{f} = 0 \quad (2.4)$$

- *boundary conditions*: to solve the system defined by Eq. 2.4 the prescribed support displacements need to be included. These conditions are derived from physical constraints which limit the degrees of freedom of the system, i.e. rigid body constraint, encastre, etc. When the boundary conditions are set the system can be solved for the unknown nodal displacements and the element internal forces.

2.4.2 SINGLE CELL FINITE ELEMENT MODELS

FE single cell models have been successfully used to study the mechanical properties of subcellular components, such as the nucleus, and to gain information on whole cell mechanics [69]. These models were designed to couple experimental evidence and are reviewed below depending on the experimental technique they were focused on.

- *Magnetic manipulation experiments*: Mijailovich and co-workers [72] designed a three-dimensional model of a cell to obtain cell mechanical properties from magnetic twisting cytometry experiments. In these experiments, a torque is applied to a bead which is bound to the cell surface. With the help of the FE model they were able to couple the relationships between torque and cell deformation, bead rotation and lateral translation and to obtain the Young's modulus of the cell from the apparent cell stiffness if indentation depth and cell height were known. The FE model consisted of a linear elastic slab with constant local height representing the cell and an embedded spherical bead. This geometry was idealised with respect to the real

cell geometry but it was shown to be accurate enough to analyse the highly localised bead torque response.

Another model was developed by Karcher and co-authors [73] for a similar application in the context of magnetocytometry. They designed a three-dimensional cylindrical domain representing a cell monolayer incorporating viscoelastic properties of the cytoskeleton (bulk material) and membrane (shell) contributions with an embedded spherical bead. They also allowed for cell height and material property modulation to represent different cell types. They found a negligible contribution of the membrane when large beads or long bead enforcing were simulated and highlighted a time-dependent behaviour of the force response.

- *AFM experiments:* McGarry and Prendergast [74] proposed an FE model of an adherent eukaryotic cell which included the structurally relevant sub-cellular components, i.e. nucleus, cytoplasm, membrane and cytoskeleton network. The aim of the study was to investigate the ability of the model to predict the non-linear structural behaviour of the cell without needing complex material properties parameter definition. They designed six different three-dimensional models representing different stages of cell spreading on a substrate. The cytoskeleton consisted of a network of compression-bearing struts and tensional cables picturing the microtubules and the actin respectively, bound to each other at common nodes representing the adhesion complexes. The material properties for all components were linear elastic with a pre-stress applied to the actin filaments. AFM indentations were simulated by concentrated load application on locations at a known distance from the cytoskeleton connection nodes. They found that the main contributor to the non-linear cell stiffness was the cytoskeleton, followed by the cytoplasm and the membrane.

An FE model of a single cell to study the contribution of the different cytoskeletal fibres to cell mechanics was designed in previous work from this group [75]. A multi-structural three-dimensional model was proposed including cytoplasm, nucleus, microtubules, actin cortex and actin bundles and the different cytoskeletal components were selectively removed to in-

investigate their structural role. The material properties for all components were set as linear elastic and the actin bundles were pre-stressed. An idealised elliptical geometry was used for the cell with a morphologically accurate disposition of the cytoskeleton; a rigid sphere was modelled representing the AFM tip and displaced to locally compress the cell over the nucleus. The simulations showed that the major contributors to compressive load bearing were the actin cortex and the microtubules and that none of the included cytoskeletal components was able to maintain cell rigidity by themselves.

A geometrically-refined version of the model in [75] was proposed by [76] where confocal images were used to obtain a realistic cell topology and sub-cellular component organisation. The FE model included nucleus, cytoplasm, membrane/cortex, apical and basal actin stress fibres, locally compressed by a bead mimicking the AFM probe. By discerning between the apical and basal actin stress fibres, they highlighted the contribution of the former in modulating the membrane strain under compression together with the cortex. A decreased elastic modulus of both these components reduced the apparent cell elastic modulus and increased the average tensile strain on the membrane.

- *Fluid flow experiments:* The same model of [74] was used to analyse the response of an adherent bone cell to substrate strain and fluid flow [77]. To simulate the substrate strain each node at the cell-substrate interface was axially displaced; to mimic the fluid flow an even force was applied to the membrane surface, the magnitude of which was computed by using the predicted shear stress in a parallel flow chamber. The results showed different responses of the cell depending on the applied mechanical stimulus, with the fluid flow affecting the cell entirety and the substrate strain having a local effect.

A similar approach was previously adopted by Charras and Horton [78], as they used AFM acquired cell topography and material properties to create a three-dimensional FE model. They then applied different loading conditions to simulate mechanical stimuli such as substrate stretch, fluid shear

stress and intermittent hydrostatic pressure, or manipulation techniques such as microbead or micropipette experiments. The elastic modulus of the cell was varied to mimic cellular adaptation to mechanical stimulation and the strain distribution was analysed as output. They found that most stimulation methods except fluid shear stress caused strains of comparable magnitude; they hypothesised that a different detection mechanism to flow and the co-existence of different pathways in response to mechanical stress would be present.

Ferko and co-authors [79] were interested in mechanical load transmission in endothelial cells exposed to blood fluid flow. They designed a cell-specific FE model representing an endothelial confluent monolayer, with microscopy determined focal adhesion positioning, and analysed the contribution of focal adhesions and material non-homogeneity on the cell mechanical response. The model included the nucleus and cytoplasm modelled as linear elastic materials and the endothelial glycocalyx modelled as a $0.4\mu\text{m}$ thick poroelastic Brinkman layer. The results showed heterogeneous deformations of the cytoplasm consequent to shear stress and amplification of mechanical response near focal adhesions, in the presence of the glycocalyx and if the nucleus stiffness was artificially enlarged.

- *Compression experiments:* Slomka and Gefen [80] designed a confocal-based FE single cell model including nucleus, cytoplasm, membrane and cytoskeletal network and simulated large deformations occurring in experiments where cells were compressed or stretched. Mechanical loads were applied through the substrates, which were simulated in contact with the cell, and the strain measures were computed. Isotropic compressible Neo-Hookean material properties were assigned to the nucleus, cytoplasm and membrane, while the cytoskeletal fibres were assumed linear elastic. Localised membrane and nuclear surface stimulation were observed with both loading modes.

Very few studies in the literature built single cell FE models which included different cell components and a realistic cell geometry [74–76, 80]. In particular, in the context of AFM experiments simulation the contribution of different indenting locations to the overall computed Young's modulus was not investigated, nor

its dependency on the indentation depth. In this context, a single cell FE model based on confocal images was designed to address these questions.

2.4.3 CONCLUSIONS AND BACKGROUND FOR THE PRESENT WORK

Bone mechanotransduction plays an important role in the bone remodelling processes. A more detailed elucidation of the mechanical properties of the bone cells would be needed to better understand the magnitude of forces locally detected by the cells *in vivo*. In addition to the mechanical properties of the cell body, information on the stiffness and characteristics of the bone glycocalyx could provide further evidence on the mechanisms which involve the cell coating in mechanical stimulation transmission. The use of computational modelling techniques could complement the experimental findings with quantitative information not easily accessible with experimental approaches.

3

Variability of the mechanical properties of a single bone cell population

This chapter presents the results obtained by AFM nano-indentation on bone cells focusing on the variability of the mechanical properties in a single bone cell population¹. The protocol design and an evaluation of the necessary sample size to reflect standard population heterogeneity are reported. The pre-processed data relative to this chapter are available at the following DOI: [10.15131/shef.data.5632771](https://doi.org/10.15131/shef.data.5632771).

3.1 INTRODUCTION

The rationale of this study was to design a suitable protocol to test live bone cells with AFM nano-indentation and to extract the Young's modulus values from the obtained data. Particular focus was placed on the repeatability of the experimental method, on the choice of mathematical models for Young's modulus fitting and on

¹Part of the work presented in this Chapter is planned to be submitted as a scientific paper.

the minimum sample size needed to obtain reliable mechanical properties from a standard cell line population.

Single cells within populations display some degree of heterogeneity [81]. This is due to cells at different stages of cell cycle or differentiation [82–84], belonging to lineages with multiple cell types [85, 86], responding to spatially localised stimuli, migrating to different locations, differently adhering to the substrate or displaying different genetic modifiers [87]. These factors of heterogeneity affect the cell cytoskeleton, which is involved in maintaining cell shape, directing cell movement, responding to mechanical stimulation and generally allowing the cell to adapt to environmental cues [88].

The reorganisation of the cytoskeleton affects cell mechanical properties due to its close relationship with cell structure [89]. This was demonstrated experimentally by various works in which the cytoskeleton has been selectively removed and the global mechanical properties recorded [90–93]. The mechanical properties of cells could, therefore, be a classifier for cells in different conditions (reviewed in [40]), i.e. allowing to discern between cells at different stages of differentiation [52, 91] and of cell cycle [45], distinguish between motile and stationary cells [43, 94], or distinguish between physiological and pathological cells for example in the context of cancer research (reviewed in [93]).

Different AFM experimental protocols and data analysis techniques have been used to test single cells leading to difficulties when comparing different results. The determination of the Young's modulus is prone to the effect of various factors, such as the experimental set-up (cantilever choice and calibration), the testing conditions (load speed, indenting location) and the way data is analysed (contact point fitting, range of indentation, model for stiffness fitting) [39, 40, 43, 93]. In addition to these experimental challenges, differences in cell elasticity have been observed depending on: cell cycle stages [45], differentiation stages [48, 52, 91], time in culture [46, 95, 96], culture conditions [97], adhesion substrate [44], degree of monolayer confluence [98], and cell migration [94]. Moreover, great ranges of variability in the recorded cell stiffness values have often been found, despite the type and conditions of cells used [40, 44, 99, 100].

The methodological variability factors can be reduced by careful optimisation of the experimental protocols. However, it is not always straightforward to per-

form accurate sample selection due to the time- and user-intensive nature of the AFM experiments, which allow for a limited number of cells to be tested in one day [39]. Moreover, some of the variability factors are intrinsic of a heterogeneous cell population and therefore considering a homogeneous sub-sample might represent an oversimplification of the physiological conditions.

The aim of this study was therefore to design a protocol to test and analyse the mechanical properties of a standard (not sub-sampled) cell population. The experimental methodology and post-processing were carefully controlled to minimise experimental variation and focus on the cell heterogeneity aspect. An unusually large number of AFM indentation data were acquired and analysed to quantify the minimum sample size required to achieve statistical significance of the recorded average stiffness values, i.e. the sample size for which the average value does not change if further data is added.

3.2 MATERIALS & METHODS

3.2.1 CELLS

In this study, late stage osteoblasts/early stage osteocytes MLO-A5 cells were used [101]. These cells were originally isolated from transgenic mice long bone and present a dendritic morphology. The cell line represents the stage of differentiation of young osteocytes responsible for triggering mineralisation of the osteoid as they spontaneously mineralise *in vitro* within 7 – 8 days or within 2 – 3 days in the absence or presence of β -glycerophosphate (β -GP), respectively. They have been used for different mechanotransduction studies and shown to be mechanoresponsive [31, 102, 103]. MLO-A5 cells were kindly donated by Prof. Lynda Bonewald (University of Missouri, Kansas City, MO, USA).

Cells were cultured in Minimum Essential Alpha Eagle medium (MEM, Lonza) supplemented with 10% Foetal Bovine Serum (FBS, Labtech), 100 *units/ml* penicillin, 100 $\mu\text{g/ml}$ streptomycin and 2 *mM* glutamine (PSG, Sigma). Cells were kept at 37°C and passaged on standard tissue culture plastic when reaching 90% confluence (passage 27 – 30). Prior to AFM experiments, cells were seeded onto tissue culture treated Petri dishes ($D = 10\text{mm}$) at a seeding density of 200 *cell/cm*².

This density was chosen to obtain spatially separated single cells during AFM experiments. Samples were tested after 5 to 6 days of culture, before the deposition of mineral content.

3.2.2 AFM CANTILEVER PREPARATION

Spherical tipped cantilevers were produced following a similar protocol to [100]. Tip-less cantilevers (Windsor Scientific) with nominal spring constant of 0.2 N/m were customised by glueing a silica bead ($D = 6\ \mu\text{m}$, Bangs Laboratories) at the tip extremity. Firstly, a full calibration of the cantilever was performed in liquid with the AFM built-in software by recording a force spectroscopy measurement on a glass coverslip (sensitivity and spring constant determination). The sensitivity calibration enables the calculation of the force derived from the cantilever deflection and corresponds to the laser positioning [104]; the cantilever spring constant is measured by thermal noise method [105]. This method relies on the free oscillation of a diving board-like body and therefore it needs to be applied before the attachment of a mass (i.e. silica bead) to the cantilever. Subsequently, the substrate was changed and a dry coverslip was positioned under the cantilever with some epoxy glue (Araldite) at one end and some beads at the other. The cantilever was dipped into the glue and maintained in position for about 5 seconds. It was then pressed onto the bare substrate to remove excess glue and then held down on a silica bead. The customised cantilevers were stored for at least one week before use to allow for complete cross-linking of the epoxy glue.

3.2.3 AFM SET-UP

A NanoWizard 3 atomic force microscope (JPK Instruments AG) coupled to an Eclipse Ti-S optical inverted microscope (Nikon Instruments) was used for all the experiments.

The cells were washed in phosphate buffer solution (PBS) and fresh medium was added. Samples were positioned on the heated sample holder to allow for testing at 37°C . The cantilever sensitivity was calibrated on the bare tissue culture plate before each experiment. Single cells were located through the coupled optical microscope and images of cell shape were recorded for morphological analysis.

The cantilever was centred over the cell nucleus and a grid of 5 points spaced $3\ \mu\text{m}$ within each other was set [44]. Force spectroscopy measurements were obtained on the 5-point grid for 3 times to collect a total of 15 data on each cell (Fig. 3.2.1). The relative set point and the approach velocity were set to $10\ \text{nN}$ and $4\ \mu\text{m}/\text{s}$ respectively. A total of 180 cells were indented over 3 separate experiments.

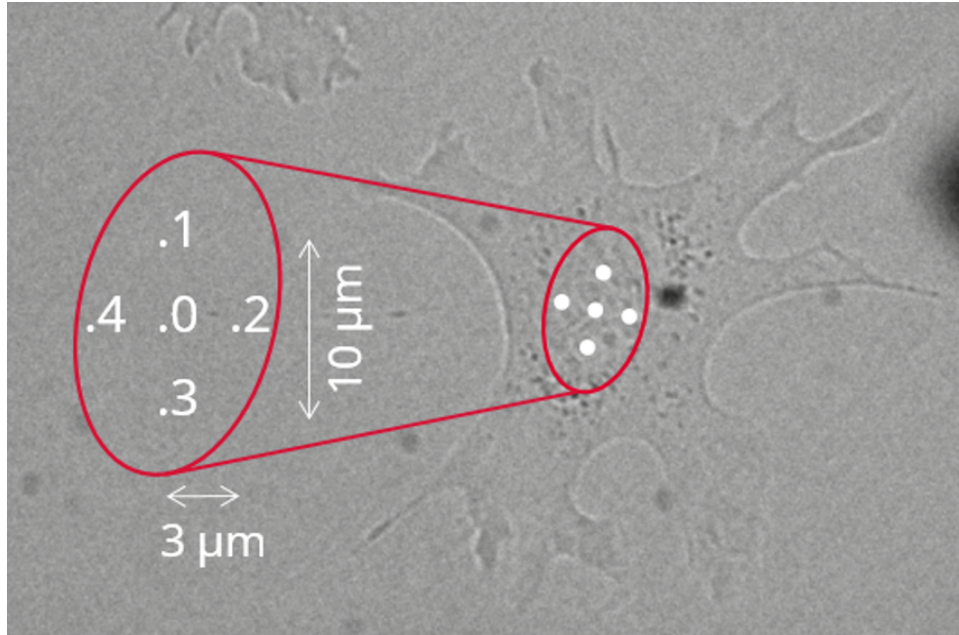


Figure 3.2.1: An MLO-A5 cell overlaid with a schematic of the indentation grid over the nucleus. The grid consists of 5 points spaced $3\ \mu\text{m}$ within each other. Each point is tested thrice following the grid numbering order three times.

3.2.4 POST-PROCESSING

The obtained data files were exported as text files from the JPK Data Processing software. All the subsequent post-processing was performed in MATLAB (Mathworks) with custom-written semi-automated algorithms to allow for careful tailoring of the analysis steps.

The methodology is summarised in Fig. 3.2.2.

CONTACT POINT DETERMINATION

The ratio of variance method proposed in [106] was used to determine the contact point, i.e. the point in the force spectroscopy curve at which the probe first comes into contact with the cell. The rationale of this algorithm is that the variance of the signal measured at two intervals belonging both to the non-contact or contact region is similar: in the non-contact region, the variance is small because there is no cantilever deflection (d) but for instrumentation noise; in the contact region, the variance is higher due to the sample indentation. It is possible to compute the ratio of variances (RoV) between two adjacent moving windows of size N (with $N = 100$ *datapoints*) separated by a trial point i while scanning the force spectroscopy curve (Eq. 3.1):

$$RoV_i = \frac{\text{var}(d_{i+1} : d_{i+N})}{\text{var}(d_{i-N} : d_{i-1})}. \quad (3.1)$$

For trial points i well in the non-contact or contact regions the RoV takes values close to 1, for trial points i close to the contact point the RoV displays a peak which can be used to localise the contact point on the curve.

Each force spectroscopy curve was visually checked to verify the algorithm's correct functioning: curves displaying no baseline were discarded and curves showing incorrect fitting were re-processed with a different moving window size N .

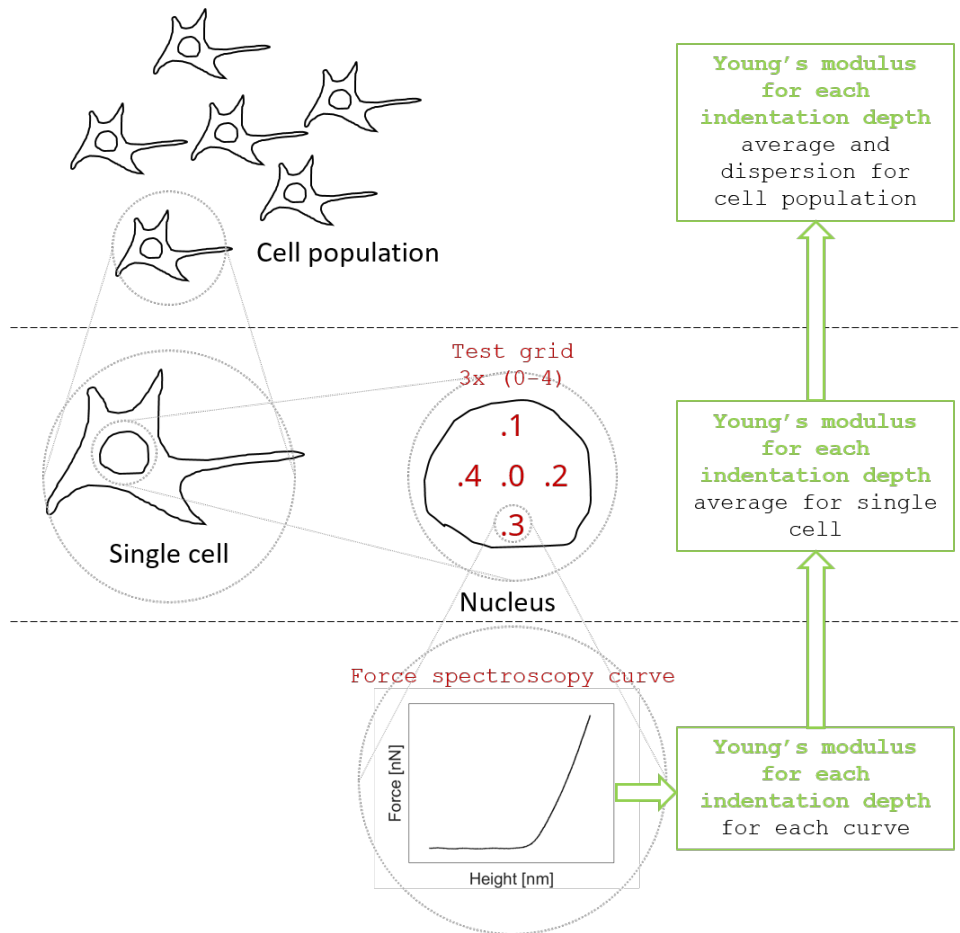


Figure 3.2.2: A cell population was tested to evaluate the average and dispersion of the stiffness values. A total of 180 MLO-A5 cells were tested. Each cell was indented over the nucleus using the 5-point grid (points 0 – 4); each point of the grid was indented three times following the numbered list. A force spectroscopy curve was obtained for each indentation, for a total of 15 curves per cell. Each curve was analysed with the custom-written algorithms (see Fig. 3.2.3 - Fig. 3.2.7) to obtain a value of Young's modulus for increasing indentation depths. The Young's modulus values were averaged for each cell. The average value for each cell was used to calculate the average and dispersion stiffness values for the cell population.

A step-by-step representation of the algorithm to prepare the data for further analysis is pictured in Fig. 3.2.3 - Fig. 3.2.6:

1. each force spectroscopy extend curve was analysed separately (Fig. 3.2.3);
2. the ratio of variance method was used to determine the contact point (Fig. 3.2.4);
3. the contact point was fitted on the force spectroscopy (Fig. 3.2.5);
4. the data were centred with the contact point (Fig. 3.2.6);

The algorithm is semi-automated: the processing of each curve requires 0.2 s of computational time on an Intel Xeon machine with 32 GB of memory plus the user time needed to confirm the goodness of the contact point fitting for each curve.

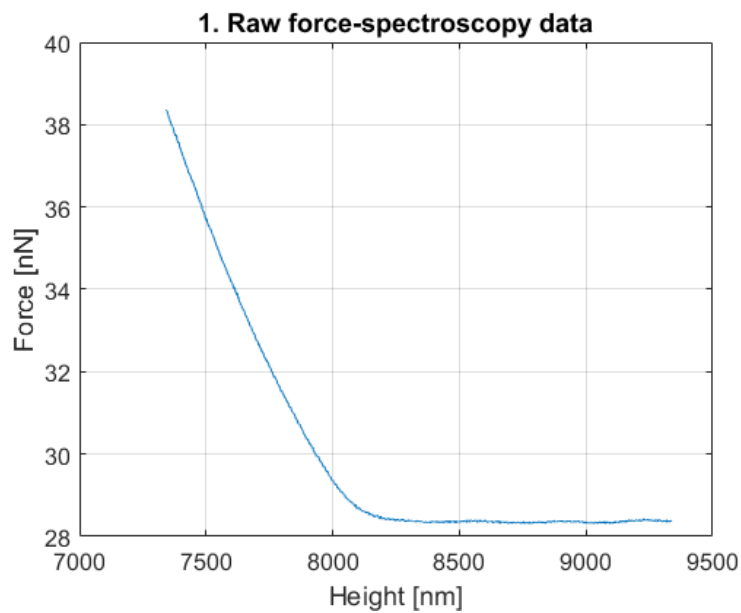


Figure 3.2.3: Data pre-processing - step 1. Example of raw extend force spectroscopy data curve (blue line) obtained by AFM nano-indentation of live bone cells.

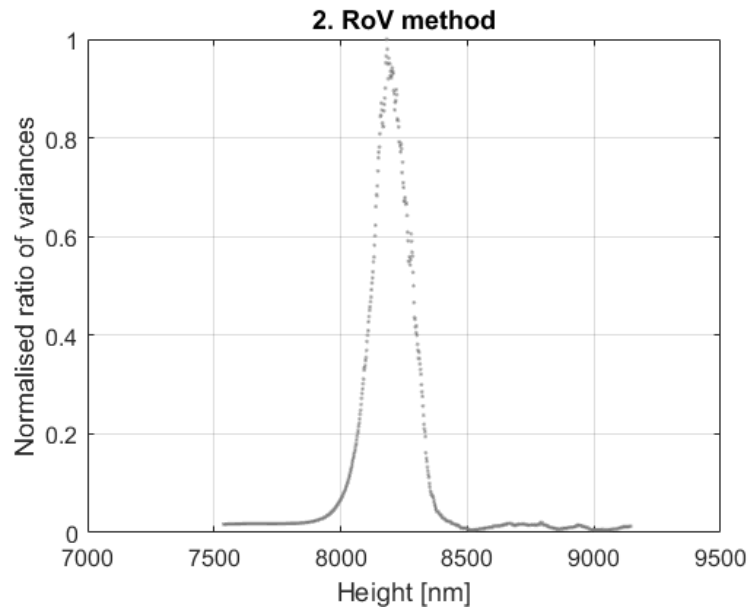


Figure 3.2.4: Data pre-processing - step 2. The ratio of variance method was used to locate the contact point (grey dots).

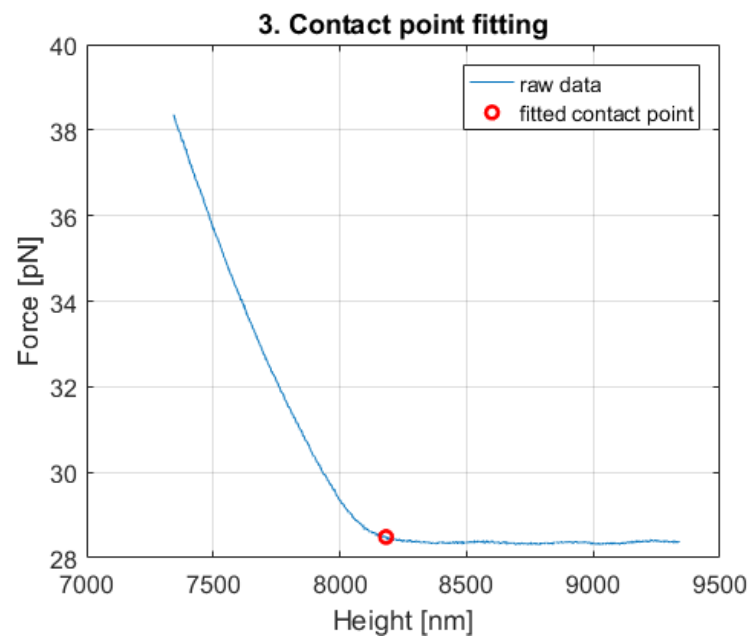


Figure 3.2.5: Data pre-processing - step 3. The contact point (red circle) was fitted on the force spectroscopy raw data curve (blue line).

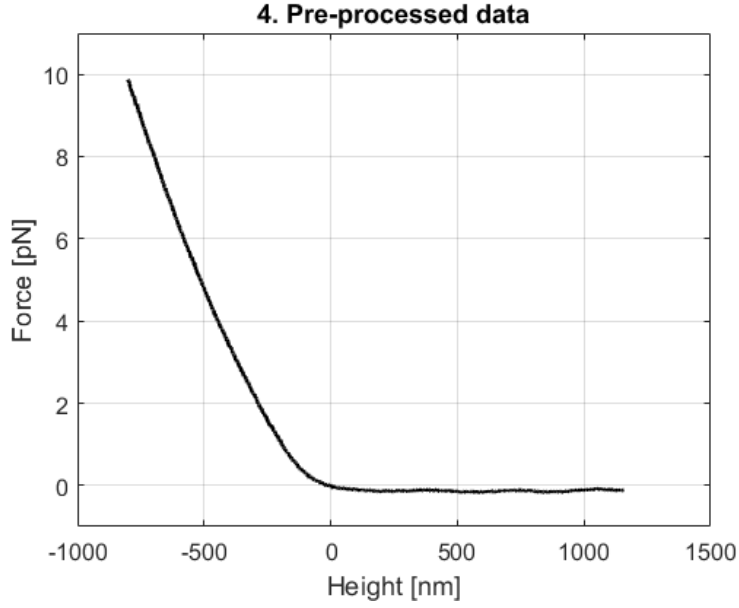


Figure 3.2.6: Data pre-processing - step 4. The force spectroscopy data curve was centred with the contact point to obtain the pre-processed curve (black line).

YOUNG'S MODULUS FITTING

The Young's modulus was obtained by Hertz model fitting on the extend force spectroscopy curve. The Hertz model formulation for a spherical indenter over a half space [40, 42] was used, as summarised below.

The force F on a cantilever for which the tip can be approximated by a sphere of radius R can be written as per Eq. 3.2:

$$F(d) = \frac{4}{3} E^* R^{\frac{1}{2}} d^{\frac{3}{2}}, \quad (3.2)$$

with E^* effective modulus of the tip-sample system and d indentation depth. E^* can be written as per Eq. 3.3:

$$\frac{1}{E^*} = \frac{1 - \nu_{probe}^2}{E_{probe}} + \frac{1 - \nu_{cell}^2}{E_{cell}}, \quad (3.3)$$

with ν_{probe} , E_{probe} and ν_{cell} , E_{cell} Poisson ratio and Young's modulus of probe and cell respectively. Assuming E_{probe} to be greater than E_{cell} and by setting $\nu_{cell} = 0.5$ as

per an incompressible material, Eq. 3.2 can be re-written as:

$$F(d) = \frac{16}{9} E_{cell} R^{\frac{1}{2}} d^{\frac{3}{2}}. \quad (3.4)$$

These solutions have been obtained under various hypotheses, such as homogeneous, isotropic and linear elastic material properties, and infinitesimal deformation. However, cells are heterogeneous in composition and present time-dependent mechanical properties [43]. Care should, therefore, be taken when using this model, by meticulously controlling the experimental conditions [43], by experimentally checking the elastic linear properties of the material and not assuming them *a priori* [39] and by verifying the assumption of constancy of the elastic modulus over depths of indentation [107].

A set of *a posteriori* analyses was therefore designed to evaluate if the Hertz model assumptions were satisfied in this context. The Young's modulus was calculated for increasing indentation depths to get an insight into the contribution of different cell components (Fig. 3.2.7). An increasing number of points was fitted representing indentation depths from 100 *nm* up to a maximum of 700 *nm*. The coefficient of determination R^2 was obtained as an indicator of the goodness of fit of the Hertz model to the data for each indentation depth. The maximum indentation value was chosen by looking for the last indentation value for which more than 90% of data were available. This analysis allowed for verification of whether the Young's modulus was constant over a range of indentation depths and if the substrate contribution was detected in the form of a sharp increase in stiffness [107, 108].

Each cell was repeatedly indented 15 times in 5 different locations. This could result in a time-dependent viscoelastic response of the cell which could potentially start to rearrange its actin cytoskeleton [93]. To investigate the occurrence of this phenomenon and to experimentally check the elastic linear material hypotheses, the Young's moduli distributions for different indenting locations within the test grid and for different series of indentation were compared.

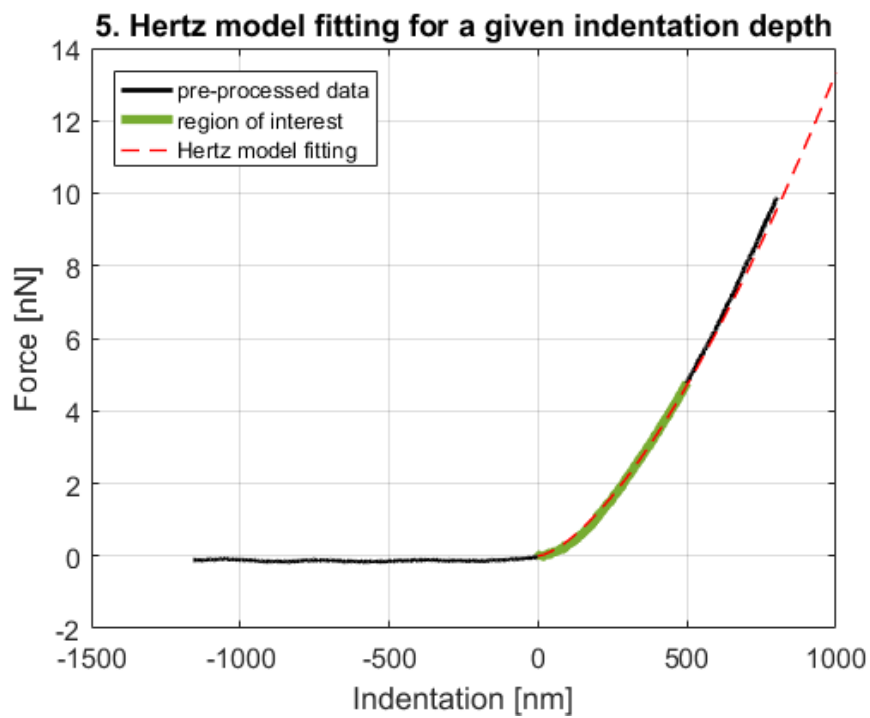


Figure 3.2.7: The pre-processed force spectroscopy data curve (black line) was fitted with the Hertz model (red dashed line) at different indentation depths to obtain the Young's modulus. An example is shown for an indentation depth of 500 nm (green region).

MORPHOLOGICAL ANALYSIS

A sub-sample of 30 cells was analysed to verify the presence of correlation between Young's modulus and cell morphology. The light microscopy images of these cells were analysed in ImageJ [109]. A mask of the cell and nucleus profiles was drawn and its area was recorded. An ellipse was then fitted to both geometries and its major and minor axes were measured. Correlation of each morphometric parameter (area, major and minor axes for nucleus only and whole cell) was tested against the Young's modulus value fitted for the cell averaged across indentation depths.

SAMPLE SIZE CONSIDERATIONS

The minimum number of cells required to obtain a stable value of Young's modulus for the population was computed, i.e. the minimum sample size for which the addition of further single cell contributions does not affect the computed average population stiffness. To this aim, a Monte Carlo approach was adopted and the average Young's modulus for samples of increasing size was calculated (i.e. by considering an increasing number of single cell contributions) across the indentation depth range. The cell acquisition order was randomised and the n cells to be included in the sample at each step were selected randomly from the randomised list. The Monte Carlo simulation was repeated 100 times and the resulting dispersion of the average stiffness for given sample sizes was analysed. To this aim, the percent deviation for each sample size across the repeats was calculated as the standard deviation divided by the mean of the population Young's modulus for each sample size. The number of cells required to obtain a percent deviation of less than 10% was reported.

3.2.5 STATISTICAL ANALYSIS

All the experimental quantities measured in this work were expressed as average and dispersion values. These correspond to the mean and standard deviation for normal distributions and to the median and inter-quartile range (IQR) for non-normal distributions. Normality was assessed by Shapiro-Wilk test (significance set to $p < .05$) with the SPSS Statistics software (IBM). Data transformation such as log-normal transformation was not adopted to avoid difficulties in data

interpretation [110]. The quartile coefficient of dispersion (CoD) was used as a standardised measure of dispersion and is defined as per Eq. 3.5:

$$CoD = \frac{q_3 - q_1}{q_3 + q_1} \quad (3.5)$$

with q_1 and q_3 first and third quartile of the distribution, respectively.

To compare Young's modulus values between locations and series of indentation the Kruskal-Wallis test was used (non-parametric test for comparison of more than two not normally distributed samples). Significance was set to $p < .01$ for all tests which were run in MATLAB (Mathworks).

The Spearman's ρ coefficient of correlation for not normally distributed scalar data was calculated for all morphometric parameters against the Young's modulus. A correlation coefficient $\in (-0.3, 0.3)$ was considered as weak association, $\in (-0.5, -0.3) \cup (+0.3, +0.5)$ as moderate, $\in (-0.9, -0.5) \cup (+0.5, +0.9)$ as strong, $\in (-0.9, -1.0) \cup (+0.9, +1.0)$ as very strong [111]. Calculations were performed in the SPSS Statistics software (IBM).

3.3 RESULTS

3.3.1 HERTZ MODEL HYPOTHESES TESTING

Due to the strong assumptions the Hertz model is built on, its applicability should not be taken for granted. Therefore, the hypotheses of the Hertz model were tested to verify their satisfaction in this context. To this aim, the Young's modulus values versus indentation depth for different indenting locations within the test grid and for different series of indentation were calculated. No statistical difference was found between the locations and series of indentation (significance set to $p < .01$), confirming that the elastic material assumption was verified (Fig. 3.3.1). It is expected that, if a rearrangement of the cytoskeleton had occurred within the time frame of the 15 indentations, the recorded values for the subsequent testing series would have changed.

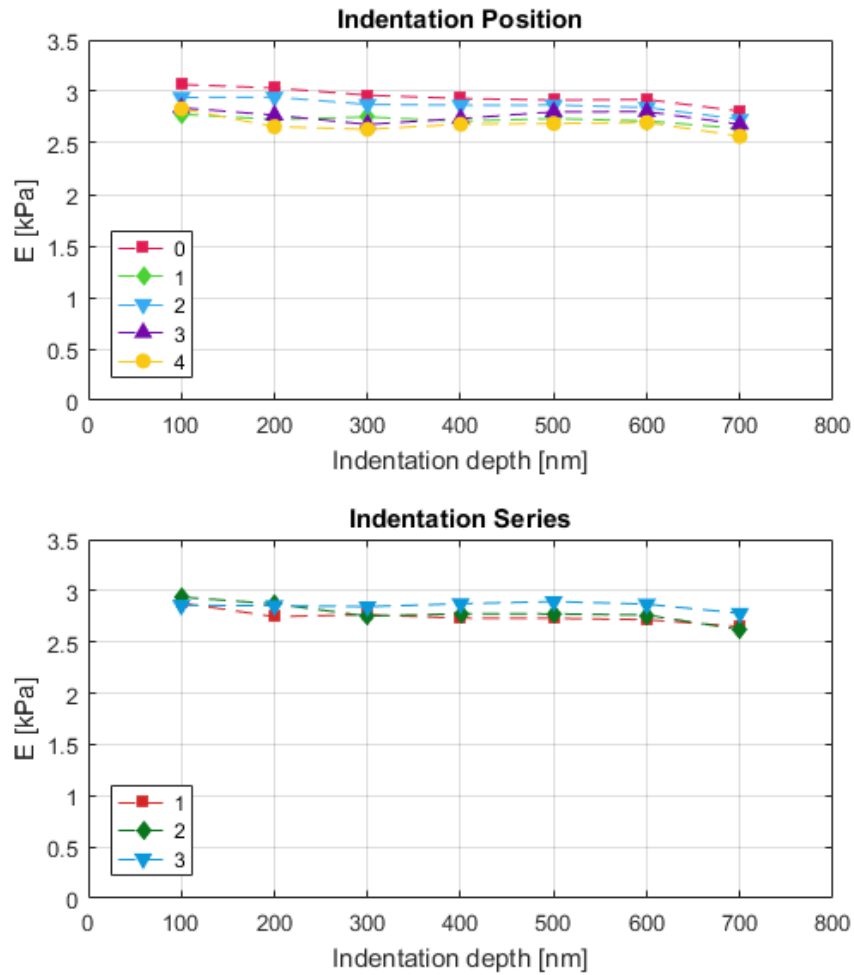


Figure 3.3.1: Young's modulus vs. indentation depth for indenting locations 0–4 of the grid positioned over the nucleus (top panel, see also Fig.3.2.1) and for the subsequent series of indentation 1 – 3 (bottom panel). Values for different locations (top panel) and series (bottom panel) of indentations were compared to test that the hypothesis of linear elastic material was satisfied. No statistical difference was found (significance set to $p < .01$).

Table 3.3.1: *Young’s modulus values [kPa] for the MLO-A5 pre-osteocyte cell population (168 cells). Average (median), dispersion (IQR), mean and standard error of the mean (SEM) values are reported for increasing indentation depths. SEM values were calculated with $N = 168$ cells.*

Indentation [nm]	Young’s modulus [kPa]			
	median	IQR	mean	SEM
100	2.93	1.31	3.12	0.08
200	2.76	1.24	3.01	0.08
300	2.71	1.37	2.96	0.09
400	2.71	1.45	2.97	0.09
500	2.74	1.49	2.98	0.09
600	2.76	1.49	2.96	0.08
700	2.76	1.43	2.85	0.07

3.3.2 YOUNG’S MODULUS

A total of 2137 indentations across 168 different cells were analysed. The Hertz model fitting quality was generally high ($R^2 = 0.9629$ (0.05)) and it was comparable for all indentation depths despite the increasing number of points used for fitting deeper indentation depths. Average and dispersion stiffness values were computed for each cell (normal distribution of indentations across each cell). By hypothesising each cell to have spatially homogeneous stiffness properties described by the average value, the average and dispersion values for the cell population were calculated using the average value from single cells (non-normal distribution of cell Young’s modulus values across the population).

In Fig. 3.3.2 histograms of the single cell average Young’s modulus values are shown for each indentation depth, normalised for the total number of cells (i.e. if all cells would take the same Young’s modulus value, the corresponding bar would be equal to 1). Population average and dispersion values are highlighted in red. The average population values of the Young’s modulus were constant with indentation depth, except for shallow indentations where a slightly higher value was calculated (Table 3.3.1). The maximum indentation of 700 nm did not show any sharp

increase suggesting that the substrate was not detected.

3.3.3 MORPHOLOGICAL ANALYSIS

MLO-A5 cells showed the expected dendritic shape [101], however, some degree of variation was observed in cellular dimensions and elongation. Some representative cellular morphologies are depicted in Fig. 3.3.3. In Table 3.3.2, values for nuclear and cell morphological parameters are reported. These include area, major and minor axes dimensions. Average (dispersion) values for nuclear and cellular areas were $289 (147) \mu m^2$ and $2240 (969) \mu m^2$, respectively. Average (dispersion) values for major and minor nuclear axes were $23 (6) \mu m$ and $16 (4) \mu m$, respectively. Average (dispersion) values for major and minor cellular axes were $68 (12) \mu m$ and $41 (16) \mu m$, respectively.

A weak correlation was found between all the morphological parameters and the cell Young's modulus ($\rho < |0.2|$), suggesting no association between shape and mechanical properties.

3.3.4 SAMPLE SIZE

All the calculations reported so far were performed on the data relative to 168 cells. However, smaller samples might be sufficient to calculate an average population stiffness values. The population average Young's modulus for increasing samples size for the computed 100 repeats is shown in Fig. 3.3.4, where dots represent the average population stiffness for increasing sample sizes and error bars the standard deviation across repeats. The percent deviation for increasing sample sizes is shown in Fig.3.3.5. This can be well fitted with a power function in the form $y = ax^b$, with y representing the percent deviation, x the number of cells and a, b fitting parameters (in this instance $a = 37$ and $b = -0.37$). Data from about 35 cells were needed to obtain a percent deviation error of 10% on the population average Young's modulus. This is, however, an indicative number, calculated for the specific protocol used in the present work.

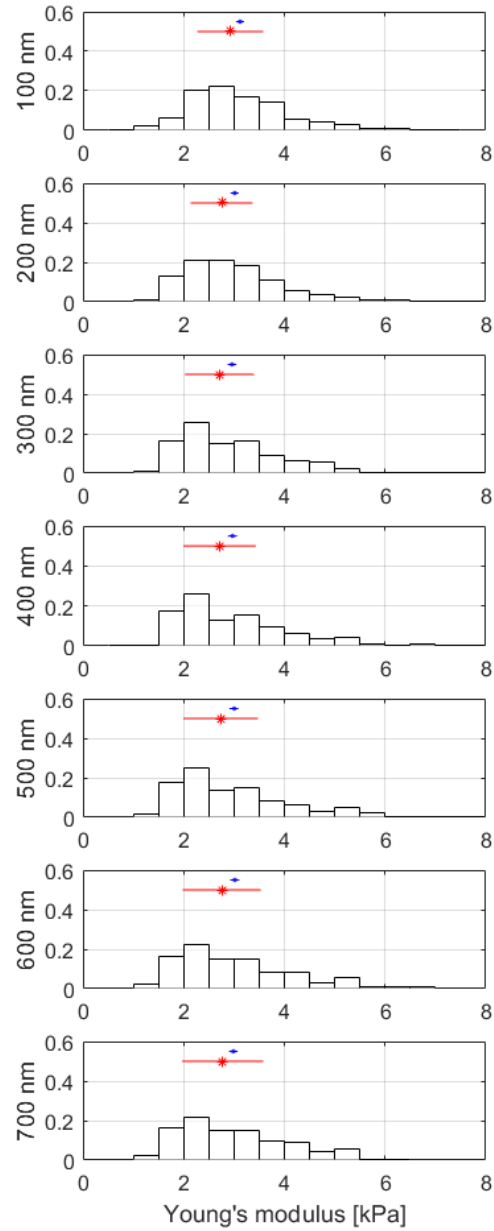


Figure 3.3.2: Histograms of single cell average Young's moduli for each indentation depth normalised for the total number of cells. The red asterisks and lines represent the average (median) and dispersion (IQR) value for the population, respectively. The blue dots and lines represent means and standard errors.

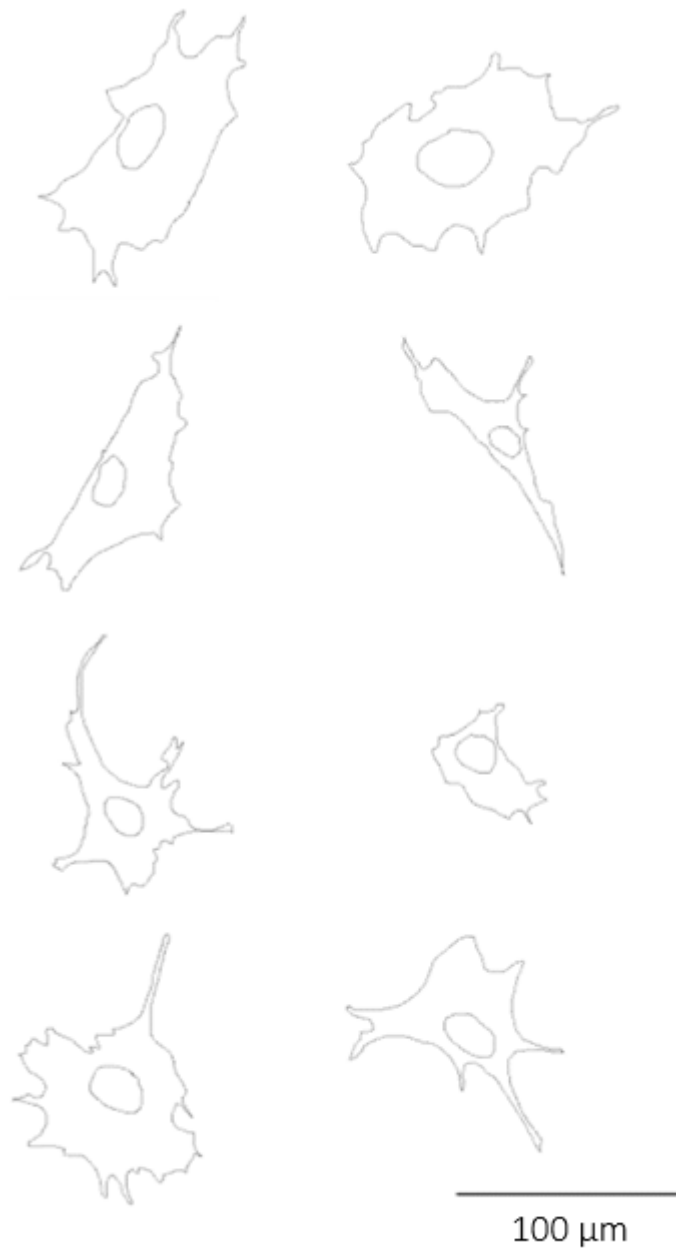


Figure 3.3.3: Representative images of the 30 MLO-A5 cells morphological profiles. The scale bar represents 100 μm . Different degrees of elongation and various sizes are noticeable.

Table 3.3.2: Areas, major and minor axes for the nucleus and the cell are reported. Weak correlation was found between the morphological parameters and the cell Young's modulus.

	Nucleus			Cell		
	Area [μm^2]	Major [μm]	Minor [μm]	Area [μm^2]	Major [μm]	Minor [μm]
1	589	30	25	2413	61	51
2	293	23	16	1981	65	39
3	352	24	19	1699	54	40
4	283	23	16	2943	70	53
5	235	19	15	2269	84	35
6	210	26	10	1709	70	31
7	187	16	15	2217	64	44
8	598	32	23	5074	103	62
9	367	30	16	3681	91	51
10	755	36	27	2742	68	51
11	339	24	18	2262	71	41
12	385	30	16	4379	112	50
13	213	22	12	2671	97	35
14	365	26	18	2630	69	48
15	356	25	18	2015	69	37
16	255	20	16	1997	67	38
17	284	21	17	1680	62	35
18	123	15	10	1230	73	21
19	202	19	13	1955	62	40
20	258	21	16	1434	56	32
21	346	22	20	1878	59	40
22	562	33	22	3619	75	62
23	443	26	22	3414	75	58
24	220	18	15	1140	49	30
25	257	24	13	2105	56	48
26	139	15	12	1566	68	29
27	325	22	19	1917	60	41
28	207	18	14	2759	66	53
29	342	25	18	3698	73	64
30	281	25	14	2392	61	50

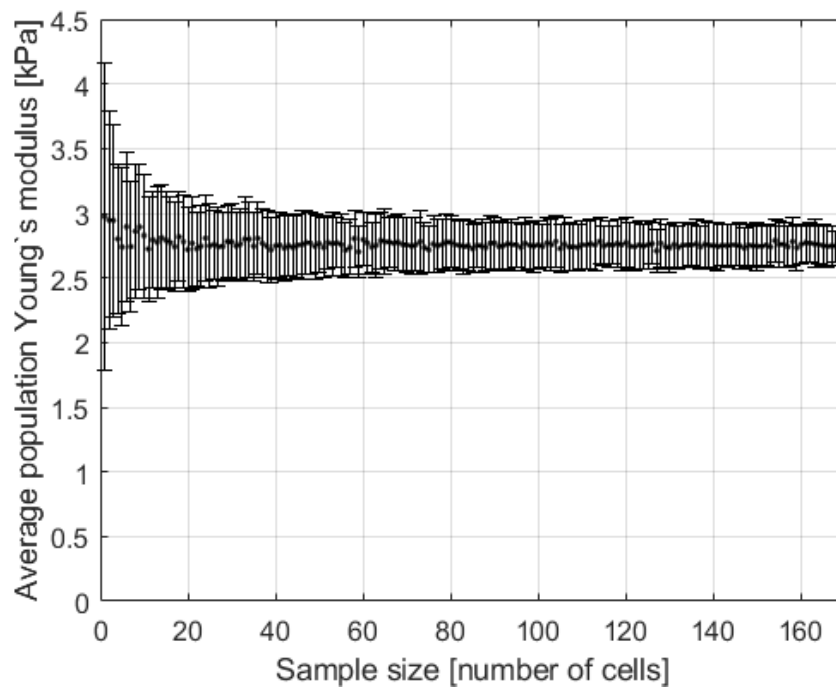


Figure 3.3.4: *Young's modulus average values for increasing sample size resulting from 100 repeats of the Monte Carlo analysis. The x-axis represents the randomised sample size and the y-axis the average population Young's modulus computed for it. Dots represent the mean and error bars the standard deviation across repeats.*

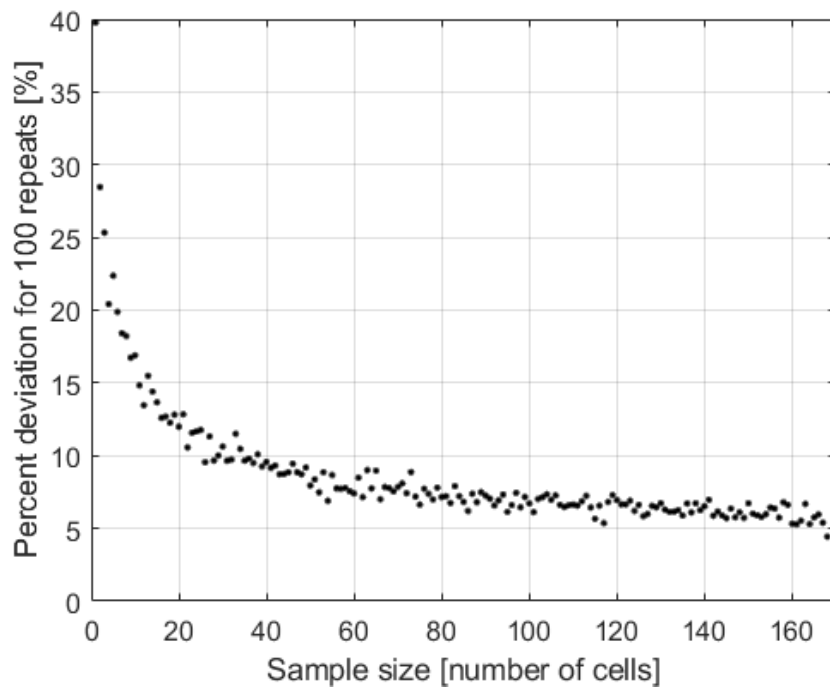


Figure 3.3.5: *The percent deviation of the average population Young's modulus was calculated for increasing sample sizes. A percent deviation lower than 10% was obtained with sample sizes of about 35 cells.*

3.4 DISCUSSION

3.4.1 YOUNG'S MODULUS FITTING

An unusually large number of pre-osteocyte MLO-A5 cells was tested by AFM nano-indentation. The experimental protocol was carefully controlled to minimise experimental error. To this aim, the cantilever sensitivity was always calibrated when changing samples and the testing conditions (i.e. temperature, day of culture at which the cells were tested, cell seeding density, cell culture protocols) were maintained constant. The load rate was set prior to experiments to make sure the measurements were comparable as it was shown that cell response changes with an increase in load rate [112]. The indenting location was controlled by centring a 5-point grid over the nucleus for repeatability.

A spherical tip was selected as an indenter. The choice of a spherical tip over a sharp (conical or pyramidal) tip lead to various advantages [113–115]. The applied force is distributed over a wider area reducing the stress and strain of the cell and therefore reducing the risk of cell damage. In terms of subsequent mathematical fitting, the probe geometry is better defined and the Hertz model accurately describes the case of a spherical indenter over an elastic body; moreover, the calculated Young's modulus values are more robust due to the reduced impact of nanoscopic inhomogeneities.

The elastic modulus values fitted when using spherical indenters reflect the mechanical property contributions of the different elements composing the cell in the tested region, e.g. the membrane, the cytoskeleton. This mesoscopic elasticity can have more relevance for clinical applications than the single element's nanoscopic characteristics [115]. The Young's modulus obtained with spherical tips is generally lower than the one obtained with sharp tips, probably due to the larger contact area, the errors in estimating the tip geometry and the fact that sharp tips may generate local large strains causing hyperelastic cell responses [116].

When testing soft samples in liquid, the contact point is not clearly marked due to the poor signal-to-noise ratio of the deflection signal and to the non-linear force-displacement relationship for small indentations [106]. The accurate estimation of the contact point is vital because it directly affects the fitting procedure needed to

calculate the Young's modulus [115]. The *RoV* method used in this context has been compared with others in terms of performance in contact point localisation [106]. Despite not being considered as the most precise method, it was shown to have sufficient accuracy and low computational cost and it was therefore selected for the present study due to the large acquired database.

The Hertz model was used to fit the Young's modulus of cells, a common choice for cell and biological sample indentation experiments [10, 40, 43] as introduced in Chapter 2 (Section 2.3.2). The indentation over a half space by a spherical body was hypothesised. Conversely, other works used the Hertz model for a spherical indenter over a spherical body when working with adherent cells [107] so a preliminary data-set was employed in this study to evaluate the radius of curvature of adherent MLO-A5 cells. This data-set included 10 cells which were tested by AFM Quantitative Imaging (QI^{TM}) mode to obtain their morphology (Fig. 3.4.1). QI^{TM} is a force spectroscopy based imaging mode which can give quantitative information on sample thickness, adhesion and slope in high resolution. A $50 \times 50 \mu m$ or $60 \times 60 \mu m$ QI^{TM} image of each cell was obtained and analysed with the AFM built-in software to obtain the thickness of the cell in respect to the substrate and the length of the two major axes. The cell thickness at the nucleus and the length of the shorter axis were used to calculate the radius of curvature by the equation of the circle passing through 3 points. The shorter axis was chosen as a safety factor to avoid underestimating the radius of curvature. Moreover, the cells were often bigger in size than the imaging window which led to an axis measurement lower than the real case. A mean (range) radius of curvature was calculated as $106.2 (33.5 - 194.7) \mu m$. These values are well above the radius of the probe ($3 \mu m$) and therefore justify the choice of using a half space as the model indented body.

The Hertz model was originally developed for a soft indenter on a rigid surface and the calculations were based on the assumption that the deformation of the sample was much smaller than the radius of the spherical probe [42]. This assumption does not apply when considering soft samples such as cells and therefore other fitting models have been proposed. A number of studies in the literature (e.g. [96, 107, 117]) utilise the model derived by Sneddon for the case of

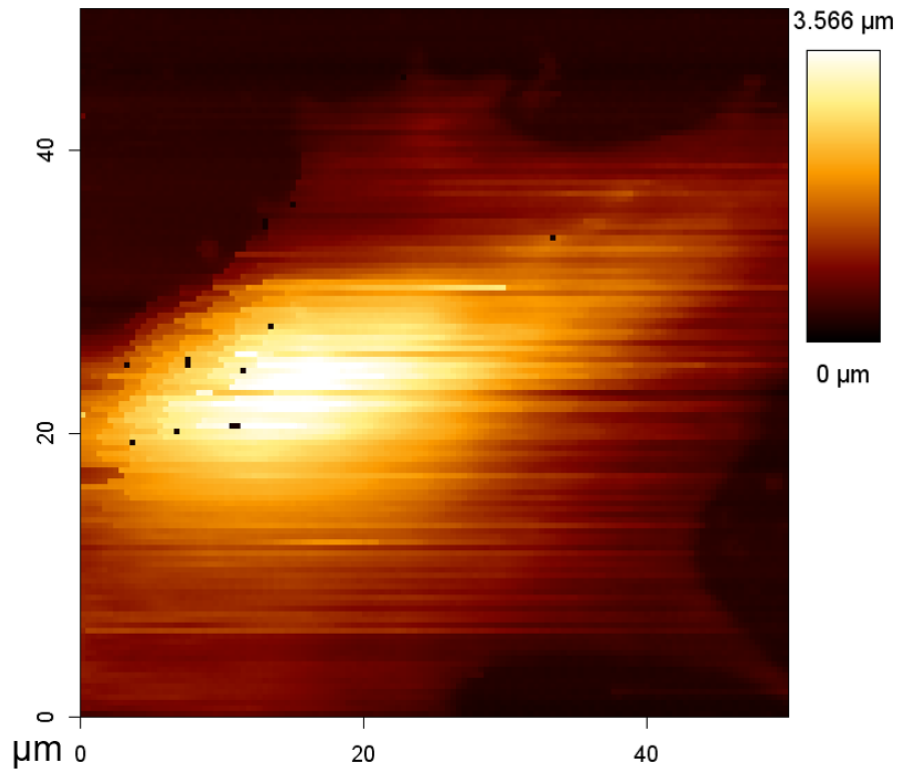


Figure 3.4.1: QI^{TM} image of an MLO-A5 cell. The colour bar represents the relative thickness of the cell to the substrate. The highest part (in yellow) corresponds to the nucleus.

a rigid indenter on a deformable surface [118] which does not hold constraints on the sample deformation and can be applied for indenters of different shapes. However, in the case of spherical indenters with radius larger than approximately $1 - 2 \mu\text{m}$ the Hertz model well approximates the Sneddon model despite its rigid assumptions and is more convenient presenting an analytical form [115].

Other models such as the Johnson-Kendall-Roberts (JKR) model [119] and the Derjaguin-Muller-Toporov (DMT) model [120] addressed the issue of adhesion between the tip and the sample which was not considered by the Hertz model. The JKR theory takes into account adhesion inside the contact area and can be applied for large tips indenting soft samples with large adhesion; the DMT model considers adhesion outside the contact area and is used for small tips indenting stiff samples with small adhesion [121]. In the present work, adhesion forces were neglected since a significant deviation between the approach and retract curve at the end of the indentation was not observed [92].

Another correction proposed for the Hertz model relates to the thin-layer effect. The Hertz model assumes an elastic half space and therefore a sample for which the thickness is much larger than the maximum indentation. Adherent cells are however soft thin bodies standing on rigid substrates (e.g. tissue culture plate) and this assumption implies neglecting the substrate's contribution. One common solution consists in limiting the indentation to small percentages of the cell height (e.g. 10% – 20% [60]) but this restricts mechanical insight on the contribution of different cell components as only the superficial region is considered [115]. Alternatively, an analytic approximate correction factor to the Hertz model for spherical indenters has been proposed for the case of small indentations which takes into account the effect of the limited sample thickness [113]. In this study, a different approach relying on the analysis of data *a posteriori* was used, i.e. checking for the presence of sharp increases in the Young's modulus for high indentation depths [107, 108].

The Hertz model hypothesises linear elastic properties of the material tested. In the case of cells, this premise cannot be assumed *a priori* [39]. As an experimental verification, the Young's modulus obtained for different indenting locations and series were compared. If a viscoelastic response was to occur within the time frame of the repeated measurements, this would reflect in a change in the stiffness for

subsequent series. No statistical difference was found, confirming that this model hypothesis could be assumed in this case.

The Young's modulus for increasing indentation depths was found to be broadly constant. For shallow indentations, slightly higher values were calculated, possibly representing the properties of the actin cortex. It was, in fact, proposed that indentation depths lower than 200 nm would give stiffness properties of the heterogeneous actin cortex region, while larger indentation depths should allow for the evaluation of the cell body stiffness [93]. Moreover, in superficial regions, the contribution of the glycocalyx or cellular brush might play a role and it has been suggested that appropriate variations of the Hertz model should be used to best fit this region and discern between the brush and the cell body contribution [60, 107]. This topic will be further discussed in Chapter 4. It should be noted that higher values for shallow indentations could also be linked to errors in the contact point fitting [106] or reduced sensitivity of the cantilever at low forces [61].

Constant Young's modulus with indentation depth was found in another work on bone cells, in which the Hertz fitted Young's modulus was found to be independent from the indentation depth for human osteoblasts tested up to 500 nm in the range of 50% – 95% of maximum indentation [48]. However, contrasting results were obtained in other works on ovary and epithelial cells [107, 112]. This could be due to different cell types displaying different cytoskeleton arrangement and overall cell and nucleus thicknesses which would affect the indentation measurements [40, 122]. Moreover, cellular brushes of different nature and composition may influence the shallow indentation results at different ratios. Finally, considerations on the sample size should be taken into account and will be subsequently discussed.

The maximum indentation of 700 nm did not show any sharp increase suggesting that the substrate was not detected. The average thickness of adherent MLO-A5 cells measured with QI^{TM} AFM mode on the preliminary data-set under similar culture conditions (Fig. 3.4.1) was 2.46 (0.30) μm . Therefore, a maximum indentation of 700 nm could affect $\sim 28\%$ of cell height. This result is in accordance with previous work on Chinese hamster ovary cells where indentations up to 50% of the cell thickness did not show a substrate contribution [112].

3.4.2 COMPARISON WITH OTHER BONE CELL YOUNG'S MODULUS VALUES

For comparison with other stiffness values recorded for bone cells, let us consider an average value of Young's modulus across the 100–700 *nm* range of indentations of 2.77 *kPa* (Table 3.3.1). In Table 3.4.1, literature data on AFM indentation of bone cells are listed. Only works in which values for cell nucleus were available are reported (see Table 2.3.1 for generic bone cell values).

Most Young's modulus average values sit in the range of 0.5 – 10 *kPa*, as the one calculated in the present work. More detailed comparison is made difficult by the employment of different Hertz model corrections, different probe shapes (i.e. higher stiffness modulus values are obtained with sharp cantilevers with respect to beaded cantilevers [97]) and loading rates (i.e. cells apparent stiffness modulus increases with the loading rate [112]).

Many works, some of which are reported in Table 3.4.1, report Young's moduli data as the mean value and standard error of the mean (SEM) (Fig. 3.3.2 in blue, and Table 3.3.1). To this aim, multiple Young's modulus values are first grouped (e.g. by cell or by location) and a mean value is calculated; then a variability range analysis is performed on these mean values to calculate their standard error. This representation does not allow for direct analysis of the population heterogeneity, as the dispersion is calculated on the mean values and not on the original data. Moreover, the average population Young's modulus values are likely to be not normally distributed (i.e. the distribution is positively skewed as the Young's modulus can't take negative values) and, therefore, the representation through a mean and not a median would result in calculating higher stiffness values unless some statistical corrections to render normality were applied.

3.4.3 MLO-A5 POPULATION HETEROGENEITY

Calculating the population dispersion could serve as an indicator of the heterogeneity of cells within the population. For the MLO-A5 cells used in this study a quartile coefficient of dispersion (CoD) of 0.24 (average across indentation depth range of 100 – 700 *nm*) was calculated, which could represent the heterogeneity of a standard population with cells at different phases of the cell cycle or stages

Table 3.4.1: Available Young's modulus values for bone cell nuclei tested by AFM. Cell type indicates the bone cell family tested; Young's modulus values are expressed as mean (standard error of the mean); Sample size refers to the number of cells tested.

Cell type	Young's modulus [kPa]	Sample size [cells]	Ref
Pre-Osteoblast	0.9 (0.4)	~ 20	[44]
Osteoblast	8.3 (0.4)	23	[52]
	2.6 (1.8)	~ 5	[50]
	0.6 (0.1)	25	[51]
	1.4 (0.2)	30	[48]
Pre-Osteocyte	3.2 (0.3)	10	[52]
Osteocyte	3.2, 2.2, 2.0	3	[53]
	2.7 (0.3)	34	[52]

of differentiation. To verify the rationality of this result, let us consider two scenarios. In the first scenario, a cell population is composed by 70% of cells in the G₁ phase and 30% of cells in phase S of the cell cycle (the considered percentage of cells in the S phase is higher than the one found in a standard population [123], however no stiffness data were available for cells in G₂ and M phases). By using the differences in cell stiffness found by Kelly and co-workers [45] between cells in the two phases and calculating the CoD value, a value of 0.26 was obtained. In the second scenario the same approach was used to calculate the quartile coefficient of dispersion for a population of bone cells differentiating from osteoblasts (50%) to osteocytes (50%) (i.e. this situation could represent the MLO-A₅ cell line as pre-osteocytes). The CoD calculated by using differences in cell stiffness data from Sugawara and co-workers [52] was 0.25.

These scenarios are simplistic examples based on multiple assumptions, comparing data relative to various cell types acquired with different experimental methodologies. Moreover, it has not yet been elucidated how the superposition of different cellular events (i.e. differentiation, division, migration) affect the cellular stiffness. However, they could in first approximation confirm the goodness of the population dispersion as an indicator of cell physiological heterogeneity.

A further confirmation of the MLO-A₅ population heterogeneity being com-

parable to a standard bone cell population could be obtained by comparing the SEM of the Young's modulus values. The Young's modulus SEM values in the literature ranged between $\sim 10\text{--}50\%$ of the corresponding mean values (Table 3.4.1). In the present work (Table 3.3.1) the calculated SEM was $\sim 3\%$ of the mean value. The values are therefore comparable with a lower ratio obtained in this study possibly due to the large sample size. As previously discussed this is an indirect estimate, as the SEM is calculated on the mean values and not on the raw data.

The sample size analysis performed gave an estimate of the required sample to capture the population heterogeneity by evaluating the effect of the sample size on the average stiffness. A required sample size of about 35 cells was calculated for an admitted percent deviation for the average stiffness value of 10%. This value is specific for the present protocol and cell population, but appears to be higher than other works on indentation of cells which refer to smaller sample sizes (Table 3.4.1). The method presented in this context to estimate suitable sample sizes might therefore be considered as a useful tool to provide more accurate cell stiffness evaluations. This would well fit in the wider context of a recently growing body of literature on single cell analysis and related sample sizes [124–127].

3.4.4 MORPHOLOGICAL ANALYSIS

A weak correlation was found between all the morphological parameters and the cell Young's modulus ($\rho < |0.2|$), suggesting no association between shape and mechanical properties. Similar values for the Spearman's correlation coefficients were found for human mesenchymal stem cells chemically differentiated into osteoblasts [48] and analogous results were published for murine fibroblasts [128].

Conversely, a recent report performing a detailed analysis of various cell types morphology found increasing nuclear apparent elastic modulus with cellular and nuclear size [129]. To explain this apparent discrepancy it should be highlighted that the stiffness calculation in [129] relied on intracellular forces only as no external load was present. The stiffness parameters explored in the present study and in [129] are therefore of different nature as in this context the cellular response to external loading and not its unloaded physiological state was considered.

It should be also noted that this analysis was examining the overall cell and nuc-

lear shapes and not the cytoskeletal fibre organisation. It has been in fact suggested that the spatial organisation of actin filaments would contribute to cell stiffness [43] and it has been shown that there is a strong relationship between the amount of actin and myosin and the cellular elastic modulus [128].

3.5 CONCLUSIONS

In the present work, a large sample of MLO-A5 pre-osteocyte cells was tested by AFM. The experimental protocol and post-processing were carefully controlled and the hypotheses of the Hertz model were experimentally verified in this specific context.

An average (dispersion) Young's modulus value of 2.77 (1.40) *kPa* was computed, which is in the order of magnitude of others previously calculated for bone cells. Detailed comparisons with values in the literature were difficult because of the use of different elastic modulus fitting models, probe shapes and loading rates. Constant Young's modulus over all the tested indentation depths was found, i.e. up to $\sim 28\%$ of cell height, and no substrate contribution was observed.

The population mechanical property heterogeneity that should be expected for a standard bone cell population was quantified and the minimum sample size to obtain a reliable population average Young's modulus was calculated. The computed sample size was of about 35 cells accepting a maximum percent deviation of 10% on the average population stiffness.

In the following chapters, additional studies will be presented to account for the glycocalyx contribution within shallow indentation depths and to test different bone cell lines to evaluate their heterogeneity and mechanical changes during bone cell differentiation.

4

Evaluation of the bone glycocalyx mechanical properties by AFM nano-indentation

The protocol developed in Chapter 3 is applied to verify the possibility of sensing the glycocalyx during nano-indentation experiments. Additional methods and results are presented in this chapter. The pre-processed data relative to this chapter are available at the following DOI: [10.15131/shef.data.5632774](https://doi.org/10.15131/shef.data.5632774).

4.1 INTRODUCTION

The rationale of this study was to test if possible to measure the mechanical properties of the glycocalyx of live bone cells by AFM nano-indentation. Protocol parameters such as the cantilever stiffness and probe size were tailored to this aim and the post-processing was adjusted accordingly.

The glycocalyx is defined as the dynamic collection of various membrane-bound macromolecules that can be found on the surface of cells. It is composed of glycoproteins and proteoglycans, constituted by a core protein to which GAGs chains are attached [4]. It can be found in different cell types and accomplish various functions depending on the tissue and its physiological or pathological condition. The glycocalyx components can be connected to the cell membrane via transmembrane linkers or can span through the membrane phospholipidic double layer. They have a strong negative charge and attract water causing the glycocalyx to be a soft and water-saturated material [12].

Traditionally, proteoglycans have been challenging to characterise because of their variety. Natural cell membrane proteins called lectins that bind to specific carbohydrate groups have been used as they have an affinity for specific sugar units, but identifying the predominant sugars is often not sufficient to specify the proteoglycan molecule [130]. More recently, specific proteoglycan antibodies and binding proteins have been identified and helped the glycocalyx component detection with better specificity. In endothelium, the most prominent GAGs are heparan sulphate (HS) in a percentage of 50 – 90% (in particular syndecans, glypicans, and perlecans), with the remaining composed of chondroitin/dermatan sulphate (CS, in particular biglycan) and hyaluronic acid (HA) [4]. The bone glycocalyx main component is HA [29, 131], together with other proteoglycans such as CS (decorin [32] and biglycan [33]) or HS (perlecan [38]) making a minor contribution.

Regarding the thickness of the endothelial glycocalyx, *in vitro* and *in vivo* measurements have led to highly variable values depending on the imaging method used for assessment. These values ranged from 0.02 μm to 8.9 μm *in vivo* or *ex vivo* and from 0.01 μm to 3 μm *in vitro*, causing questioning of the validity of *in vitro* models [132]. Its high water content and ability to collapse when dehydrated or in a non-physiological state have made glycocalyx visualisation and measurements laborious. A major difficulty of imaging proteoglycan pericellular layers is related to the fixation methods needed to maintain the physiological hydration of the mesh [133, 134]. Recently, a protocol was developed to image the endothelial glycocalyx using transmission electron microscopy coupled to rapid freezing/freeze substitution fixation [132] (Fig. 4.1.1). This technique allowed for high spatial resol-

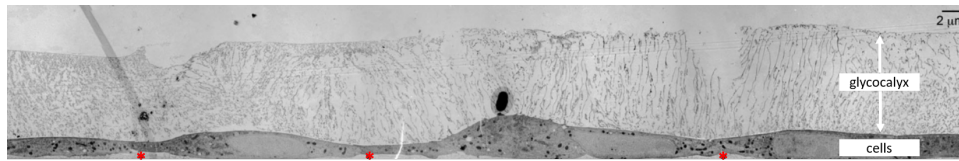


Figure 4.1.1: Transmission electron microscopy of glyocalyx-covered endothelial cells fixed by rapid freezing/freeze substitution and stained by osmium tetroxide. The red asterisks indicate the glyocalyx on the lower cell surface. Figure adapted from [132] with permission.

tion imaging of the glyocalyx in its hydrated and protein-rich configuration. It was tested on bovine aortic endothelial cells and rat fat pad endothelial cells, resulting in $11.35 \pm 0.21 \mu\text{m}$ and $5.38 \pm 1.13 \mu\text{m}$ glyocalyx thickness measured, respectively. These values were closer to the ones obtained *in vivo* and confirmed the validity of *in vitro* studies. Regarding the bone glyocalyx, no quantitative data are available. For osteocytes, it has been proposed it would span the gap between the osteocytes processes and the cement line in the lacunocanalicular network (i.e. $0.1 - 1 \mu\text{m}$) [20].

Important roles in health and disease are attributed to the glyocalyx. Its gel-like structure modulates cell binding and adhesion by providing resistance or allowing interaction with specific molecules. To enable interactions the proteoglycan molecules are pushed aside or squashed allowing contact [135–139]. In endothelium, the glyocalyx is involved in the physiological functions of homeostasis, permeability, regulation, lubrication and mechanotransduction [4, 140, 141]. When disrupted, these functions fail and pathological situations arise (reviewed in [140, 142–146]), even if not clear if as a cause or consequence of vascular impairment [147]. In cancer, the glyocalyx composition and expression can increase the tumorigenicity of cells and affect their interactions limiting the access of chemotherapeutic drugs (reviewed in [148]). The glyocalyx plays a role in pathogen recognition and inflammatory response within the immune system (reviewed in [149]). Damage to the bladder glyocalyx leads to cystitis and painful bladder syndrome (reviewed by [150, 151]).

As reviewed in Chapter 2 (Section 2.2), the endothelial glyocalyx has been ascribed a mechanosensor role in the transduction of the blood flow mechanical

signal, with its GAG branches transmitting the fluid stimulus into the inner cell compartments [23, 24]. Its contribution to mechanotransduction has also been shown experimentally [25, 26] by selective removal of its components and consequent analysis of signalling response [34] or by observation of its composition when exposed to flow [152]. Analogously, the glycocalyx in bone was suggested to be involved in mechanotransduction. Starting from the model proposed by [20] (Fig. 2.2.1, see Chapter 2, Section 2.2), this hypothesis has been taken forward with refined models [28] and experimental techniques [29–31].

There is therefore an interest in exploring bone glycocalyx mechanical properties to better elucidate its mechanoresponsive role. Some elastic modulus values obtained with AFM are available for the endothelial glycocalyx (Table 2.3.2, see Chapter 2, Section 2.3.3), but no reference values were found for bone cells. In this study, the possibility of detecting the bone cell glycocalyx by AFM nano-indentation was tested. The experimental protocol developed in Chapter 3 was employed and the post-processing steps were modified to focus on the cell membrane region instead of the cell body. Spherical probes of different sizes were employed to investigate if this affected the surface layer penetration. Different mathematical models were fitted to obtain a range of information on glycocalyx morphology and mechanical properties.

4.2 MATERIALS & METHODS

4.2.1 PRELIMINARY CONSIDERATIONS

Force spectroscopy data from the experiments presented in Chapter 3 were used as a preliminary database. The visual analysis proposed by [54, 55, 153] for which the force spectroscopy curves are searched for sharp changes in slope was performed on those data. The rationale behind this approach was that indenting a two-layer material (glycocalyx + cell body) should result in a first part of the curve with a lower slope (glycocalyx indentation, softer material) followed by a second part of the curve with a higher slope (cell body indentation, stiffer material). The indentation at which the slope changes would represent the thickness of the upper material. This approach was successfully utilised on bovine aortic endothelial cells and

a similar approach was shown to yield relevant data when testing bacterial walls [61]. On the available MLO-A5 database, however, no clear contribution from the glycocalyx was detectable in the force spectroscopy curves. When comparing the present protocol to others [54, 55, 153] it was noticed that the cantilevers used were one order of magnitude stiffer than elsewhere. Moreover, no agreement on the colloidal probe size to be used to detect the glycocalyx was found, with diameters ranging 1 – 20 μm [54–56, 58, 153]. It was therefore concluded that the glycocalyx was not sensed with the probe used in previous experiments and the protocol and data collection presented in this chapter was designed.

4.2.2 GLYCOCALYX IMAGING

Confocal imaging was performed on fixed MLO-A5 cells to verify the presence of the glycocalyx. Fluorescent staining was carried out on the main bone glycocalyx component, HA [29, 131]. HA has a conserved composition expressed in all animals with a developed immune response and therefore it is not immunogenic and there are no specific antibodies able to recognise it [134]. Hence, a specific binding protein, the Hyaluronic Acid Binding Protein (HABP), is employed for specific HA detection in cell cultures. HABP is composed of the HA binding domain from aggrecan and it is stabilised by its native link molecule [154–156]; it can be coupled with biotin which allows for detection with secondary fluorescent tags bound to streptavidin [134].

The following protocol was used:

- MLO-A5 cells were seeded at 100 cell/cm^2 on a tissue culture treated 8 well μ -Slide (ibidi GmbH) consisting of a coverslip with eight separated chambers (1 cm^2 each);
- cells were fixed after 3 days in culture with 3.7% formaldehyde or 10% formalin for 15 minutes;
- cells were blocked with 3% Bovine Serum Albumin (BSA) for 1 hour;
- cells were incubated with HABP solution (5 $\mu\text{g}/\text{ml}$ biotinylated HABP in 6% BSA in PBS) at 4°C overnight;

- cells were rinsed with PBS and stained for HA with the streptavidin-conjugated fluorophore (1% fluorophore in 1% BSA in sodium phosphate buffer) for 1 hour at room temperature;
- cells were rinsed with PBS and stained for actin with Alexa FluorTM 594 Phalloidin (0.67 ng/ml fluorophore in PBS) for 30 minutes;
- cells were rinsed with PBS and stained for nuclei with 4',6 - diamidino - 2 - phenylindole (DAPI) (1 µg/ml fluorophore in PBS) for 10 minutes;
- after a final wash with PBS, samples were readily imaged by confocal microscopy.

BSA and biotinylated HABP from bovine nasal cartilage were sourced from Sigma-Aldrich, Streptavidin-Alexa FluorTM 488 conjugate and Alexa FluorTM 594 Phalloidin from ThermoFisher. During preliminary experiments, two controls were designed to verify specific staining. In the inhibitor control, exogenous HA was added with HABP in 10 : 1 proportion to inhibit HABP; in the streptavidin control, no HABP was added to check the specificity of the streptavidin-biotin binding.

Confocal images were acquired at the Kroto Research Institute Confocal Imaging Facility. 512 x 512 pixel images were obtained using a Zeiss LSM 510 Meta inverted confocal microscope mounted with a Plan-Apochromat 63x/1.4 oil DIC objective, with a pixel dwell time of 51.2 µs. Streptavidin-Alexa FluorTM 488 conjugate was excited using a laser wavelength of 488 nm (40% transmission) and emission was detected between 500 – 550 nm as a result of the band pass filter used; Alexa FluorTM 594 Phalloidin was excited using a laser wavelength of 543 nm (77% transmission) and emission was detected above 560 nm as a result of the long pass filter used; DAPI was excited using a laser wavelength of 800 nm (9% transmission) and emission was detected between 435 – 485 nm as a result of the band pass filter used. A 27 image Z-stack was obtained with similar parameters with a pixel dwell time of 12.8 µs. Image analysis was performed using Zeiss LSM Image Browser; Z-stack reconstruction was performed in ImageJ [109].

4.2.3 CELLS

Late stage osteoblasts/early stage osteocytes MLO-A5 cells were used. Cells (passage 27–28) were cultured following the same protocol presented in Section 3.2.1 (Chapter 3).

4.2.4 AFM CANTILEVER PREPARATION

Spherical tipped cantilevers were prepared as per Section 3.2.2 (Chapter 3). To increase the possibility of sensing the glycocalyx, softer cantilevers were chosen with nominal spring constant equal to 0.01 N/m (Windsor Scientific) and silica beads of different sizes were tested ($D = 1, 2.5, 6\ \mu\text{m}$, Bangs Laboratories).

4.2.5 AFM SET-UP

The AFM set-up was the same described in Section 3.2.3 (Chapter 3). A total of 80 cells (15 data per cell) for each probe size ($D = 1, 2.5, 6\ \mu\text{m}$) were indented, each on a separate experiment.

4.2.6 POST-PROCESSING

As per Chapter 3, the obtained data files were exported as text files from the JPK Data Processing software. All the subsequent post-processing was performed in MATLAB (Mathworks) with custom-written algorithms to allow for careful tailoring of the analysis steps. The contact point determination was performed as described in Section 3.2.4.

To address the aim of collecting the mechanical properties of the glycocalyx layer, four different approaches were employed, as detailed below.

1. *Slope detection*: the force spectroscopy curves were analysed to detect a sharp change in slope after shallow indentations [54, 55, 153]. The indentation depth at which the change in slope was detected would represent the thickness of the glycocalyx layer.
2. *Hertz model*: the same approach described in Section 3.2.4 (Chapter 3) was used to fit the Young's modulus over different indentation depths. With

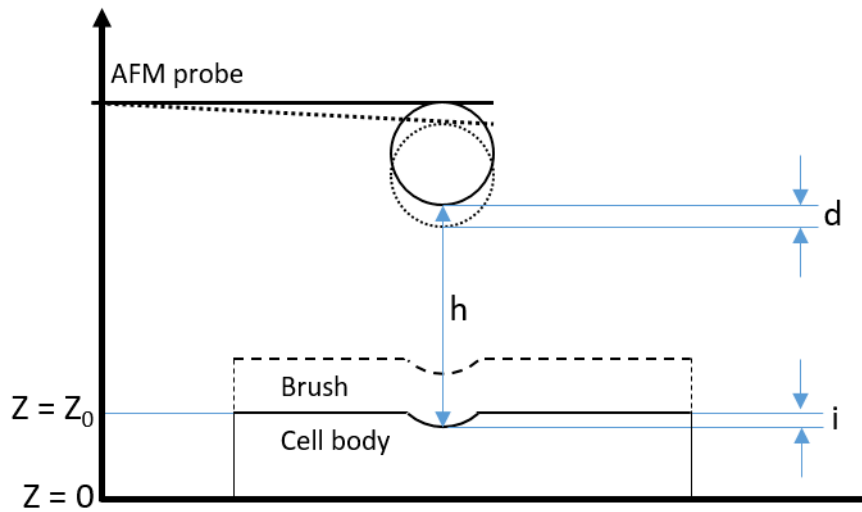


Figure 4.2.1: Schematic of a cell covered by glycocalyx being indented by a spherical AFM probe. Z represents the relative position of the cantilever, d the cantilever deflection, Z_0 the undeformed sample position, i the sample deformation, h the separation between probe and sample. Figure adapted from [60].

softer cantilevers and differently sized probes, this should lead to detect distinct mechanical properties for shallow and deep indentations. Average and dispersion values were calculated as per Section 3.2.5.

3. *Brush model:* the so-called brush model [59, 60] was implemented. This model was suggested to separate the contributions of the deformation of the cell body and the brush layer (or glycocalyx). Starting from geometrical considerations a two-step fitting is performed: firstly the elastic modulus is fitted for forces near the maximum load, where it can be hypothesised that the brush is completely squeezed; secondly, the force dependency due to the brush is sought and its grafting density and length are fitted for the case of an entropic brush. This model does not provide information on the glycocalyx mechanical properties but has been used to evaluate the cell body mechanical properties free from the brush layer contribution [98, 107].

Brush model derivation

In this section the model derivation illustrated in [60] is described, using as

reference the notation depicted in Fig. 4.2.1. The separation between probe and sample h can be written as (Eq. 1 in [60]):

$$h = Z - Z_0 + i + d, \quad (4.1)$$

with Z height of the cantilever, Z_0 undeformed sample position, i the sample deformation and d cantilever vertical deflection ($d = F/k$ with F measured force and k cantilever stiffness). The Hertz model for a sphere-sphere interaction can be written as:

$$F = \frac{4}{3} i^{3/2} \frac{4}{3} E \sqrt{\frac{R_p R_c}{R_p + R_c}}, \quad (4.2)$$

with E Young's modulus of the cell, R_p and R_c radii of the probe and cell, respectively. By writing F as ($k d$) one can write:

$$i = \left(\frac{9}{16} \frac{k}{E} \sqrt{\frac{R_p + R_c}{R_p R_c}} \right)^{2/3} d^{2/3}. \quad (4.3)$$

Therefore Eq. 4.1 can be expressed as (Eq. 2 in [60]):

$$h = Z - Z_0 + \left(\frac{9}{16} \frac{k}{E} \sqrt{\frac{R_p + R_c}{R_p R_c}} \right)^{2/3} d^{2/3} + d. \quad (4.4)$$

In the first step the cell elastic modulus E and the undeformed sample position Z_0 are fitted. To this aim, the forces near the maximum load are considered, when $h = 0$. Then Eq. 4.1 becomes:

$$Z_0 - Z - d = i. \quad (4.5)$$

By substituting Eq. 4.3, Eq. 4.5 reads (Eq. 3 in [60]):

$$Z_0 - Z - d = \left(\frac{9}{16} \frac{k}{E} \sqrt{\frac{R_p + R_c}{R_p R_c}} \right)^{2/3} d^{2/3}. \quad (4.6)$$

Hence, Eq. 4.6 can be used to fit the unknown parameters E and Z_0 near the

maximum load (last 200 nm indentation).

In the second step the force dependency due to the brush is sought and its grafting density and length are calculated. The force F as function of the distance between the probe and the sample h can be written as (Eq. 7 in [60]):

$$F(h) = kd = k(h - Z + Z_0 - i). \quad (4.7)$$

To obtain the brush grafting density N and length L , the force can be fitted in the case of an entropic brush by (Eq. 8 in [60]):

$$F(h) \approx 50 k_B T \frac{R_p R_c}{R_p + R_c} N^{3/2} \exp\left(-2\pi \frac{h}{L}\right) L, \quad (4.8)$$

with k_B Boltzmann constant and T temperature. This approximation is only valid if $0.2 < h/L < 0.8$.

Considerations and modifications to the original brush model

In the first step, the model requires fitting the Z vs. d data with Eq. 4.6 in the region near the maximum load (last 200 nm of indentation) to get the cell body Young's modulus E and the undeformed sample position Z_0 . In this region, the curve can be approximated by a line which slope depends on the stiffness of the substrate and therefore be written in the form:

$$x = ay + p_1,$$

where the parameter a contains information on the cell Young's modulus E and the coefficient p_1 represents the intercept with the x-axis (Fig. 4.2.2). This hypothesis was verified by fitting an equation of the form $x = \beta y^\gamma$ on this portion of the data and obtaining values for γ close to 1 ($\gamma = 0.97 \pm 0.02$). The brush model, however, proposes to fit this region with a function of the form:

$$x = -y - by^{2/3} - p_2,$$

with $b = \left(\frac{9}{16} \frac{k}{E} \sqrt{\frac{R_p + R_c}{R_p R_c}}\right)^{2/3}$ and therefore containing information on E and $p_2 = Z_0$ (Eq. 4.6). As this part of the curve is linear as shown in red

in Fig. 4.2.2, the fitting with a non-linear function is not reliable, especially if interested in the coefficient b containing information on E , which is the case here. Moreover, the linear term of the non-linear function carries no coefficient and therefore the slope of the fitting line is forced to be equal to 1.

A different approach to get E and Z_0 was therefore considered. The Young's modulus E was obtained by using a Hertz model fitting up to the maximum indentation. As discussed in Section 3.2.4 (Chapter 3), the variation of a sphere indenting a half space was used, differently from [60] where the sphere-sphere case was chosen. Conversely to the approach detailed in Section 3.2.4, a given maximum indentation depth was not set (e.g. where 90% of data were available), but all the available points were fitted. To obtain the undeformed sample position Z_0 a line function $d = -aZ + p$ was fitted on the region near the maximum load (red in Fig. 4.2.3) and Z_0 was obtained as p/a (red circle in Fig. 4.2.3).

The second step was maintained unchanged and therefore Eq. 4.8 was fitted on the probe-sample separation h vs. force F curves (Fig. 4.2.4), with the only variation of the sphere-half plane form instead of the sphere-sphere one. The parameters relative to the brush grafting density N and length L were obtained and the relationship $0.2 < h/L < 0.8$ was verified.

Average and dispersion values were computed following the method in Section 3.2.5 for the four fitted parameters E , Z_0 , N and L .

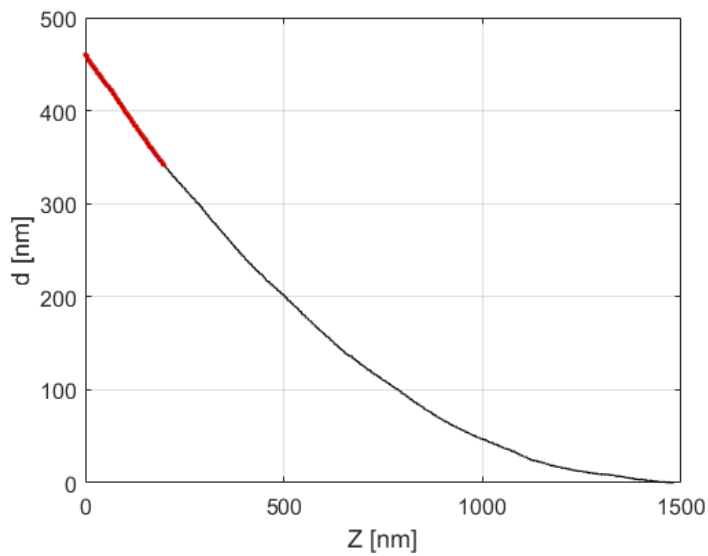


Figure 4.2.2: The relative position of the cantilever Z is plotted against the cantilever deflection d in a representative example. The curve portion coloured in red represents the region near the maximum load (last 200 nm of indentation) where the first step of the brush model is fitted.

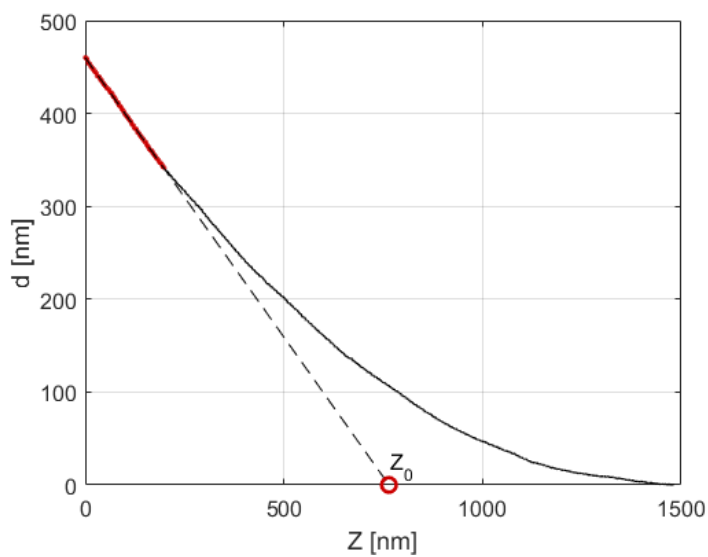


Figure 4.2.3: The relative position of the cantilever Z is plotted against the cantilever deflection d . The curve portion coloured in red represents the region near the maximum load (last 200 nm of indentation). To obtain Z_0 , a line (black dashed) is fitted on the red region and its intercept with the x -axis is sought (red circle).

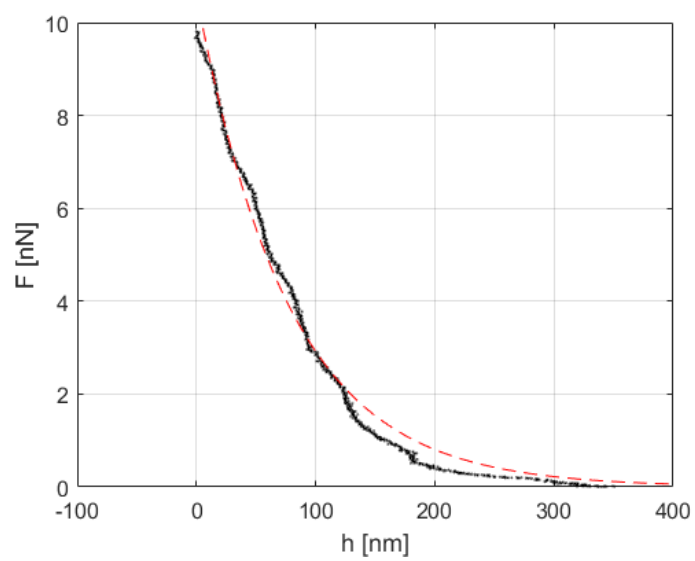


Figure 4.2.4: The probe-sample separation h is plotted against the force F . Eq. 4.8 (red dashed) is fitted to obtain the brush grafting density N and length L .

4. *Non-Hertzian point-wise approach and two-layer composite compliance model:* a non-Hertzian point-wise approach was proposed to compute an apparent elastic modulus dependent on indentation depth. This would provide information on material non-linearity and heterogeneity in a depth-dependent manner by also accounting for specific indenter geometries [39, 108, 157]. Material non-linearities for cell indentations have been found for shallow depths [108], i.e. when the glycocalyx might play a role. In fact, this model was successfully employed to study the endothelial glycocalyx mechanical properties when tested by AFM with a spherical probe [56]. To compute the glycocalyx indentation δ , the displacement at each point of the force spectroscopy curve is subtracted to a hypothetical rigid substrate deflection-displacement line, with the slope equal to the negative cantilever stiffness as calibrated with the AFM microscope system (Fig. 4.2.5). The $F(\delta)$ force-indentation curve can be then calculated. A geometry function $\Phi(\delta)$ is used to account for the indenter spherical shape:

$$\Phi(\delta) = \frac{4}{3\pi} \sqrt{R\delta^3}, \quad (4.9)$$

with R probe radius. This function is then applied to the point-wise elastic modulus $E(\delta)$ calculation:

$$E(\delta) = \frac{F(\delta)}{2\pi \Phi(\delta)}. \quad (4.10)$$

The indentation depth δ at which $E(\delta)$ shows an inflection can be used as an estimate of the glycocalyx thickness δ_G .

A composite compliance model can be then applied to discern between the contributions of the cell body and the glycocalyx, once the cell population average value of E is obtained for given indentation depths δ :

$$\frac{1}{E(\delta)} = \frac{1}{E_G} \exp\left(-\frac{a\delta}{\delta_G}\right) + \frac{1}{E_C} \left(1 - \exp\left(-\frac{a\delta}{\delta_G}\right)\right), \quad (4.11)$$

where E_C and E_G are the Young's modulus values of the cell body and glycocalyx, respectively, and a is a parameter defining the mechanical interac-

tions between the two layers.

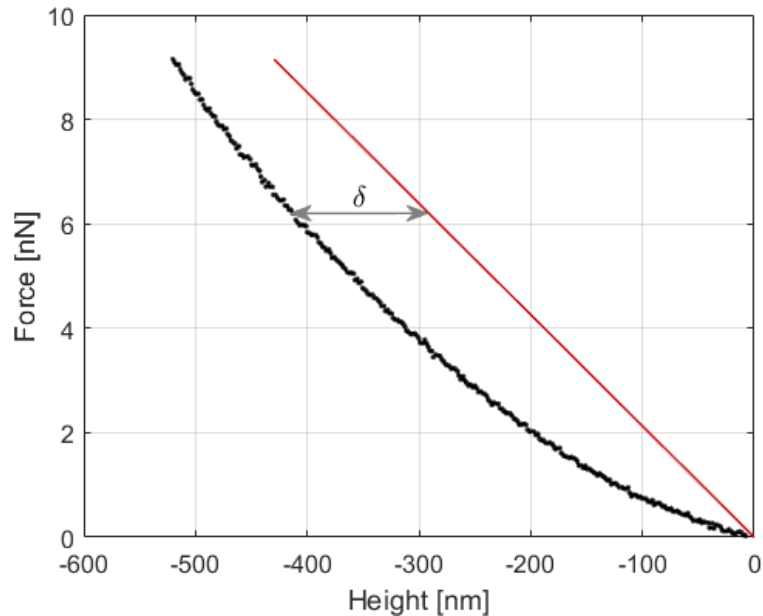


Figure 4.2.5: The force spectroscopy data (in black) are subtracted point by point to a hypothetical rigid substrate indentation curve (red line). This difference represents the sample indentation δ (grey double arrow).

4.3 RESULTS

4.3.1 GLYCOLYX IMAGING

Confocal imaging was performed on fixed MLO-A5 cells stained for HA, actin and nuclei (Fig. 4.3.1). The cells were not permeabilised to avoid affecting the cell membrane and indirectly the HA coating. For this reason the actin staining protocol was not optimal and its signal was rather poor. The HA signal was detectable on the cell surface, confirming the presence of an HA-rich glycocalyx in a dome-like structure around the cell (Fig. 4.3.2).

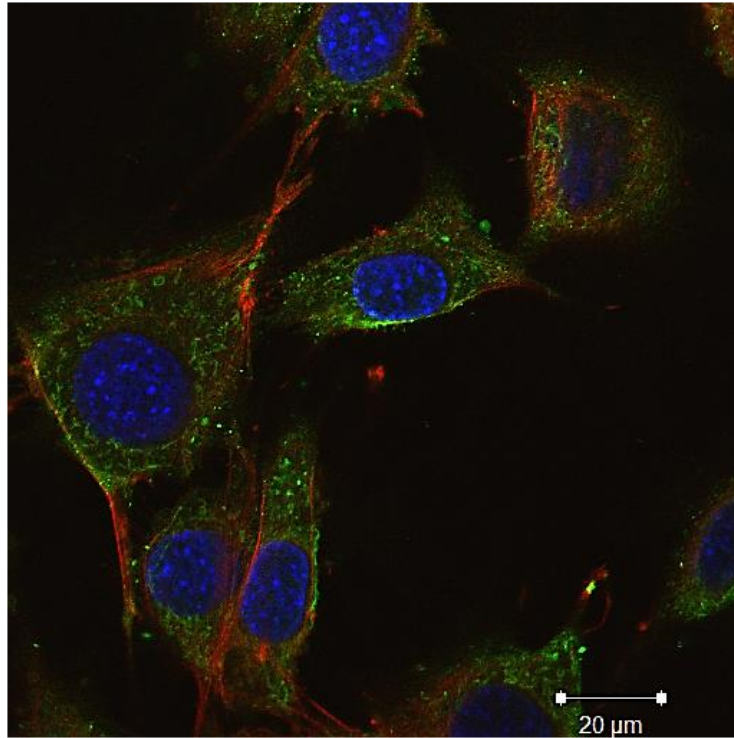


Figure 4.3.1: Confocal image of fixed MLO-A5 cells. HA is coloured in green, actin in red and nuclei in blue. Images are representative of about 5 – 6 cells imaged per slide, three slides were imaged. Scale bar equal to 20 μm .

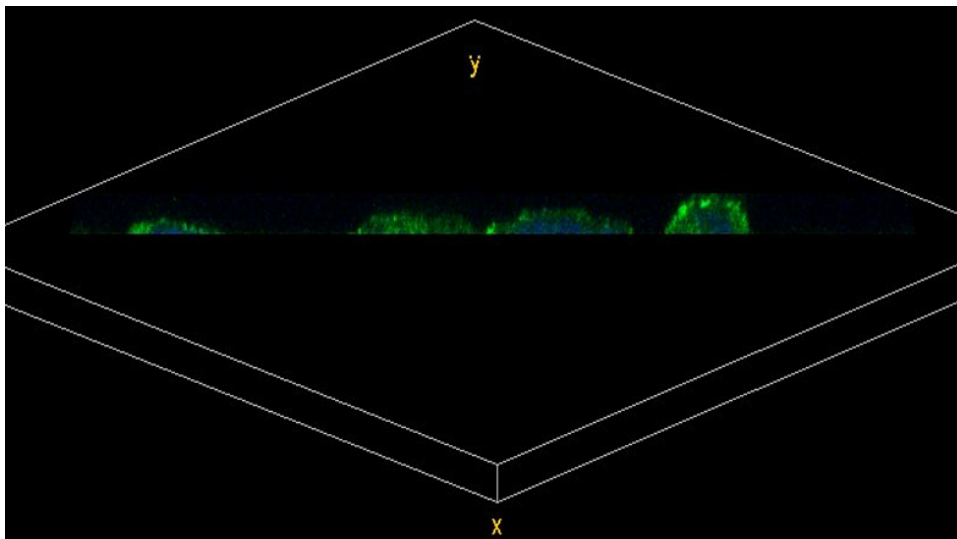


Figure 4.3.2: Confocal image of fixed MLO-A5 cells. HA is coloured in green, nuclei in blue. This image represents a Z-stack reconstruction of 27 images. The scale is the same as Fig. 4.3.1.

4.3.2 SLOPE DETECTION

The obtained force spectroscopy curves were analysed to detect a two-slope behaviour. The first slope would represent the indentation of the glycocalyx, the second slope the indentation of the cell body. As in the case of the force spectroscopy database of Chapter 3, this was however not possible as no clear distinction of curve shape was identified with any probe size. In Fig. 4.3.3 and Fig. 4.3.4 a representative example is shown of a force spectroscopy curve obtained with the $6\ \mu\text{m}$ probe in linear and log-log scale, respectively.

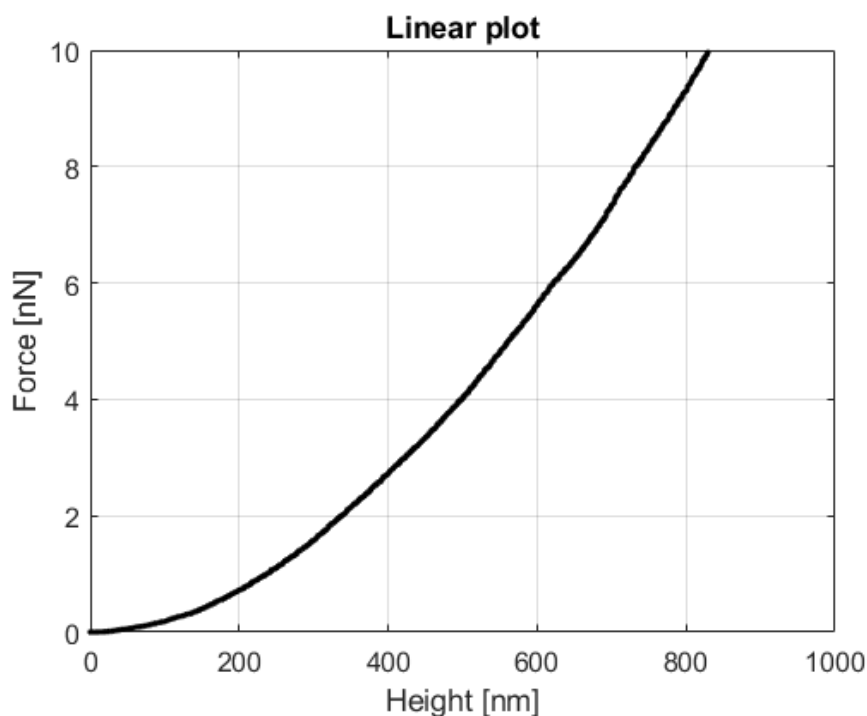


Figure 4.3.3: Example of linear plot of a representative force spectroscopy curve obtained on MLO-A5 cells with a $6\ \mu\text{m}$ spherical probe. A two-slope behaviour during indentation was not identifiable.

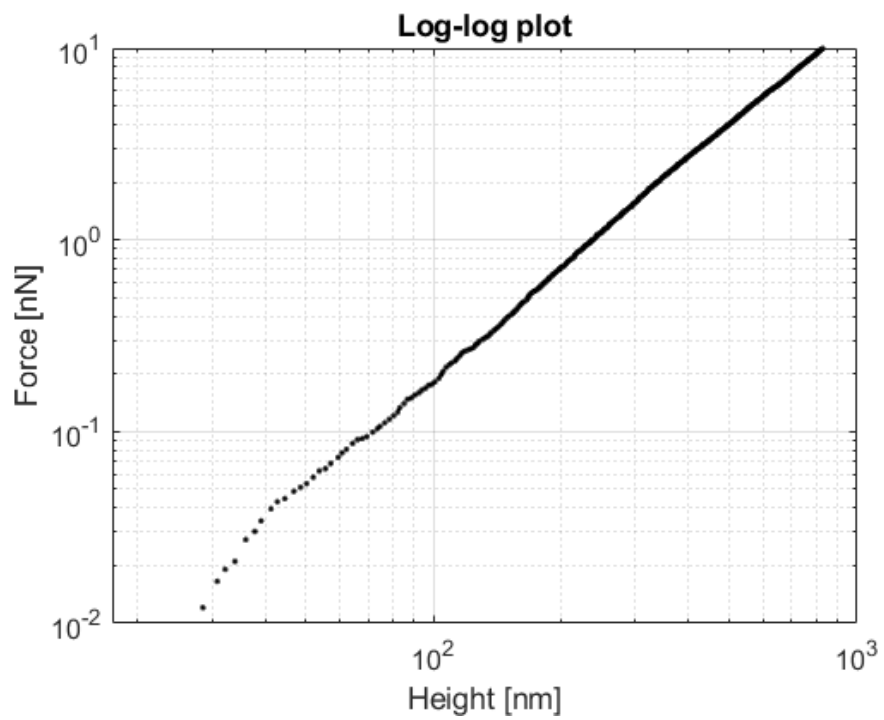


Figure 4.3.4: Example of log-log plot of a representative force spectroscopy curve obtained on MLO-A5 cells with a $6\mu\text{m}$ spherical probe. A two-slope behaviour during indentation was not identifiable.

4.3.3 HERTZ MODEL

The protocol for Young's modulus fitting described in Section 3.2.4 (Chapter 3) was performed. This was to obtain a reference value for the cell body Young's modulus over increasing indentation depths.

Young's modulus vs. indentation depth data is presented in Fig.4.3.5 as median values (not normally distributed data). Dispersion (IQR) error bars were not included for readability but can be found in Table 4.3.1 together with median, mean and SEM values. The average Young's modulus values for the $6\ \mu\text{m}$ and the $2.5\ \mu\text{m}$ probes were found to be comparable to the ones obtained with stiffer cantilevers (Table 3.3.1), although with some differences possibly due to the cantilever sensitivity. Conversely, the Young's modulus values found for the $1\ \mu\text{m}$ probe were not, possibly due to the engulfment in glue of the smallest bead during cantilever preparation. The average values for the $2.5\ \mu\text{m}$ probe showed a steeper increase with the indentation depth if compared with the $6\ \mu\text{m}$ probe ones. This could be because of the lower contact area in the case of the smaller probes, which are therefore more prone to local spatial changes in mechanical properties.

The contribution from the glycocalyx for shallow indentation depths was not detected with this method, similarly to what happened with the slope detection method for both the present database and the one described in Chapter 3. These values were therefore kept as reference for the cell body for the next two implemented methods, i.e. the brush model and the non-Hertzian point-wise approach.

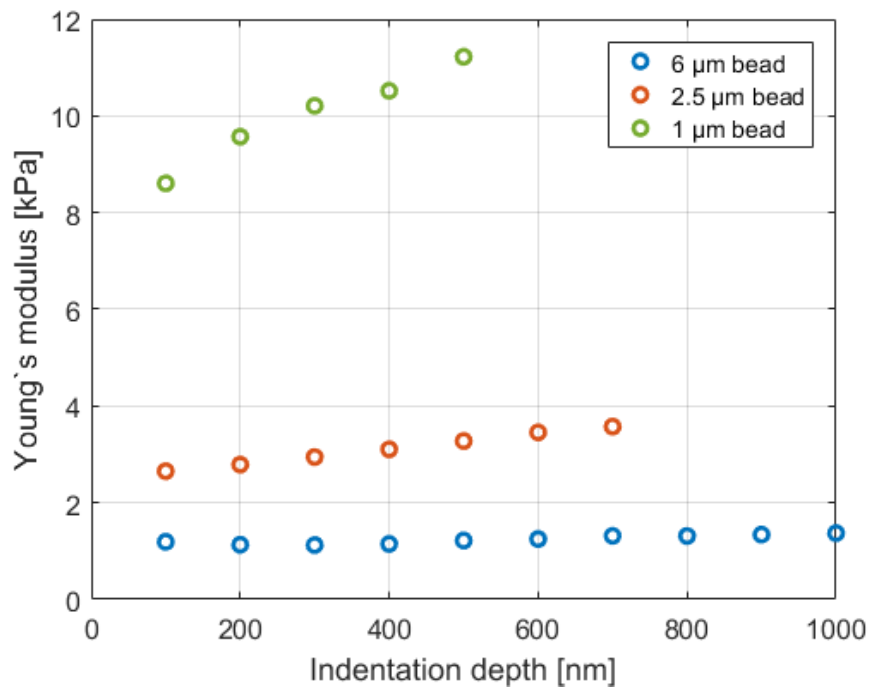


Figure 4.3.5: Average Young's modulus values against indentation depth are plotted for each probe size. While the values found for the 6 μm and the 2.5 μm probes are comparable to the ones found with stiffer cantilevers, the ones found for the 1 μm probe are not.

Table 4.3.1: Young's modulus values [kPa] for the MLO-A5 population fitted with the Hertz model. The values for the three probe sizes are included. The first column represents the indentation depth at which the value was fitted; the second and third the average (median) and dispersion (IQR) values; the fourth and fifth the mean and standard error of the mean (SEM) values. SEM values were calculated with $N = 79$ cells for the $6\ \mu\text{m}$ indenter, $N = 80$ cells for the $2.5\ \mu\text{m}$ indenter, $N = 79$ cells for the $1\ \mu\text{m}$ indenter.

	Indentation [nm]	Young's modulus [kPa]			
		median	IQR	mean	SEM
6 μm bead	100	1.19	0.68	1.22	0.05
	200	1.13	0.83	1.21	0.06
	300	1.12	0.93	1.22	0.07
	400	1.15	1.03	1.28	0.08
	500	1.22	1.14	1.36	0.09
	600	1.25	1.21	1.42	0.09
	700	1.32	1.29	1.49	0.10
	800	1.31	1.38	1.53	0.10
	900	1.34	1.44	1.53	0.10
	1000	1.37	1.50	1.53	0.09
2.5 μm bead	100	2.65	1.53	2.79	0.10
	200	2.79	1.53	2.91	0.12
	300	2.95	1.61	3.07	0.15
	400	3.10	1.89	3.29	0.17
	500	3.28	2.19	3.54	0.19
	600	3.46	2.36	3.73	0.19
	700	3.58	2.30	3.80	0.17
1 μm bead	100	8.61	5.31	9.03	0.40
	200	9.57	5.83	9.50	0.46
	300	10.21	6.88	10.01	0.53
	400	10.52	8.17	10.72	0.60
	500	11.22	8.95	11.13	0.59

4.3.4 MODIFIED BRUSH MODEL

It was possible to fit four parameters with the brush model: the cell body Young's modulus E , the undeformed position of the sample Z_0 , the grafting density of the brush N and its length L . All the quantities were not normally distributed. Values for their average, dispersion, mean and SEM for all the indenter sizes are reported in Table 4.3.2.

Similarly to the Hertz model, the Young's modulus values found for the $1\ \mu\text{m}$ probe were much higher than for the other two probe sizes, possibly due to a partial glue engulfment during cantilever customisation. As the Young's modulus calculated in this step was then used in the calculations of the brush grafting density N and length L , the values found for these parameters with the $1\ \mu\text{m}$ probe were probably unreliable.

The undeformed sample position Z_0 was lower at smaller probe dimensions. This was linked to the way this value was fitted, as the intercept with the x-axis of a line tangent to the curve Z vs. d in the last $200\ \text{nm}$ of indentation. Z represents the cantilever height, d the cantilever deflection calculated as the measured deflection force F divided by the cantilever spring constant k . The cantilever spring constants for the $6\ \mu\text{m}$, $2.5\ \mu\text{m}$ and $1\ \mu\text{m}$ probes were $0.0213\ \text{N/m}$, $0.0583\ \text{N/m}$ and $0.147\ \text{N/m}$, respectively. Let us consider a generic height vs. force curve: to obtain the Z vs. d curve, height equals Z and force divided by k equals d . If the force is divided by different values of k this causes the slope of the curve to change and consequently its intercept with the x-axis. Due to this dependency, the meaning of this fitted parameter might not be relevant.

Table 4.3.2: Cell body Young's modulus E , undeformed position of the sample Z_0 , grafting density of the brush N and its length L as fitted with the brush model for the MLO-A5 population. The values for the three probe sizes are included. The first and second columns represent the average (median) and dispersion (IQR) values; the third and fourth the mean and standard error of the mean (SEM) values. SEM values were calculated with $N = 79$ cells for the $6\ \mu\text{m}$ indenter, $N = 80$ cells for the $2.5\ \mu\text{m}$ indenter, $N = 79$ cells for the $1\ \mu\text{m}$ indenter.

			median	IQR	mean	SEM
6 μm bead	E	[kPa]	1.63	1.41	1.80	0.10
	Z_0	[nm]	1136.28	270.22	1181.48	24.75
	N	[μm^{-2}]	461.33	213.81	427.92	16.69
	L	[nm]	450.46	76.88	500.83	38.10
2.5 μm bead	E	[kPa]	4.25	2.15	4.58	0.20
	Z_0	[nm]	650.77	136.04	664.09	11.73
	N	[μm^{-2}]	957.55	577.71	1039.41	55.72
	L	[nm]	160.09	177.49	399.76	80.84
1 μm bead	E	[kPa]	12.49	8.96	12.41	0.60
	Z_0	[nm]	454.41	166.23	493.80	13.71
	N	[μm^{-2}]	2920.06	1976.63	3074.29	201.98
	L	[nm]	136.50	1639.18	1380.09	300.29

4.3.5 NON-HERTZIAN POINT-WISE APPROACH AND TWO-LAYER COMPOSITE COMPLIANCE MODEL

The first step of this approach consisted in fitting a point-wise Young's modulus for all indentation depths. Average values for depths of 50, 100, 200, ... nm were computed for the cell population with the three probe sizes (not normally distributed, Table 4.3.3). In Fig. 4.3.6 a comparison with the Hertz model for all indentation depths and probe sizes can be found. This model was designed to better capture the non-linearities of the material. Lower Young's modulus values were fitted for shallow indentations compared to the Hertz model, but overall the two methods had similar outcomes for the $6\ \mu m$ and $2.5\ \mu m$ probes.

The second step implied hypothesising a glycocalyx thickness and subsequently fitting the two-layer composite compliance model. The mean point-wise Young's modulus was plotted versus the indentation depth to identify the region of the curve showing an inflection, i.e. the indentation depth that should represent the glycocalyx thickness δ_G . In Fig. 4.3.7 an example of the $6\ \mu m$ probe is shown: the value of δ_G was identified at $450\ nm$ similarly to that obtained with the brush model. For the other two probe sizes, δ_G was identified at $350\ nm$. This value was used as a parameter for the fitting equation (Eq. 4.11), together with the parameter α representing the mechanical inter-layer interaction. The latter was chosen equal to 2.2 as fitted by [56], hypothesising similar mechanical interactions between the glycocalyx and the cell for endothelium and bone. The unknowns then were E_G and E_C , the glycocalyx and cell body Young's moduli, respectively. The fitting was performed on the mean Young's modulus values and on the mean \pm standard deviation values, to obtain the intervals of variability. Results are shown in Table 4.3.4.

Table 4.3.3: Young's modulus values [kPa] for the MLO-A5 population fitted with the point-wise approach. The values for the three probe sizes are included. The first column represents the indentation depth at which the value was fitted; the second and third the average (median) and dispersion (IQR) values; the fourth and fifth the mean and standard error of the mean (SEM) values. SEM values were calculated with $N = 79$ cells for the $6\ \mu\text{m}$ indenter, $N = 80$ cells for the $2.5\ \mu\text{m}$ indenter, $N = 79$ cells for the $1\ \mu\text{m}$ indenter.

	Indentation [nm]	Young's modulus [kPa]			
		median	IQR	mean	SEM
6 μm bead	50	0.87	0.48	0.90	0.04
	100	0.87	0.62	0.92	0.05
	200	0.84	0.81	1.02	0.08
	300	0.89	1.17	1.31	0.14
	400	1.03	1.47	1.66	0.19
	500	1.10	2.07	1.94	0.23
	600	1.25	2.62	2.17	0.24
	700	1.35	2.96	2.32	0.24
	800	1.51	3.17	2.43	0.24
	900	1.81	3.23	2.53	0.24
	1000	2.01	3.20	2.59	0.24
2.5 μm bead	50	1.81	1.08	1.93	0.08
	100	1.87	1.14	2.00	0.08
	200	2.09	1.28	2.24	0.12
	300	2.30	1.75	2.62	0.20
	400	2.58	2.23	3.10	0.26
	500	2.80	2.53	3.53	0.28
	600	3.17	2.91	3.90	0.29
	700	3.56	3.13	4.20	0.30
1 μm bead	50	5.94	3.59	6.21	0.27
	100	6.31	3.79	6.43	0.31
	200	7.22	4.83	7.09	0.39
	300	7.71	6.56	8.06	0.52
	400	8.47	8.39	9.17	0.61
	500	9.48	9.29	9.92	0.63

Table 4.3.4: Young's modulus values [kPa] for the glycocalyx (E_G) and the cell body (E_C) as fitted with the two-layer composite compliance model.

	E_G [kPa]	E_C [kPa]
6 μm bead	0.51 (0.46-0.68)	2.65 (2.35-2.81)
2.5 μm bead	1.50 (1.46-1.55)	3.60 (3.30-3.90)
1 μm bead	5.22 (5.02-5.43)	9.44 (8.79-10.09)

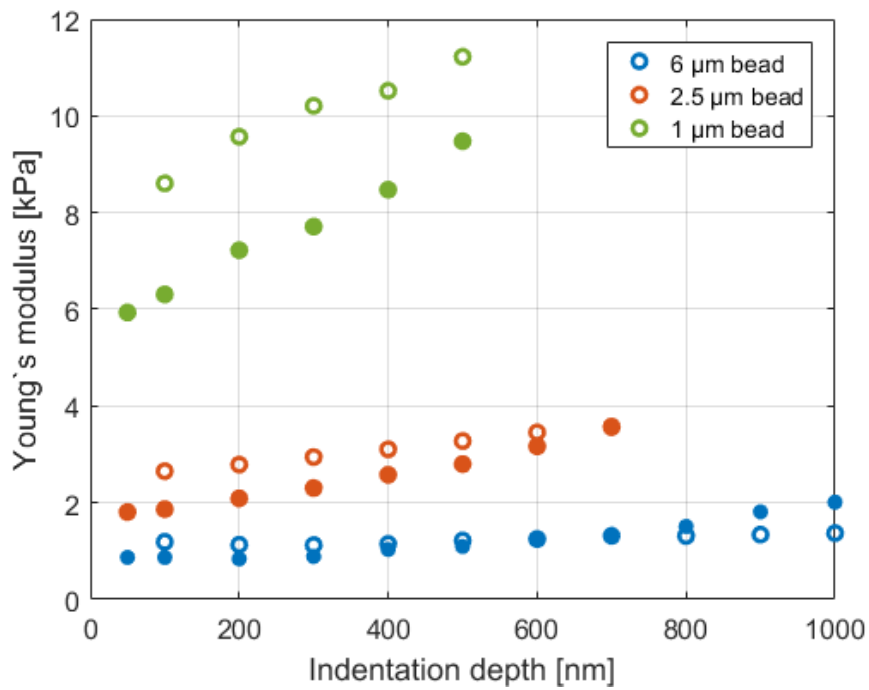


Figure 4.3.6: Comparison between indentation depth vs. Young's modulus obtained with the 6 μm , 2.5 μm and 1 μm probes for the Hertz model (empty marker) and the non-Hertzian point-wise approach (filled markers).

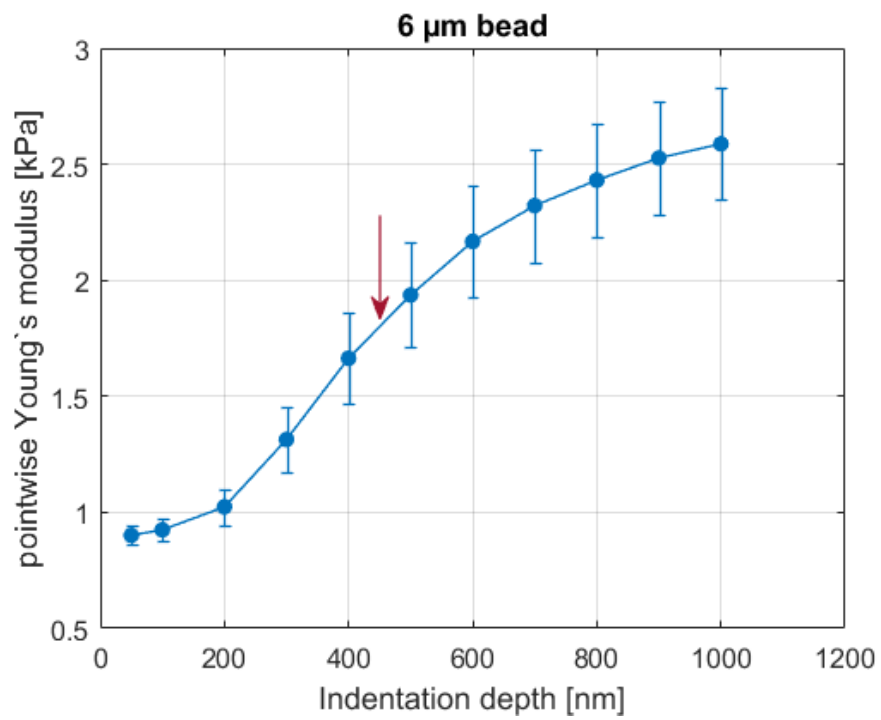


Figure 4.3.7: The mean values of Young's modulus over indentation depth for the $6\ \mu\text{m}$ probe are shown. The red arrow represents the point of inflection identified as the glycocalyx thickness δ_G .

4.3.6 CELL BODY YOUNG'S MODULUS COMPARISON

The three models gave similar qualitative outcomes for the cell body Young's modulus. In Fig. 4.3.8 the box plot for the computed Young's modulus values is shown for maximum indentation values. This indentation depth was the only comparable among the three models, as the brush model was fitted on all the available data and therefore for the maximum depth.

The non-Hertzian point-wise approach showed the widest dispersion due to the point-wise method that did not allow for smoothing of local differences during curve fitting. Its results were comparable to the Hertz model as observed previously elsewhere [157]. Statistically significant differences were found for the $6\ \mu\text{m}$ probe. However, the comparison was made only for the maximum indentation depth. When comparing an average value on the whole indentation range for each cell, no statistically significant difference was found (Mann-Whitney U-test, significance set to $p < .01$).

The Hertz and the brush models used the same fitting equation and should, therefore, give analogous results. It should be noted, however, that while the Hertz model was fitted on given indentation depths with the maximum chosen by selecting the value with more than 90% data available, the brush model used the maximum available indentation for each curve.

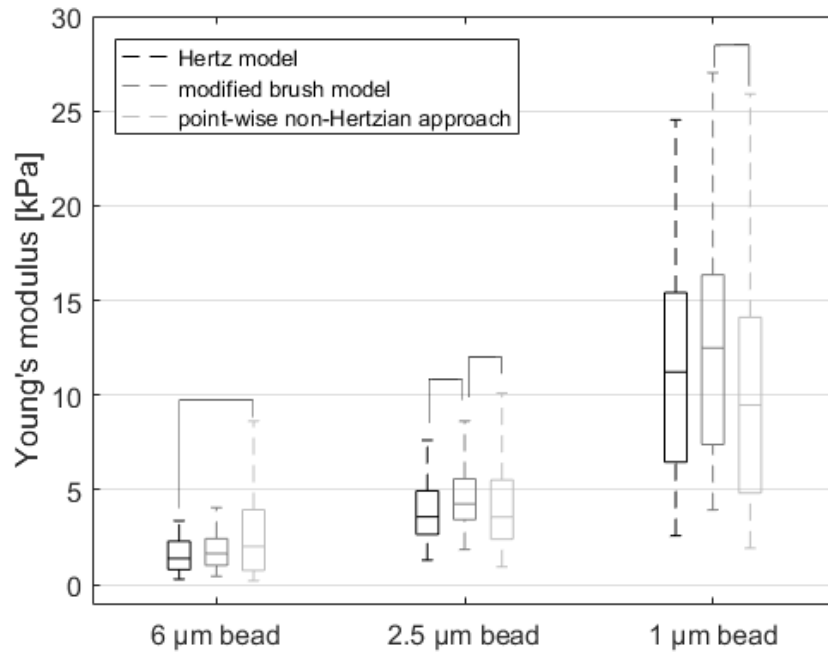


Figure 4.3.8: Cell body Young's modulus values obtained with the Hertz model, the modified brush model and the non-Hertzian point-wise approach are compared for probes of different sizes. For the Hertz model and the non-Hertzian point-wise approach Young's modulus values for the maximum indentation were considered, as the modified brush model was fitted on all the available data. Statistical comparison was performed separately for each probe size with a Kruskal–Wallis test by ranks (significance set to $p < .01$). Solid line connections represent statistically significant differences between models.

4.4 DISCUSSION

AFM nano-indentation experiments were performed on MLO-A5 pre-osteocyte cells with indenters of different size with the aim of mechanically characterising the glycocalyx. The presence of an HA-rich coating over the cell surface was shown by confocal images. However, the HA coat looked inhomogeneous on the cell. This could be related to the fixation method [134] and to the presence of other proteoglycans in the glycocalyx which were not stained in this instance (such as CS or HS). The aldehyde-based fixation method might have caused the collapse of the glycocalyx structures as the physiological hydration of the surface layer would not be maintained. Therefore no information on the glycocalyx thickness could be retrieved from these images.

Nano-indentation experiments were conversely performed on live cells in media containing a physiological salt solution and therefore no issue with glycocalyx dehydration should have arisen. The glycocalyx was consequently expected to be identifiable by AFM experiments, however, neither the slope detection method nor the Hertz model (Section 3.2.4, Chapter 3) was successful. One possible explanation for the inability to detect the glycocalyx contribution would be that it was not sensed with the present protocol. This could be caused by the chosen cantilever being too stiff to be deflected by it. However, the cantilever spring constant was chosen to equal similar protocols in the literature where the glycocalyx was sensed [54–56, 98, 153]. While in [54, 55, 153] the two-slope behaviour was detected, in [56, 98] it was not. Hence, further analyses similar to the latter two works were performed and the brush model and the non-Hertzian point-wise approach were applied to the data.

It could not be shown that cantilevers softer than the ones used in Chapter 3 led to more detailed information (i.e. clearer glycocalyx contribution) for shallow indentations. Moreover, varying the probe size led to disagreement between the fitted values and caused difficulties when comparing the results. This could possibly link to the different contact area and therefore the different subjectivity to local spatial changes. The 1 μm showed unexpected results possibly caused by the cantilever preparation process. The glue might, in fact, engulf spherical beads of small diameter [158] and this would cause a deviation from the expected spher-

ical shape of the probe. The Hertz fitting hypothesising a spherical indenter would, therefore, have low reliability [115].

The evaluation of the parameters obtained by the modified brush model was challenging. The undeformed sample position Z_0 was highly dependent on the spring constant of the employed cantilever due to the way it was calculated. For this reason, this parameter might not be meaningful. Not many values for brush grafting density were available in the literature for comparison with the present study: values in the range of $300 - 360 \mu\text{m}^{-2}$ were obtained for human cervical epithelial cells [59, 60] and lymphoblastic leukaemia cells [98], which were similar in magnitude to that computed here. The higher N values found for smaller probes could be related to the smaller surface able to sense more locally, but the lack of literature for comparison made it difficult to obtain conclusive explanations. The brush length L was fitted to median values of 160 nm and 450 nm with the $2.5 \mu\text{m}$ and $6 \mu\text{m}$ probes, respectively. These values were similar to other computed from AFM indentation experiments [54–56, 58, 98]. It should be noted that this parameter is often not readily available (unless a slope detection method can be applied). Therefore, models are fitted to obtain it and the model assumptions not always satisfied. In this case, the brush parameters were found by hypothesising an entropic brush and by fitting a model originally developed for polymers [159]. It was suggested that this model's assumptions (i.e. of stiff and homogeneous structure) would not be valid for the endothelial glycocalyx due to the electrostatic and molecular interactions between its components [55]. The bone glycocalyx was hypothesised to be similar in structure to the endothelial one, therefore care should be taken when evaluating the results obtained with this model.

The non-Hertzian point-wise approach was designed to better capture the material non-linearities [39, 108, 157] and the lower values fitted for shallow indentations when compared to the Hertz model might be an index of this feature. However, the information on the mechanical properties of the glycocalyx alone is not readily available and would require the use of a second model, i.e. the two-layer composite model. The obtained values for the glycocalyx Young's modulus were comparable to the ones found with other AFM indentation experiments [54–58]. However, it should be noted that, when using this model, the unknown parameters fitting is strongly affected by the choice of δ_G and a [56], therefore care should

be taken when interpreting these results.

4.5 CONCLUSIONS

Three samples of pre-osteocyte MLO-A5 cells were tested with different spherical probe sizes to gain information on the glycocalyx mechanical properties. The 1 μm probe gave unreliable results due to glue engulfment during cantilever preparation.

MLO-A5 cells were imaged by confocal microscopy and the presence of an HA-rich glycocalyx was confirmed. No quantitative measurement of its thickness could be obtained due to the fixation method not maintaining its hydrated state.

The slope detection method did not work on the present database, as no clear distinction in the slope of the force spectroscopy curves was detectable between the indentation of the glycocalyx and cell body.

The Hertz, brush and non-Hertzian point-wise models were used to obtain information on the cell glycocalyx. They gave qualitatively comparable results in terms of cell body Young's modulus, but statistically significant differences were observed at maximum indentation depths. This suggests that the choice of the appropriate model is crucial depending on the sought application.

The Hertz model fitting over indentation depths did not show a clear contribution from the glycocalyx, similarly to the data presented in Chapter 3. This could be due to the probe not sensing it during indentation or could suggest the need for further analyses on the data to discern between different material contributions.

Values for the brush grafting density N and the brush length L were computed by using the brush model. The strong assumption of stiff and homogeneous brush, which might not hold for the bone glycocalyx as it does not for the endothelial one [55], made the results obtained with this model possibly unreliable.

The two-layer composite compliance model was applied in combination with the point-wise Young's modulus fitting and values for the glycocalyx stiffness with a magnitude of about 30% of the cell body were obtained.

It should be noted that differences were found in all the results when comparing probes of different size and different fitting models. This highlights the need for not considering the obtained values as absolute cell characteristics indices, but always taking into account the population variability and handling the results obtained

with model fitting with care especially if the assumptions of the original model were not fully satisfied.

5

Changes in cell mechanical properties during bone differentiation

In this chapter, an application is designed to test different bone cell lines by means of AFM nano-indentation¹. The focus is on the changes in mechanical properties at different stages of bone cell differentiation. The pre-processed data relative to this chapter are available at the following DOI: [10.15131/shef.data.5632777](https://doi.org/10.15131/shef.data.5632777).

5.1 INTRODUCTION

Osteoblasts (OBs) are the bone matrix-producing cells and their main function is to form bone by secreting and mineralising bone matrix; osteocytes (OCs) derive from OB differentiation and are located in the lacunocanalicular network with the suggested function of orchestrating bone remodelling through signalling [14]. Osteocytogenesis is the process for which an OB turns into an OC. This transform-

¹Part of the work presented in this Chapter is planned to be submitted as a scientific paper.

ation involves dramatic morphological changes, such as a decrease in cell body size, the formation of dendritic processes and changes in the intracellular organelles. Despite osteocytogenesis being morphologically evident, the mechanisms controlling it are not fully understood [160, 161]. Moreover, different mechanisms might play a role depending on the different bones, types of bone formation, locations within the bone and species [160].

Osteocytogenesis has been historically regarded as a passive process, with the OBs becoming embedded in the matrix and therefore turning into OCs. Four mechanisms were proposed to explain this enclosure, with the last selected as the most probable [160]:

1. the OBs are not polarised and lay down matrix in all direction: cells become trapped by their own secretions;
2. individual OBs are polarised and lay down matrix in one direction only, different to that in adjacent layers: cells become trapped by matrix being deposited in all directions;
3. OBs in each layer are polarised in the same direction: cells are buried in matrix by the preceding generation;
4. within a layer, some OBs slow down or stop their matrix deposition rate: cells are trapped by the secretion of neighbours.

Recently, it has been proposed that osteocytogenesis is, to the contrary, an active process [161]. OBs on the bone surface were found to be highly motile and able to span distances up to 100 μm in a 24 hour period. This would suggest that the transition from motile to embedded might be associated with an arrest in motility which is likely to be linked with cytoskeletal dynamics. The formation and time evolution of dendrites would also be connected to dynamic cytoskeletal events.

The actin cytoskeleton is thought to be central in osteocytogenesis. Osteocytes have an actin-rich cytoskeleton, with fibres distributed along the entire length of the process and in a crisscross pattern over the cell body cytoplasm [162]. If this network is disrupted, the osteocytes lose their typical morphology and possibly part of its mechanosensor role, as processes retract and membrane tension decreases. Actin-binding proteins were proposed as intracellular markers for osteocyte successful differentiation [163].

Changes in the actin cytoskeleton affect the cell mechanical properties. Therefore, cells at different stages of osteocytogenesis could be identifiable by their mechanical properties. This hypothesis has been investigated in a study where OBs and OCs (osteoid and mature) isolated from embryonic chicken calvariae were tested by AFM nano-indentation on the nuclear and peripheral areas [52]. The authors found decreasing stiffness with osteocytogenesis and higher elastic moduli on the periphery than on the nucleus.

A similar experiment to investigate bone cell mechanical properties during osteocytogenesis was designed as a test application for the protocol developed in Chapter 3. Three cell lines representing different osteocytogenesis stages were selected. AFM nano-indentation tests were performed on the nuclear and peripheral areas using a spherical indenter, which should give more reliable data than the sharp tips used in [52], as discussed in Chapter 3. Larger samples were used and the minimum sample sizes to obtain reliable population average stiffness values were calculated as per Section 3.2.4. Samples from each cell line were imaged by confocal microscopy to evaluate the actin cytoskeleton due to its importance in determining cell mechanical properties.

5.2 MATERIALS & METHODS

5.2.1 CELLS

Cells from three different lines were used to represent four steps of osteocytogenesis, i.e. pre-OBs, OBs, pre-OCs and OCs. All cells derived from mouse for consistency. MLO-A5 cells data were partially presented in Chapter 3, references to the relevant Sections will be made.

MC₃T₃: PRE-OBs

The MC₃T₃ cell line represents pre-OBs. MC₃T₃ cells were originally isolated from newborn mouse calvariae. They exhibit alkaline phosphatase (ALP) activity as a marker for OBs and can mineralise and produce collagen *in vitro* [164]. MC₃T₃ cells have been used in numerous studies as models for pre-OBs and OBs, e.g. in AFM studies [44–46].

MC₃T₃ cells were cultured in MEM supplemented with 10% FBS, 100 *units/ml* penicillin, 100 $\mu\text{g/ml}$ streptomycin and 2 *mM* glutamine (penicillin streptomycin glutamine, PSG). Cells were kept at 37°C and passaged on standard tissue culture plastic when reaching 90% confluence (passage 15 – 16).

Prior to AFM experiments, cells were seeded onto tissue culture treated Petri dishes ($D = 10\text{mm}$) at a seeding density of 5000 *cell/cm*². This density was chosen to obtain spatially separated single cells during AFM experiments. Samples were tested after 2 to 3 days of culture, before the deposition of collagen.

IDG-SW₃: OBs AND OCs

IDG-SW₃ cells can represent different stages of differentiation from late OB to late OC [165]. They were derived from murine long bones and are able to produce, mineralise and embed in a mineralised collagen matrix. IDG-SW₃ cells express a temperature sensitive mutant controlled by interferon- γ (INF- γ): it induces continuous proliferation and immortalisation at 33°C in the presence of INF- γ ; at 37°C in the absence of INF- γ under differentiation conditions the cells resume their *in vivo* phenotype and are able to differentiate towards OCs. When showing OB characteristics IDG-SW₃ cells deposit collagen and mineral and express ALP; when turning towards OCs they express typical osteocytic genes, such as Dmp1 (Dentin matrix acidic phosphoprotein 1).

Dmp1 is a marker protein for osteocytogenesis: during OB maturation it becomes phosphorylated and is exported to the extracellular matrix, where it orchestrates mineralised matrix formation. In IDG-SW₃ cells, Dmp1 drives green fluorescent protein (GFP) expression, i.e. cells express green fluorescence when the protein is expressed. This feature allows observation of osteocytogenesis in IDG-SW₃ cells by fluorescence microscopy.

IDG-SW₃ cells were purchased from Kerfast (USA). They were cultured at 33°C in proliferation medium to maintain an undifferentiated and proliferative state. Proliferation medium consisted of MEM supplemented with nucleosides and 2 *mM* UltraGlutamine I, 10% FBS, 50 *units/ml* INF- γ and a solution of 100 *units/ml* penicillin and 100 $\mu\text{g/ml}$ streptomycin (penicillin streptomycin, PS, Sigma). Cells were passaged on standard tissue culture plastic when reaching 90%

confluence (passage 24 – 28).

IDG-SW₃ cultured following this protocol were considered as OBs and were tested by AFM nano-indentation as such. Prior to AFM experiments, cells were seeded onto tissue culture treated Petri dishes ($D = 10\text{mm}$) at a seeding density of $200\text{ cell}/\text{cm}^2$. This density was chosen to obtain spatially separated single cells during AFM experiments. Samples were tested after 4 to 6 days of culture.

To induce osteogenic differentiation, IDG-SW₃ cells (passage 28) were cultured at 37°C in differentiation medium. Differentiation medium consisted of MEM supplemented with nucleosides and 2 mM UltraGlutamine I, 10% FBS, 1% PS, 5 mM β -glycerophosphate (β -GP) and $50\text{ }\mu\text{g}/\text{ml}$ L-ascorbic acid 2-phosphate sesquimagnesium salt hydrate (ascorbic acid). Cells were seeded on 6-well plates at a density of $5000\text{ cell}/\text{cm}^2$ and monitored under fluorescent microscopy for the onset of GFP signal, representing the marker for osteocytogenesis.

After 10 – 12 days in culture in differentiation medium, IDG-SW₃ cells expressed a detectable GFP signal and were classified as OCs. They were passaged onto tissue culture treated Petri dishes ($D = 10\text{mm}$) at a seeding density of about $9000\text{ cell}/\text{cm}^2$. The seeding density count was made difficult by the presence of mineral deposit which caused the cells to detach as a sheet and often to bind together in clusters. Samples were tested after 1 to 3 days of culture as it was observed that the GFP signal would fade after longer periods of time. Prior to testing, each cell GFP signal was verified with the fluorescent inverted microscope coupled with the AFM microscope (Fig 5.2.1).

MLO-A₅: PRE-OCs

The MLO-A₅ cells used in this study were described in Section 3.2.1 (Chapter 3).

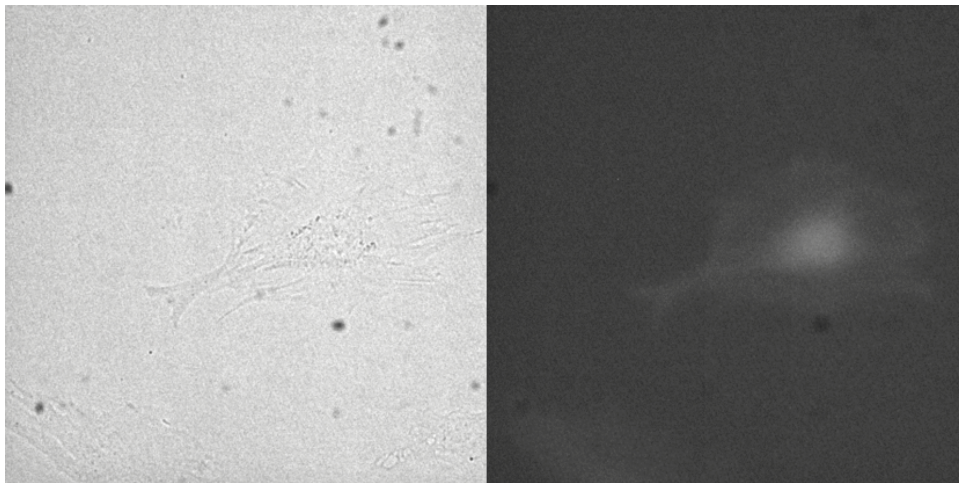


Figure 5.2.1: *An IDG-SW3 cell in bright field (left) and green fluorescence (right). The presence of green signal confirmed the started osteocytogenesis process; if no signal was detectable the cell was not tested.*

5.2.2 CONFOCAL IMAGING OF THE ACTIN CYTOSKELETON

Confocal imaging of fixed cell samples was performed on the MC₃T₃ (pre-OBs), undifferentiated IDG-SW₃ (OBs) and MLO-A₅ (pre-OCs) cells. The differentiated IDG-SW₃ were not successfully imaged due to strong mineralisation affecting the fluorescent signal.

The following protocol was used:

- cells were seeded at 2000 *cell/cm*² on a tissue culture treated ibidi μ -Slide 8 well consisting of a coverslip with 8 separated chambers (1 *cm*² each);
- cells were fixed after 1 day in culture with 3.7% formaldehyde or 10% formalin for 15 minutes;
- cells were blocked with 3% Bovine Serum Albumin (BSA) for 1 hour;
- cells were permeabilised with a solution of 1% BSA and 0.1% Triton X-100 for 20 minutes;
- cells were stained for actin with Phalloidin-Tetramethylrhodamine B isothiocyanate (TRITC) (0.67 *ng/ml* fluorophore in PBS) for 30 minutes;
- cells were rinsed with PBS and stained for nuclei with DAPI (1 μ *g/ml* fluorophore in PBS) for 10 minutes;
- after a final wash in PBS, samples were readily imaged by confocal microscopy.

Confocal Z-stack images were acquired at the Microscopy Core Facility (Medical School, University of Sheffield). 1024 \times 1024 pixel images were obtained using an inverted Zeiss LSM 510 NLO microscope mounted with a C-Apochromat 40 \times /1.2 water UV/VIS/NIR objective, with a pixel dwell time of 1.6 μ s. Phalloidin-TRITC was excited using a laser wavelength of 543 *nm* (63% transmission) and emission was detected between 565 – 615 *nm* (IR) as a result of the band pass filter used; DAPI was excited using a laser wavelength of 740 *nm* (1.1% transmission) and emission was detected between 394 – 480 *nm* as a result of the filter used. Image analysis and Z-stack reconstructions were performed using Zeiss LSM Image Browser.

5.2.3 AFM CANTILEVER PREPARATION

Spherical silica beads ($D = 6 \mu\text{m}$, Bangs Laboratories) were glued to tip-less cantilevers (Windsor Scientific) with nominal spring constant of 0.2 N/m , similarly to what was described in Section 3.2.2 (Chapter 3).

5.2.4 AFM SET-UP

The set-up was similar to the one outlined in Section 3.2.3 (Chapter 3), with applied modifications as described below. Samples were positioned on the heated sample holder to allow for testing at 37°C for the MC_3T_3 (pre-OB), MLO-A₅ (pre-OC) and differentiated IDG-SW₃ (OC) cells, at 33°C for the undifferentiated IDG-SW₃ (OB) cells.

Cell nucleus and periphery were tested for MC_3T_3 (pre-OB), MLO-A₅ (pre-OC) and differentiated IDG-SW₃ (OC) cells, nucleus only for the undifferentiated IDG-SW₃ (OB) cells. When testing for nucleus and periphery two separate grids of 5 points spaced $3 \mu\text{m}$ within each other were set on the nucleus and towards the edges of the cells (i.e. periphery) (Fig. 5.2.2). Force spectroscopy measurements were obtained on the nucleus 5–point grid for 3 times first and on the periphery 5–point grid for 3 times second to collect a total of 15 data on each location.

A total of 178 MC_3T_3 (pre-OBs) cells were indented over 3 separate experiments, 192 undifferentiated IDG-SW₃ (OBs) cells were indented over 4 separate experiments, 180 MLO-A₅ (pre-OCs) cells were indented over 3 separate experiments (nucleus data presented in Chapter 3), 160 differentiated IDG-SW₃ (OCs) cells were indented over 4 separate experiments.

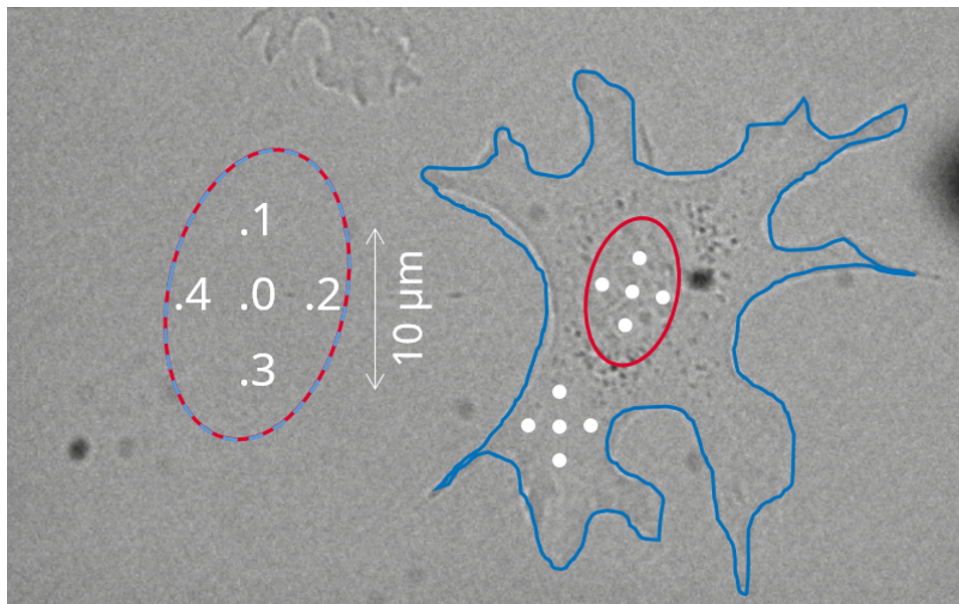


Figure 5.2.2: An MLO-A5 cell overlaid with a schematic of the indentation grids over the nucleus (red) and periphery (blue). Both grids consists of 5 points spaced $3\ \mu\text{m}$ within each other. Each point is tested thrice following the grid numbering three times.

5.2.5 POST-PROCESSING

Post-processing was performed as described in Section 3.2.4 (Chapter 3), with the following modifications. The contact point determination, Young's modulus fitting and sample size considerations were performed for all cell lines as previously outlined, with separate post-processing for the nucleus and periphery where the periphery data were available.

The morphological analysis was performed on 30 cell light microscopy images for each cell line in ImageJ [109]. Correlation of the morphometric parameters of cell and nucleus areas, nucleus major and minor axes was tested against the nucleus Young's modulus value averaged across indentation depths; correlation of the morphometric parameters of cell area, major and minor axes was tested against the periphery Young's modulus value averaged across indentation depth. Spearman's correlation coefficients ρ were calculated for each correlation pair.

5.3 RESULTS

5.3.1 CONFOCAL IMAGING OF THE ACTIN CYTOSKELETON

Confocal images of the basal actin cytoskeleton and nuclei of the MC3T3 cells (pre-OB), undifferentiated IDG-SW3 cells (OB) and MLO-A5 cells (pre-OC) are shown in Fig. 5.3.1. The Z-stack reconstruction (example of an IDG-SW3 cell in Fig. 5.3.2) exhibited the presence of most actin fibres located in the basal region (i.e. close to the adhesion substrate), with fewer located in the apical region (i.e. over the nucleus, Fig. 5.3.3).

The MC3T3 (pre-OB) and the undifferentiated IDG-SW3 (OB) cells showed fibres in a crisscross pattern as observed elsewhere for mesenchymal stem cells differentiated towards the osteoblast lineage [49, 50]. The stronger fluorescent signal and the apparent cross-section of the actin fibres of the OBs compared to the pre-OBs might be considered as a sign of differentiation progression [49]. The MLO-A5 (pre-OC) cells showed actin-rich, not fully developed processes as expected for cells turning towards OCs [162].

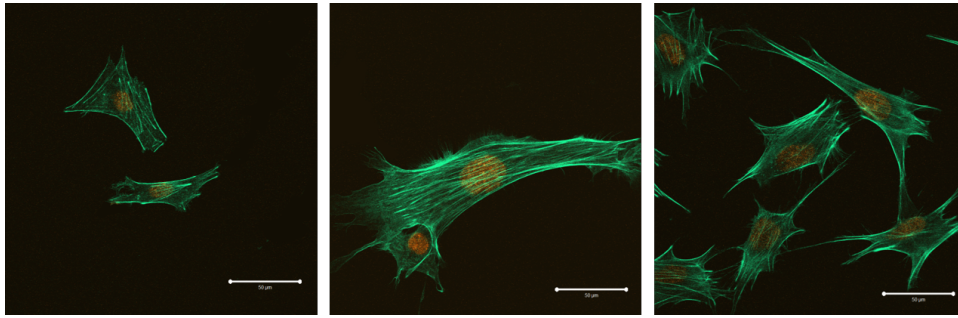


Figure 5.3.1: Confocal images of cells stained for actin (green) and nuclei (orange) are shown. Basal fibres for MC3T3 cells (pre-OB), undifferentiated IDG-SW3 cells (OB) and MLO-A5 cells (pre-OC) are shown from left to right. Scale bar equal to 50 μm . Images are representative of about 5 – 6 cells imaged per slide, three slides were imaged for each cell line.

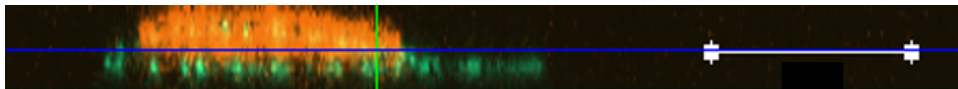


Figure 5.3.2: Confocal Z-stack reconstruction of undifferentiated IDG-SW3 (OB) cells stained for actin (green) and nuclei (orange). Most of the green signal from actin is located towards the basal region. Scale bar equal to 20 μm .

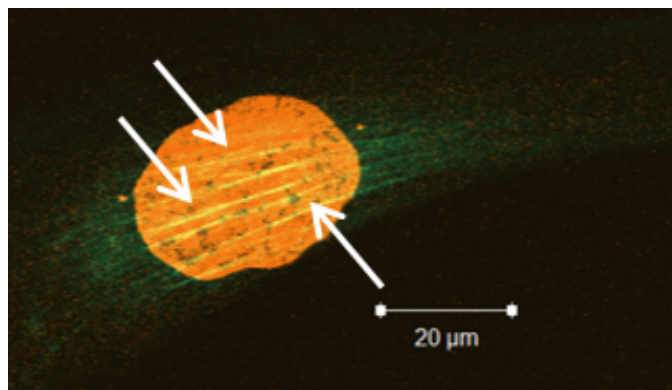


Figure 5.3.3: Confocal image of the apical actin cytoskeleton of undifferentiated IDG-SW3 (OB) cells stained for actin (green, white arrows) and nuclei (orange). Scale bar equal to 20 μm .

5.3.2 YOUNG'S MODULUS

A total of 2033 and 2453 indentations across 175 and 177 different MC₃T₃ (pre-OB) cells were analysed for the nucleus and periphery, respectively; a total of 1778 indentations across 190 different IDG-SW₃ (OB) cells were analysed for the nucleus; a total of 2137 and 2556 indentations across 168 and 180 different MLO-A₅ (pre-OC) cells were analysed for the nucleus and periphery, respectively; a total of 1214 and 645 indentations across 144 and 79 different IDG-SW₃ (OC) cells were analysed for the nucleus and periphery, respectively.

Average and dispersion values were computed for each cell, nucleus and periphery were analysed separately (normal distribution of indentations across each cell). By hypothesising each cell to have spatially homogeneous stiffness properties described by the average value, the average and dispersion values for the cell population were calculated by using the average value from single cells (not normal distribution of cell Young's modulus values across the population).

Histograms of the single cell average Young's modulus values normalised for the total number of cells were calculated for each indentation depth and cell line, for the nucleus and periphery. In Fig. 5.3.4, Fig. 5.3.5, Fig. 5.3.6 and Fig. 5.3.7 histograms relative to the nucleus can be found for MC₃T₃ (pre-OB), undifferentiated IDG-SW₃ (OB), MLO-A₅ (pre-OC) and differentiated IDG-SW₃ (OC) cells. In Fig. 5.3.8, Fig. 5.3.9, Fig. 5.3.10 histograms relative to the periphery can be found for MC₃T₃ (pre-OB), MLO-A₅ (pre-OC) and differentiated IDG-SW₃ (OC) cells. Summaries for all cell lines are reported in Fig. 5.3.14 and Fig. 5.3.15 with consistent scale for comparison.

Average (median), dispersion (IQR), mean and SEM values are reported in Table 5.3.1 and Table 5.3.2 for all the cell lines and indentation depths, for the nucleus and periphery, respectively. The average population values of the Young's modulus were constant with the indentation depth on the nucleus, but not on the periphery where they tended to increase with the increasing indentation depth. The periphery Young's modulus values resulted in higher values than the nuclear ones for all cell lines (Fig. 5.3.11, Fig. 5.3.12 and Fig. 5.3.13, Table 5.3.1, Table 5.3.2; summary in Fig. 5.3.16). MC₃T₃ (pre-OB) and MLO-A₅ (pre-OC) cells showed lower and less disperse Young's moduli for both the nucleus and peripheral regions

(Fig. 5.3.4, Fig 5.3.8, Fig. 5.3.6 and Fig. 5.3.9). In contrast, the undifferentiated (OB) and differentiated IDG-SW₃ (OC) cells showed wide dispersion ranges and higher values (Fig. 5.3.5, Fig. 5.3.7 and Fig. 5.3.10).

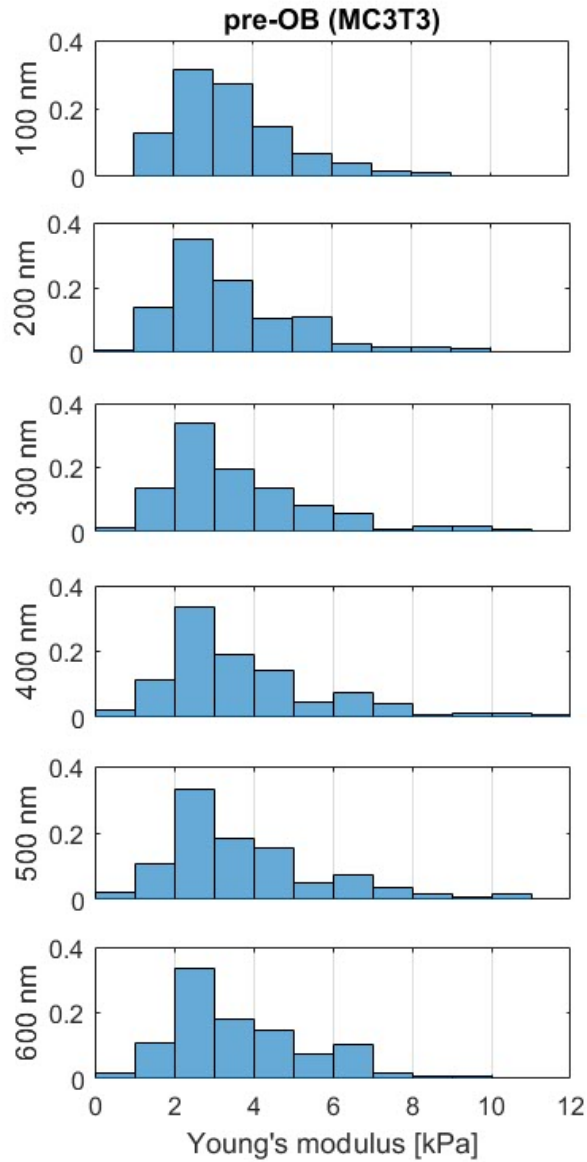


Figure 5.3.4: Histograms of single cell average Young's moduli for each indentation depth normalised for the total number of cells for the nucleus of pre-OB (MC3T3) cells.

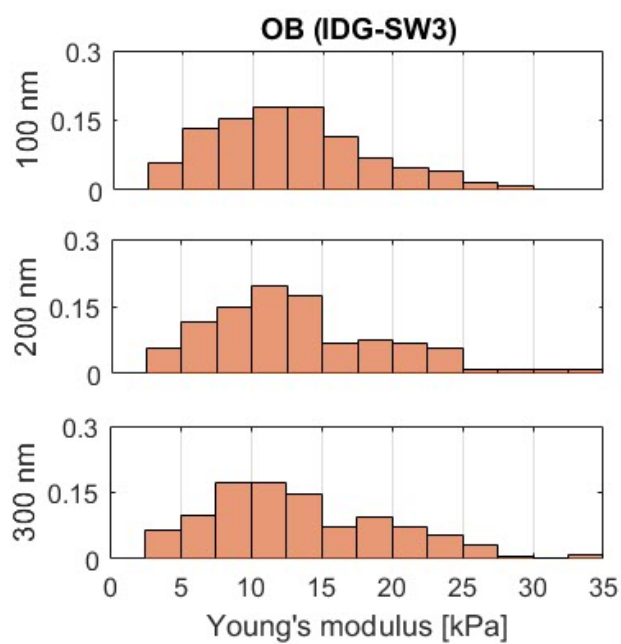


Figure 5.3.5: Histograms of single cell average Young's moduli for each indentation depth normalised for the total number of cells for the nucleus of OB (IDG-SW3) cells.

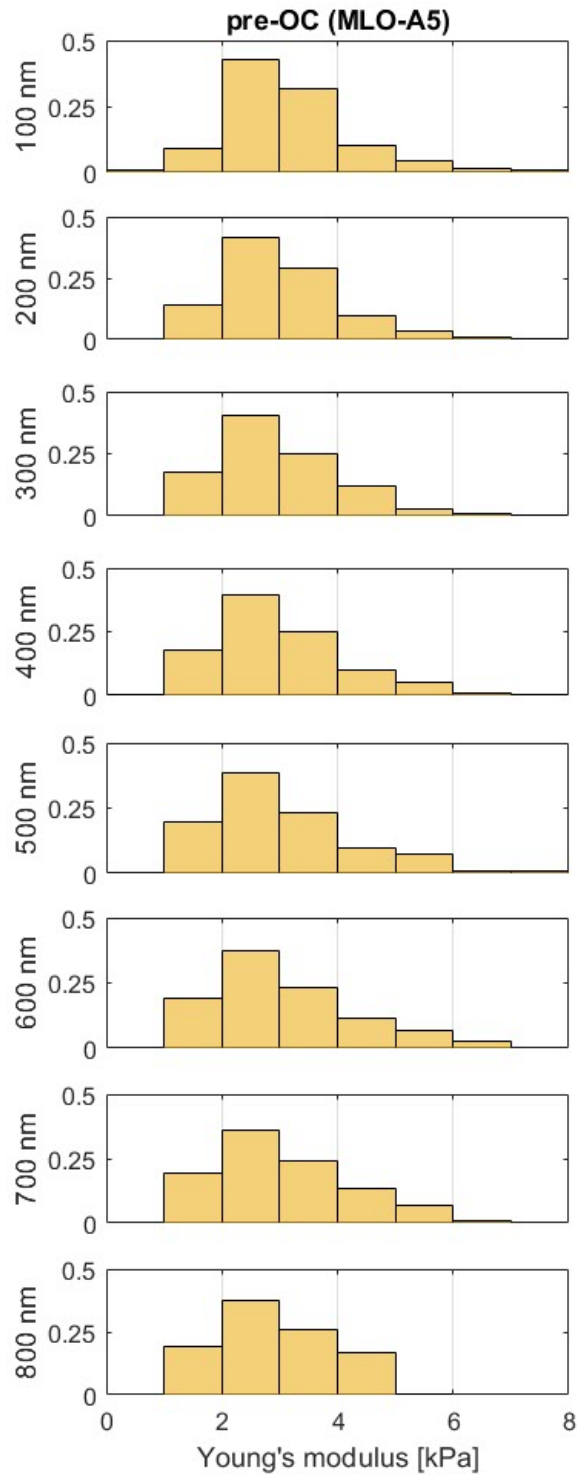


Figure 5.3.6: Histograms of single cell average Young's moduli for each indentation depth normalised for the total number of cells for the nucleus of pre-OC (MLO-A5) cells.

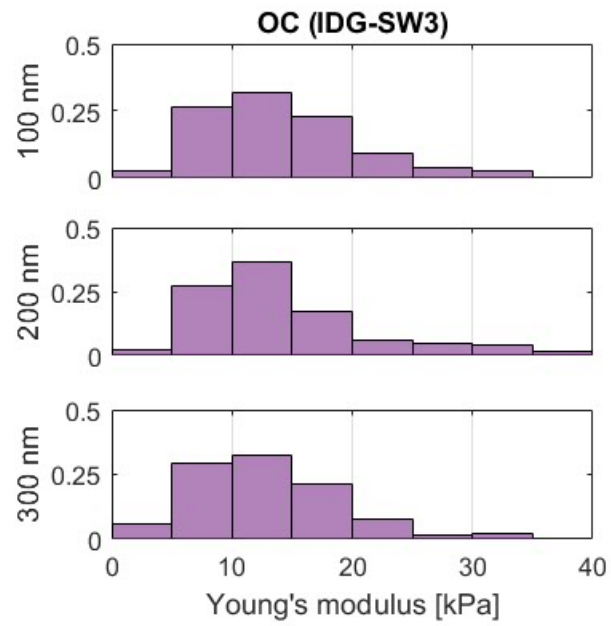


Figure 5.3.7: Histograms of single cell average Young's moduli for each indentation depth normalised for the total number of cells for the nucleus of OC (IDG-SW3) cells.

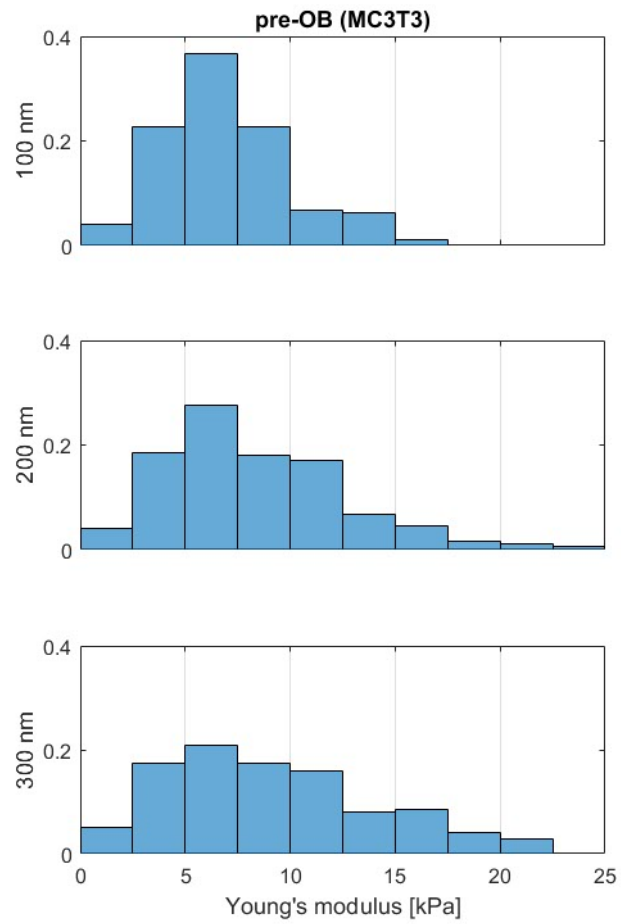


Figure 5.3.8: Histograms of single cell average Young's moduli for each indentation depth normalised for the total number of cells for the periphery of pre-OB (MC3T3) cells.

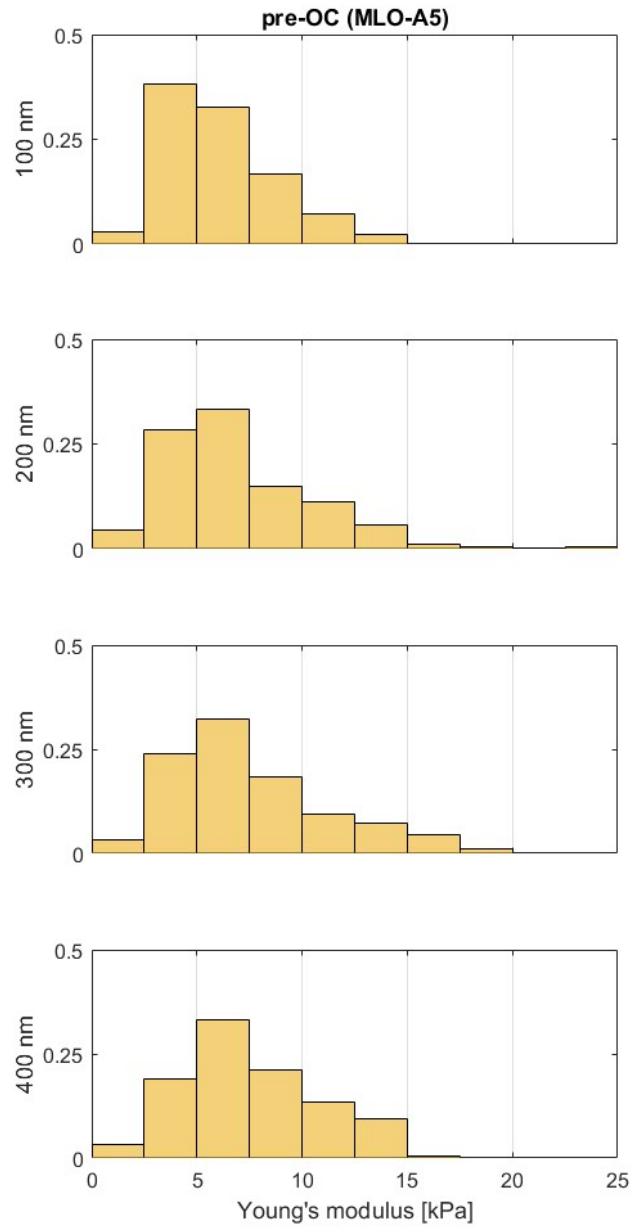


Figure 5.3.9: Histograms of single cell average Young's moduli for each indentation depth normalised for the total number of cells for the periphery of pre-OC (MLO-A5) cells.

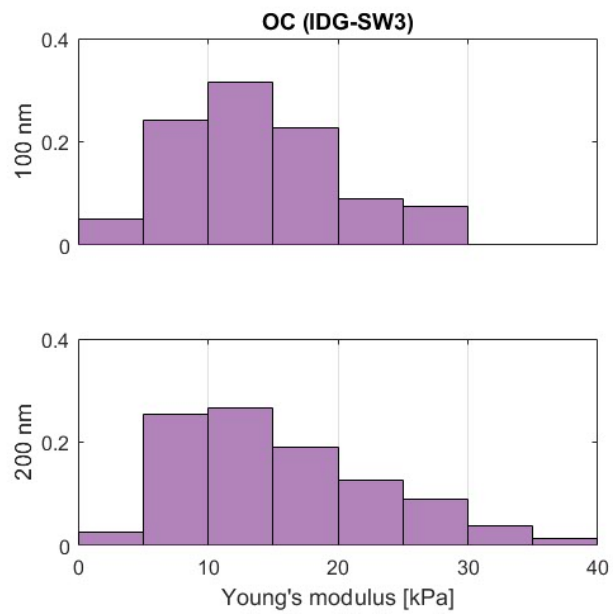


Figure 5.3.10: Histograms of single cell average Young's moduli for each indentation depth normalised for the total number of cells for the periphery of OC (IDG-SW3) cells.

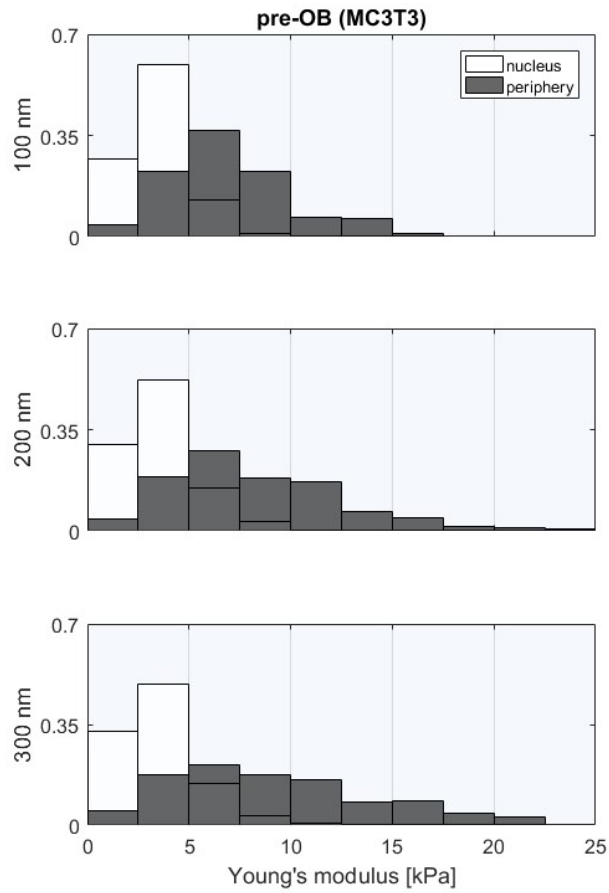


Figure 5.3.11: Histograms of single cell average Young's moduli for each indentation depth normalised for the total number of cells for the nucleus and the periphery of pre-OB (MC3T3) cells where both available.

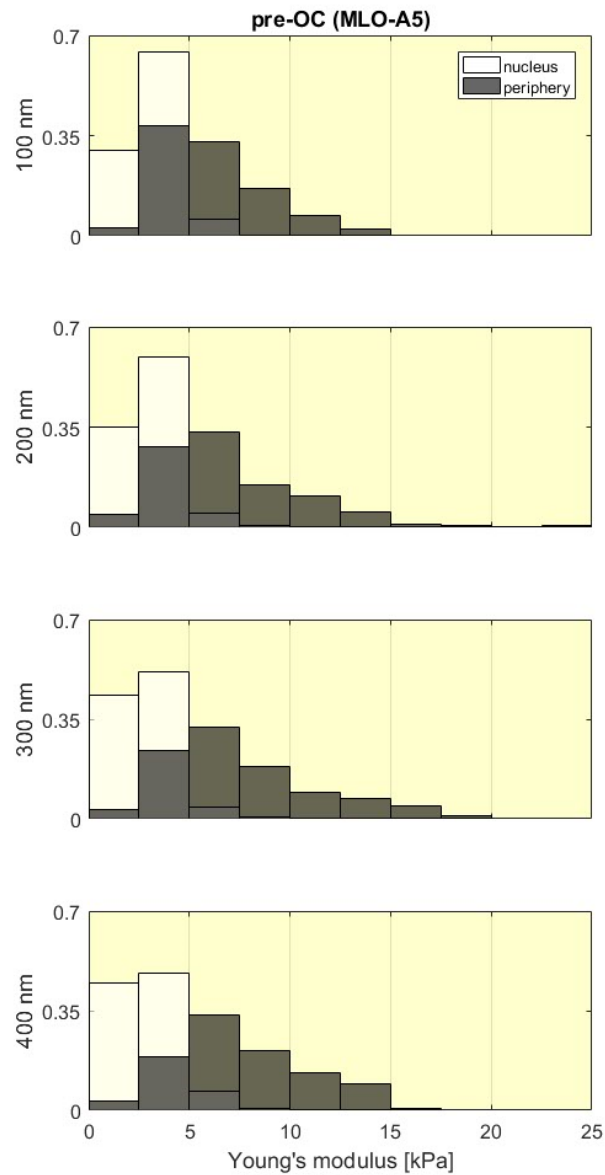


Figure 5.3.12: Histograms of single cell average Young's moduli for each indentation depth normalised for the total number of cells for the nucleus and the periphery of pre-OC (MLO-A5) cells where both available.

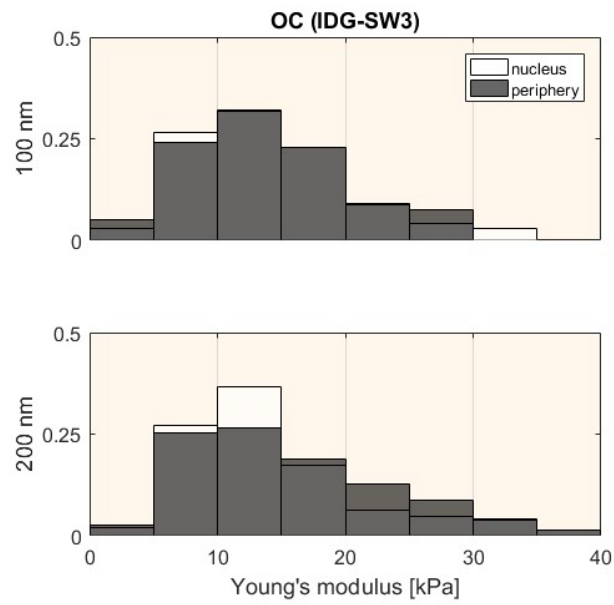


Figure 5.3.13: Histograms of single cell average Young's moduli for each indentation depth normalised for the total number of cells for the nucleus and the periphery of OC (IDG-SW3) cells where both available.

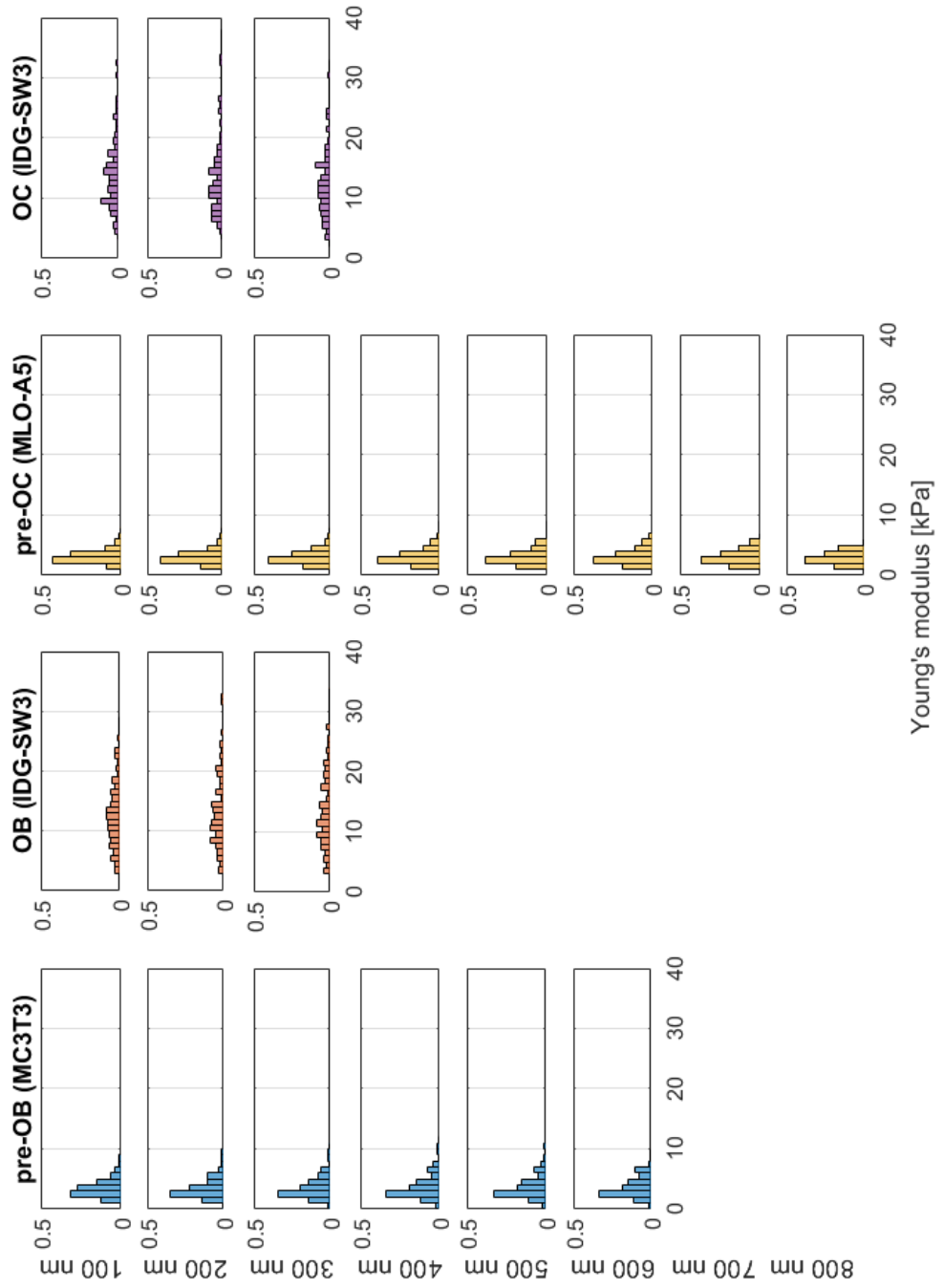


Figure 5.3.14: Histograms of single cell average Young's moduli for each indentation depth normalised for the total number of cells for the nucleus.

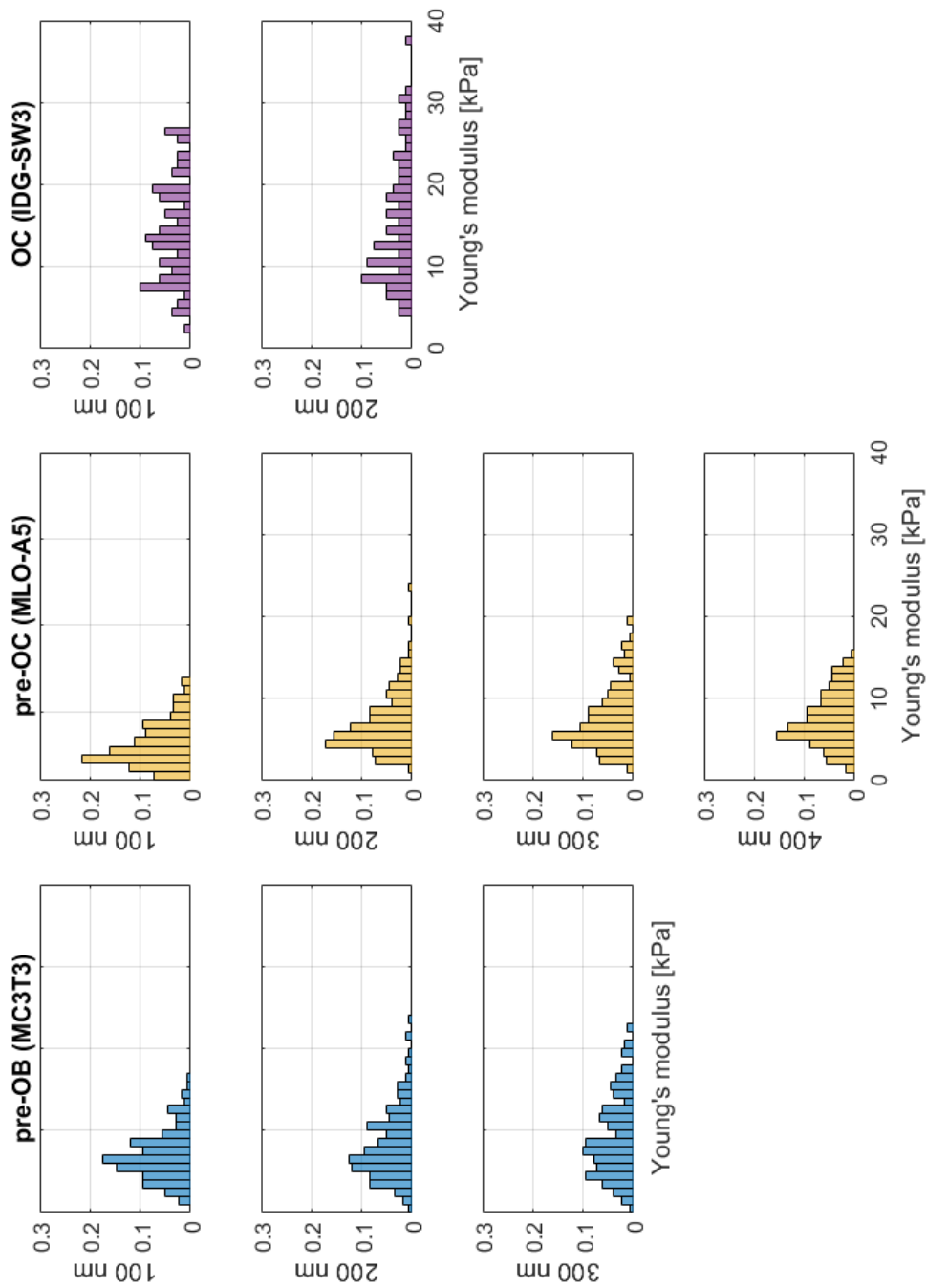


Figure 5.3.15: Histograms of single cell average Young's moduli for each indentation depth normalised for the total number of cells for the periphery.

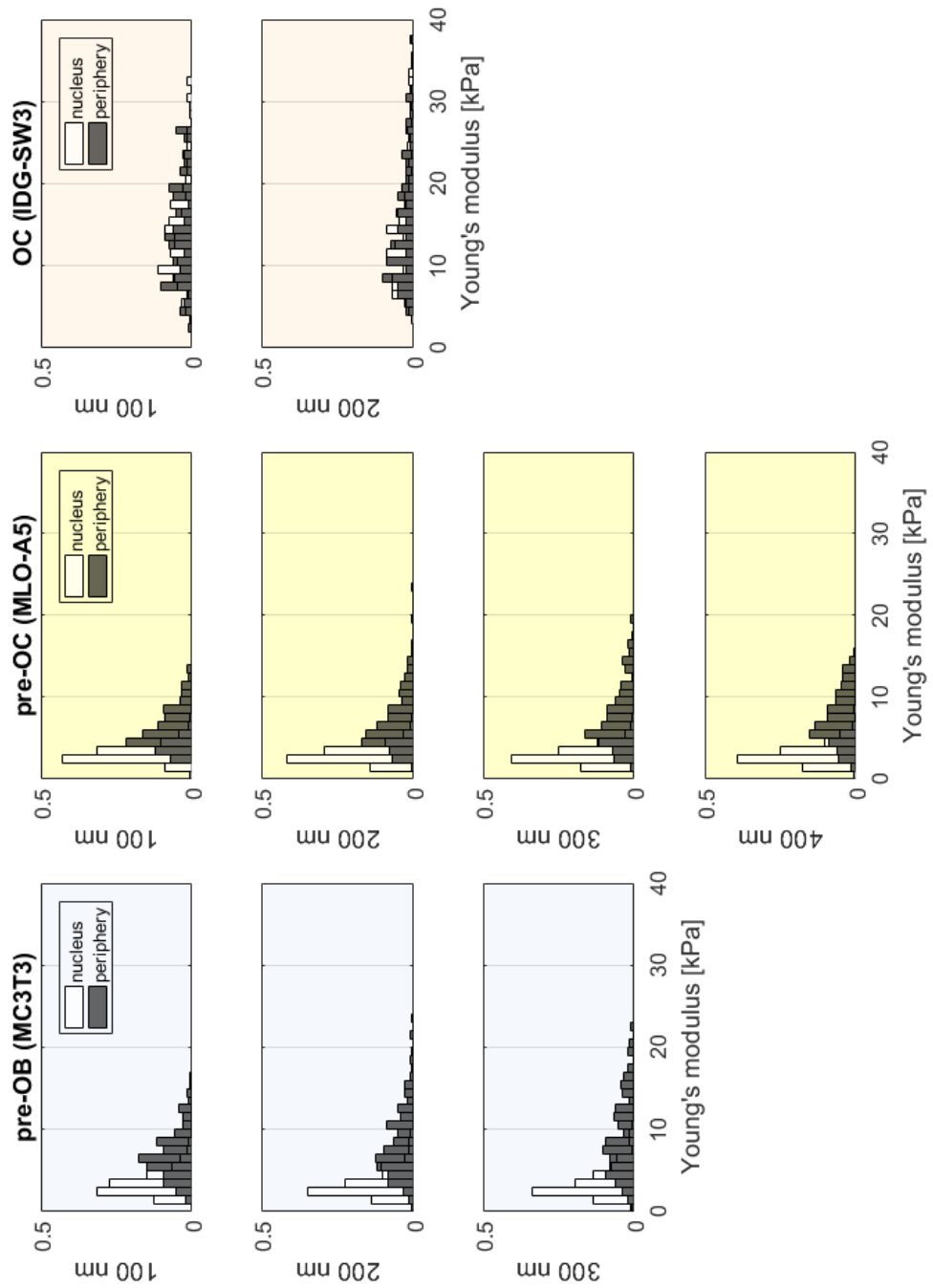


Figure 5.3.16: Histograms of single cell average Young's moduli for each indentation depth normalised for the total number of cells for the nucleus and the periphery where both available.

Table 5.3.1: Young's modulus values [kPa] for the nucleus. The values for MC3T3 (pre-OB), undifferentiated IDG-SW3 (OB), MLO-A5 (pre-OC) and differentiated IDG-SW3 (OC) cells are reported. The first column represents the indentation depth at which the value was fitted; the second and third the average (median) and dispersion (IQR) values; the fourth and fifth the mean and standard error of the mean (SEM) values. SEM values were calculated with $N = 175$ cells for the MC3T3 (pre-OB) cells, $N = 190$ cells for the undifferentiated IDG-SW3 (OB) cells, $N = 168$ cells for the MLO-A5 (pre-OC), $N = 144$ cells for the differentiated IDG-SW3 (OC) cells.

Nucleus	Indentation [nm]	Young's modulus [kPa]			
		median	IQR	mean	SEM
pre-OB (MC ₃ T ₃)	100	3.27	1.91	3.47	0.11
	200	3.03	1.88	3.49	0.12
	300	3.03	2.05	3.57	0.14
	400	3.10	2.14	3.67	0.15
	500	3.15	2.16	3.72	0.15
	600	3.19	2.16	3.66	0.13
OB (IDG-SW ₃)	100	12.25	7.76	12.64	0.40
	200	12.36	8.21	13.39	0.46
	300	12.33	8.91	13.55	0.45
pre-OC (MLO-A ₅)	100	2.93	1.31	3.12	0.08
	200	2.76	1.24	3.01	0.08
	300	2.71	1.37	2.96	0.09
	400	2.72	1.45	2.97	0.09
	500	2.74	1.49	3.00	0.09
	600	2.76	1.55	3.02	0.09
	700	2.78	1.62	2.99	0.09
	800	2.81	1.50	2.89	0.07
OC (IDG-SW ₃)	100	13.50	7.66	14.29	0.52
	200	12.26	7.63	14.18	0.60
	300	11.87	7.24	12.77	0.50

Table 5.3.2: Young's modulus values [kPa] for the cell periphery. The values for MC3T3 (pre-OB), MLO-A5 (pre-OC) and differentiated IDG-SW3 (OC) cells are reported. The first column represents the indentation depth at which the value was fitted; the second and third the average (median) and dispersion (IQR) values; the fourth and fifth the mean and standard error of the mean (SEM) values. SEM values were calculated with $N = 177$ cells for the MC3T3 (pre-OB) cells, $N = 180$ cells for the MLO-A5 (pre-OC), $N = 79$ cells for the differentiated IDG-SW3 (OC) cells.

Periphery	Indentation [nm]	Young's modulus [kPa]			
		median	IQR	mean	SEM
pre-OB (MC ₃ T ₃)	100	6.40	3.65	6.90	0.23
	200	7.49	5.35	8.26	0.32
	300	8.21	6.88	9.16	0.37
pre-OC (MLO-A ₅)	100	5.56	3.36	6.15	0.19
	200	6.12	4.00	7.01	0.26
	300	6.53	4.74	7.54	0.28
	400	6.93	4.66	7.48	0.24
OC (IDG-SW ₃)	100	13.34	9.70	14.12	0.69
	200	14.33	11.90	15.56	0.86

5.3.3 MORPHOLOGICAL ANALYSIS

Some illustrative cellular morphologies are depicted in Fig. 5.3.17 for all cell lines. The onset of dendritic processes formation is visible for the MLO-A5 (pre-OC) and differentiated IDG-SW₃ (OC) cells, but fully developed osteocyte-like processes [52, 162] were not observed. Average (dispersion) values for nuclear and cellular areas, major and minor axes are reported in Table 5.3.3. Similar dimensions for MC₃T₃ (pre-OB) cells were reported in [44, 45, 166]; for MLO-A5 (pre-OC) cells in [103]; for undifferentiated IDG-SW₃ (OB) cells in [167]. None of the morphological parameters changed monotonically with the differentiation stages.

A weak correlation was found between all the morphological parameters and the nucleus Young's modulus ($\rho < |0.2|$). The only exception was for the undifferentiated IDG-SW₃ cells (OB) where a moderate correlation was found ($|0.3| < \rho < |0.5|$). Moderate correlations were also calculated for the MC₃T₃ (pre-OB) cells between periphery Young's modulus and cell area and between periphery Young's modulus and cell minor axis; for the differentiated IDG-SW₃ cells (OC) between periphery Young's modulus and cell area and between periphery Young's modulus and cell major axis.

5.3.4 SAMPLE SIZE

The effect of the sample size on the average stiffness of nucleus and periphery obtained for all the cell populations was evaluated. For each cell line and location the minimum sample size to obtain a percent deviation of 10% on the population average Young's modulus was computed (Table 5.3.4). More cells were needed to obtain a reliable stiffness measure for the periphery than the nucleus, reflecting the higher heterogeneity of the former. In the case of the differentiated IDG-SW₃ (OC) cells the tested sample size was not sufficient to obtain a percent deviation of 10% for the periphery measures.

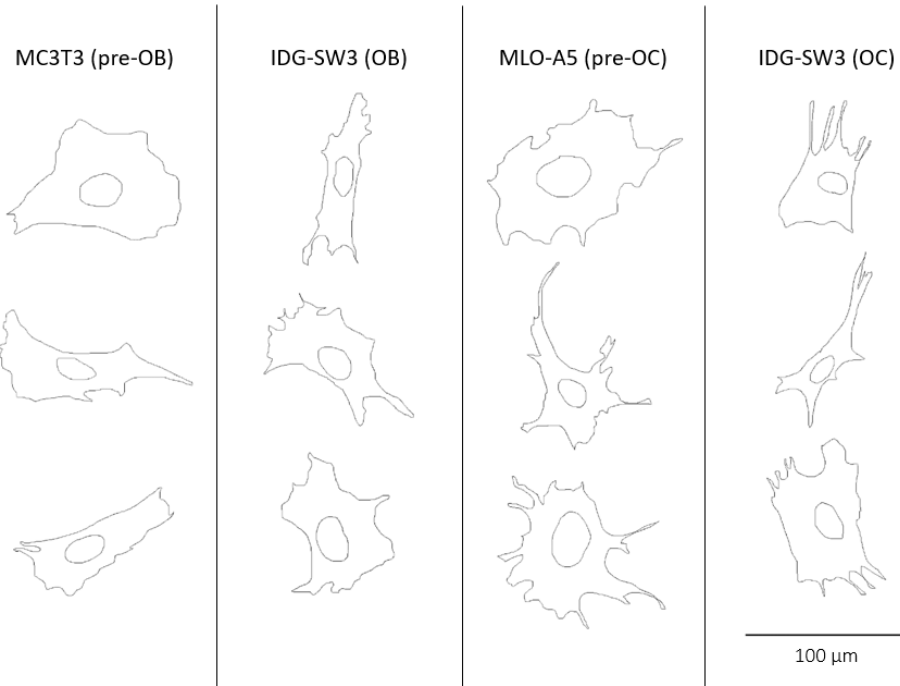


Figure 5.3.17: Representative images of the 30 morphological profiles analysed for each cell line: MC3T3 (pre-OB), undifferentiated IDG-SW3 (OB), MLO-A5 (pre-OC) and differentiated IDG-SW3 (OC) cells. The scale bar represents 100 μm . A gradual change in shape can be observed but full osteocyte differentiation was not observed. Different degrees of elongation and various sizes are noticeable.

Table 5.3.3: Areas, major and minor axes average (dispersion) values for the nucleus and the cell are reported for the MC3T3 (pre-OB), undifferentiated IDG-SW3 (OB), MLO-A5 (pre-OC) and differentiated IDG-SW3 (OC) cells. Area distributions were not normal and therefore median (IQR) are shown; all the other parameters were normally distributed and therefore mean (standard deviation) are shown.

		Area [μm^2]	Major [μm]	Minor [μm]
Nucleus	pre-OB	211 (124)	22 (4)	14 (3)
	OB	215 (120)	22 (5)	12 (3)
	pre-OC	289 (147)	24 (5)	17 (4)
	OC	182 (121)	21 (4)	12 (4)
Cell	pre-OB	2088 (1443)	84 (22)	38 (14)
	OB	1620 (1202)	70 (21)	31 (10)
	pre-OC	2240 (969)	70 (14)	44 (11)
	OC	1301 (996)	69 (20)	30 (14)

Table 5.3.4: Minimum sample size to obtain a maximum percent deviation of 10% on the average Young's modulus for the nucleus and the periphery are reported for the MC3T3 (pre-OB), undifferentiated IDG-SW3 (OB), MLO-A5 (pre-OC) and differentiated IDG-SW3 (OC) cells. Values marked by asterisks represent analysis terminated due to the tested sample size being reached: more cells than the ones tested were needed to obtain the set value for the percent deviation.

		Sample size [cells]
Nucleus	pre-OB	58
	OB	49
	pre-OC	35
	OC	52
Periphery	pre-OB	67
	pre-OC	56
	OC	79*

5.4 DISCUSSION

Large samples of bone cells belonging to different cell lines were tested by AFM nano-indentation to investigate the change in mechanical properties during osteocytogenesis. The cell population average Young's modulus for increasing indentation depths was calculated using the Hertz model for the cell nucleus and periphery.

The average population values of the Young's modulus were constant with the indentation depth on the nucleus, similarly to what was reported in Section 3.3.2 (Chapter 3) for the MLO-A5 data. Conversely, the same result was not observed on the periphery, where Young's modulus values tended to increase with the increasing indentation depth. This could be related to the substrate contribution, as the cells showed lower thickness towards the edges (Fig. 3.4.1, Chapter 3), or to a less homogeneous structure of the cell outside the nucleus. While centring the measure over the nucleus provided consistency between cells, the peripheral measurements might have tested areas richer or poorer in cytoskeletal fibres (e.g. moving or stationary cell fronts).

The cytoskeletal fibres have been proposed to be the major contributors to cell stiffness (reviewed in [43]). The close correlation between the actin filaments and the cell stiffness has been suggested following numerous studies in which the actin fibres were disrupted by use of pharmacological agents resulting in lower cell Young's modulus compared to non treated controls. Recently, robust quantitative correlation between the amount of stress fibres and cell stiffness was shown [128]. In particular, the amount of actin and myosin fibres caused a linear increase in the cell stiffness, while the actin fibre thickness caused no mechanical differences. Moreover, reinforcement of the cell cytoskeleton was observed in the presence of aligned and/or peripheral actin fibres.

A weak correlation was found between most of the morphological parameters and the nucleus Young's modulus, suggesting no association between cell shape and nuclear mechanical properties, similarly to what was discussed for the MLO-A5 cells in Section 3.3.3 (Chapter 3). Some moderate correlations were found for morphological parameters related to the cell periphery. These moderate correlations might be indirectly related to the actin organisation [128]. However, this

hypothesis could not be verified as no information on the actin cytoskeleton topology was available for the cells used for the morphological analysis.

The periphery Young's modulus showed higher values than the nuclear ones for all cell lines (Fig. 5.3.16, Table 5.3.1, Table 5.3.2). Similar trends were observed for bone cells [52] and for other cell lines (e.g. epithelial cells [96, 168], fibroblasts [128], endothelial cells [169, 170]). It has been proposed that peripheral regions stiffer than nuclear ones would be detected for cell with high levels of actomyosin [128], as qualitatively confirmed by the acquired confocal images.

MC3T3 (pre-OB) and MLO-A5 (pre-OC) cells showed lower and less disperse Young's moduli for both the nucleus and peripheral regions (Fig. 5.3.14 and Fig. 5.3.15). In contrast, the undifferentiated (OB) and differentiated IDG-SW3 (OC) cells showed wide dispersion ranges and higher values. This could be related to the intrinsic characteristics of the cell lines, given that they were acquired from different sources and were not differentiated from a single origin as in [52]. They could, therefore, represent partially overlapped differentiation stages and this would explain the lack of monotonic relationship between the Young's modulus or the morphological parameters and the stage of osteocytogenesis.

In the case of the differentiated IDG-SW3 (OC) cells, the co-presence of different phenotypes might also have occurred, similarly to what has been observed for other cell types in [171]. Conversely to their results, however, a bi-modal distribution could not be clearly fitted on the present data possibly suggesting a more complex phenotype interaction. The fluorescent GFP signal was not quantified: a cell was tested if displaying any intensity of fluorescence. This might have caused the grouping of different sub-populations such as early (less intense signal) and late (more intense signal) osteocytes into a single population and therefore recording higher population variability. The hypothesised presence of mixed phenotypes in the differentiated IDG-SW3 (OC) cells was also corroborated by the sample size analysis, for which it was found that the tested sample size was not sufficient to obtain a maximum percent deviation of 10% on the population average stiffness for the periphery.

Moreover, the morphological analysis performed on light microscopy images showed lack of fully developed osteocyte-like processes [52, 162]. The differentiated IDG-SW3 cells might, therefore, represent an earlier stage of differentiation

prior to fully differentiated terminal osteocyte.

It should be also noted that, during culture in osteogenic media prior to re-seeding and testing, differentiated IDG-SW₃ cells reached confluence and heavily mineralised. Cell detachment from culturing substrates was made difficult by the formed matrix and some mineral debris might have been moved with the cell onto the new substrate. If this was the case, an unknown degree of the Young's modulus distribution might have been caused by the mineral deposited over the cells [46]. Moreover, the re-seeding at low density might have inhibited some osteocyte-like features and possibly changed the mechanical characteristics.

The sample size analysis allowed for an estimate of the needed sample to obtain reliable population average stiffness values. It should be noted that the computed sample sizes are specific to the cell lines and protocol used and might therefore not represent absolute values. If a population showed lower heterogeneity, fewer cells would be needed to obtain reliable mechanical property measurements. An estimate of the sample heterogeneity should be made during the protocol preparation as absolute sample sizes proposed for other cell types might not be appropriate [60].

5.5 CONCLUSIONS

In this study, large samples of bone cells at different stages of osteocytogenesis were tested by AFM nano-indentation. These were MC₃T₃ (pre-OB), undifferentiated IDG-SW₃ (OB), MLO-A₅ (pre-OC) and differentiated IDG-SW₃ (OC) cells.

A lower Young's modulus in cells representing later stages of osteocytogenesis was expected during differentiation, with the cell periphery stiffer than the nucleus [52]. While the difference between cell regions was shown, a monotonic relationship between osteocytogenesis stages and mechanical properties was not found. The choice of testing separate cell lines instead of a single differentiating population might have caused this discrepancy, as some cell lines might represent overlapping differentiation stages.

The differentiated IDG-SW₃ cells proved difficult to test. They had to be cultured in osteogenic media at high confluence to achieve differentiation (i.e. detection of GFP signal). During this culture stage, they produced an abundant mineralised matrix which made them difficult to passage and might have affected

subsequent measurements. Moreover, the GFP signal was not quantified prior to single cell testing but only visually verified. For this reason, cells at different stages of osteocytogenesis might have been grouped in the same population and collectively regarded as OCs. The morphological analysis revealed no differentiated IDG-SW₃ cells with fully developed dendritic processes. This evidence suggests that the tested cells might be in a pre-OC stage and therefore partially overlap with the MLO-A₅ population. Finally, the number of differentiated IDG-SW₃ cells was not sufficient to compute the Young's modulus with a maximum percent deviation of 10% in the peripheral region.

6

Single molecule force spectroscopy of Hyaluronic Acid

This chapter includes the results on single glyocalyx molecule testing. The experiments presented in this chapter were performed under the additional supervision of Prof. Taiji Adachi at the Institute for Frontier Life and Medical Sciences (Department of Biosystems Science, Kyoto University, Japan)¹. The pre-processed data relative to this chapter are available at the following DOI: [10.15131/shef.data.5632783](https://doi.org/10.15131/shef.data.5632783).

6.1 INTRODUCTION

Hyaluronic Acid (HA) is a glycosaminoglycan composed of a repeated disaccharide units in the form of a linear polymer [172]. It is synthesised by three related trans-membrane proteins (HAS₁, HAS₂, HAS₃) and extruded towards the outer

¹Part of the work presented in this Chapter is planned to be submitted as a scientific paper.

surface of cells [173]. It is cleaved by specific enzymes (hyaluronidases) and can form chains of different lengths, in normal physiological conditions in the range of $2 - 25 \mu\text{m}$ with a molecular mass of $10^6 - 10^7$ [174]. HA is involved in various physiological cell functions, such as cell proliferation, locomotion and recognition. Moreover, its abnormal production and function in pathological conditions such as inflammation, sepsis and oedema have been observed [172]. HA is often over-expressed in tumours and can be prognostic for malignant progression [174].

HA is considered as a contributor to mechanotransduction and signals mediation due to tension, shear or tissue compression (reviewed in [173]) and it has been suggested that its mechanical and swelling properties could change cellular functions such as adhesion and spreading. Moreover, HA can form structures, such as cables [175] and microvilli [67], which could play a role in signal transmission. It has been shown that cells over-expressing HA synthases spontaneously formed HA-rich microvilli containing filamentous actin. This phenomenon was observed in various cell types *in vitro* and *in vivo*, suggesting a conserved function common to different lineages [176, 177]. Furthermore, HA has the ability to change local membrane properties. This was demonstrated by observing that membrane tethers pulling changed when the HA-glycocalyx was disrupted. This observation led to the hypothesis that HA could act as an external cytoskeleton by being able to modify and control cell shape [65].

In conjunction with other proteoglycans, HA forms the cell glycocalyx, or brush, which has been observed on cells belonging to different tissues (e.g. endothelium [25], cartilage [178], bone [27], muscle [179], brain [180]). This proteoglycan collection on the outer surface of cells has been investigated as a cell mechanotransducer [4, 28, 181]. Different hypotheses have been formulated to explain the underlying mechanisms of glycocalyx-mediated mechanotransduction [4, 182]. Firstly, a *decentralised* mechanism could take place, where the mechanosensing happens at the glycocalyx level while the mechanotransduction happens at sites distinct from the surface (i.e. cytoskeleton, focal adhesions, nucleus). The idea is that the glycocalyx fibre deflection due to fluid shear stress causes molecular displacement of signalling proteins on the cell cytoskeleton [26]. A simple model has been proposed to explain this signal mediation mechanism in endothelial cells called the “wind in the trees” model [4]. In addition to this *decentralised* mech-

anism, a *centralised* mechanism could also take place for which the glycocalyx acts as a mechanosensor *and* a mechanotransducer. This would be mediated by glycocalyx fibres directly connected to membrane *caveolae* where an abundance of signalling molecules reside [4]. Moreover, HA and the glycocalyx can regulate the membrane permeability by selectively controlling the local concentration gradients and transport of ions, amino acids and growth factors [4, 183]. Finally, the glycocalyx could shield or expose membrane domains [29] or change local membrane properties [65].

The connection between the glycocalyx/HA and the cell cytoskeleton appears to be crucial for signal mediation and for exploring the occurrence of the different hypothesised mechanotransduction mechanisms. HA is anchored to the cell through its synthases or through surface receptors, such as CD44 [173]. It has been hypothesised that both synthases [67] and CD44 [66] could selectively bind to the actin cytoskeleton. The actin-binding link molecules have been identified for the CD44 receptor, but not for the HAS family. CD44 has no actin-binding sites on its cytoplasmic domain, suggesting an indirect interaction mediated by cytoskeleton-associated proteins, which have been identified in the ERM (ezrin-radixin-moesin) protein family and in the related protein merlin. Both these link molecules have active and inactive forms allowing for switch-like binding between HA and the actin cytoskeleton [66]. One protein of the ERM family, ezrin, has been mechanically characterised by single molecule AFM [184]. It was shown that a phosphorylation-induced extension could modulate the molecule activation for cytoskeleton attachment and therefore switch on the mechanism for which the binding occurs. This mechanism would involve the complete unfolding of the protein which could then function as a spring linker and mechanotransducer. Similarly, a mechanotransductive role was hypothesised for merlin in the context of coherent cell migration [185]. This evidence would suggest that these proteins are good candidates for mechanical signal transmission from the outer to the inner cell compartments through the glycocalyx.

AFM single molecule force spectroscopy has been widely used to study single molecules mechanical properties [10]. This technique allows for high resolution force or distance controlled pulling of molecules, which can be attached to a substrate or directly to live or fixed cells. The AFM probe is activated by attaching

chemical groups of interest and then lowered on the target molecule. When the chemical bond is activated, the probe is retracted and the force-distance curve is recorded. By analysing these force-distance data it is possible to obtain information on the properties of the target molecule.

Recently, a methodology was developed to evaluate the attachment of the target molecule to the cytoskeleton in case of switch-like anchoring mechanisms [186–189] (Fig. 6.1.1). If the target molecule was anchored to the cytoskeleton, the force-distance curve would exhibit a clear rise in force before the rupture event (i.e. before the unbinding between the probe and the target molecule), due to the cytoskeleton acting as a spring and pulling the target molecule away from the probe. If the target molecule was not anchored to the cytoskeleton, the force-distance curve would show long plateaux with constant force representing tethers being pulled out of the cell membrane, due to the plasma membrane offering constant tension against the probe before the rupture event [189]. Therefore, it would be possible to distinguish between cytoskeleton anchored and non-anchored target molecules by analysing the force-distance curve in the proximity of the rupture events.

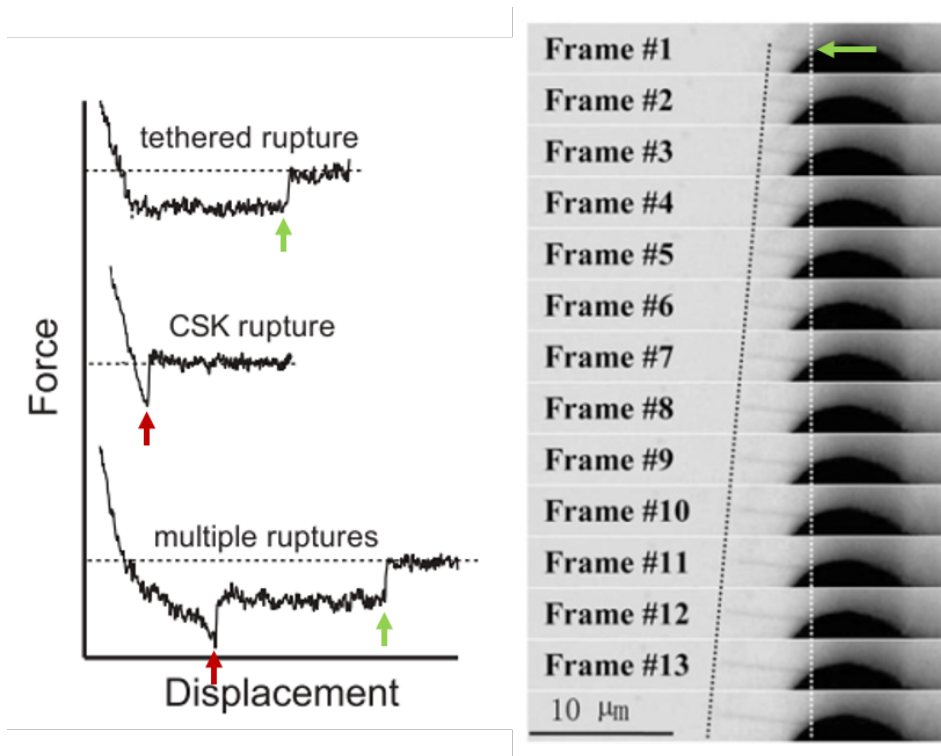


Figure 6.1.1: Left panel: the rupture events observed on the retract curve of AFM SMFS experiments are classified as cytoskeleton (CSK) anchored (red) or membrane tethers (green) depending on the local force-distance curve characteristics. If the target molecule was anchored to the cytoskeleton, the force-distance curve would exhibit a clear rise in force before the rupture event; if the target molecule was not anchored to the cytoskeleton, the force-distance curve would show long plateaux with constant force representing tethers being pulled out of the cell membrane. Figure adapted from [188]. Right panel: an example of a tether (green arrow) being pulled from the cell membrane imaged from a lateral view. Figure adapted from [190].

6.2 MATERIALS & METHODS

6.2.1 CELLS

Murine pre-osteoblast cells MC₃T₃-E₁ (Riken cell bank, passage 22 – 23) were cultured in Minimum Essential Alpha Eagle medium (MEM, Lonza) supplemented with nucleosides and 2 mM UltraGlutamine I, 10% Foetal Bovine Serum and a solution of 100 units/ml penicillin and 100 µg/ml streptomycin (penicillin streptomycin, PS). Cells were kept at 37°C and passaged when 70% confluent. Prior to AFM analysis, cells were seeded onto tissue culture treated Petri dishes ($D = 10\text{ mm}$).

6.2.2 SAMPLES

Hyaluronic Acid Binding Protein (HABP) was used to specifically bind HA on the cell surface. This molecule is commonly employed for the detection of HA on cell culture [134] and it is composed of the HA binding domain from aggrecan and its native stabiliser link molecule [154–156].

Four different samples were employed for experiments, designed as follows:

1. **HABP/HA**: cantilever functionalised with HABP, untreated cell sample;
2. **BSA/HA**: cantilever functionalised with bovine serum albumin (BSA), untreated cell sample;
3. **untreated/HA**: non functionalised cantilever, untreated cell sample;
4. **HABP/HAase**: cantilever functionalised with HABP, cell sample treated with hyaluronidase (HAase).

Sample 1 (**HABP/HA**) represented the study experiment, with the cantilever functionalised to target the HA molecules on cells. Samples 2 – 4 were considered as controls, to verify the specificity of the protocol. In these cases, no pulling events should be observed.

The BSA used for cantilever functionalisation in Sample 2 (**BSA/HA**) should block all the non-specific bonds, as a non-reactive protein coating non-specific protein binding sites. As a further verification, Sample 3 (**untreated/HA**) was designed with no cantilever functionalisation.

In the last case (**HABP/HAase**), the HA was removed from the cell by enzymatic treatment with HAase (from *Streptomyces hyalurolyticus*, Sigma-Aldrich). To this aim, the protocol described in [29] was used and cells were treated with 160 U/ml HAase/MEM for 1 hour prior to AFM experiments.

6.2.3 CANTILEVER FUNCTIONALISATION

Low spring constant cantilevers with pyramidal tip (Olympus) were used for all the experiments (nominal spring constant 0.02 N/m, tip radius 15 nm). The cantilever functionalisation method was similar to the one described in [191]. The steps of activation are listed below and were the same for Sample 1 (**HABP/HA**, functionalisation molecule: HABP), Sample 2 (**BSA/HA**, functionalisation molecule: BSA) and Sample 4 (**HABP/HAase**, functionalisation molecule: HABP). The cantilevers used to test cells in Sample 3 (**untreated/HA**) were not treated, but washed in ultra-pure water prior to experiments.

The following activation steps were performed just before the experiments:

- *deposition of (-SH) groups*: cantilevers were oxidised using an ozone cleaner and submerged in 2% (3 – Aminopropyl)triethoxysilane (APTES)/ultra-pure water for 15 minutes to deposit (-SH) groups on the probe surface;
- *attachment of intermediate linker molecules*: after washing, the cantilevers were submerged in 6 mM Maleimide-PEG-NHS ester/Tris for 30 minutes. This compound bound to the (-SH) groups and exposed NHS esters for subsequent binding to the carboxyl groups of the functionalisation molecules;
- *functionalisation*: after washing, the functionalisation molecule was bound to the exposed NHS ester groups by submerging the cantilever in 100 nM HABP/Tris solution (Sample 1 **HABP/HA** and Sample 4 **HABP/HAase**) or 1% BSA/ultra-pure water (Sample 2 **BSA/HA**) for 1 hour;
- *blocking*: the excess maleimide was quenched with 50 mM 2-mercaptoethanol/ ultra-pure water by submerging the cantilevers for 1 minute;

- *washing*: after a final washing, the functionalised cantilevers were kept submerged in ultra-pure water until mounting on the AFM holder.

6.2.4 AFM SET-UP

A NanoWizard 3 Atomic Force Microscope (JPK Instruments AG) coupled to a IX series optical inverted microscope (Olympus) enclosed in a metal box to reduce environmental noise was used for all the experiments.

The cell sample was washed with PBS and fresh medium was added before testing for a maximum of 2 hours at room temperature. The cantilever sensitivity was calibrated and the system was allowed some time for temperature stabilisation before each experiment. The cantilever spring constant was manually imposed as equal to the nominal value given by the manufacturer due to difficulties in using the built-in calibration system after the cantilever chemical functionalisation.

Cells were located through the optical microscope and tested within an area of $10 \times 10 \mu\text{m}^2$. A 16-point grid was drawn and force spectroscopy measurements were obtained on the grid for 3 times to collect a total of 48 data on each cell. The relative set point and the approach velocity were set to 0.5 nN and $2 \mu\text{m}/\text{s}$ respectively. A total of 150 cells were tested over 4 separate experiments for Sample 1 (**HABP/HA**); 15 cells were tested for each of the control samples.

6.2.5 POST-PROCESSING

The obtained data files were exported as text files from the JPK Data Processing software. All the subsequent post-processing was performed in MATLAB (Mathworks) with custom-written semi-automated algorithms to allow for careful tailoring of the analysis steps.

The contact point determination was performed as described in Section 3.2.4. If an offset of the retract baseline was observed with respect to the extend baseline, this was considered to be due to the hydrodynamic effect of the cantilever movement in liquid and was corrected before further analysis by translating the retract curve so that the baselines would match [192].

Force-distance retract curves were analysed as the focus was on the pulling of the target molecules that occurred when the probe was moved away from the cell

surface. A clear decrease in force representing the unbinding between the probe and the target molecule was defined as a rupture event. Multiple rupture events could be observed in one retract curve if multiple target molecules were initially bound to the probe. The force-distance ratio (measured in $[pN/nm]$) preceding the rupture event was described as slope and used to classify the rupture events.

LOCALISATION OF RUPTURE EVENTS

Rupture events were searched for in the region of the force-distance curve where the probe was not in contact with the cell body, i.e. after the contact point. If a curve displayed any rupture events occurring in the indentation region (i.e. before the contact point), it was excluded from further analysis, as this would most likely be due to membrane piercing, an incomplete detachment of tethers in previous locations or noise.

An algorithm was designed to detect the rupture events by screening the first derivative of the signal after smoothing to remove high frequency noise [188]. In fact, the first derivative is null for a constant value of force as expected after the contact point; when a rupture event is encountered the first derivative shows a peak due to the close-to-vertical line that marks the unbinding between the probe and the target molecule. These peaks were detected and their force and distance from the contact point were recorded. The slope in an interval of 50 nm preceding the rupture events was also computed.

The algorithm steps are summarised below:

1. each force spectroscopy retract curve was analysed separately (Fig. 6.2.1);
2. the raw data were smoothed using a spline function (Fig. 6.2.2);
3. the first derivative of the force was calculated (Fig. 6.2.3);
4. a threshold was set to localise peaks corresponding to rupture events (Fig. 6.2.4);
5. the interval corresponding to the peak in the derivative was analysed back on the force spectroscopy data (Fig. 6.2.5);
6. the local minimum representing the rupture event was searched in the interval (Fig. 6.2.6);

7. the 50 nm preceding the rupture event were fitted with a line to determine the local slope (Fig. 6.2.7).

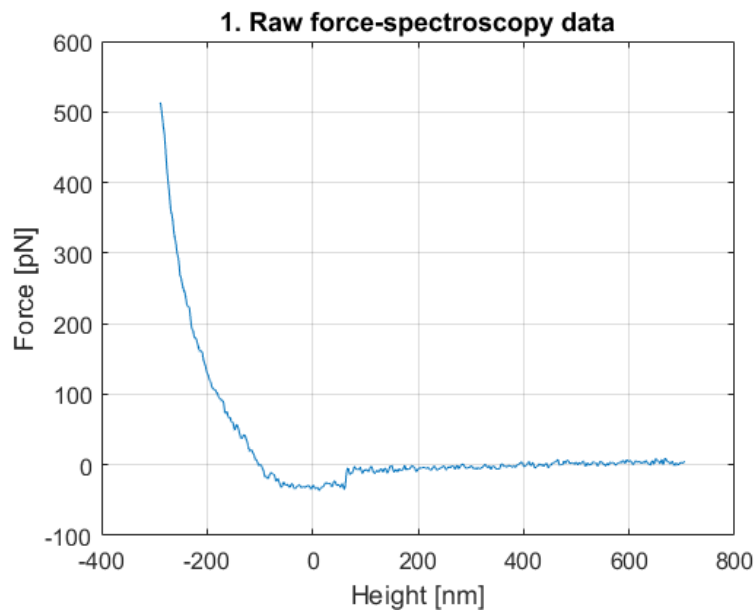


Figure 6.2.1: Localisation of rupture events - step 1. Example of force spectroscopy retract curve raw data (blue line) obtained by AFM SMFS targeting HA on live pre-osteoblast cells.

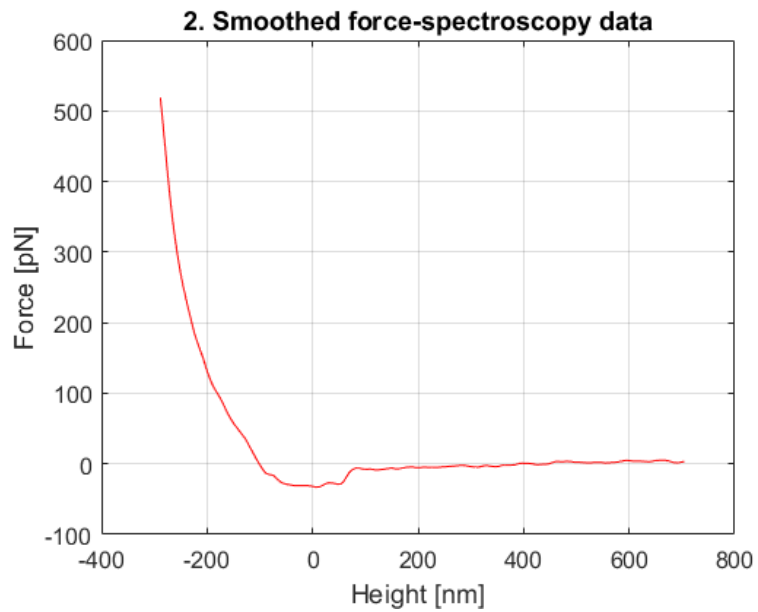


Figure 6.2.2: Localisation of rupture events - step 2. The force spectroscopy data showed in Fig. 6.2.1 was smoothed using a spline function (red line) to remove the high frequency noise.

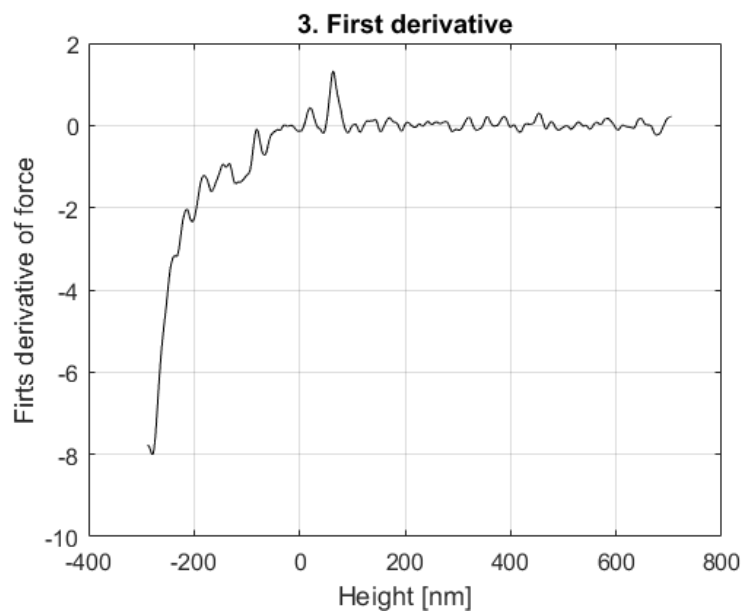


Figure 6.2.3: Localisation of rupture events - step 3. The first derivative (black line) of the smoothed force showed in Fig. 6.2.2 was calculated to localise the rupture events.

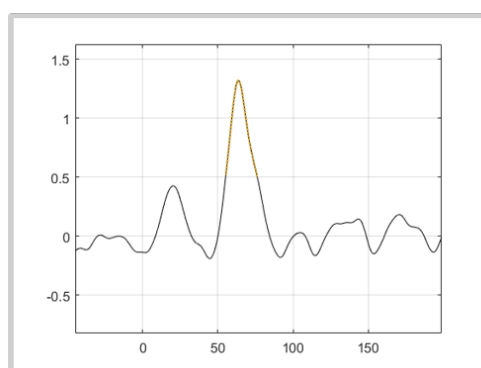
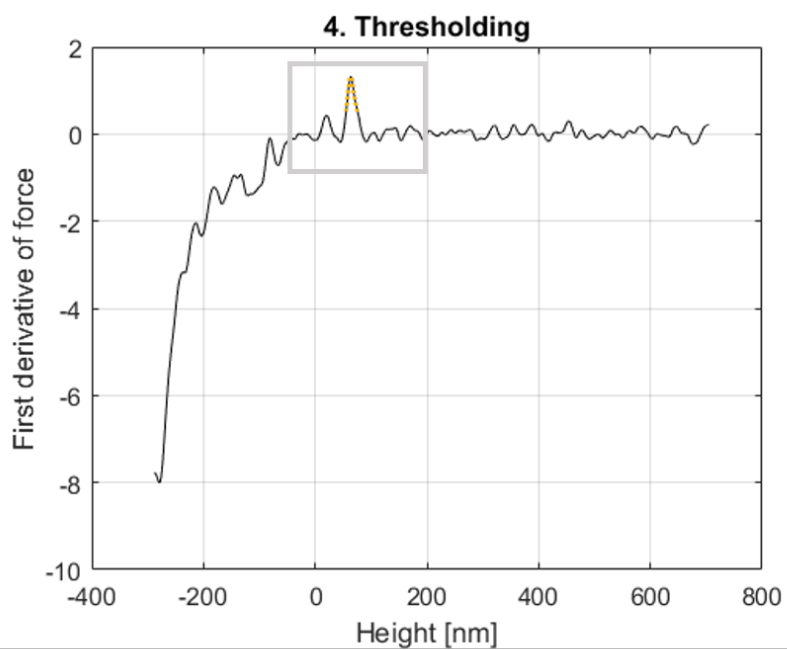


Figure 6.2.4: Localisation of rupture events - step 4. A threshold was set on the derivative showed in Fig. 6.2.3 to localise peaks corresponding to rupture events (yellow dashed line). The area marked in grey is zoomed in the bottom panel.

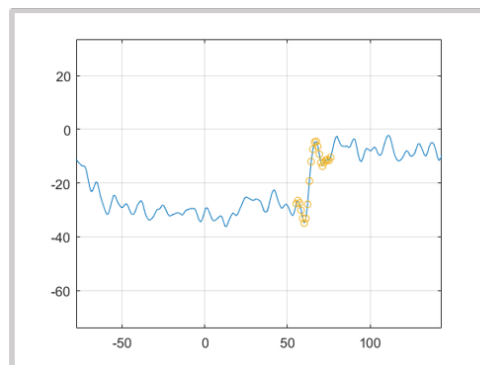
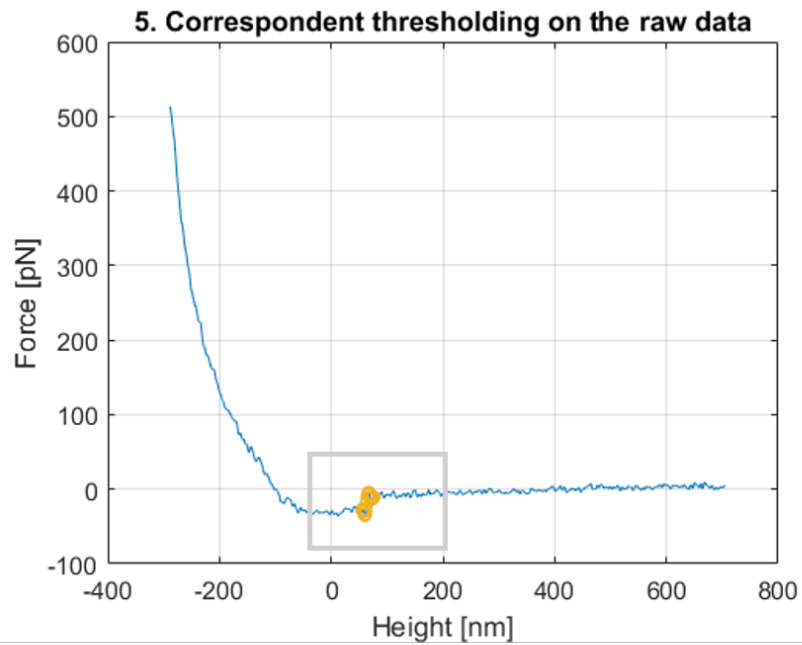


Figure 6.2.5: Localisation of rupture events - step 5. The interval corresponding to the peak in the derivative was analysed back on the force spectroscopy data (yellow circles). The area marked in grey is zoomed in the bottom panel.

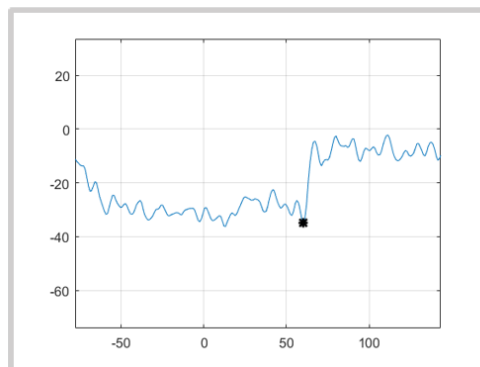
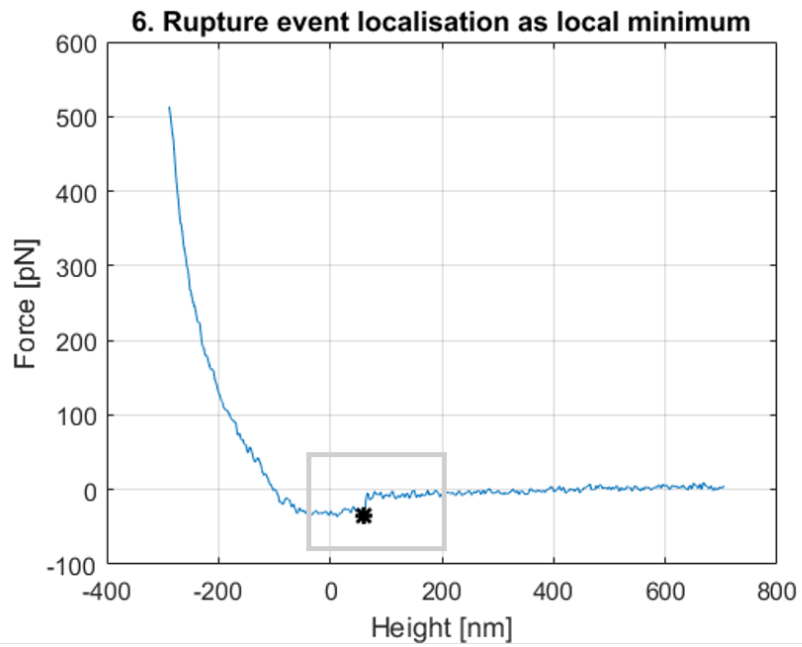


Figure 6.2.6: Localisation of rupture events - step 6. The local minimum (black star) representing the rupture event was searched in the interval. The area marked in grey is zoomed in the bottom panel.

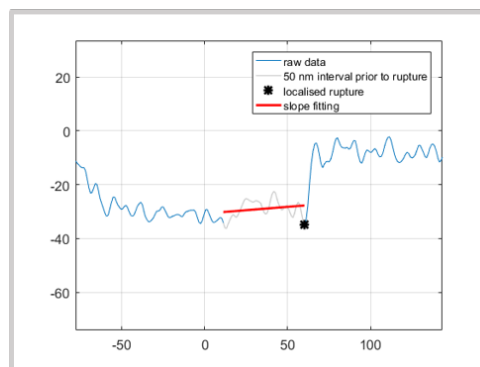
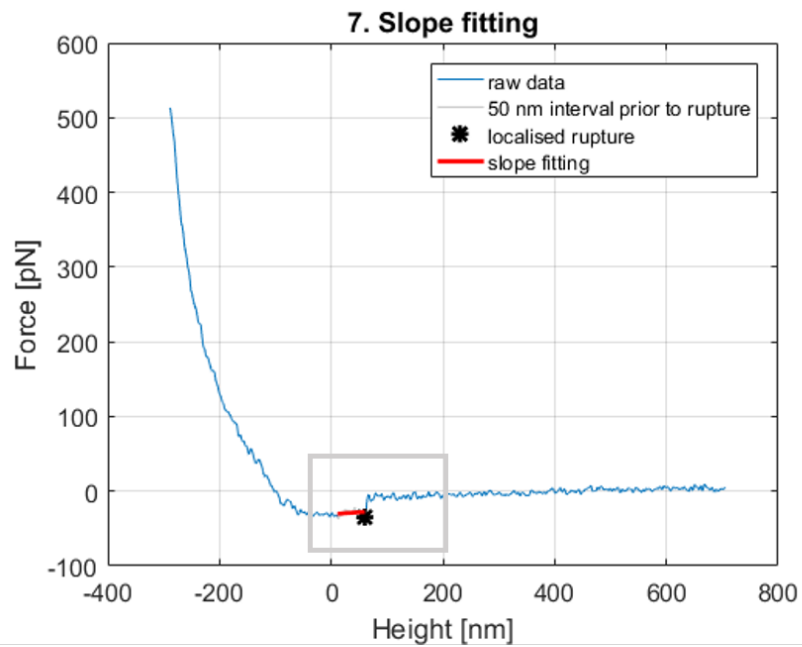


Figure 6.2.7: Localisation of rupture events - step 7. The 50 nm preceding the rupture event (grey line) were fitted with a line (red line) to determine the local slope. The area marked in grey is zoomed in the bottom panel.

SUCCESSFUL TARGET RATE

If a force-distance curve showed at least one rupture event it was considered as successfully targeting the molecule of interest (HA) on the cell surface. The number of successful target curves was counted over the total number of data curves for each sample as an estimate of the ease of binding between the probe and the target molecule for each pair. This quantity was expected to be higher for Sample 1 (**HABP/HA**) than in the control samples due to the intended specificity of the binding.

CLASSIFICATION OF RUPTURE EVENTS

It was possible to distinguish between those HA molecules that were anchored or non-anchored to the cytoskeleton by analysing each rupture event. If the target molecule was anchored to the cytoskeleton, the rupture event would be preceded by a clear rise in force; otherwise, the rupture event would be preceded by a long force plateau representing a membrane tether pulling.

The parameter defined as slope (Fig. 6.2.7) could, therefore, act as a marker for the two types of rupture events: if the slope preceding the rupture event was higher than a threshold, this would represent a cytoskeleton anchored rupture; otherwise a membrane tether rupture (i.e. non-anchored rupture) [187, 188] (Fig. 6.2.8). To define this threshold, it was necessary to evaluate the variability range of a force that could be described as constant. Hence, the variability of the baseline slope of the extend curves was considered. The baseline is, in fact, holding zero force as it is extracted before the contact between the probe and the sample.

The slope of the last 50 nm of all extend baseline data was calculated (Fig. 6.2.9). The resulting histogram was fitted with a normal distribution with the following descriptive parameters: $\mu = -0.002 \text{ pN/nm}$ and $\sigma = 0.103 \text{ pN/nm}$. About 99.7% of data lies in the space defined by $\mu \pm 3\sigma$ and therefore in the interval $(-0.311 \text{ pN/nm}, 0.308 \text{ pN/nm})$. This interval was used to define the membrane tether rupture slope variability range: if the slope of the rupture event fell in the interval it could be considered horizontal (constant force) and therefore the rupture was classified as membrane tether rupture; if the slope was higher then a linear increase in force was observed and the rupture event was classified as cytoskeleton

anchored.

The membrane tether ruptures were classified with their associated force, calculated as the sudden release of force due to tether rupture. If multiple tethers were formed, the tether force corresponded to the force step between one tether and the subsequent one [193]. The tether length was computed as the distance of the rupture events from the contact point.

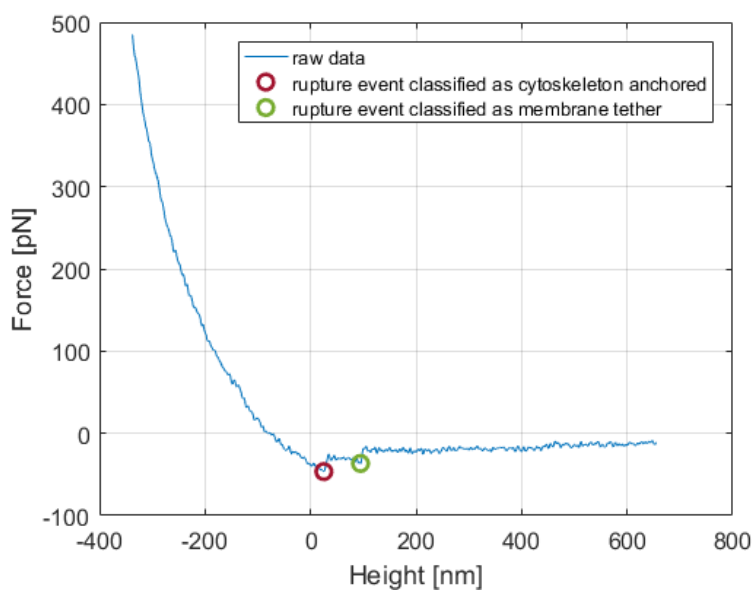


Figure 6.2.8: Example of rupture event classification. The localised rupture events are marked in green if classified as membrane tether ruptures, in red if classified as cytoskeleton anchored ruptures.

SINGLE AND MULTIPLE RUPTURE EVENTS

If only one rupture event was observed in a curve, it was classified as single; if more than one rupture event was observed in a curve, they were classified as multiple. The percentage of single and multiple rupture events and their associated force were calculated to verify the occurrence of specific rupture patterns.

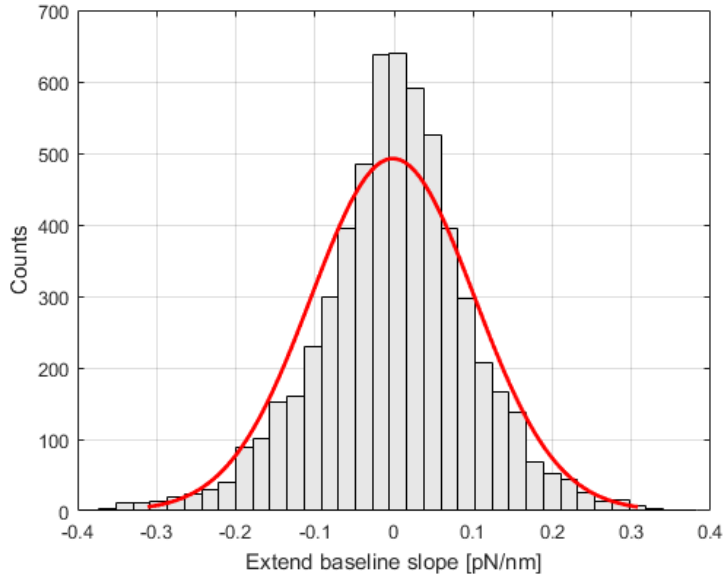


Figure 6.2.9: The histogram of the slope of all extend baseline data is shown. The red line represents a normal distribution fit ($\mu = -0.002 \text{ pN/nm}$ and $\sigma = 0.103 \text{ pN/nm}$).

INTRINSIC BOND CHARACTERISATION

The theory used to describe the rupture of chemical bonds has been initially studied by Bell, who proposed this phenomenological formula [194]:

$$\tau(F) = \tau_0 \exp\left(-\frac{F\gamma}{k_B T}\right), \quad (6.1)$$

with F rupture force, k_B Boltzmann constant, T temperature, τ_0 intrinsic lifetime of the bond, γ energy barrier width. Further theoretical studies followed to develop a framework to describe single bond ruptures, in terms of an activation energy barrier ΔG that has to be overcome before bond rupture and which is effectively lowered by the external force applied to the system [121, 195]. The following formula, often referred to as the Bell-Evans model, has been proposed [195]:

$$F = \frac{k_B T}{\gamma} \log \frac{\tau_0 \gamma r}{k_B T}, \quad (6.2)$$

with r loading rate. Eq. 6.2 has been widely used in single molecule force spectroscopy studies (e.g. [188, 196]) to compute the intrinsic bond lifetime τ_0 and the width of the energy barrier γ , having performed experiments at different loading rates.

In the present study, the experiments were carried out with constant pulling force and therefore the Bell-Evans model could not be employed. A methodology to retrieve force-dependent lifetime information of the system in similar cases has been proposed as outlined below [197, 198]. The force-dependent lifetime of the system $\tau(F)$ can be expressed as:

$$\tau(F) = \frac{\int_F^\infty p(f) df}{\dot{F}(F) p(F)}, \quad (6.3)$$

with $p(F)$ distribution of rupture forces and $\dot{F}(F)$ loading rate. If hypothesising a stiff molecular system pulled by a spring k_s at velocity V , the loading rate \dot{F} does not depend on the force and can be expressed as $\dot{F} = k_s V$. Considering a probability density function rupture force histogram $p(F)$ with N bins of width ΔF starting at F_0 and finishing at $F_N = F_0 + \Delta F$, Eq. 6.3 can be evaluated at the mid-point of each bin as:

$$\tau(F_0 + (k - 1/2)\Delta F) = \frac{\Delta F \left(\frac{1}{2}h_k + \sum_{i=k+1}^N h_i \right)}{h_k \dot{F}}, \quad (6.4)$$

for $k = 1, 2, \dots, N$ and h bin height. The rupture force vs. force-dependent lifetime data can be fitted with the Bell model (Eq. 6.1), as a particular case ($\nu = 1$) of the following equation derived from the Kramers theory [199]:

$$\tau(F) = \tau_0 \left(1 - \frac{\nu F \gamma}{\Delta G} \right)^{1-1/\nu} \exp \left\{ - \frac{\Delta G}{k_B T} \left[1 - \left(1 - \frac{\nu F \gamma}{\Delta G} \right)^{1/\nu} \right] \right\}. \quad (6.5)$$

This methodology was used on rupture event data, separately for the cytoskeleton anchored and the membrane tethers. A minimum force threshold of 20 pN and 10 pN for the cytoskeleton anchored and the membrane tethers, respectively, was set to ensure full significance of each bin in the force histograms [192].

6.3 RESULTS

6.3.1 STUDY SAMPLE VS. CONTROL SAMPLES

A total of 5905 force spectroscopy data were analysed for Sample 1 (**HABP/HA**), 687 for Sample 2 (**BSA/HA**), 696 for Sample 3 (**untreated/HA**) and 563 for Sample 4 (**HABP/HAase**).

The successful target rate was calculated for each sample as shown in Table 6.3.1. The successful target rate was comparable in the three series of testing for each cell and in Sample 3 (**untreated/HA**) it was remarkably lower than in the study sample (Sample 1, **HABP/HA**) and the other two control samples.

The distance from the contact point at which the rupture events occurred was calculated as an indicator of the interaction specificity. Low distance values would be a sign of a non-specific interaction: the interaction would happen close to the contact point and would not be maintained over increasing height of the cantilever in respect to the sample. The rupture distance from the contact point for each sample was compared (Fig. 6.3.1) and a statistical difference was found between the study sample and all the control samples (Kruskal–Wallis test by ranks, significance set to $p < .01$).

Table 6.3.1: *The calculated successful target rate is reported for each sample as an index of the number of successful binding events between probe and target molecule. This quantity was calculated as the percentage of curves displaying some rupture events over the total number of analysed curves.*

Sample 1 HABP/HA	Sample 2 BSA/HA	Sample 3 untreated/HA	Sample 4 HABP/HAase
65.19%	67.92%	16.67%	66.11%

6.3.2 CYTOSKELETON ANCHORED VS. MEMBRANE TETHER RUPTURES

In Fig 6.3.2 the distance from the contact point against the slope of each rupture event of the study sample (**HABP/HA**) is shown. It could be noted that few rupture events with low distance from the contact point were present, which may rep-

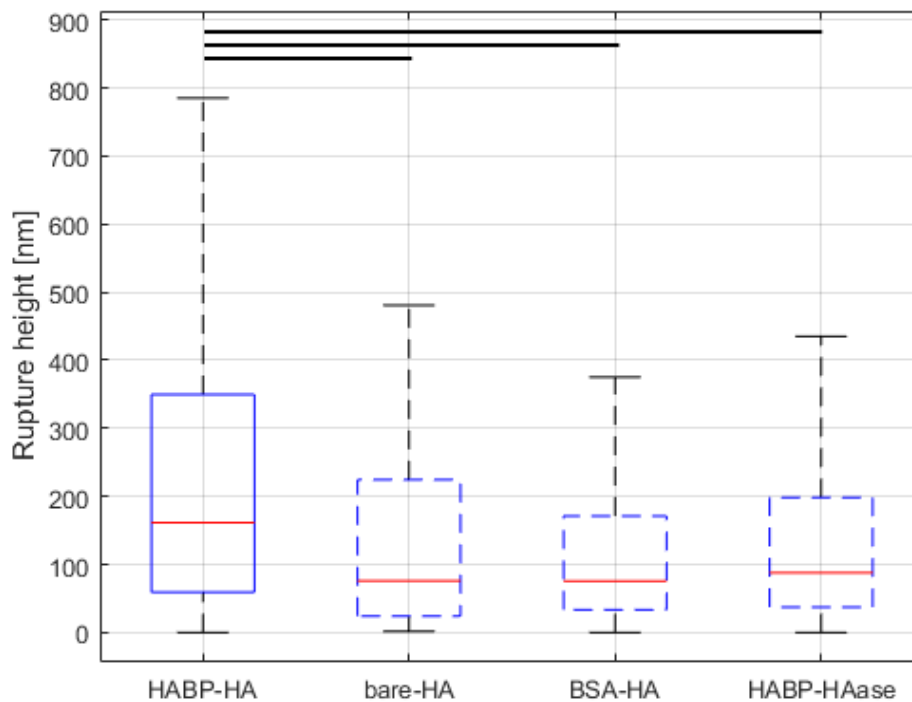


Figure 6.3.1: Box plot of rupture distance from the contact point for the study sample (Sample 1 - **HABP/HA**, solid line) and the control samples (Sample 2 - **BSA/HA**, Sample 3 - **untreated/HA**, Sample 4 - **HABP/HAase**, dashed line). The rupture distance from the contact point for the study sample was statistically significantly higher suggesting specificity of the bond between HABP and HA (Kruskal–Wallis test by ranks, significance set to $p < .01$).

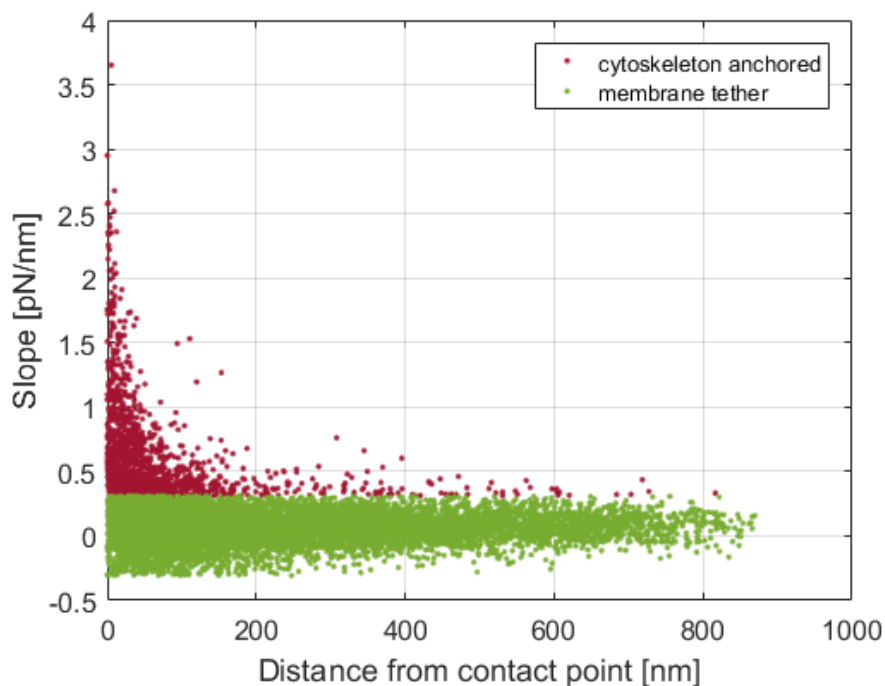


Figure 6.3.2: Scatter plot of the rupture events in Sample 1 (*HABP/HA*). The x-axis represents the distance from the contact point, the y-axis the slope of the curve before rupture. The rupture events classified as cytoskeleton anchored are shown in red, as membrane tethers in green.

resent non-specific binding. A threshold could be used to rule out these events from further analysis. However, a good threshold definition would be necessary to avoid removing useful data and could not be found in this case.

Over the total number of rupture events, 14.4% were classified as cytoskeleton anchored and 85.6% as membrane tethers. This fact would underline that about one HA molecule every ten has an active indirect link to the actin cytoskeleton. The number of cytoskeleton anchored rupture events remained constant over the three series of testing for each cell. Tether formation can be characterised by the tether force, i.e. the sudden release of force due to tether rupture. If multiple tethers are formed, the tether force corresponds to the force step between one tether and the subsequent one [193]. The average (median) calculated tether force was 16 pN, with a dispersion (IQR) of 10 pN (Fig. 6.3.3). The average (median) cal-

culated tether length was equal to 199 nm, with a dispersed distribution (IQR of 291 nm and maximum values up to 870 nm).

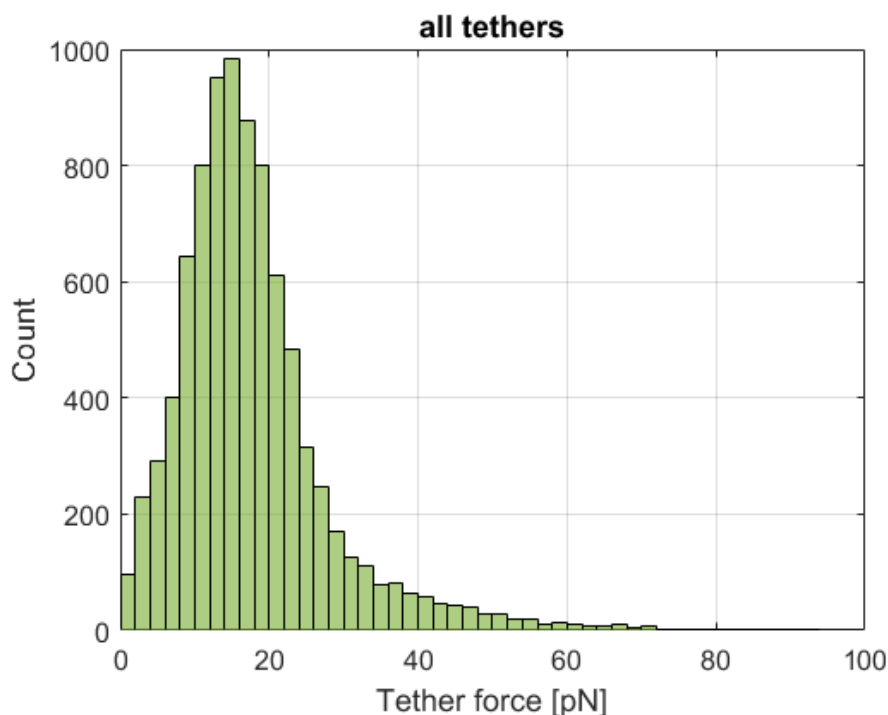


Figure 6.3.3: Probability histogram of the membrane tether force in Sample 1 (**HABP/HA**). The median value is equal to 16 pN, the IQR to 10 pN.

6.3.3 SINGLE AND MULTIPLE RUPTURE EVENTS

A further classification made on the rupture events regarded their occurrence as single or multiple events within one retraction curve: if single, only one rupture event per curve was recorded, if multiple, more than one. Over the total number of successfully targeted retract curves in Sample 1 (**HABP/HA**), about 4 every ten showed single ruptures, the rest multiple ruptures (Fig. 6.3.4). About 99% of the curves in the multiple sample contained 2 to 6 rupture events.

The percentage of occurrence of the cytoskeleton anchored or membrane tether rupture events was similar to the one found without discerning between single or multiple events (Section 6.3.2). 14.1% of the single rupture events were classified

as cytoskeleton anchored, 85.9% as membrane tethers; 14.5% of the multiple rupture events were classified as cytoskeleton anchored, 85.5% as membrane tethers.

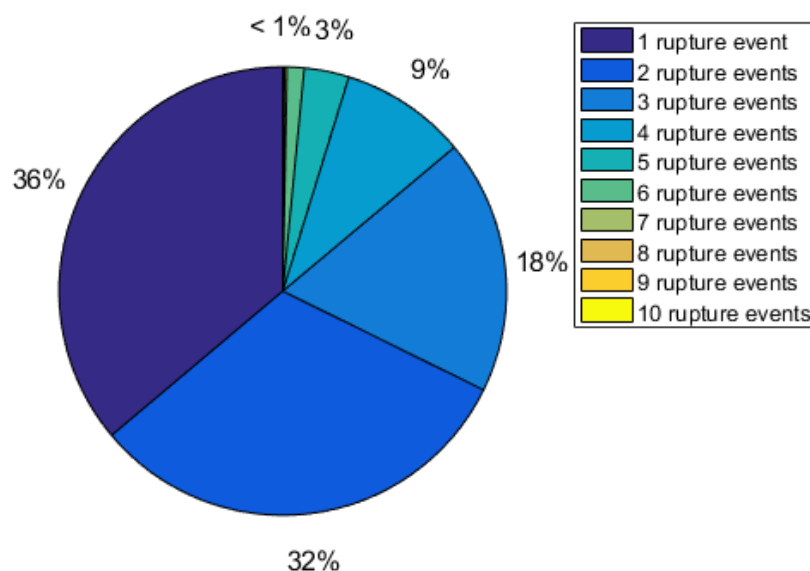


Figure 6.3.4: Pie chart of the number of rupture events in the successfully targeted curves in Sample 1 (*HABP/HA*). If only one rupture event was observed it was classified as single, if more than one as multiple. About 99% of the curves in the multiple sample contained 2 to 6 rupture events.

In Fig. 6.3.5 the slope of the multiple rupture events is shown. The slope of the first (I) rupture event was statistically significantly higher than the slope of the second to sixth (II-VI) rupture events (Kruskal–Wallis test by ranks, significance set to $p < .01$). The size of samples VII-X was too low for accurate statistical analysis as less than 1% of multiple rupture data showed more than 6 rupture events. Moreover, the first rupture in case of multiple rupture events would classify as a cytoskeleton anchored one with ~ 2.5 fold higher rate (36.4%) than in case of single ruptures.

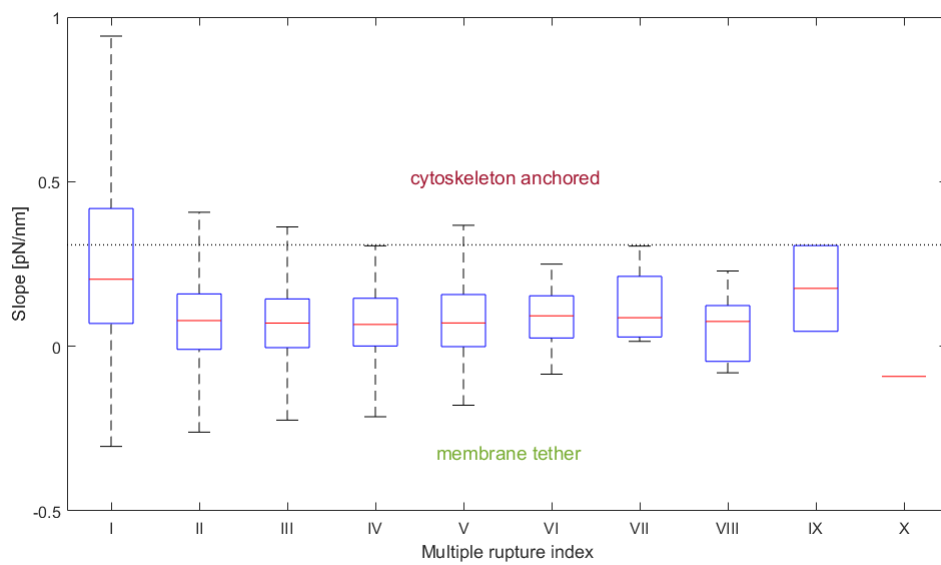


Figure 6.3.5: Box plot of the slope of multiple rupture events. The slope of the first (I) event is statistically significantly different from the slope of the second to sixth (II-VI) rupture events (Kruskal-Wallis test by ranks, significance set to $p < .01$). The size of samples VII-X was too low for accurate statistical analysis as less than 1% of data were in these samples.

6.3.4 INTRINSIC BOND CHARACTERISATION

The methodology proposed in [197, 198] was employed to investigate the intrinsic bond lifetime τ_0 and the energy barrier width γ . For this aim, the force-dependent system lifetime τ was calculated from the force histograms.

The obtained data should collapse onto a master curve if the molecule kinetics can be explained by a single exponential function [198]. However, this was not the case for either the cytoskeleton anchored nor the membrane tether rupture events (Fig. 6.3.6) and it was therefore not possible to calculate the intrinsic bond lifetime τ_0 and the energy barrier width γ for either type of rupture event.

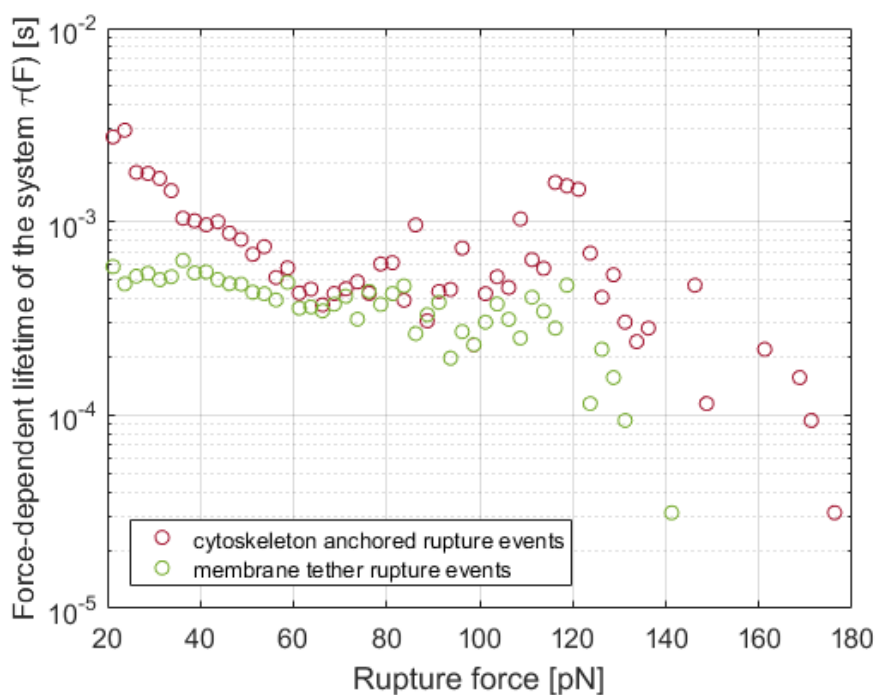


Figure 6.3.6: The calculated force-dependent lifetime of the system for the cytoskeleton anchored (red circles) and the membrane tether (green circles) rupture events is shown. Calculated points did not collapse on a master curve as expected for single-exponential molecule kinetics.

6.4 DISCUSSION

HA was targeted by AFM single molecule force spectroscopy on live pre-osteoblast MC₃T₃ cells. An HA-rich glycocalyx involved in mechanotransduction is expected on these cells [29]. To hypothesise possible mechanotransduction mechanisms the anchoring of the HA molecule to the cytoskeleton was investigated.

The study sample in which the AFM cantilever was functionalised with HABP was compared to control samples, where the cantilever was either blocked with BSA, not functionalised, or the cells were treated with HAase to degrade the HA glycocalyx. The successful target rate, i.e. the number of force spectroscopy curves showing rupture events counted over the total number of data, was calculated for each sample as an indicator of the ease of binding between the probe and the target molecule. This quantity was comparable in the three series of testing for each cell, suggesting that no HA fragments remained attached to the cantilever causing the saturation of binding sites.

The amount of HABP absorbed on the cantilever was not measured. However, it was observed that the successful target rate would not decrease during series of testing on the same or on different cells throughout the experiments. This would suggest that the cantilever binding sites were not saturated or damaged for the duration of the experiments and that the chosen concentration of functionalisation molecule was appropriate.

For the untreated cantilever in Sample 3 (**untreated/HA**) the successful target rate was markedly lower than in the other samples. This could be related to the absent functionalisation of the cantilever, which resulted in fewer interactions between the probe and the sample. The other control samples showed, however, successful target percentages comparable to the study sample. This could be explained by the presence of non-specific interactions caused by the cantilever functionalisation process. The distance from the contact point at which the rupture event occurred was therefore calculated to corroborate this hypothesis and was shown to be statistically significantly lower in all control samples with respect to the study sample. The specificity of the bond between HABP and HA in the study sample was hence considered to be satisfied and further analyses were carried out to classify the rupture events.

Over the total number of rupture events, 14.4% were classified as cytoskeleton anchored and 85.6% as membrane tethers, suggesting that about one HA molecule every ten has an active indirect link to the actin cytoskeleton. It should be noted that this link could occur through the CD44 receptor or through the HA synthases as it was not possible to distinguish between the two cases when pulling on the HA molecule. Moreover, if the linkage was through CD44, the linker molecule could differ (i.e. ERM family, merlin or oligomers of these proteins [184]) making the category of cytoskeleton anchored bonds rather heterogeneous. The number of cytoskeleton anchored rupture events remained constant over the three series of testing for each cell, suggesting that if the HA/actin binding were severed during measurements they would reform within the time frame of 30 s corresponding to the delay between probing the same spot.

Membrane tethers are structures involved in cell-cell adhesion, communication and motion which originate from the cell membrane [65]. The membrane surface tension regulates various intracellular events and its maintenance is finely regulated [47, 193]. The cell membrane is capable of accommodating small and large variations in the surface tension using different mechanisms: small surface tension fluctuations are buffered by use of the membrane reservoir, i.e. extra membrane stored in the form of undulations, folds, ruffles, microvilli and *caveolae*; large variations are facilitated by membrane material dynamic recycling mechanisms. The ability to create membrane tethers resides in the existence of the membrane reservoir, which is affected by the membrane composition and mechanical properties, the interactions with the cytoskeleton and the lipid bilayer turnover.

It has been shown that the tether growth once started does not depend on the chemical nature of the attachment between the force transducer and the cell membrane [65]. In previous works employing AFM, membrane tethers were pulled by cantilevers which were either untreated [65] or treated with non-specific adhesive molecules [65, 193]. In the case of untreated cantilevers, the contact with the cell was maintained for 2 – 30 s before retracting to facilitate the tether formation. In the present study, no prolonged contact was performed and the HABP/HA binding behaved similarly to non-specific adhesion by forming the link within the time frame of the measurement. Therefore it was hypothesised that the HABP/HA binding is strong enough to allow for the initiation of tethers, despite pulling through

the HA molecule and not directly on the membrane.

The average tether force calculated in this study was 15.88 pN , in the range of $10 - 60 \text{ pN}$ measured in the literature for various cells [65]. The quantity dispersion was hypothesised to represent the membrane heterogeneity, both in terms of composition and mechanical properties. The average tether length for osteoblasts differentiated from human mesenchymal stem cells was measured as $4.0 \pm 1.1 \text{ }\mu\text{m}$ [47]. The average tether length calculated in this study was however much shorter, equal to 199 nm , with a much dispersed distribution. This was related to a limitation in the employed protocol. In fact, the cantilever was kept close to the cell surface and was translated between subsequent spots of the testing grid. For this reason, the tethers were pulled vertically for a limited range ($\sim 1 \text{ }\mu\text{m}$) and not allowed to develop in full length.

Therefore three scenarios could occur: i) all the tethers would rupture during the vertical movement; ii) some of the tethers would be maintained during the lateral cantilever movement and would be ruptured during the translation; iii) some of the tethers would be maintained during the lateral cantilever movement and would still be present during indentation of the subsequent test grid spot. The first two cases were difficult to discern due to the hydrodynamic effect: if some residual tethers were still be bound to the cantilever, the zero force condition (i.e. baseline) would not have been reached on the retract curve, similarly to previous observations [65]. Similar outcomes would, however, be observed in the case of the hydrodynamic effect, as the cantilever would be pushed to bend up due to the liquid resistance when moving downwards and to bend down when moving upwards. In the present protocol, it was chosen to correct the retract curves for the hydrodynamic effect, having observed that the offset between baselines was comparable to previous indentation experiments with untreated cantilevers. Therefore longer tethers in the second scenario were probably overlooked and the total average tether length underestimated. Data belonging to the third scenario were excluded from the analysis, as recognisable from unexpected peaks during the cantilever extend/cell indentation region.

It was possible to hypothesise that patterns in the HA molecule pulling were present by analysing the multiple rupture events. Multiple rupture events were observed in about 60% of the force spectroscopy curves, with most curves show-

ing from 2 to 6 rupture events. The slope of the first rupture event was statistically significantly higher than the slope of the following rupture events and showed a higher incidence of cytoskeleton anchored ruptures than in case of single rupture events. These results would suggest that a cytoskeletal bond needs to be broken to improve the ability to pull multiple tethers from the cell membrane. Similar results were obtained on red blood cells and it was hypothesised that at the beginning of tether formation the link with the cytoskeleton would be partially broken and further tether elongation would be accompanied by the elongation of the intact components of the cytoskeleton [186]. The resulting tether would therefore not be completely disconnected from the cytoskeleton and possibly maintain an actin cytoskeleton core, analogous to what was observed in the formation of HA-rich microvilli [67, 176, 177].

It was not possible to calculate the intrinsic bond lifetime τ_0 and the energy barrier width γ for either type of rupture events, as the molecular kinetics could not be explained by a single exponential function [198]. This result would suggest that both categories were heterogeneous and contained events of different nature. As previously discussed, the cytoskeleton anchor link might be one or more proteins of the ERM family or merlin and this could result in different bond characteristics, while the membrane tethers might or might not conserve an actin-rich core. Moreover, non-specific interactions might have played a role, as they were not ruled out before the analysis.

6.5 CONCLUSIONS

In this study, HA molecules on the surface of pre-osteoblast cells were investigated by single molecule force spectroscopy.

HA molecules were successfully targeted by using HABP-functionalised cantilever. The specificity of the HABP-HA bond was supported by the observation of the control's successful target rates. In fact, untreated cantilevers showed few binding events and cantilevers treated with BSA showed weak interactions which could not sustain the increasing pulling force of the cantilever. If cells were treated with HAase similar weak interactions were observed, possibly linked to the cantilever interacting with membrane domains exposed by the removal of the glycocalyx.

It was possible to distinguish between cytoskeleton anchored and membrane tether rupture events by analysing the slope preceding the observed ruptures during retraction of the cantilever from the cell. Both categories were heterogeneous: the HA can be linked to the membrane by its synthases (HAS) or the receptor CD44 and these could anchor to the cytoskeleton with different molecules; the local composition and mechanical properties of the membrane could affect the membrane tether characteristics and rupture force. This heterogeneity was also observed in the evaluation of the single chemical bond intrinsic characteristics, where the interplay of different molecules was hypothesised.

The HABP-HA bond was shown to be strong enough to pull membrane tethers. This would suggest that the HA molecule acts as a rigid linker between the cantilever and the cell membrane. This observation is in accordance with the conformation of the HA molecule, in which repeated disaccharide units form a linear structure organised as a random coil [200]. No domain unfolding or mechanical denaturation are therefore expected, as they were not observed in the retraction curves.

Different mechanotransductive mechanisms involving HA could be hypothesised from the observed results. Single cytoskeleton anchored rupture events were interpreted to represent HA molecules linked directly to the cytoskeleton and therefore transmitting mechanical stimuli into the inner cell compartments, with *decentralised* mechanosensing at sites distinct from the cell surface [4, 182]. Single membrane tethers were conversely predicted to be examples of *centralised* mechanosensing, with the glycocalyx molecules directly connected to areas of the membrane where an abundance of signalling molecules reside [4]. Finally, multiple rupture events with an initial link to the cytoskeleton probably represent microvilli-like structures with an actin-rich core, similar to the ones observed for cells overexpressing HA synthases and hypothesised to have a signalling role [67, 173, 176, 177].

The present findings would, therefore, support the idea of the HA having a structural role and being able to organise and support the cell membrane as an external cytoskeleton deeply involved in the glycocalyx-mediated mechanotransduction.

7

Single cell Finite Element modelling

In this chapter the computational results are presented¹. The Finite Element (FE) single cell model design and the simulation parameters are explained together with the obtained outcomes.

7.1 INTRODUCTION

Single cells in a population show variable behaviours and characteristics [81]. This heterogeneity has stochastic as well as deterministic sources and historically has often been overlooked when focusing on common mechanisms between cells. Most information collected on cell processes was obtained averaging the characteristics of a cell population and generalising them to all cells. However, when the same characteristics were studied at the single cell level different patterns might emerge. Moreover, single cell studies lead to insights not achievable with bulk analysis, for example in cancer biology [201] or immune system response [202].

¹Part of the work presented in this Chapter is planned to be submitted as a scientific paper.

Some of the factors dictating cell population heterogeneity, such as cell cycle or differentiation stages [82–84], cell migration and adhesion [87], have a direct impact on the cell cytoskeleton and therefore on the cell mechanical properties. Moreover, when testing cell mechanical properties with experimental techniques further variability might be introduced. In the case of AFM measurements, the experimental set-up, the testing and culture conditions, and the post-processing of data might all cause additional experimental error [39, 40, 43, 93].

For these reasons, the development of a computational framework could be of help. In fact, the use of theoretical models could provide better control over the organisation and interplay between intracellular components. Moreover, it has been suggested that the use of confocal microscopy based FE models with an accurate representation of intracellular structures could strongly support experimental work on cell mechanics [69, 80]. These models would, in fact, allow for realistic representation and quantification of mechanical stimuli acting *in vitro* or *in vivo* on individual cells. Moreover, numerical simulations including different cell components could provide insights into the contribution of individual elements to whole-cell mechanics [75] and on the distribution of forces for structural stability [74].

The generation and transmission of forces in the cytoskeleton have been modelled using discrete theories, such as tensegrity, for which the cytoskeletal fibres are described as a network which distributes forces within the cell. In single cell tensegrity models, the structural integrity of the cell is based on pre-stress and interdependence of cytoskeletal components, but the role of individual fibres in generating and transmitting forces is not elucidated [75]. Therefore, a new category of models has been introduced including discrete and continuous formulations to embed the cytoskeletal fibres in a continuum representing the cytoplasm [74–76, 80]. The tensegrity principles are maintained but the individual elements can move independently and the integrity of the cell is not solely dependent on the fibre network.

In Chapter 3 and Chapter 5 results related to cell body AFM indentation experiments were presented. Wide ranges of variability were observed in the Young's modulus for all tested cell populations and it was hypothesised this would be related to their intrinsic heterogeneity in terms of the cytoskeletal arrangement. The

development of a computational model simulating the experimental conditions could, therefore, add some quantitative information on the contribution of the single cell components to the whole cell stiffness. The hypothesis would be that a multi-structural model could describe the response of a cell to the mechanical indentation in terms of local stresses and strains. In addition, it could provide insights on the intracellular force and deformation distributions caused by external mechanical stimulation.

An image-based single cell model was therefore designed as a preliminary step to study the heterogeneity of a population. The model comprised the nucleus, the cytoplasm and the actin cytoskeleton. The latter was modelled as actin bundles resisting tensional forces [74–76, 80] and actin cortex responding to compression [75, 76]. The use of confocal stack images of a single pre-osteocyte MLO-A5 cell allowed for faithful representation of the cell shape and of the arrangement of the actin bundles. AFM indentation with a spherical bead was simulated in different cell regions to investigate the effect of the compression of multiple intracellular components with different mechanical properties.

7.2 MATERIALS & METHODS

7.2.1 CONFOCAL IMAGING

Confocal imaging of fixed cell samples stained for nuclei and actin was performed on the MLO-A5 pre-osteocyte cells as described in Chapter 5 (Section 5.2.2). Z-stack images spaced $0.49 \mu m$ were obtained with 1024×1024 pixel resolution. The cell chosen for the model design well represented the population morphology: its dimensions for the area, major and minor axes of the nucleus and the whole cell were in the ranges for the population average as measured in Section 3.3.3 (Chapter 3).

7.2.2 GEOMETRY RECONSTRUCTION

The single cell model geometry reconstruction consisted of two steps: first, the confocal images were segmented in ImageJ [109] to obtain separate masks for the nucleus and cytoplasm; then the images were imported in Simpleware ScanIP

(Synopsis, Inc.) for three-dimensional reconstruction and FE meshing.

SEGMENTATION

Confocal images for each slice and each channel (DAPI for nuclei and phalloidin for actin) were separately analysed (Fig. 7.2.1). A threshold was set to select the pixels showing channel signal against the black background and a mask was created on the selection. Binary processes of dilation/erosion were employed to obtain solid fields for the nuclei. A similar process was used to predict the cell surface area (i.e. cytoplasm) by dilation of the actin fibre signal.

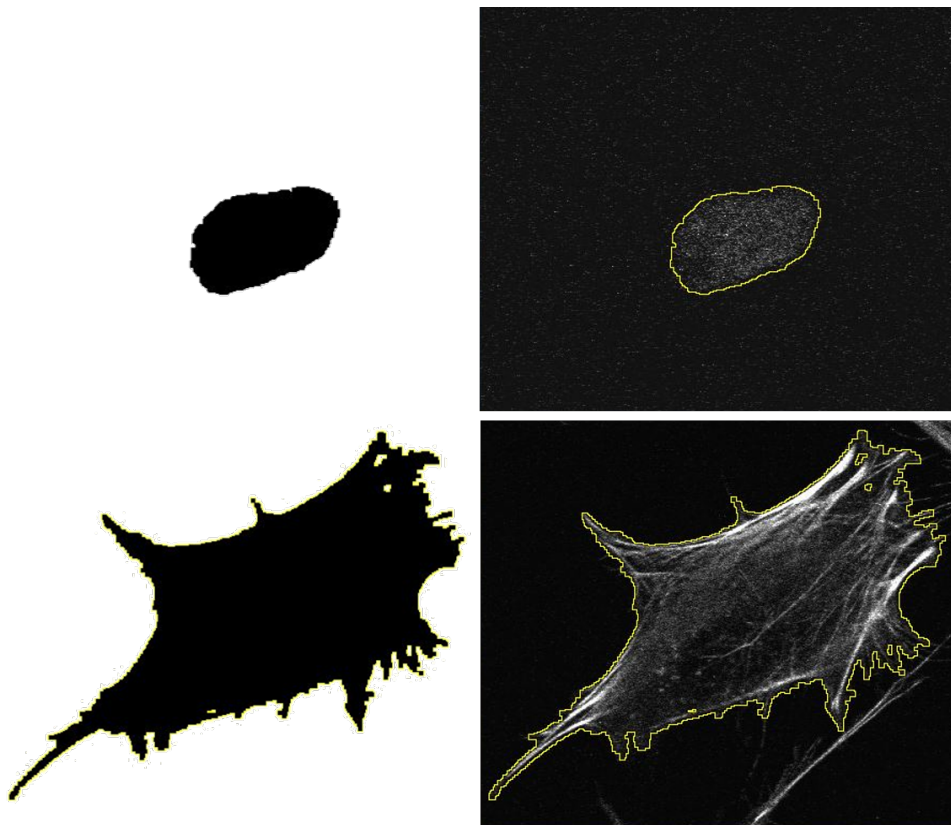


Figure 7.2.1: *The confocal images segmentation process is presented. A mask (left column) was created by using a threshold on raw images (right column) for the nucleus (top row) and cytoplasm (bottom row), respectively.*

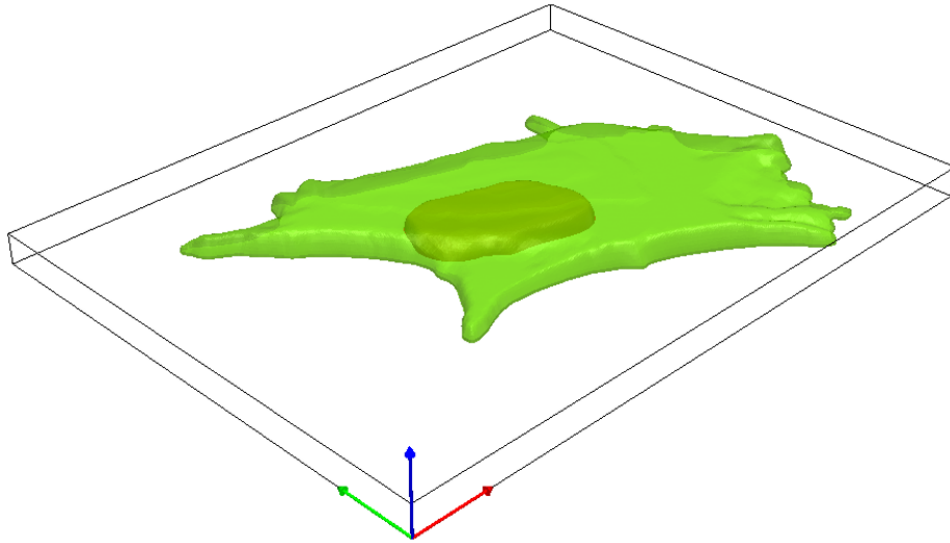


Figure 7.2.2: *Three-dimensional solid reconstruction in Simpleware ScanIP of the two solids representing the nucleus (green, semi-transparent) and the cytoplasm (red, opaque). The mesh was created so that the nodes and elements were congruent at the interface between the two regions.*

RECONSTRUCTION AND MESHING

The masks for the nucleus and cytoplasm for all slices were imported into Simpleware ScanIP. By using Boolean operations, two separate solids were created consisting of the nucleus and the cell volume subtracting the nucleus. Recursive Gaussian smoothing was performed to obtain a more realistic geometry (Fig.7.2.2). An FE model was prepared with built-in utility, by congruously meshing the volumes with smoothed tetrahedral quadratic elements and by defining two placeholder materials for further modification in the subsequent steps.

7.2.3 INDENTATION SIMULATIONS

The FE model obtained in Simpleware ScanIP was imported as an input file in Abaqus (Simulia, Dassault Systèmes). Actin fibres and cortex were added and boundary conditions and simulation parameters were set to simulate the indentation of a spherical bead at different locations over the cell. The obtained model was constituted by two parts, the cell and the indenting bead.

SINGLE CELL MODEL REFINEMENT

Discrete three-dimensional truss elements were added representing the actin bundles (Fig.7.2.3). The disposition of these bundles was chosen following the information contained in the confocal images. Basal and apical bundles were included close to the substrate and the nucleus, respectively. The basal actin bundles roughly followed the morphology of the cell and were tied to the cytoplasm at nodes regarded as focal adhesions. The apical actin bundles were designed to join the nucleus and the cytoplasm in a parallel fashion, similarly to what was previously reported in [76, 80], and were therefore tied to the nucleus on one end and to the cytoplasm on the mid-point and on the opposite end. A cross-section of all truss elements was chosen equal to $0.2 \mu m^2$, as measured from the confocal images. The actin bundles were not pre-stressed as stated by the tensegrity theory. This choice was made to reduce computational costs, as it was shown that the pre-stress does not significantly contribute to the exerted forces when compression was simulated [203].

The actin cortex was modelled as a thin shell homogeneously covering the cell surface [75, 76]. A thickness of $0.2 \mu m$ was chosen [43, 75, 93]. The cell membrane was not included in the model as it was considered negligible in terms of mechanical deformation resistance, as it is much softer than the actin cortex [75, 76].

Having imported the nucleus and cytoplasm from Simpleware ScanIP as two separate solid with congruous mesh at the interface, it was possible to assign different materials to each of them. Materials [76] and element types for each sub-cellular component are summarised in Table 7.2.1. Homogeneous, isotropic and elastic material properties were assumed, defined in terms of Young's modulus and Poisson's ratio. A hybrid formulation was attributed to all elements to account for the almost incompressible material behaviour. Second-order tetrahedral three-dimensional hybrid elements (C3D10H) were used for the nucleus and cytoplasm; three-nodes hybrid quadratic truss elements (T3D2H) for the actin bundles; three-dimensional triangular small-strain thin shell elements (STR165) for the actin cortex. The obtained cell part is shown in Fig. 7.2.4.

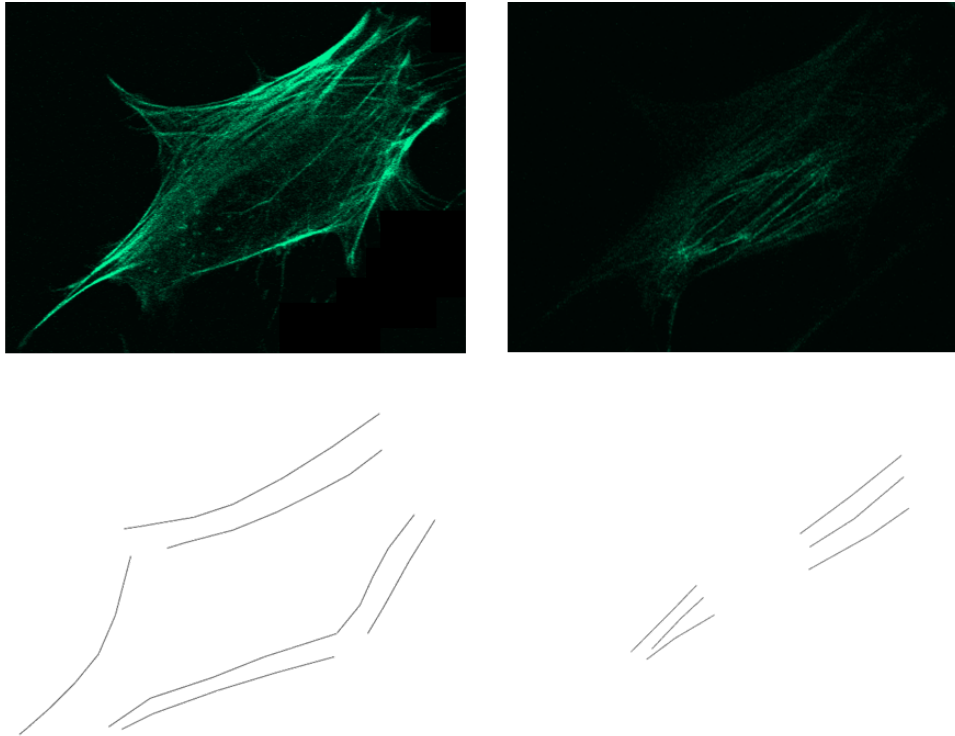


Figure 7.2.3: *Confocal images of basal (top left) and apical (top right) actin bundles are shown together with the modelled fibres (bottom row). Basal bundles follow the shape of the cell, while apical bundles are centred over the nucleus.*

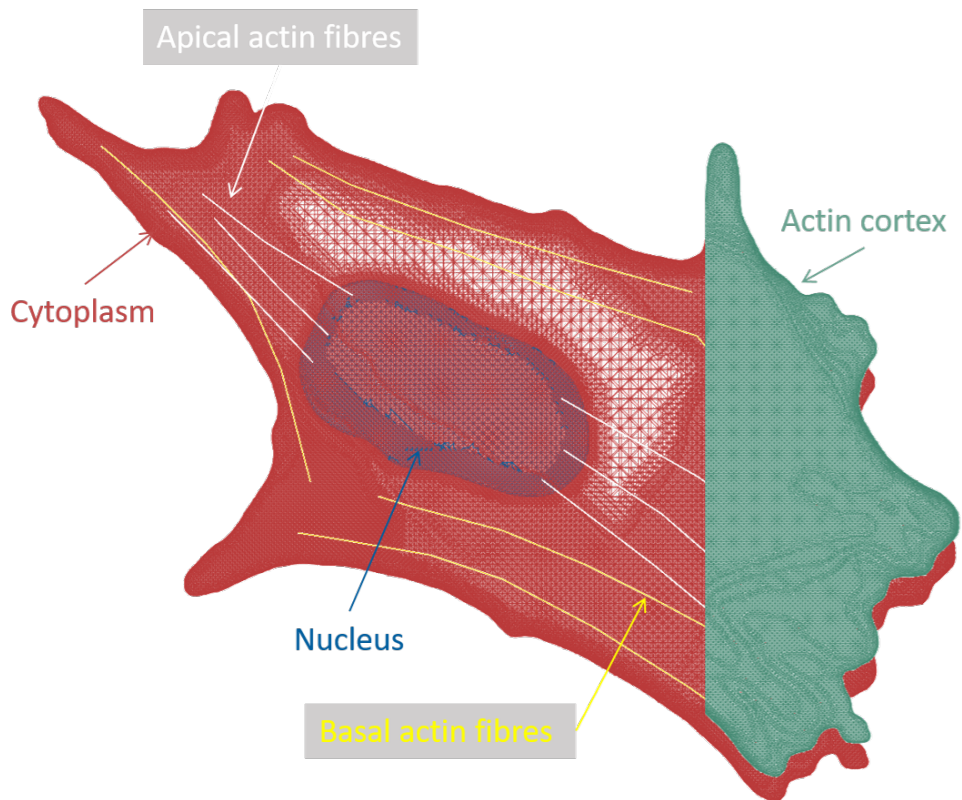


Figure 7.2.4: FE model for the single cell part, including nucleus (blue), cytoplasm (red), apical (white) and basal (yellow) actin bundles and actin cortex (green). The actin cortex covers the cell surface completely and it is in contact with it, the depicted representation was chosen for clarity only. The texture represents the meshed elements, which dimensions are dependent on the geometry complexity (e.g. the area of the cytoplasm close to the nucleus shows fewer elements as it is mainly flat).

Table 7.2.1: *Material properties [76], Abaqus element type and number of elements of each modelled cellular component are summarised. An elastic material definition was used in terms of Young's modulus (E) and Poisson's ratio (ν).*

		Nucleus	Cytoplasm	Actin cytoskeleton		
				Bundles		Cortex
				Apical	Basal	
E	[kPa]	5.1	1	10	10	2.4
ν	[-]	0.3	0.49	0.3	0.3	0.3
Element	Type	C3D10H	C3D10H	T3D2H	T3D2H	STR165
Element	No.	174821	1102047	72	30	114789

RIGID SPHERICAL INDENTER

The spherical bead used as indenter was modelled as three-dimensional rigid shell with radius equal to $3\ \mu\text{m}$, similar to the one used for cell body indentation experiments (Chapter 3, Section 3.2.2). A reference point was set on the sphere centre for rigid constraint and subsequent boundary condition definitions. The system reference axes XYZ were designed with the origin on the sphere surface closest to the cell.

BOUNDARY CONDITIONS AND CONTACT

The indentation was controlled by setting the bead displacement in the Z direction for $1\ \mu\text{m}$, with the ideal substrate of cell attachment on the XY plane. The other degrees of freedom for the bead were constrained. To model the cell adherent to the substrate the nodes at the cell base were constrained on the Z directions. In the nodes denominated as focal adhesions, i.e. where the basal actin bundles were tied to the cytoplasm, a total encastre was enforced.

A contact interaction was defined between the bead and the top surface of the cell, with an isotropic friction coefficient of 0.001. A finite surface to surface sliding was allowed with the bead set as master surface and the cell as slave surface.

SIMULATION PARAMETERS

Two steps were set for the simulation. At the initial step, the contact interaction and the cell boundary conditions were active; during the following static general step, the bead boundary conditions (i.e. displacement) was added. Large deformation theory was employed [80] and an initial increment size of 0.01 s was set, with 0.0001 s and 0.1 s minimum and maximum limits for the automatic incrementation mode, respectively.

Simulations ran as batch jobs on high computing performance facilities (Iceberg, University of Sheffield) and took on average about one hour of system time when launched on a 2x8-core Intel E5-2670 machine with 256 GB of memory.

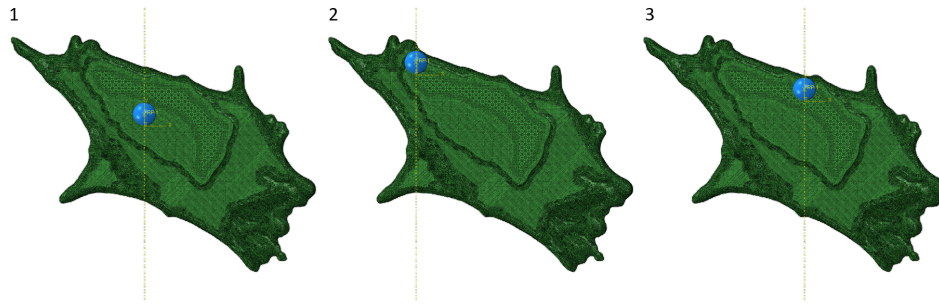


Figure 7.2.5: Spherical bead (blue) indenting the single cell body (green) at different locations. Indenting location 1 was centred over the nucleus; indenting locations 2 and 3 were positioned towards the cell periphery.

INDENTING LOCATIONS

Three separate versions of the model were run with the spherical bead indenting different locations of the cell (Fig. 7.2.5). Indenting location 1 was centred over the nucleus; indenting locations 2 and 3 were positioned towards the cell periphery away from the nucleus.

OUTPUT

The calculation of the Young's modulus of the modelled cell at different indenting locations was of interest for comparison with the experimental data. To this aim the total reaction forces in the Z direction were requested as output at each time increment. These were used against the bead displacement to plot force-displacement curves similar to the ones obtained with the AFM. An algorithm was written in MATLAB (Mathworks) to fit the curves with the Hertz model for different indentation depths, similarly to that detailed in Section 3.2.4 (Chapter 3).

The built-in Abaqus visualisation tools were employed to explore the strain transmission to the actin bundles. This allowed study of the actin cytoskeleton involvement during indentation of the nucleus and periphery. The maximum stress on the actin cortex was also computed to verify it would not exceed the membrane surface tension value hypothesised for cells.

7.3 RESULTS

7.3.1 INDENTING LOCATIONS

Three separate simulations were run on three different indenting locations, one on the nucleus (indenting location 1) and two towards the cell periphery (indenting locations 2 and 3). The rationale was to test if a variation in the reaction forces at the cell base could be observed depending on the location. This could be a one possible reason for the stiffness variability observed experimentally (Chapter 3 and Chapter 5).

An indentation of $1\ \mu\text{m}$ was set as a displacement boundary condition. In the case of the indenting location 3, the simulation reached convergence and the total displacement was achieved; in the other two cases this was not obtained as the simulation did not complete due to excessive element distortion. This was expected due to the irregular geometry of the single cell model obtained from confocal images. The maximum indentation achieved for indenting location 1 was therefore of $580\ \text{nm}$ and for indenting location 2 of $105\ \text{nm}$. The results for periphery indenting location 2 and 3 were comparable and therefore indenting location 3 was used as the periphery reference having reached complete convergence.

The Young's modulus was obtained by fitting the Hertz model on the displacement vs. reaction forces on the Z-direction. The reaction forces at the cell base are visualised in Fig. 7.3.1 for indenting location 1. The comparison between the FE and single cell AFM results for a sample of MLO-A5 tested over the nucleus and the periphery (Chapter 5) is shown in Fig. 7.3.2. The indentation depth vs. force curves were comparable for the nucleus, but lower forces in the FE model were exerted at similar indentation depths in the case of the periphery.

The resulting overall Young's modulus obtained by fitting the displacement-dependent reaction forces with the Hertz model for the FE model is shown in red in Fig. 7.3.2 for indenting locations 1 (nucleus, bottom left panel) and 3 (periphery, bottom right panel). In the case of indentation over the nucleus (i.e. indenting location 1), the Young's modulus tended to increase with the indentation depth, while a constant average stiffness was calculated for the experimental values. Conversely, the indentations towards the cell periphery converged to a Young's

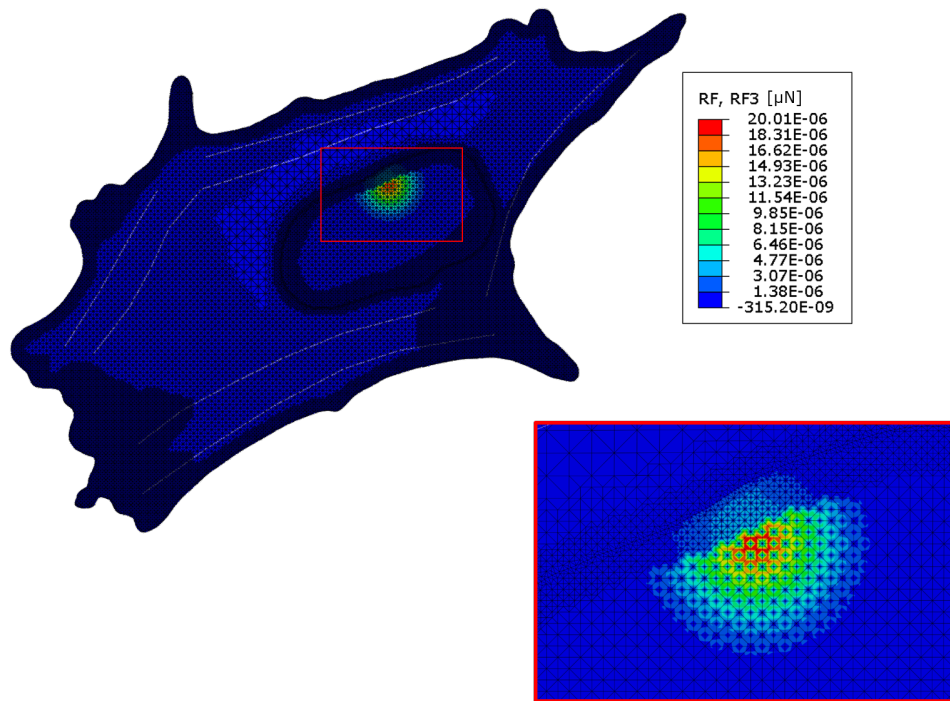


Figure 7.3.1: Reaction forces in the Z-direction for the cell base in the case of indenting location 1 at maximum indentation ($\sim 600\text{ nm}$). The region in the red square represents a zoom of the nucleus area, where the indentation was performed.

modulus value of about 1.2 kPa constant for increasing indentation depths. This value was lower than the experimental stiffness values obtained when testing the cell periphery.

All computed values were in the ranges of dispersion for the pre-osteocyte MLO-A₅ cells (Section 5.3.2, Chapter 5). It is interesting to notice that the values found for the nucleus and periphery simulated indentations were different, due to the contribution to the overall stiffness of the different materials and their local morphology. Conversely to what was observed in the experiments, the Young's modulus was higher on the nucleus.

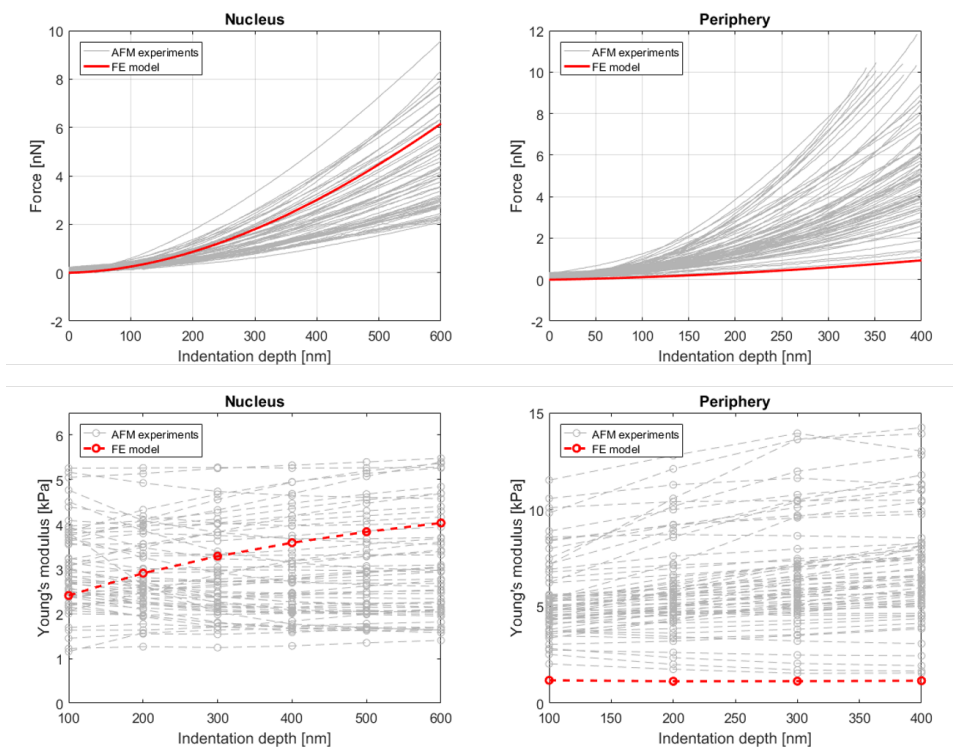


Figure 7.3.2: The FE results (red) were compared to the AFM experimental results for one sample of 80 MLO-A5 (Chapter 5), for indentations over the nucleus (left) and the periphery (right). In the top panels, the indentation depth vs. force plots can be found; in the bottom panels, the indentation depth vs. fitted Young's modulus.

7.3.2 ACTIN CYTOSKELETON CONTRIBUTION

The localised strain of the modelled continuous cell components (i.e. actin cortex, cytoplasm and nucleus) might be considered as trivial due to the compression applied by the bead displacement. On the other hand, it is interesting to verify the actin bundles strain as this could represent a measure of the involvement of this cytoskeletal component during indentation. The maximum principal strain for the actin bundles was considered. For both the indentation simulations over the nucleus and periphery, the basal actin bundles showed zero strain or deformation, suggesting their role was secondary for the simulated bead displacement magnitude. In contrast, the apical actin bundles were strained for both nucleus and periphery indentations, as shown in Fig. 7.3.3. When the indentation was performed over the nucleus (indenting location 1) the strain was more localised but of higher magnitude, up to $\sim 700 \mu \varepsilon$ of true strain, in respect to the periphery (indenting location 3). Similar values for actin bundle strains were found in [76], where analogous assumptions on the material properties and geometrical fibre disposition were made.

The maximum stress on the actin cortex was also analysed, to verify that its value would not exceed the documented values for membrane surface tension [75, 203]. This verification confirmed that the modelled actin cortex layer would withstand the imposed deformation without collapsing, as the maximum von Mises stress value was of $766 Pa$ and the membrane surface tension hypothesised to be in the range of $2400 Pa$.

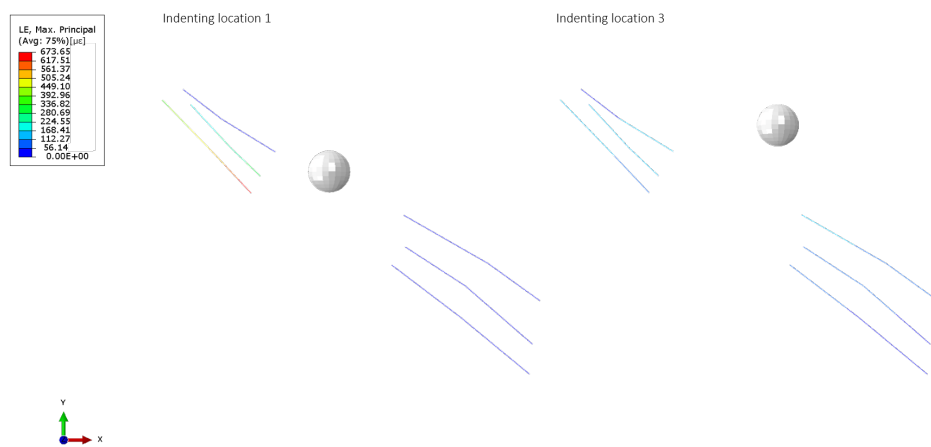


Figure 7.3.3: True strain of the apical actin bundles for the indentation over the nucleus (indenting location 1) and periphery (indenting location 3). The comparison was made at the deepest indentation value available for both simulations, i.e. $\sim 600 \text{ nm}$.

7.4 DISCUSSION

An FE model was designed to simulate single cell indentation by AFM. This included different cell components, i.e. the nucleus, cytoplasm, actin cortex, apical and basal actin fibres, and was based on confocal images of a pre-osteocyte MLO-A₅ cell. Simulations of indentation over the cell nucleus and periphery with a spherical bead were performed, representing analogous AFM experiments presented in Chapter 3 and Chapter 5.

The Young's modulus for increasing indentation depths was computed and was different for the nucleus and periphery, highlighting the importance of the realistic model geometry and the inclusion of different cell components. The computed values were in the range of experimental values for MLO-A₅ cells, despite showing higher stiffness for the nucleus than for the periphery, oppositely to the average experimental findings. However, it should be noted that some single cells also showed a similar behaviour experimentally. The Young's modulus calculated for the periphery was close to the lowest bound of the experimental stiffness distribution, suggesting that the cytoskeleton modelling was not adequate to fully capture the cell characteristics, as discussed below.

The FE model Young's modulus values and trends were also closely related to the particular morphology of the reconstructed cell: the nucleus at the site of indenting location 1 was covered by a layer of cytoplasm of about 750 nm and by the actin cortex which was 200 nm of thickness; therefore, for an indentation of ~ 600 nm the nucleus was only indirectly indented due to the compression of the above layers. For this reason, the calculated Young's modulus for the nucleus might not have reached a plateau representing a stable value where all the materials were directly compressed. For indentations over the cell periphery, the calculated Young's modulus was mainly due to the contribution of the actin cortex and cytoplasm elasticity. The actin bundles, in fact, were designed to withstand tensional forces only and therefore contributed to a lesser extent to the overall cell stiffness. Similar results were reported previously, where the contributions of the actin cortex and bundles were studied by selectively changing their mechanical properties [76, 203] or by selectively removing them from the single cell model [75].

The material properties used for the single cell components were taken from dif-

ferent cell types and might not be accurate for pre-osteocyte MLO-A5 cells. In fact, due to the difficulty in experimentally isolating single contributions, not many data were available from the literature and they were sourced from different cell types in different experimental conditions [75, 76]. The impact of changing the mechanical properties of single cell components on the overall simulated Young's modulus has been previously investigated [75, 76, 203]. It was shown that computationally changing the actin cortex thickness and Young's modulus, the actin bundles number and Young's modulus, and the cytoplasm rigidity would give rise to a change in the overall cell Young's modulus. The material properties could, therefore, be adjusted to obtain a better match to the average experimental values, however, this was not considered appropriate in this context not being able to back up any structural changes with experimental evidence for the MLO-A5 pre-osteocyte cells.

Another limitation could reside in the modelling of all materials as isotropic elastic, despite the fact that cells are heterogeneous in composition and present time-dependent mechanical properties [43]. However, similar hypotheses were considered when using the Hertz model to obtain the Young's modulus from AFM data in the present work and were shown accurate enough for the stated objectives (Chapter 3). Moreover, information on the time-dependent nature of single cell components material properties was not readily available in the literature. Hence, to define them in the model would imply making assumptions which could be not physiologically relevant for cells and would be hard to verify [203].

The cytoskeleton, and in particular actin, has been proposed as the major contributors to cell stiffness [43]. In the present model, the cytoskeleton was modelled only as the actin component, in the form of the actin cortex and apical and basal bundles. The actin cortex played a role in withstanding the AFM bead compression and the bundles were involved in transmitting the load within the cell, as also suggested by experimental evidence [43]. However, the absence of other components, such as myosin, could have impacted on the strain distribution, as it was suggested that this molecule might reinforce and add tension to the actin scaffold [128]. Moreover, the absence of microtubules and intermediate filaments might have impacted on the force transmission within the cell [75, 203].

The number and geometry of the actin bundles were simplified for modelling purposes. It has been previously shown that the spatial organisation of the actin

fibres play a role in the overall cell stiffness, with the presence of aligned and/or peripheral actin fibres reinforcing the cytoskeleton [128]. Similar results were obtained computationally [203], as it was demonstrated that the number and orientation of actin bundles would affect the computed Young's modulus. The Young's modulus obtained for the periphery with the FE model was close to the lowest bound of dispersion of the experimental values, suggesting that the simplified modelling of the peripheral cytoskeleton caused the inability of the model to capture this fibre reinforcement. It would be therefore of interest in the future to model different single cells of which values of Young's modulus obtained by AFM were available to evaluate the ability of the computational models to replicate experimental results.

The glycocalyx was not included in the single cell FE model. Similarly to the cell membrane, this was considered too soft to give a relevant contribution when AFM bead indentation was performed if modelled as a homogeneous layer. Different modelling approaches previously used for the endothelial glycocalyx could have been employed, considering the glycocalyx as a porous medium [204, 205] or focusing on its fibres properties [24, 206]. However, for this aim, more in-depth information on the interactions between fibres of different nature in the bone glycocalyx (e.g. HA and other proteoglycans) would be needed.

Finally, it should be mentioned that the computational model represented a static snapshot of the cell. For example, no dynamic polymerisation of the actin cytoskeleton was included and no molecular structures were taken into account [74]. Moreover, all the cell components were considered as homogeneous, failing to represent the intrinsic local heterogeneity of living organisms and cells in particular. The inclusion of different cell components and of a realistic cell morphology represented however an attempt towards more reliable single cell computational models and the importance of these features was highlighted.

7.5 CONCLUSIONS

A single cell FE model was built based on confocal images. Different cell components were included and AFM nano-indentation experiments were simulated. The importance of a realistic cell morphology and the contribution of different com-

ponents was highlighted showing how indenting different locations led to computing different overall stiffness values in the range of those calculated experimentally for the same cell type.

8

Discussion

8.1 GENERAL DISCUSSION

Mechanotransduction mechanisms could be further elucidated by a better understanding of the intrinsic properties of the cells. In particular, the mechanical properties of cells are vital in the transmission of mechanical forces, determining to which magnitude a given stimulus is sensed and how the forces and deformations are related locally [9, 10].

In the present thesis, the mechanical properties of bone cells were studied experimentally by AFM and computationally by FE modelling. Distributions of stiffness values for different bone cell populations were experimentally acquired. Particular focus was placed on the glycocalyx, on the ability of AFM nano-indentation techniques to elucidate its mechanical properties and on the potential mechanotransduction mechanisms involving the connection of the glycocalyx to the cytoskeleton. Computational simulations were designed to complement the experimental findings.

A protocol was optimised for AFM nano-indentation of large samples. This involved careful control of the experimental set-up and tailored post-processing to obtain the Young's modulus of cells from force spectroscopy data as a measure of cell stiffness. The Hertz model was used for fitting, although this relies on assumptions which are not necessarily applicable to cells. To account for this, the Young's modulus for various indentation depths was calculated to verify its expected constancy and confirm the fact that the rigid substrate contribution was negligible. Moreover, multiple indentations on neighbouring locations were performed and compared and no time-dependent viscoelastic response was observed, confirming that in this specific case the elastic material assumption could be utilised. No adhesion between the tip and the cell was detected, suggesting that the use of more complex models (such as the JKR or DMT) was not needed in this instance. These findings were considered sufficient to permit the use of the Hertz model, which also allowed for easier comparison with available literature studies using this common approach.

Large ranges of dispersion were found for all the tested bone cell populations, highlighting their intrinsic heterogeneity. Suitable sample sizes and data representation are needed in order to capture this feature. In the present work, a method to evaluate the accuracy of the computed average stiffness values was employed based on Monte Carlo analysis. It was calculated that, depending on the heterogeneity of the population, samples ranging from 35 to 70 cells were needed if accepting a maximum percent deviation of 10%. It should be noted that these sample sizes are specific for the cell populations and protocol used in this study and should not be taken as reference values. However, they highlight the need for suitably large samples to avoid generalising population characteristics based on unrepresentative sub-samples.

Different stiffness values were observed for the nucleus versus the periphery for all the bone cell populations tested. In particular, the periphery had more heterogeneous stiffness distributions: centring the measure over the nucleus provided some degrees of consistency between different cells. The periphery might have had different ratios of intracellular components changing the measured Young's modulus (e.g. more cytoskeletal fibres resulting in material reinforcement, more cytoplasm resulting in larger thickness). The periphery of all bone cell populations

also was shown to be stiffer. It was suggested that this might be related to cells with high levels of actomyosin [128], as qualitatively confirmed by the acquired confocal images of actin fibre distributions in this context.

Particular focus was placed on the glycocalyx, given its hypothesised role in bone mechanotransduction. This proteoglycan-rich cell outer layer has been mechanically characterised for endothelial cells, but equivalent information on bone cells is lacking.

A modification of the protocol optimised to test cell body stiffness by AFM nano-indentation was employed to explore the possibility of detecting the bone glycocalyx. Softer cantilevers and indenters of different sizes were used to account for the softer and fibrous nature of the material. A layer of HA could be observed on cells by confocal microscopy, however, the contribution of the glycocalyx could not be visually identified as the indentation of a two-layer material, as reported previously for the glycocalyx of bovine aortic endothelial cells [54, 55, 153] or for bacterial walls [61]. Previously developed mathematical models (the brush model [59, 60] and the non-Hertzian point-wise approach [56]) were therefore used to discern the contribution of the glycocalyx from the cell body material properties. No agreement was found on the glycocalyx properties computed for the different indenters and different fitting models. Therefore, it was not possible to confidently extract any quantitative finding from the acquired data, as it was not possible to show that the glycocalyx was sensed by the probe and to fully satisfy the assumptions of the employed models.

A different experimental approach was therefore selected to study the single glycocalyx molecule contribution to mechanotransduction. This involved performing AFM single molecule force spectroscopy on HA molecules and analysing the attachment of the targeted molecules to the actin cytoskeleton. HA molecules anchored to the cytoskeleton could be distinguished by the spring-like response to pulling and were considered to represent examples of *decentralised* mechanosensing, with the transmission of mechanical stimuli from the glycocalyx to the inner cell compartments, i.e. the cytoskeleton, and therefore at sites distinct from the cell surface [4, 182]. HA molecules not anchored to the cytoskeleton presented the force plateaus typical of membrane tethers and would exemplify cases of *centralised* mechanosensing, with the glycocalyx molecules directly connected to

areas of the membrane where an abundance of signalling molecules resides [4]. Events representing multiple probe-molecule interactions also occurred and they were hypothesised to relate to the formation of tethers with an actin core, similar to the microvilli-like structures observed for cells over-expressing HA synthases and hypothesised to have a signalling role [67, 173, 176, 177].

As a further tool to explore bone cell mechanical properties, a single cell FE model was built. This was based on the confocal images of a pre-osteocyte cell and included different cell components, namely the nucleus, cytoplasm, actin cortex and actin fibres. An AFM nano-indentation experiment was simulated by compressing the single cell with a spherical bead in different locations. Similarly to what was observed experimentally, different stiffness values were computed for the nucleus and periphery depending on the cell components involved and on their geometrical organisation. The strain distribution was analysed, highlighting the role of the actin cytoskeleton similarly to that reported from experimental data, as reviewed in [43].

8.2 LIMITATIONS AND FUTURE DIRECTIONS

For AFM nano-indentation measures in the present study, an effort was made to reduce experimental error by carefully controlling protocols and post-processing. One aspect that was not taken into consideration was the calibration step for cantilever characterisation, which was not optimised in this context but performed with the conventional procedure of recording a force curve on a bare region of the substrate and using the built-in AFM microscope application to obtain information on the cantilever sensitivity and spring constant. Recently, however, a multicentre study aimed at standardising AFM procedures for soft biological samples detected an important source of experimental error in this step [207]. In particular, they found that the erroneous cantilever sensitivity determination was a major cause of discrepancies in the results between different labs, both for soft gels and cells. A new standardised procedure was therefore proposed to calculate the correct deflection sensitivity from thermal fluctuations of the free cantilever with an independently determined value for the spring constant obtained with a vibrometer.

The systematic use of similar procedures might in the future improve the previ-

ously reported issues of comparing results in cells mechanical properties obtained with different protocols [40, 207]. This experimental error was however overlooked in the present work and therefore might have caused not fully repeatable results. In future works, similar standardised methodologies should be incorporated as they would help to ascribe the correct degree of variability to cell physiological heterogeneity, further reducing the experimental inaccuracies. The considerations of a suitable sample size and data representation discussed in the present thesis remain however valid and highlight the need for common procedures for AFM nano-indentation of biological samples.

All the measurements performed in the present work for cell mechanical properties focused on the cell stiffness represented by the Young's modulus and therefore on the elastic material characterisation. The viscoelastic characteristics of cells are however a key factor in the regulation of various cell processes [208, 209] and their understanding would provide better insights on mechanotransduction. AFM has been used to characterise cell viscoelasticity by superimposing a low-amplitude sinusoidal oscillation to an initial cell indentation and by analysing the cell time-dependent response [209]. This methodology was used for example to study human lung epithelial cell response to cyclic breathing stimulation [210] or to correlate the local viscoelastic properties of the lamellipodium and its speed of extension in the context of cancer cell motility [211]. Dynamic AFM techniques were also proposed to obtain local stiffness, stiffness gradient and viscoelastic dissipation parameters in high throughput cell property mapping by combined use of the zeroth, first and second harmonics of cantilever vibration [212].

A future development of the presented protocol might incorporate the measurement of viscoelastic properties of bone cells by AFM nano-indentation coupled with oscillation. This further characterisation could be also used for the single cell computational model, defining additional material properties which could change the simulated strain transmission. A local mapping such as the one proposed in [212] would, in addition, provide information on the spatial heterogeneity within a single cell, which was neglected in the present study.

Cell lines were used in this study. This appeared to be a convenient choice to obtain repeatable results on controlled cell populations. When studying the changes in mechanical properties during bone differentiation it, however, became

clear that it was not straightforward to associate a cell line with a specific phase of differentiation. Moreover, large variations were observed in cell shape within a single population, suggesting some degree of phenotype variability. Concerns about the use of cell lines were previously expressed [213]. Firstly, the cell lines might not be representative of the primary cell counterpart despite showing analogous functional features, due to the often not fully characterised properties of a given primary population. Moreover, serial passage as part of cell banking procedures or cross cell contamination might cause genotypic and phenotypic variations, resulting in a genetic drift from the original cell line.

Good cell culture practice was observed when handling the cells used in the present study. However, no verification of the genetic profiling was performed to check if a given cell population would ascribe to the stated cell type. Standard methods to perform this analysis would include karyotyping, isoenzyme analysis and mitochondrial DNA typing [214]. This made it difficult to test the hypothesis formulated in the bone differentiation study, for which the non-monotonic relationship between osteocytogenesis stages and mechanical properties was linked to an overlap between different cell populations in terms of differentiation stages. Further work in this direction could include obtaining genetic profiles of the cell lines used or evaluating cells biochemically differentiated from a progenitor population.

It was not possible to confidently discern the mechanical properties of the glycocalyx with the protocol used in the present study. The use of mathematical models was challenging not having observed a clear two-layer behaviour of the cell and glycocalyx and therefore needing to rely on model assumptions not easily verifiable in this context. Different methodologies could be employed to complement AFM results, such as reflectance interference contrast microscopy [215] or passive micro-rheology [216], which has been previously used to test the mechanical properties of the endothelial glycocalyx. In reflectance interference contrast microscopy, the relative movement of two reflecting surfaces are tracked. The light interference pattern created by the reflections of a glass bead fluctuating over the cells in culture and of the culture coverslip itself can be evaluated as a measure of the stiffness of the glycocalyx layer [215]. In passive micro-rheology experiments, the thermal fluctuations of optically trapped colloidal particles are measured. In-

dentations of the glycocalyx could be performed by manipulating the particle position to measure its shear elastic and viscous moduli [216].

A different approach to characterise the mechanical properties of the glycocalyx by AFM would be a relative measure between an untreated control and a sample in which the glycocalyx was enzymatically degraded. Similar techniques were employed before for the endothelial glycocalyx in [55–57]. A drawback of this approach would be the difficulty of choosing which glycocalyx molecules to target with the degrading enzymes, as the bone glycocalyx composition is not fully characterised. The associated risk would be to selectively remove only some of the glycocalyx components and therefore underestimate its mechanical contribution.

Some of the challenges related to the mechanical characterisation of the bone glycocalyx could, therefore, relate to the lack of information on its composition and structure. HA [29], perlecan [38], decorin [32] and biglycan [33] have all been detected as bone glycocalyx components, but the ways in which these molecules interact is still not fully elucidated. Moreover, cells at different stages of bone differentiation might express different glycocalyx compositions. A thorough characterisation might help to predict what mechanical property ranges might be expected and therefore aiding selecting the most suitable experimental methodology. This could also facilitate the modelling tasks and therefore a better understanding of the mechanotransduction role of the bone glycocalyx.

Single molecule force spectroscopy experiments were carried out on the HA coating of bone cells to evaluate the attachment of the HA molecules to the cytoskeleton. Different underlying mechanotransduction mechanisms involving HA were hypothesised depending on the anchoring characteristics. Future work might be directed towards experimental testing of these hypotheses. HA synthases or the ERM proteins which are hypothesised as cytoskeleton linkers could be inhibited to evaluate the correspondent occurrence of rupture events. Moreover, recently developed advanced imaging techniques have been used for subcellular processes visualisation. Fluorescence-resonance energy transfer (FRET) technology, for example, exploits a quantum mechanics phenomenon where two fluorescent proteins have an energy transfer when close to each other at given relative angles to study molecular signals at subcellular levels in live cells [217]. In the context of mechanotransduction, FRET imaging was used to analyse relevant signalling mo-

lecules, such as calcium signalling and pathways associated with cytoskeleton remodelling. Moreover, FRET-based force sensors able to detect intracellular tension were also designed, relying on the unfolding of proteins at strategic cell locations such as focal adhesions or adherens junctions [218].

A multi-structural FE model of a single cell was designed and used to simulate AFM nano-indentation experiments. The importance of an accurate cell geometry was highlighted, particularly in terms of the arrangement of the different components. Future works might concentrate on the design of more single cell models to evaluate the variability of calculated stiffness values for simulated populations. This could be achieved by building additional models with the methodology described in this work, however, this might be time-consuming due to the image segmentation process. A different approach would be to use statistical shape modelling methods [219]. To build these models, a training image set of example objects is first considered and labelled for relevant points. The statistical variation of these points is then studied and used as a flexible shape template to build multiple models. Similar methods were employed in combination with FE in a range of applications, for example for bone modelling aimed at skeleton disease research [220] or for tissue specific models including simplified cell geometries to represent the biphasic mechanics of chondrocytes [221].

The single cell model designed in this context could also be employed to simulate different loading scenarios relevant to study bone mechanotransduction, such as matrix strain, hydraulic pressure or interstitial fluid flow driven by bone matrix deformation [16, 18]. If combined with the addition of the glycocalyx layer, fluid shear stress could be simulated to quantify the magnitude of mechanical stimulation detected at the cell surface. Such simulations could help elucidate the hypothesised role of the bone glycocalyx fibres as tethering elements acting as strain-amplifiers in respect to the cell membrane and cytoskeleton in osteocytes [20, 28].

8.3 SUMMARY AND CONCLUSIONS

The present thesis focused on the mechanical characterisation of bone cells and their glycocalyx. A combined experimental and computational approach was employed with the use of atomic force microscopy and finite element modelling. Ex-

perimental protocols were designed to test cells by nano-indentation and to target hyaluronic acid molecules by single molecule force spectroscopy. A computational framework was developed describing a multi-structural single cell model with realistic geometry.

The key findings of the present work are summarised below.

- The cell populations showed a wide degree of variation in terms of stiffness. Suitable sample sizes were needed to capture this heterogeneity and stiffness distributions should be preferred over stiffness average values to represent mechanical properties data.
- The mechanical properties of the bone glycocalyx could not be extracted by atomic force microscopy nano-indentation of cells. Better characterisation of the bone glycocalyx structure and components will help optimise experimental protocols for this aim.
- The cell lines representing different stages of bone differentiation showed changes in cell stiffness, although the expected monotonic relationship between osteocytogenesis stages and mechanical properties was not found due to the overlap of differentiation stages between the selected cell lines.
- Hyaluronic acid, a main component of the bone glycocalyx, was targeted by single molecule force spectroscopy using the hyaluronic acid binding protein. The hyaluronic acid selective bind to the cytoskeleton was observed and possible mechanotransduction mechanisms were proposed depending on the observed cytoskeleton anchoring.
- Finite element modelling of single cell showed different stiffness values for indenting locations over different cell components. The modelled actin cytoskeleton was involved in withstanding compression and distributing strain within the cell.

Bibliography

- [1] F J Alenghat and D E Ingber. Mechanotransduction All Signals Point to Cytoskeleton, Matrix, and Integrins. *Science's stake: signal transduction knowledge environment*, February 1, 2002.
- [2] E H Burger and J Klein-Nulend. Mechanotransduction in bone — role of the lacuno- canalicular network. *The FASEB Journal*, 13:101–112, 1999.
- [3] B D Hoffman, C Grashoff, and M Schwartz. Dynamic molecular processes mediate cellular mechanotransduction. *Nature*, 475:316–323, 2011.
- [4] J M Tarbell and M Y Pahakis. Mechanotransduction and the glycocalyx. *Journal of Internal Medicine*, 259(4):339–350, Apr 2006.
- [5] D M Knapik, P Perera, J Nam, A D Blazek, B Rath, B Leblebicioglu, H Das, L C Wu, T E Hewett, S K Agarwal, A G Robling, D C Flanigan, B S Lee, and S Agarwal. Mechanosignaling in bone health, trauma and inflammation. *Antioxidants & redox signaling*, 20(6):970–85, 2014.
- [6] J Li, R L Duncan, D B Burr, and C H Turner. L-type calcium channels mediate mechanically induced bone formation in vivo. *Journal of bone and mineral research : the official journal of the American Society for Bone and Mineral Research*, 17(10):1795–1800, 2002.
- [7] P P Cherain, A J Siller-Jackson, S Gu, X Wang, L F Bonewald, E Sprague, and J X Jiang. Mechanical Strain Opens Connexin 43 Hemichannels in Osteocytes: A Novel Mechanism for the Release of Prostaglandin. *Molecular biology of the cell*, 16(July):3100–3106, 2005.
- [8] A Neve, A Corrado, and F P Cantatore. Osteocytes: Central conductors of bone biology in normal and pathological conditions. *Acta Physiologica*, 204:317–330, 2012.
- [9] D Shin and K Athanasiou. Cytoindentation for obtaining cell biomechanical properties. *Journal of orthopaedic research : official publication of the Orthopaedic Research Society*, 17(9):880–890, 1999.

- [10] P C Braga and D Ricci. *Atomic Force Microscopy in Biomedical Research: Methods and Protocols*, volume 736. Springer Science+Business Media, 2011.
- [11] B Alberts, A Johnson, J Lewis, M Raff, K Roberts, and P Walter. *Molecular Biology of the Cell*. Garland Science, New York, 4th edition edition, 2002.
- [12] S Marcotti and G C Reilly. Sugar-coating the cell: The Role of the Glycocalyx in Mechanobiology. In Simon C. F. Rawlinson, editor, *Mechanobiology: Exploitation for Medical Benefit*, chapter 3, pages 43–54. Wiley-Blackwell, 2017.
- [13] S F Gilbert. *Developmental Biology*. Sinauer Associates, Sunderland (MA), 6th edition edition, 2000.
- [14] R Florencio-Silva, G Sasso Rodrigues Da Silva, E Sasso-Cerri, M J Simões, and P S Cerri. Biology of Bone Tissue: Structure, Function, and Factors That Influence Bone Cells. *BioMed Research International*, 2015, 2015.
- [15] C Crowder and S D Stout, editors. *Bone histology: an anthropological perspective*. CRC Press - Taylor and Francis group, Boca Raton (FL), 2012.
- [16] S P Fritton and S Weinbaum. Fluid and Solute Transport in Bone: Flow-Induced Mechanotransduction. *Annual Review of Fluid Mechanics*, 41(1):347–374, Jan 2009.
- [17] Y Qin and M Hu. Mechanotransduction in musculoskeletal tissue regeneration: effects of fluid flow, loading, and cellular-molecular pathways. *Bio-Med research international*, 2014:863421, Jan 2014.
- [18] J Klein-Nulend, R G Bacabac, and A D Bakker. Mechanical loading and how it affects bone cells: The role of the osteocyte cytoskeleton in maintaining our skeleton. *European Cells and Materials*, 24:278–291, 2012.
- [19] J A Siddiqui and N C Partridge. Physiological Bone Remodeling: Systemic Regulation and Growth Factor Involvement. *Physiology*, 31:233–245, 2016.
- [20] S Weinbaum, S C Cowin, and Y Zeng. A model for the excitation of osteocytes by mechanical loading-induced bone fluid shear stresses. *Journal of Biomechanics*, 27(3):339–360, 1994.
- [21] J Klein-Nulend, A van der Plas, C M Semeins, N E Ajubi, J A Frangos, P J Nijweide, and E H Burger. Sensitivity of osteocytes to biomechanical stress

in vitro. *The FASEB journal : official publication of the Federation of American Societies for Experimental Biology*, 9:441–445, 1995.

- [22] J You, Clare E Yellowley, H J Donahue, Y Zhang, Q Chen, and C R Jacobs. Substrate Deformation Levels Associated With Routine Physical Activity Are Less Stimulatory to Bone Cells Relative to Loading-Induced Oscillatory Fluid Flow. *Journal of biomechanical engineering*, 122:387–393, 2000.
- [23] J M Squire, M Chew, G Nneji, C Neal, J Barry, and C Michel. Quasi-periodic substructure in the microvessel endothelial glycocalyx: a possible explanation for molecular filtering? *Journal of structural biology*, 136(3):239–255, Dec 2001.
- [24] S Weinbaum, X Zhang, Y Han, H Vink, and S C Cowin. Mechanotransduction and flow across the endothelial glycocalyx. *Proceedings of the National Academy of Sciences of the United States of America*, 100(13):7988–7995, 2003.
- [25] J M Tarbell. Shear stress and the endothelial transport barrier. *Cardiovascular Research*, 87:320–330, 2010.
- [26] F E Curry and R H Adamson. Endothelial glycocalyx: Permeability barrier and mechanosensor. *Annals of Biomedical Engineering*, 40(4):828–839, 2012.
- [27] S Weinbaum, Y Duan, M M Thi, and L You. An Integrative Review of Mechanotransduction in Endothelial, Epithelial (Renal) and Dendritic Cells (Osteocytes). *Cell Mol Bioeng*, 4(4):510–537, 2011.
- [28] L You, S C Cowin, M B Schaffler, and S Weinbaum. A model for strain amplification in the actin cytoskeleton of osteocytes due to fluid drag on pericellular matrix. *Journal of Biomechanics*, 34:1375–1386, 2001.
- [29] G C Reilly, T R Haut, C E Yellowley, H J Donahue, and C R Jacobs. Fluid flow induced PGE 2 release by bone cells is reduced by glycocalyx degradation whereas calcium signals are not. *Biorheology*, 40:591–603, 2003.
- [30] S Burra, D P Nicolella, W L Francis, C J Freitas, N J Mueschke, K Poole, and J X Jiang. Dendritic processes of osteocytes are mechanotransducers that induce the opening of hemichannels. *Proceedings of the National Academy of Sciences of the United States of America*, 107(31):13648–13653, Aug 2010.
- [31] H L Morris, C I Reed, J W Haycock, and G C Reilly. Mechanisms of fluid-flow-induced matrix production in bone tissue engineering. *Proceedings of*

the Institution of Mechanical Engineers. Part H, Journal of engineering in medicine, 224(12):1509–1521, Dec 2010.

- [32] R T Ingram, B L Clarke, L W Fisher, and L A Fitzpatrick. Distribution of noncollagenous proteins in the matrix of adult human bone: evidence of anatomic and functional heterogeneity. *Journal of bone and mineral research: the official journal of the American Society for Bone and Mineral Research*, 8:1019–1029, 1993.
- [33] M Takagi, M Maeno, a Kagami, Y Takahashi, and K Otsuka. Biochemical and immunocytochemical characterization of mineral binding proteoglycans in rat bone. *The journal of histochemistry and cytochemistry : official journal of the Histochemistry Society*, 39(1):41–50, Jan 1991.
- [34] M Y Pahakis, J R Kosky, R O Dull, and J M Tarbell. The role of endothelial glycocalyx components in mechanotransduction of fluid shear stress. *Biochemical and Biophysical Research Communications*, 355:228–233, 2007.
- [35] R Kumagai, X Lu, and G S Kassab. Role of glycocalyx in flow-induced production of nitric oxide and reactive oxygen species. *Free Radical Biology and Medicine*, 47(5):600–607, 2009.
- [36] E Zimmerman, B Geiger, and L Addadi. Initial stages of cell-matrix adhesion can be mediated and modulated by cell-surface hyaluronan. *Biophysical journal*, 82(April):1848–1857, 2002.
- [37] L M McNamara, R J Majeska, S Weinbaum, V Friedrich, and M B Schaffler. Attachment of osteocyte cell processes to the bone matrix. *Anatomical Record*, 292(November 2008):355–363, 2009.
- [38] W R Thompson, S Modla, B J Grindel, K J Czymmek, C B Kirn-Safran, L Wang, R L Duncan, and M C Farach-Carson. Perlecan/Hspg2 deficiency alters the pericellular space of the lacunocanalicular system surrounding osteocytic processes in cortical bone. *Journal of Bone and Mineral Research*, 26(3):618–629, 2011.
- [39] K D Costa. Single-cell elastography: probing for disease with the atomic force microscope. *Disease markers*, 19:139–154, 2004.
- [40] T G Kuznetsova, M N Starodubtseva, N I Yegorenkov, S A Chizhik, and R I Zhdanov. Atomic force microscopy probing of cell elasticity. *Micron*, 38(8):824–833, 2007.

- [41] D J Müller and Y F Dufrêne. Atomic force microscopy: A nanoscopic window on the cell surface. *Trends in Cell Biology*, 21(8):461–469, 2011.
- [42] H Hertz. Über die Berührung fester elastischer Körper. *J. die Reine Angewandte Mathematik*, 92:156–171, 1881.
- [43] Q Luo, D Kuang, B Zhang, and G Song. Cell stiffness determined by atomic force microscopy and its correlation with cell motility. *Biochimica et Biophysica Acta - General Subjects*, 1860(9):1953–1960, 2016.
- [44] E Takai, K D Costa, A Shaheen, C T Hung, and X E Guo. Osteoblast elastic modulus measured by atomic force microscopy is substrate dependent. *Annals of Biomedical Engineering*, 33(7):963–971, 2005.
- [45] G M Kelly, J I Kilpatrick, M H van Es, P P Weafer, P J Prendergast, and S P Jarvis. Bone cell elasticity and morphology changes during the cell cycle. *Journal of Biomechanics*, 44(8):1484–1490, 2011.
- [46] R Subbiah, M Suhaeri, M P Hwang, W Kim, and K Park. Investigation of the changes of biophysical/mechanical characteristics of differentiating preosteoblasts in vitro. *Biomaterials Research*, 19(1):24, 2015.
- [47] I Titushkin and M Cho. Modulation of cellular mechanics during osteogenic differentiation of human mesenchymal stem cells. *Biophysical journal*, 93(10):3693–702, 2007.
- [48] T Bongiorno, J Kazlow, R Mezencev, S Griffiths, R Olivares-Navarrete, J F McDonald, Z Schwartz, B D Boyan, T C McDevitt, and T Sulchek. Mechanical stiffness as an improved single-cell indicator of osteoblastic human mesenchymal stem cell differentiation. *Journal of Biomechanics*, 47(9):2197–2204, 2014.
- [49] G Yourek, M A Hussain, and J J Mao. Cytoskeletal changes of mesenchymal stem cells during differentiation. *ASAIO journal (American Society for Artificial Internal Organs : 1992)*, 53(2):219–28, 2014.
- [50] D Docheva, D Padula, C Popov, W Mutschler, H Clausen-Schaumann, and M Schieker. Researching into the cellular shape, volume and elasticity of mesenchymal stem cells, osteoblasts and osteosarcoma cells by atomic force microscopy: Stem Cells. *Journal of Cellular and Molecular Medicine*, 12(2):537–552, 2008.
- [51] P Muthukumar, C T Lim, and T Lee. Estradiol influences the mechanical properties of human fetal osteoblasts through cytoskeletal changes. *Biochemical and Biophysical Research Communications*, 423(3):503–508, 2012.

- [52] Y Sugawara, R Ando, H Kamioka, Y Ishihara, S A Murshid, K Hashimoto, N Kataoka, K Tsujioka, F Kajiya, T Yamashiro, and T Takano-Yamamoto. The alteration of a mechanical property of bone cells during the process of changing from osteoblasts to osteocytes. *Bone*, 43:19–24, 2008.
- [53] R G Bacabac, D Mizuno, C F Schmidt, F C MacKintosh, J J W A Van Loon, J Klein-Nulend, and T H Smit. Round versus flat: Bone cell morphology, elasticity, and mechanosensing. *Journal of Biomechanics*, 41(7):1590–1598, 2008.
- [54] H Oberleithner, K Peters, Wland Kusche-Vihrog, S Korte, H Schillers, K Kliche, and K Oberleithner. Salt overload damages the glycocalyx sodium barrier of vascular endothelium. *Pflugers Archiv European Journal of Physiology*, 462:519–528, 2011.
- [55] A Wiesinger, W Peters, D Chappell, D Kentrup, S Reuter, H Pavenstädt, H Oberleithner, and P Kümpers. Nanomechanics of the endothelial glycocalyx in experimental sepsis. *PloS one*, 8(11):e80905, Jan 2013.
- [56] R O’Callaghan, K M Job, R O Dull, and V Hlady. Stiffness and heterogeneity of the pulmonary endothelial glycocalyx measured by atomic force microscopy. *American journal of physiology. Lung cellular and molecular physiology*, 301(3):L353–L360, Sep 2011.
- [57] K Bai and W Wang. Spatio-temporal development of the endothelial glycocalyx layer and its mechanical property in vitro. *Journal of the Royal Society, Interface / the Royal Society*, 9(74):2290–8, Sep 2012.
- [58] G Marsh and R E Waugh. Quantifying the mechanical properties of the endothelial glycocalyx with atomic force microscopy. *Journal of visualized experiments : JoVE*, page e50163, 2013.
- [59] I Sokolov, S Iyer, V Subba-Rao, R M Gaikwad, and C D Woodworth. Detection of surface brush on biological cells in vitro with atomic force microscopy. *Applied Physics Letters*, 91, 2007.
- [60] I Sokolov, M E Dokukin, and N V Guz. Method for quantitative measurements of the elastic modulus of biological cells in AFM indentation experiments. *Methods (San Diego, Calif.)*, 60(2):202–13, Apr 2013.
- [61] R G Bailey, R D Turner, N Mullin, N Clarke, S J Foster, and J K Hobbs. The Interplay between Cell Wall Mechanical Properties and the Cell Cycle in *Staphylococcus aureus*. *Biophysical journal*, 107:2538–2545, 2014.

- [62] T E Fisher, P E Marszalek, and J M Fernandez. Stretching single molecules into novel conformations using the atomic force microscope. *Nature structural biology*, 7(9):719–24, 2000.
- [63] H Clausen-Schaumann, M Seitz, R Krautbauer, and H E Gaub. Force spectroscopy with single bio-molecules. *Current Opinion in Chemical Biology*, 4(5):524–530, 2000.
- [64] S S Wijeratne, J R Martinez, B J Grindel, E W Frey, J Li, L Wang, M C Farach-Carson, and C Kiang. Single molecule force measurements of perlecan/HSPG2: A key component of the osteocyte pericellular matrix. *Matrix Biology*, pages 1–12, 2015.
- [65] M Sun, J S Graham, B Hegedüs, F Marga, Y Zhang, G Forgacs, and M Grandbois. Multiple membrane tethers probed by atomic force microscopy. *Biophysical journal*, 89:4320–9, 2005.
- [66] R F Thorne, J W Legg, and C M Isacke. The role of the CD44 transmembrane and cytoplasmic domains in co-ordinating adhesive and signalling events. *Journal of cell science*, 117(Pt 3):373–80, Jan 2004.
- [67] A Kultti, K Rilla, R Tiihonen, A P Spicer, R H Tammi, and M I Tammi. Hyaluronan synthesis induces microvillus-like cell surface protrusions. *Journal of Biological Chemistry*, 281(23):15821–15828, 2006.
- [68] E M Puchner and H E Gaub. Force and function: probing proteins with AFM-based force spectroscopy. *Current Opinion in Structural Biology*, 19(5):605–614, 2009.
- [69] A Vaziri and A Gopinath. Cell and biomolecular mechanics in silico. *Nature materials*, 7:15–23, 2008.
- [70] D L Logan. *A First Course In The Finite Element Method*. Nelson (Thomson Canada Limited), Toronto, Canada, fourth edition edition, 2007.
- [71] O C Zienkiewicz, R L Taylor, and J Z Zhu. *The Finite Element Method: Its Basis and Fundamentals*. Elsevier Ltd, seventh ed edition, 2013.
- [72] S M Mijailovich, M Kojic, M Zivkovic, B Fabry, and J J Fredberg. A finite element model of cell deformation during magnetic bead twisting. *J Appl Physiol*, 93:1429–1436, 2002.
- [73] H Karcher, J Lammerding, H Huang, R T Lee, R D Kamm, and M R Kaazempur-Mofrad. A Three-Dimensional Viscoelastic Model for

- Cell Deformation with Experimental Verification. *Biophysical Journal*, 85(November):3336–3349, 2003.
- [74] J G McGarry and P J Prendergast. A three-dimensional finite element model of an adherent eukaryotic cell. *European cells & materials*, 7(2000):27–33; discussion 33–34, 2004.
- [75] S Barreto, C H Clausen, C M Perrault, D A Fletcher, and D Lacroix. A multi-structural single cell model of force-induced interactions of cytoskeletal components. *Biomaterials*, 34(26):6119–6126, Aug 2013.
- [76] Y Yao, D Lacroix, and A F T Mak. Effects of oxidative stress-induced changes in the actin cytoskeletal structure on myoblast damage under compressive stress: confocal-based cell-specific finite element analysis. *Biomechanics and Modeling in Mechanobiology*, 2016.
- [77] J G McGarry, J Klein-Nulend, M G Mullender, and P J Prendergast. A comparison of strain and fluid shear stress in stimulating bone cell responses—a computational and experimental study. *FASEB journal*, 19(3), 2005.
- [78] G T Charras and M A Horton. Determination of cellular strains by combined atomic force microscopy and finite element modeling. *Biophysical journal*, 83(2):858–879, 2002.
- [79] M C Ferko, A Bhatnagar, M B Garcia, and P J Butler. Finite-element stress analysis of a multicomponent model of sheared and focally-adhered endothelial cells. *Annals of Biomedical Engineering*, 35(2):208–223, 2007.
- [80] N Slomka and A Gefen. Confocal microscopy-based three-dimensional cell-specific modeling for large deformation analyses in cellular mechanics. *Journal of Biomechanics*, 43(9):1806–1816, 2010.
- [81] L Pelkmans. Using Cell-to-Cell Variability— A New Era in Molecular Biology. *Science*, 336(April):425–6, 2012.
- [82] T Krieger and B D Simons. Dynamic stem cell heterogeneity. *Development*, 142(8):1396–1406, 2015.
- [83] M Crisan and E Dzierzak. The many faces of hematopoietic stem cell heterogeneity. *Development*, 143:4571–4581, 2016.
- [84] P Satir. Chirality of the cytoskeleton in the origins of cellular asymmetry. *Philosophical Transactions of the Royal Society B: Biological Sciences*, 371, 2016.

- [85] H Ema, Y Morita, and T Suda. Heterogeneity and hierarchy of hematopoietic stem cells. *Experimental Hematology*, 42(2):74–82, 2014.
- [86] M Esteve Ràfols. Adipose tissue: cell heterogeneity and functional diversity. *Endocrinología y nutrición : órgano de la Sociedad Española de Endocrinología y Nutrición*, 61(2):100–12, 2014.
- [87] Q F Wills, E Mellado-Gomez, R Nolan, D Warner, E Sharma, J Broxholme, B Wright, H Lockstone, W James, M Lynch, M Gonzales, J West, A Leyrat, S Padilla-Parra, S Filippi, C Holmes, M D Moore, and R Bowden. The nature and nurture of cell heterogeneity: accounting for macrophage gene-environment interactions with single-cell RNA-Seq. *BMC Genomics*, 18:53, 2017.
- [88] B Wickstead and K Gull. The evolution of the cytoskeleton. *Journal of Cell Biology*, 194(4):513–525, 2011.
- [89] E Moeendarbary and A R Harris. Cell mechanics: Principles, practices, and prospects. *Wiley Interdisciplinary Reviews: Systems Biology and Medicine*, 6(5):371–388, 2014.
- [90] C Rotsch and M Radmacher. Drug-induced changes of cytoskeletal structure and mechanics in fibroblasts: an atomic force microscopy study. *Biophysical journal*, 78(1):520–535, 2000.
- [91] A M Collinsworth, S Zhang, W E Kraus, and G A Truskey. Apparent elastic modulus and hysteresis of skeletal muscle cells throughout differentiation. *American journal of physiology. Cell physiology*, 283(4):C1219–C1227, 2002.
- [92] M E Grady, R J Composto, and D M Eckmann. Cell elasticity with altered cytoskeletal architectures across multiple cell types. *Journal of the Mechanical Behavior of Biomedical Materials*, 61:197–207, 2016.
- [93] M Lekka. Discrimination Between Normal and Cancerous Cells Using AFM. *BioNanoScience*, 6(1):65–80, 2016.
- [94] M Nagayama, H Haga, and K Kawabata. Drastic change of local stiffness distribution correlating to cell migration in living fibroblasts. *Cell Motility and the Cytoskeleton*, 50(4):173–179, 2001.
- [95] H Sato, N Kataoka, F Kajiyama, M Katano, T Takigawa, and T Masuda. Kinetic study on the elastic change of vascular endothelial cells on collagen matrices by atomic force microscopy. *Colloids and Surfaces B: Biointerfaces*, 34(2):141–146, 2004.

- [96] T K Berdyeva, C D Woodworth, and I Sokolov. Human epithelial cells increase their rigidity with ageing in vitro : direct measurements. *Physics in Medicine and Biology*, 50(1):81–92, Jan 2005.
- [97] Y W Chiou, H K Lin, M J Tang, H H Lin, and M L Yeh. The Influence of Physical and Physiological Cues on Atomic Force Microscopy-Based Cell Stiffness Assessment. *PLoS ONE*, 8(10), 2013.
- [98] N V Guz, S J Patel, M E Dokukin, B Clarkson, and I Sokolov. AFM study shows prominent physical changes in elasticity and pericellular layer in human acute leukemic cells due to inadequate cell–cell communication. *Nanotechnology*, 27(49):494005–017, 2016.
- [99] L Ming-Han, C Yon-Hong, and Z Yue. Cellular mechanical properties reflect the differentiation potential of nucleus pulposus-derived progenitor cells. *Am J Transl Res*, 8(10):4446–4454, 2016.
- [100] M Li, L Liu, X Xiao, N Xi, and Y Wang. Viscoelastic Properties Measurement of Human Lymphocytes by Atomic Force Microscopy Based on Magnetic Beads Cell Isolation. *IEEE Transactions on Nanobioscience*, 15(5):398–411, 2016.
- [101] Y Kato, A Boskey, L Spevak, M Dallas, M Hori, and L F Bonewald. Establishment of an osteoid preosteocyte-like cell MLO-A5 that spontaneously mineralizes in culture. *Journal of bone and mineral research : the official journal of the American Society for Bone and Mineral Research*, 16(9):1622–33, Sep 2001.
- [102] R M Delaine-Smith, S MacNeil, and G C Reilly. Matrix production and collagen structure are enhanced in two types of osteogenic progenitor cells by a simple fluid shear stress stimulus. *European Cells and Materials*, 24:162–174, 2012.
- [103] R M Delaine-Smith, A Sittichokechaiwut, and G C Reilly. Primary cilia respond to fluid shear stress and mediate flow-induced calcium deposition in osteoblasts. *FASEB journal : official publication of the Federation of American Societies for Experimental Biology*, 28(1):430–9, Jan 2014.
- [104] P Carl and H Schillers. Elasticity measurement of living cells with an atomic force microscope: data acquisition and processing. *Pflügers Archiv - European Journal of Physiology*, 457(2):551–559, 2008.
- [105] J L Hutter and J Bechhoefer. Calibration of atomic-force microscope tips. *Review of Scientific Instruments*, 64(7):1868–1873, 1993.

- [106] N Gavara. Combined strategies for optimal detection of the contact point in AFM force-indentation curves obtained on thin samples and adherent cells. *Nature Publishing Group*, 6:21267:1–13, 2016.
- [107] N Guz, M Dokukin, V Kalaparthy, and I Sokolov. If Cell Mechanics Can Be Described by Elastic Modulus: Study of Different Models and Probes Used in Indentation Experiments. *Biophysical Journal*, 107(3):564–575, 2014.
- [108] K D Costa, A J Sim, and F C P Yin. Non-Hertzian approach to analyzing mechanical properties of endothelial cells probed by atomic force microscopy. *Journal of biomechanical engineering*, 128(April 2006):176–184, 2006.
- [109] C A Schneider, W S Rasband, and K W Eliceiri. NIH Image to ImageJ: 25 years of image analysis. *Nature Methods*, 9(7):671–675, 2012.
- [110] D Grayson. Some Myths and Legends in Quantitative Psychology. *Understanding Statistics*, 3(2):101–134, 2004.
- [111] J Cohen. A power primer. *Psychological Bulletin*, 112(1):155–159, 1992.
- [112] M Zhao, C Srinivasan, D J Burgess, and B D Huey. Rate- and depth-dependent nanomechanical behavior of individual living Chinese hamster ovary cells probed by atomic force microscopy. *Journal of Materials Research*, 21(8):1906–1912, 2006.
- [113] E K Dimitriadis, F Horkay, J Maresca, B Kachar, and R S Chadwick. Determination of elastic moduli of thin layers of soft material using the atomic force microscope. *Biophysical journal*, 82(5):2798–2810, 2002.
- [114] E Spedden and C Staii. Neuron biomechanics probed by atomic force microscopy. *International Journal of Molecular Sciences*, 14(8):16124–16140, 2013.
- [115] L Puricelli, M Galluzzi, C Schulte, A Podestà, and P Milani. Nanomechanical and topographical imaging of living cells by atomic force microscopy with colloidal probes. *Review of Scientific Instruments*, 86(3), 2015.
- [116] H Liu, Y Sun, and C A Simmons. Determination of local and global elastic moduli of valve interstitial cells cultured on soft substrates. *Journal of biomechanics*, 46(11):1967–71, Jul 2013.
- [117] M Lekka, P Laidler, D Gil, J Lekki, Z Stachura, and a Z Hryniewicz. Elasticity of normal and cancerous human bladder cells studied by scanning force microscopy. *European biophysics journal : EBJ*, 28(4):312–316, 1999.

- [118] I N Sneddon. The relation between load and penetration in the axisymmetric Boussinesq problem for a punch of arbitrary profile. *International Journal of Engineering Science*, 3(1):47–57, 1965.
- [119] K L Johnson, K Kendall, and A D Roberts. Surface Energy and the Contact of Elastic Solids. *Proceedings of the Royal Society A: Mathematical, Physical and Engineering Sciences*, 324(1558):301–313, 1971.
- [120] B V Derjaguin, V M Muller, and Y U P Toporov. Effect of contact deformation on the adhesion of particles. *Journal of colloid and interface science*, 52(3):105–108, 1975.
- [121] H Butt, B Cappella, and M Kappl. Force measurements with the atomic force microscope: Technique, interpretation and applications. *Surface Science Reports*, 59(1-6):1–152, 2005.
- [122] G T Charras, P P Lehenkari, and M A Horton. Atomic force microscopy can be used to mechanically stimulate osteoblasts and evaluate cellular strain distributions. *Ultramicroscopy*, 86(1-2):85–95, 2001.
- [123] V Roukos, G Pegoraro, T C Voss, and T Misteli. Cell cycle staging of individual cells by fluorescence microscopy. *Nature Protocols*, 10(2):334–348, 2015.
- [124] M Krzywinski and N Altman. Points of significance: Power and sample size. *Nature Methods*, 10(12):1139–1140, 2013.
- [125] X Chen, J C Love, N E Navin, L Pachter, M J T Stubbington, V Svensson, J V Sweedler, and S A Teichmann. Single-cell analysis at the threshold. *Nature Biotechnology*, 34(11):1111–1118, 2016.
- [126] J C Caicedo, S Cooper, F Heigwer, S Warchal, P Qiu, C Molnar, A S Vasilevich, J D Barry, H S Bansal, O Kraus, M Wawer, L Paavolainen, M D Herrmann, M Rohban, J Hung, H Hennig, J Concannon, I Smith, P A Clemons, S Singh, P Rees, P Horvath, R G Linington, and A E Carpenter. Data-analysis strategies for image-based cell profiling. *Nature Methods*, 14(9):849–863, 2017.
- [127] J M Phillip, P H Wu, D M Gilkes, W Williams, S McGovern, J Daya, J Chen, I Aifuwa, J S H Lee, R Fan, J Walston, and D Wirtz. Biophysical and biomolecular determination of cellular age in humans. *Nature Biomedical Engineering*, 1(7), 2017.

- [128] N Gavara and R S Chadwick. Relationship between cell stiffness and stress fiber amount, assessed by simultaneous atomic force microscopy and live-cell fluorescence imaging. *Biomechanics and Modeling in Mechanobiology*, 15(3):511–523, 2016.
- [129] M C Keeling, L R Flores, A H Dodhy, E R Murray, and N Gavara. Actomyosin and vimentin cytoskeletal networks regulate nuclear shape, mechanics and chromatin organization. *Scientific Reports*, 7(1):5219, 2017.
- [130] A Varki, RD Cummings, JD Esko, HH Freeze, P Stanley, CR Bertozzi, GW Hart, ME Etzler, and (eds.). *Essentials of Glycobiology, 2nd edition*. Cold Spring Harbor Laboratory Press, Cold Spring Harbor (NY), 2nd edition, 2009.
- [131] K J Noonan, J W Stevens, R Tammi, M Tammi, J a Hernandez, and R J Midura. Spatial distribution of CD44 and hyaluronan in the proximal tibia of the growing rat. *Journal of orthopaedic research : official publication of the Orthopaedic Research Society*, 14(4):573–581, 1996.
- [132] E E Ebong, F P Macaluso, D C Spray, and J M Tarbell. Imaging the endothelial glycocalyx in vitro by rapid freezing/freeze substitution transmission electron microscopy. *Arteriosclerosis, thrombosis, and vascular biology*, 31(8):1908–15, Aug 2011.
- [133] S P Evanko, S Potter-Perigo, P Y Johnson, and T N Wight. Organization of hyaluronan and versican in the extracellular matrix of human fibroblasts treated with the viral mimetic poly I:C. *The journal of histochemistry and cytochemistry: official journal of the Histochemistry Society*, 57(11):1041–1060, 2009.
- [134] C A de la Motte and J A Drazba. Viewing hyaluronan: imaging contributes to imagining new roles for this amazing matrix polymer. *The journal of histochemistry and cytochemistry : official journal of the Histochemistry Society*, 59(3):252–257, 2011.
- [135] U Rutishauser, A Acheson, A K Hall, D M Mann, and J Sunshine. The Neural Cell Adhesion Molecule (NCAM) as a Regulator of Cell-Cell Interactions. *Science*, 240(4848):53–57, 1988.
- [136] M Soler, C Merant, C Servant, M Fraterno, C Allasia, J C Lissitzky, P Bongrand, and C Foa. Leukosialin (CD43) behavior during adhesion of human monocytic THP-1 cells to red blood cells. *Journal of leukocyte biology*, 61(5):609–618, 1997.

- [137] M Soler, S Desplat-Jego, B Vacher, L Ponsonnet, M Fraterno, P Bongrand, J M Martin, and C Foa. Adhesion-related glycocalyx study: quantitative approach with imaging-spectrum in the energy filtering transmission electron microscope (EFTEM). *FEBS letters*, 429(1):89–94, 1998.
- [138] S Sabri, M Soler, C Foa, a Pierres, a Benoliel, and P Bongrand. Glycocalyx modulation is a physiological means of regulating cell adhesion. *Journal of cell science*, 113 (Pt 9:1589–1600, 2000.
- [139] H H Lipowsky. The endothelial glycocalyx as a barrier to leukocyte adhesion and its mediation by extracellular proteases. *Annals of Biomedical Engineering*, 40(4):840–848, 2012.
- [140] S Reitsma, D W Slaaf, H Vink, M Van Zandvoort, and M G A Oude Egbrink. The endothelial glycocalyx: Composition, functions, and visualization. *Pflugers Archiv European Journal of Physiology*, 454(3):345–359, 2007.
- [141] S Weinbaum, J M Tarbell, and E R Damiano. The structure and function of the endothelial glycocalyx layer. *Annual review of biomedical engineering*, 9:121–167, 2007.
- [142] M Nieuwdorp, MC Meuwese, H Vink, JBL Hoekstra, JJP Kastelein, and ESG Stroes. The endothelial glycocalyx: a potential barrier between health and vascular disease. *Current Opinion in Lipidology*, 16:507–11, 2005.
- [143] B F Becker, D Chappell, D Bruegger, T Annecke, and M Jacob. Therapeutic strategies targeting the endothelial glycocalyx: Acute deficits, but great potential. *Cardiovascular Research*, 87(2):300–310, 2010.
- [144] M Henrich, M Gruss, and M A Weigand. Sepsis-induced degradation of endothelial glycocalix. *The Scientific World Journal*, 10:917–923, 2010.
- [145] C S Alphonsus and R N Rodseth. The endothelial glycocalyx: A review of the vascular barrier. *Anaesthesia*, 69(7):777–784, Jul 2014.
- [146] H Kolářová, B Ambrúzová, L Svihálková Šindlerová, A Klinke, and L Kubala. Modulation of Endothelial Glycocalyx Structure under Inflammatory Conditions. *Mediators of inflammation*, 2014:694312, 2014.
- [147] B van den Berg and H Vink. Glycocalyx perturbation: cause or consequence of damage to the vasculature? *American journal of physiology. Heart and circulatory physiology*, 290:H2174–H2175, 2006.

- [148] M J Mitchell and M R King. Computational and experimental models of cancer cell response to fluid shear stress. *Frontiers in oncology*, 3(March):44, 2013.
- [149] R L Schnaar. Glycans and glycan-binding proteins in immune regulation: A concise introduction to glycobiology for the allergist. *Journal of Allergy and Clinical Immunology*, 135(3):609–615, 2015.
- [150] C L Parsons. The Role of the Urinary Epithelium in the Pathogenesis of Interstitial Cystitis/Prostatitis/Urethritis. *Urology*, 69(4 SUPPL.), 2007.
- [151] V Iacovelli, L Topazio, G Gaziev, P Bove, G Vespasiani, and E Finazzi Agrò. Intravesical glycosaminoglycans in the management of chronic cystitis. *Minerva Urologica e Nefrologica*, 65(4):249–262, 2013.
- [152] M Gouverneur, J a E Spaan, H Pannekoek, R D Fontijn, and H Vink. Fluid shear stress stimulates incorporation of hyaluronan into endothelial cell glycocalyx. *American journal of physiology. Heart and circulatory physiology*, 290:H458–H452, 2006.
- [153] H Oberleithner, C Callies, K Kusche-Vihrog, H Schillers, V Shahin, C Riethmüller, G A MacGregor, and H E de Wardener. Potassium softens vascular endothelium and increases nitric oxide release. *Proceedings of the National Academy of Sciences*, 106(8):2829–2834, 2009.
- [154] V C Hascall and D Heinegard. Aggregation of Cartilage Proteoglycans. *The Journal of biological chemistry*, 249(13):4242–4249, 1974.
- [155] A Tengblad. Affinity chromatography on immobilized hyaluronate and its application to the isolation of hyaluronate binding proteins from cartilage. *Biochimica et biophysica acta*, 578:281–289, 1979.
- [156] J A Ripellino, M M Klinger, R U Margolis, and R K Margolis. The hyaluronic acid binding region as a specific probe for the localization of hyaluronic acid in tissue sections. Application to chick embryo and rat brain. *Journal of Histochemistry & Cytochemistry*, 33(10):1060–1066, 1985.
- [157] K D Costa and F C Yin. Analysis of indentation: implications for measuring mechanical properties with atomic force microscopy. *Journal of biomechanical engineering*, 121(5):462–471, 1999.
- [158] Q K Ong and I Sokolov. Attachment of nanoparticles to the AFM tips for direct measurements of interaction between a single nanoparticle and surfaces. *Journal of colloid and interface science*, 310(2):385–90, Jun 2007.

- [159] H J Butt, M Kappl, H Mueller, R Raiteri, W Meyer, and J Ruhe. Steric forces measured with the atomic force microscope at various temperatures. *Langmuir*, 15(7):2559–2565, 1999.
- [160] T A Franz-Odenaal, B K Hall, and P E Witten. Buried alive: How osteoblasts become osteocytes. *Developmental Dynamics*, 235(1):176–190, 2006.
- [161] S L Dallas and L F Bonewald. Dynamics of the Transition from Osteoblast to Osteocyte. *Annals of the New York Academy of Sciences*, March(1192):437–443, 2010.
- [162] K Tanaka-Kamioka, H Kamioka, H Ris, and S S Lim. Osteocyte shape is dependent on actin filaments and osteocyte processes are unique actin-rich projections. *Journal of bone and mineral research : the official journal of the American Society for Bone and Mineral Research*, 13(10):1555–1568, 1998.
- [163] H Kamioka, Y Sugawara, T Honjo, T Yamashiro, and T Takano-Yamamoto. Terminal differentiation of osteoblasts to osteocytes is accompanied by dramatic changes in the distribution of actin-binding proteins. *Journal of bone and mineral research : the official journal of the American Society for Bone and Mineral Research*, 19(3):471–478, 2004.
- [164] H Kodama, Y Amagai, H Sudo, S Kasai, and S Yamamoto. Establishment of a clonal osteogenic cell line from newborn mouse calvaria. *Journal of Oral Biology*, 23:899–901, 1981.
- [165] S M Woo, J Rosser, V Dusevich, I Kalajzic, and L F Bonewald. Cell line IDG-SW₃ replicates osteoblast-to-late-osteocyte differentiation in vitro and accelerates bone formation in vivo. *Journal of Bone and Mineral Research*, 26(11):2634–2646, 2011.
- [166] H Xu, J Zhang, J Wu, Y Guan, Y Weng, and P Shang. Oscillatory fluid flow elicits changes in morphology, cytoskeleton and integrin-associated molecules in MLO-Y₄ cells, but not in MC₃T₃-E₁ cells. *Biological Research*, 45:163–169, 2012.
- [167] H Xu, J Duan, L Ren, P Yang, R Yang, W Li, D Zhao, P Shang, and J X Jiang. Impact of flow shear stress on morphology of osteoblast-like IDG-SW₃ cells. *Journal of Bone and Mineral Metabolism*, pages 3–10, 2017.
- [168] I Sokolov, S Iyer, and C D Woodworth. Recovery of elasticity of aged human epithelial cells in vitro. *Nanomedicine: Nanotechnology, Biology and Medicine*, 2(1):31–36, 2006.

- [169] M Sato, K Nagayama, N Kataoka, M Sasaki, and K Hane. Local mechanical properties measured by atomic force microscopy for cultured bovine endothelial cells exposed to shear stress. *Journal of Biomechanics*, 33(1):127–135, 2000.
- [170] A Schaefer, J te Riet, K Ritz, M Hoogenboezem, E C Anthony, F P J Mul, C J de Vries, M J Daemen, C G Figdor, J D van Buul, and P L Hordijk. Actin-binding proteins differentially regulate endothelial cell stiffness, ICAM-1 function and neutrophil transmigration. *Journal of Cell Science*, 127(20):4470–4482, 2014.
- [171] E Canetta, A Riches, E Borger, S Herrington, K Dholakia, and A K Adya. Discrimination of bladder cancer cells from normal urothelial cells with high specificity and sensitivity: combined application of atomic force microscopy and modulated Raman spectroscopy. *Acta biomaterialia*, 10(5):2043–55, May 2014.
- [172] T C Laurent and R E Fraser. Hyaluronan. *The FASEB Journal*, 6:2397–2404, 1992.
- [173] S P Evanko, M I Tammi, R H Tammi, and T N Wight. Hyaluronan-dependent pericellular matrix. *Advanced Drug Delivery Reviews*, 59(13):1351–1365, 2007.
- [174] B P Toole. Hyaluronan: from extracellular glue to pericellular cue. *Nature reviews. Cancer*, 4(7):528–539, 2004.
- [175] C A de la Motte, V C Hascall, J Drazba, S K Bandyopadhyay, and S A Strong. Mononuclear leukocytes bind to specific hyaluronan structures on colon mucosal smooth muscle cells treated with polyinosinic acid:polycytidylic acid: inter-alpha-trypsin inhibitor is crucial to structure and function. *The American journal of pathology*, 163(1):121–133, 2003.
- [176] K Rilla, R Tiihonen, A Kultti, M Tammi, and R Tammi. Pericellular Hyaluronan Coat Visualized in Live Cells With a Fluorescent Probe Is Scaffolded by Plasma Membrane Protrusions. *Journal of Histochemistry and Cytochemistry*, 56(10):901–910, 2008.
- [177] V Koistinen, T Jokela, S Oikari, R Kärnä, and M Tammi. Hyaluronan-positive plasma membrane protrusions exist on mesothelial cells in vivo. *Histochemistry and Cell Biology*, 145(5):531–544, 2016.
- [178] Z Zhang. Chondrons and the Pericellular Matrix of Chondrocytes. *Tissue Engineering Part B: Reviews*, 21(3):150127064140006, 2014.

- [179] P Juffer, A D Bakker, J Klein-Nulend, and R T Jaspers. Mechanical Loading by Fluid Shear Stress of Myotube Glycocalyx Stimulates Growth Factor Expression and Nitric Oxide Production. *Cell Biochemistry and Biophysics*, 69(3):411–419, 2014.
- [180] A Bignami, M Hosley, and D Dahl. Hyaluronic acid and hyaluronic acid-binding proteins in brain extracellular matrix. *Anatomy and embryology*, 188:419–433, 1993.
- [181] A R Pries, T W Secomb, and P Gaehtgens. The endothelial surface layer. *Pflugers Archiv : European journal of physiology*, 440(5):653–666, Apr 2000.
- [182] B M Fu and J M Tarbell. Mechano-sensing and transduction by endothelial surface glycocalyx: composition, structure, and function. *Wiley interdisciplinary reviews. Systems biology and medicine*, 5(3):381–90, 2013.
- [183] C B Henry and B R Duling. Permeation of the luminal capillary glycocalyx is determined by hyaluronan. *The American journal of physiology*, 277(2 Pt 2):H508–H514, 1999.
- [184] D Liu, L Ge, F Wang, H Takahashi, D Wang, Z Guo, S H Yoshimura, T Ward, X Ding, K Takeyasu, and X Yao. Single-molecule detection of phosphorylation-induced plasticity changes during ezrin activation. *FEBS Letters*, 581(18):3563–3571, 2007.
- [185] T Das, K Safferling, S Rausch, N Grabe, H Boehm, and J P Spatz. A molecular mechanotransduction pathway regulates collective migration of epithelial cells. *Nature Cell Biology*, 17(3):276–287, 2015.
- [186] R Afrin and A Ikai. Force profiles of protein pulling with or without cytoskeletal links studied by AFM. *Biochemical and Biophysical Research Communications*, 348(1):238–244, 2006.
- [187] F Rico, C Chu, M H Abdulreda, Y Qin, and V T Moy. Temperature modulation of integrin-mediated cell adhesion. *Biophysical Journal*, 99(5):1387–1396, 2010.
- [188] C Chu, E Celik, F Rico, and V T Moy. Elongated Membrane Tethers, Individually Anchored by High Affinity $\alpha 4 \beta 1$ /VCAM-1 Complexes, Are the Quantal Units of Monocyte Arrests. *PLoS ONE*, 8(5), 2013.
- [189] E Sariisik, C Popov, J P Müller, D Docheva, H Clausen-Schaumann, and M Benoit. Decoding Cytoskeleton-Anchored and Non-Anchored Receptors from Single-Cell Adhesion Force Data. *Biophysical Journal*, 109(7):1330–1333, 2015.

- [190] B Liu and J Shao. Tangential tether extraction and spontaneous tether retraction of human neutrophils. *Biophysical Journal*, 103(11):2257–2264, 2012.
- [191] K Maki, S Han, Y Hirano, S Yonemura, T Hakoshima, and T Adachi. Mechano-adaptive sensory mechanism of α -catenin under tension. *Scientific Reports*, 6(1):24878, 2016.
- [192] M Schlierf and M Rief. Temperature softening of a protein in single-molecule experiments. *Journal of Molecular Biology*, 354(2):497–503, 2005.
- [193] A Pietuch, B R Brückner, and A Janshoff. Membrane tension homeostasis of epithelial cells through surface area regulation in response to osmotic stress. *Biochimica et Biophysica Acta - Molecular Cell Research*, 1833(3):712–722, 2013.
- [194] G I Bell. Models for the specific adhesion of cells to cells. *Science*, 200:618–627, 1978.
- [195] E Evans and K Ritchie. Dynamic strength of molecular adhesion bonds. *Biophysical journal*, 72(4):1541–55, 1997.
- [196] A Harder, V Walhorn, T Dierks, X Fernández-Busquets, and D Anselmetti. Single-molecule force spectroscopy of cartilage aggrecan self-adhesion. *Biophysical Journal*, 99(November):3498–3504, 2010.
- [197] O K Dudko, G Hummer, and A Szabo. Intrinsic rates and activation free energies from single-molecule pulling experiments. *Physical Review Letters*, 96(10):1–4, 2006.
- [198] O K Dudko, G Hummer, and A Szabo. Theory, analysis, and interpretation of single-molecule force spectroscopy experiments. *Proceedings of the National Academy of Sciences*, 105(41):15755–15760, 2008.
- [199] H A Kramers. Brownian motion in a field of force and the diffusion model of chemical reactions. *Physica*, VII(4):284–304, 1940.
- [200] M K Cowman, C Spagnoli, D Kudasheva, M Li, A Dyal, S Kanai, and E A Balazs. Extended, relaxed, and condensed conformations of hyaluronan observed by atomic force microscopy. *Biophysical journal*, 88(1):590–602, 2005.
- [201] L Wang, K J Livak, and C J Wu. High-dimension single-cell analysis applied to cancer. *Molecular Aspects of Medicine*, 2017.

- [202] E Papalexi and R Satija. Single-cell RNA sequencing to explore immune cell heterogeneity. *Nature Reviews Immunology*, 2017.
- [203] S Barreto, C M Perrault, and D Lacroix. Structural finite element analysis to explain cell mechanics variability. *Journal of the Mechanical Behavior of Biomedical Materials*, 38:219–231, 2014.
- [204] S I Barry, K H Parkerf, and G K Aldis. Fluid flow over a thin deformable porous layer. *Journal of Applied Mathematics and Physics*, 42(September):633–648, 1991.
- [205] E R Damiano and T M Stace. A mechano-electrochemical model of radial deformation of the capillary glycocalyx. *Biophysical journal*, 82(March):1153–1175, 2002.
- [206] Y Han, S Weinbaum, J A E Spaan, and H Vink. Large-deformation analysis of the elastic recoil of fibre layers in a Brinkman medium with application to the endothelial glycocalyx. *Journal of Fluid Mechanics*, 554:217, 2006.
- [207] H Schillers, C Rianna, J Schäpe, T Luque, H Doschke, M Wälte, J J Uriarte, N Campillo, G P A Michanetzis, J Bobrowska, A Dumitru, E T Herruzo, S Bovio, P Parot, M Galluzzi, A Podestà, L Puricelli, S Scheuring, Y Misirlis, R Garcia, M Odorico, J Teulon, F Lafont, M Lekka, F Rico, A Rigato, J Pellequer, H Oberleithner, D Navajas, and M Radmacher. Standardized Nanomechanical Atomic Force Microscopy Procedure (SNAP) for Measuring Soft and Biological Samples. *Scientific Reports*, 7(1):5117, 2017.
- [208] C Verdier. Rheological properties of living materials. From cells to tissues. *Journal of Theoretical Medicine*, 5(2):67–91, 2003.
- [209] Y Abidine, R Michel, A Duperray, and C Verdier. Microrheology of complex systems and living cells using AFM. *Computer Methods in Biomechanics and Biomedical Engineering*, 16(July):15–16, 2013.
- [210] J Alcaraz, L Buscemi, M Grabulosa, X Trepas, B Fabry, R Farré, and D Navajas. Microrheology of human lung epithelial cells measured by atomic force microscopy. *Biophysical journal*, 84(3):2071–9, 2003.
- [211] S Park, D Koch, R Cardenas, J Käs, and C K Shih. Cell Motility and Local Viscoelasticity of Fibroblasts. *Biophysical Journal*, 89(6):4330–4342, 2005.
- [212] A Raman, S Trigueros, A Cartagena, A P Z Stevenson, M Susilo, E Nauman, and S Antoranz Contera. Mapping nanomechanical properties of live cells using multi-harmonic atomic force microscopy. *Nature Nanotechnology*, 6(12):809–814, 2011.

- [213] G Kaur and J M Dufour. Cell lines: Valuable tools or useless artifacts. *Spermatogenesis*, 2(1):1–5, 2012.
- [214] R J Geraghty, A Capes-Davis, J M Davis, J Downward, R I Freshney, I Knezevic, R Lovell-Badge, J R W Masters, J Meredith, G N Stacey, P Thraves, and M Vias. Guidelines for the use of cell lines in biomedical research. *British Journal of Cancer*, 111(6):1021–1046, 2014.
- [215] K M Job, R O Dull, and V Hlady. Use of reflectance interference contrast microscopy to characterize the endothelial glycocalyx stiffness. *AJP: Lung Cellular and Molecular Physiology*, 302(12):L1242–L1249, Jun 2012.
- [216] N Nijenhuis, D Mizuno, J A E Spaan, and C F Schmidt. High-resolution microrheology in the pericellular matrix of prostate cancer cells. *Journal of The Royal Society Interface*, 9(73):1733–1744, 2012.
- [217] B Liu, T J Kim, and Y Wang. Live cell imaging of mechanotransduction. *Journal of The Royal Society Interface*, 7:S365–S375, 2010.
- [218] E K Paluch, C M Nelson, N Biais, B Fabry, J Moeller, B L Pruitt, C Wollnik, G Kudryasheva, F Rehfeldt, and W Federle. Mechanotransduction: use the force(s). *BMC Biology*, 13(1):47, 2015.
- [219] T F Cootes, A Hill, C J Taylor, and J Haslam. Use of active shape models for locating structures in medical images. *Image and Vision Computing*, 12:355–365, 1994.
- [220] N Sarkalkan, H Weinans, and A A Zadpoor. Statistical shape and appearance models of bones. *Bone*, 60:129–140, 2014.
- [221] C J Bennetts, S Sibole, and A Erdemir. Automated generation of tissue-specific three-dimensional finite element meshes containing ellipsoidal cellular inclusions. *Computer Methods in Biomechanics and Biomedical Engineering*, 18(12):1293–1304, 2015.

Alphabetical Index

Atomic Force Microscopy	17, 38, 73, 108, 142, 171, 188, 190
Bone cells	10
Osteoblasts	10, 104, 111
Osteocytes	11, 104
Pre-Osteoblasts	103, 111, 140
Pre-Osteocytes	37, 73, 105, 111, 169
Brush model	74
Confocal imaging	81, 110
Cytoskeleton	9, 110, 131, 137, 181
Finite Element Modelling	28, 171, 190, 194
Glycocalyx	9, 61, 68, 81, 136, 185, 189, 192
Hertz model	21, 44, 58, 73, 110, 177
Hyaluronic Acid	26, 68, 81, 135
Mechanotransduction	13, 165, 187
Nano-indentation	21, 22, 38, 73, 108, 171, 188, 190
Point-wise approach	80
Sample size	47, 51, 128
Single Molecule Force Spectroscopy	25, 142, 189, 193
Young's modulus	21, 44, 191
Glycocalyx	22, 87, 90
Osteoblasts	21, 126
Osteocytes	22, 126, 127
Pre-Osteoblasts	21, 126, 127
Pre-Osteocytes	22, 50, 126, 127